2nd Conference of International Consortium on Terahertz Photonics and Optoelectronics

PROGRAM AND PROCEEDINGS

FIR-LAB

International Research Network
"Bright Far-Infrared Optoelectronic Sources to Field-Matter Interaction Studies, Life Sciences and Enviromental Monitoring"
2nd Workshop

July 6–7, 2019

TERA RJUSE 2019 TECH
N. Novgorod

8th **R**ussia-**J**apan-**US**A-**E**urope Symposium
on Fundamental & Applied Problems
of **Tera**hertz Devices
& **Tech**nologies

July 8–11, 2019

Nizhny Novgorod, Russia, 2019

Organizers

Ministry of Science and Higher Education of the Russian Federation
Institute for Physics of Microstructures — Branch of Federal Research Center Institute of Applied Physics, RAS
Federal Research Center Crystallography and Photonics, RAS
Physical Science Department, RAS
Scientific Council on Physics of Semiconductors, RAS
Lobachevsky State University of Nizhny Novgorod
Charitable Foundation "From heart to heart"

Chairs

Juliette Mangeney, *Laboratoire de Physique, ENS, France*
Alexandre Shkurinov, *Lomonosov Moscow State University, Russia*
Vladimir Gavrilenko, *Inst. for Physics of Microstructures, Russia*
Victor Ryzhii, *Tohoku Univ., Japan & IUHFSE RAS, Russia*
Taiichi Otsuji, *Tohoku Univ., Japan*

Organizing Committee

Vladimir Gavrilenko, Sergey Morozov, Alexandre Dubinov,
Inst. for Physics of Microstructures, RAS, Russia

Alexandre Shkurinov, Anton Ikonnikov,
Lomonosov Moscow State University, Russia

RJUSE Steering Committee

Hans Hartnagel, *Technical Univ., Darmstadt, Germany*
Valeriy Karasik, *Bauman Moscow State Tech. Univ., Russia*
Wojciech Knap, *CNRS Montpellier, France & IHPP PAS Unipress, Poland*
Vladimir V. Mitin, *Univ. Buffalo, SUNY, USA*
Taiichi Otsuji, *Chair, Tohoku Univ., Japan*
Maxim Ryzhii, *Aizu Univ., Japan*
Victor Ryzhii, *Tohoku Univ., Japan & IUHFSE RAS, Russia*
Akira Satou, *Tohoku Univ., Japan*
Sergei Shapoval, *IMTHPM, RAS, Russia*
Michael S. Shur, *Rensselaer Polytechnic Inst., USA*

RJUSE Technical Programme Committee

Vladimir Gavrilenko, *Chair, Inst. for Physics of Microstr., RAS, Russia*
Alexandre Shkurinov, *Lomonosov Moscow State University, Russia*
Sergey Morozov, *Inst. for Physics of Microstructures, RAS, Russia*
Anton Ikonnikov, *Lomonosov Moscow State University, Russia*
Alexandre Dubinov, *Inst. for Physics of Microstructures, RAS, Russia*
Wojciech Knap, *CNRS Montpellier, France & IHPP PAS Unipress, Poland*
Akira Satou, *Tohoku Univ., Japan*
Vladimir Mitin, *Univ. Buffalo, SUNY, USA*
Victor Ryzhii, *Tohoku Univ., Japan & IUHFSE RAS, Russia*
Taiichi Otsuji, *Tohoku Univ., Japan*

International Research Network **“Bright Far-Infrared Optoelectronic Sources to Field-Matter Interaction Studies, Life Sciences and Enviromental Monitoring”** (**IRN FIR-LAB**) was created in 2017 by Agreement between French (CNRS, UPD, UPMC, ENS) and Russian (MSU, RFBR) institutions for 2018–2021 year to coordinate scientific activities between laboratories making up this network falling into the scope:

- propagation of FIR/THz beams in atmosphere;
- high power FIR/THz sources;
- FIR/THz field-matter interaction studies;
- FIR/THz plasmonics, metamaterials, nanomaterials
- applications.

1st IRN FIR-LAB meeting was carried out in July 3-4, 2018 at École Normale Supérieure, Paris.

Based on the successful organizations of preceding Russia-Japan-USA-Europe (**RJUSE**) symposia in Japan, Russia, USA and Poland the 8th RJUSE is organized in Nizhny Novgorod, Russia, on July 08–11, 2019. The symposium aims to bring together researchers who tackle “Fundamental & Applied Problems in Terahertz Devices & Technologies”, so as to stimulate discussions on the state-of-the-art results and promote the collaborations in the following topics:.

THz physics

- Carrier transport & quantum effects in devices;
- Nonequilibrium carrier dynamics;
- 2D materials & their heterostructures;
- Terahertz properties of Dirac matter.

THz devices & electronic/optical components

- Sub-THz/THz transistors, mixers, etc.;
- Metamaterials, photonic crystals;
- Surface-plasmon-polaritons;
- Electronic/photonic/plasmonic devices;
- Nonlinear optics based devices;
- Superconductors, bolometers, etc.

THz applications

- Wireless communications;
- Imaging;
- Spectroscopy;
- Astronomy.

Conference venue

2nd Conference of International Consortium on Terahertz Photonics and Optoelectronics will be held in the Institute for Physics of Microstructures (IPM) of Russian Academy of Sciences, 7 Akademicheskaya Str., Nizhny Novgorod.

IPM building is located at the border of Nizhny Novgorod, 9 km away from the city center (Kremlin). The Institute for Physics of Microstructures of the Russian Academy of Sciences (IPM) was founded on the base on the Solid State Physics Division of the Institute of Applied Physics of Russian Academy of Science in 1993. Since 2016 IPM is a branch of the Federal Research Centre "Institute of Applied Physics of Russian Academy of Science". The main scientific directions of IPM include physics, technology and diagnostics of solid-state micro- and nanostructures, multilayer X-ray and UV optics, silicon optoelectronics, spectroscopy, spectrometry and electronics of THz and subTHz ranges, physics of superconductors and superconductor electronics.

Nizhny Novgorod is the fifth-largest city in Russia with population of 1.25 million people. In the historic part of the city there are a large number of universities, theaters, museums and churches. Nizhny Novgorod is located about 400 km east of Moscow, where the Oka River empties into the Volga. From 1932 to 1990, it was known as Gorky after the writer Maxim Gorky, who was born there.

The city was founded in 1221 by Prince Yuri II of Vladimir. In 1612 Kuzma Minin and Prince Dmitry Pozharsky organized in Nizhny Novgorod an army for the liberation of Moscow from the Poles. In 1817 Nizhny Novgorod became a great trade center of the Russian Empire. In 1896 an All-Russia Exhibition was organized at Nizhny Novgorod fair. During the Soviet period, the city turned into an important industrial center. In particular, the Gorky Automobile Plant was constructed in this period. During World War II, Gorky became the biggest provider of military equipment to the Eastern Front. Nowadays Nizhny Novgorod is a large industrial, cultural and scientific center of the Russian Federation and the main center of river tourism in Russia.

International Research Network
"Bright Far-Infrared Optoelectronic Sources to Field-Matter Interaction Studies, Life Sciences and Enviromental Monitoring"

2nd Workshop Program

July 6, 2019 – Saturday

Special session devoted to the KOMFI Project: "Informative characteristics of socially significant diseases in the terahertz frequency range: the multimodal studies of biological tissues, fluids and exhaled breath»

Chair: Alexander Shkurinov

	Yury Kistenev, *Tomsk State University, Tomsk, Russia* Project 1: Molecular imaging of oncological pathologies of biological tissues in the terahertz spectral region using time-resolved laser spectroscopy, big data analysis technologies and machine learning	Sat-0-1
10:00-12:00	Vladimir Vaks, *Institute for Physics of Microstructures RAS, Nizhny Novgorod, Russia* Project 2: Development of scientific and methodological basis of the use of THz radiation for selective diagnostics based on the control of metabolites in exhaled air in oncological diseases	Sat-0-2
	Maxim Nazarov, *National Research Center «Kurchatov Institute», Moscow, Russia* Project 3: Multispectral diagnostics of human fluids for the determination of informative features of socially significant diseases in the terahertz frequency range	Sat-0-3
	Olga Smolyanskaya, *ITMO University, Saint Petersburg, Russia* Project 4: Imaging of biological tissues (bio-imaging) using magnetic nanoparticles and hyperosmotic agents	Sat-0-4
12:20-13:40	**Lunch**	
14:00-14:20	**Opening Ceremony** ***Juliette Mangeney, Jean-Louis Coutaz, Alexander Shkurinov***	

Session Sat-1: Terahertz air- and liquid photonics

Chair: Wojciech Knap

14:20-14:40	Arnaud Couairon, *Centre de Physique Theorique, Ecole polytechnique, CNRS, Institut Polytechnique de Paris, France* Secondary emission from the plasma generated by organized superfilaments	Sat-1-1

14:40-15:00	Olga Kosareva, *Lomonosov Moscow State University, Moscow, Russia* THz yield dependence on the initial and local phase shift in a two-color filament	Sat-1-2
15:00-15:20	Leonid Seleznev, *P.N. Lebedev Physical Institute of Russian Academy of Sciences, Moscow, Russia* THz radiation spectra emitted by a single-color infrared and ultraviolet filaments	Sat-1-3
15:20-15:40	Alexei Balakin, *Lomonosov Moscow State University, Moscow, Russia* Generation of Terahertz Radiation from Liquid Nitrogen	Sat-1-4
15:40-16:00	Maxim Nazarov, *National Research Center «Kurchatov Institute», Moscow, Russia* Efficient conversion of intense laser pulses to THz in a low pressure gas	Sat-1-5
16:00-16:40	**Coffee break**	
	Session Sat-2: Biomedical applications of THz waves ***Chair: Juliette Mangeney***	
16:40-17:00	Yury Kistenev, *Tomsk State University, Tomsk, Russia* Breathomics Applications of IR and Terahertz Spectroscopy and Machine Learning	Sat-2-1
17:00-17:20	Olga Smolvanskava, *ITMO University, Saint Petersburg, Russia* Interaction of terahertz radiation with bio-like objects: theoretical and numerical modelling, real objects and phantom experiments	Sat-2-2
17:20-17:40	Valery Tuchin, *Research-Educational Institute of Optics and Biophotonics, Saratov State University, Saratov, Russia* Research and development of effective optical technologies for diagnostics in dermatology	Sat-2-3
17:40-18:00	Vladimir Vaks, *Institute for Physics of Microstructures RAS, Nizhny Novgorod, Russia* Spectroscopy of pre-cancer states with using THz emitters based on superlattices	Sat-2-4
18:00-18:20	Olga Cherkasova, *Institute of Laser Physics of SB RAS, Novosibirsk, Russia* Theoretical and experimental analysis of the mechanisms of the interaction of terahertz radiation with neurons	Sat-2-5

July 7, 2019 – Sunday

Session Su-1: Terahertz nonlinear phenomena

Chair: Alexei Baranov

9:00-9:20	Tamara Pogosian, *ITMO University, Saint Petersburg, Russia* Controllable synthesis of DAST submicron crystals and their microstructuration by direct laser writing	Su-1-1
9:20-9:40	Igor Denisyuk, *ITMO University, Saint Petersburg, Russia* Co-crystal 4-aminopyridine-4-nitrophenol-4- nitrophenolate for terahertz applications	Su-1-2
9:40-10:00	Yuri Klimachev, *P.N. Lebedev Physical Institute of Russian Academy of Sciences, Moscow, Russia* Numerical study of $ZnGeP_2$ and GaSe crystals for CO laser down-conversion into the THz range	Su-1-3
10:40-11:00	Jean-Louis Coutaz, *IMEP-LAHC, UMR CNRS 5130, Universite Savoie Mont-Blanc, Campus scientifique, 73376 Le Bourget du Lac Cedex, France* Towards sub-wavelength THz imaging through nonlinear optical techniques	Su-1-4
11:00-11:20	**Coffee break**	

Session Su-2: Semiconductor and nanotechnologies in THz phonics

Chair: Vladimir Vaks

11:20-11:40	Wojciech Knap, *Charles Coulomb Laboratory, University of Montpellier&CNRS, Montpellier, France* THz Cyclotron Emission from HgCdTe Alloys with Dirac-like Band Structure	Su-2-1
11:40-12:00	Juliette Mangeney, *Laboratoire de Physique de l'Ecole Normale Superieure, ENS, Université PSL, CNRS, Sorbonne Université, Université Paris-Diderot, Sorbonne Paris Cité, Paris, France* THz excited state level spacing in encapsulated graphene quantum dots	Su-2-2
12:00-12:20	Vladimir Rumyantsev, *Institute for Physics of Microstructures RAS, Nizhny Novgorod, Russia* Terahertz emission from HgCdTe quantum wells under long-wavelength optical pumping	Su-2-3
12:20-13:40	**Lunch**	

13:40-14:00	Alexei Baranov, *Institute of Electronics and Systems (IES), UMR 5214 CNRS - University of Montpellier, France* Terahertz Quantum Cascade Laser with Non-Resonant Depopulation	Su-2-4
14:00-14:20	Jean-Francois Lampin, *Terahertz Photonics Group, Institute of Electronics Microelectronics and Nanotechnology (IEMN) UMR CNRS 8520, Lille University, Villeneuve d'Ascq, France* Molecular THz lasers pumped by mid-infrared quantum cascade lasers	Su-2-5
14:20-14:40	Andrei Kanaev, *Laboratoire des Sciences des Procedes et des Materiaux (LSPM), CNRS, Université Paris 13, Villetaneuse, France* Fundamental principles for the development of new functional nanocomposite materials based on oxide 3D nanostructures for applications in THz optics and information transfer	Su-2-6
14:40-15:20	**Coffee break**	

Session Su-3: THz spectroscopy

Chair: Jean-Francois Lampin

15:00-15:20	Mikhail Tretyakov, *Institute of Applied Physics RAS, Nizhniy Novgorod, Russia* Experimental study and modeling of the spectral line shape and continuum absorption by atmospheric molecules in the THz range	Su-3-1
15:20-15:40	Maud Rotger, *University of Reims Champagne-Ardenne, Reims, France* Rovibrational Spectroscopy of the Ground-State and some Fundamental Bands of SO_2F_2	Su-3-2
15:40-16:00	**Closing remarks**	

8th Russia-Japan-USA-Europe Symposium on Fundamental & Applied Problems of Terahertz Devices & Technologies

Program

July 8, 2019 – Monday

10:00-10:20	**Opening Ceremony** ***Vladimir Gavrilenko, Taiichi Otsuji, Victor Ryzhii***	
	Session Mo-1: THz plasmonic detectors ***Chair: T.Otsuji***	
10:20-11:0 0	W. Knap. THz plasma oscillations in field effect structures: from first discoveries to nowadays applications *(plenary)*	Mo-1-1
11:00-11:30	V.Y. Kachorovskii, I.V. Gorbenko, M.S. Shur. Plasmonic helicity-driven detector of terahertz radiation *(invited)*	Mo-1-2
11:30-12:00	**Coffee break**	
	Session Mo-2: THz spectroscopy of semiconductor heterostructures ***Chair: W.Knap***	
12:00-12:30	D. Yavorskiy, J. Wróbel, T. Wojtowicz, J. Łusakowski. Terahertz excitations of a two-dimensional electron gas in CdTe-based quantum wells *(invited)*	Mo-2-1
12:30-12:50	A.S. Kazakov, A.V. Galeeva, A.I. Artamkin, S.A. Dvoretskiy, N.N. Mikhailov, M.I. Bannikov, S.N. Danilov, L.I. Ryabova, D.R. Khokhlov. Nonlocal transport of photoexcited carriers in terahertz spectral range in epitaxial $Hg_{1-x}Cd_xTe$ films with the inverted band structure	Mo-2-2
12:50-13:10	D.V. Kozlov, V.V. Rumyantsev, A.M. Kadykov, M.A. Fadeev, N.S. Kulikov, V.V. Utochkin, N.N. Mikhailov, S.A. Dvoretskiy, V.I. Gavrilenko, H.-W. Hübers, F. Teppe, S.V.Morozov. Terahertz photoluminescence from $HgTe/Hg_{1-x}Cd_xTe$ quantum well heterostructures due to valence band – acceptor transitions	Mo-2-3
13:10-13:30	F. Bayer, W. Beugeling, R. Schlereth, H. Buhmann, L.W. Molenkamp, T. Kiessling. Time-domain terahertz Faraday spectroscopy of the 3D topological insulator HgTe	Mo-2-4
13:30-15:00	**Lunch**	

Session Mo-3: THz photonics

Chair: V.Ryzhii

15:00-15:30	D. Svintsov. Two-dimensional terahertz plasmons in hydrodynamic electron fluids *(invited)*	Mo-3-1
15:30-16:00	E.V. Yakovlev, N.P. Kryuchkov, K.A. Komarov, S.O. Yurchenko. 2D colloids in rotating electric fields: tunable interactions and particle-resolved studies of generic phenomena *(invited)*	Mo-3-2
16:00-16:30	**Coffee break**	

Session Mo-4: Medical diagnostics

Chair: J.Łusakowski

16:30-17:00	K.I. Zaytsev, I.N. Dolganova N.V. Chernomyrdin, G.M. Katyba, A.A. Gavdush, V.E. Karasik, V.N. Kurlov, G.A. Komandin, A.A. Potapov, I.V. Reshetov, V.V. Tuchin. Prospects for human brain glioma diagnosis using terahertz spectroscopy and imaging *(invited)*	Mo-4-1
17:00-17:20	V.L. Vaks, M.B. Chernyaeva, E.G. Domracheva, S.I. Pripolzin, A.A. Yablokov, W. Knap. High resolution THz spectrometer based on semiconductor devices for medical diagnostics	Mo-4-2

July 9, 2019 – Tuesday

Session Tu-1: THz sources

Chair: H.-W.Hübers

09:00-09:40	T. Otsuji, D. Yadav, S. Boubanga-Tombet, T. Watanabe, A.A. Dubinov, V. Ryzhii. Graphene-based van der Waals heterostructures towards a new type of terahertz quantum-cascade lasers *(plenary)*	Tu-1-1
09:40-10:10	S.V. Morozov, V.I. Gavrilenko, V.V. Rumyantsev, M.A. Fadeev, V.V. Utochkin, N.S. Kulikov, A.A. Dubinov, V.Ya. Aleshkin, N.N. Mikhailov, S.A. Dvoretskii, F. Teppe, C. Sirtori. Long wavelength stimulated emission in HgTe/CdHgTe quantum well heterostructures *(invited)*	Tu-1-2
10:10-10:30	A.A. Andronov, A.V. Ikonnikov, K.V. Maremianin, V.I. Pozdniakova, Y.N. Nozdrin, A.A. Marmalyuk, A.A. Padalitsa, M.A. Ladugin, V.A. Belyakov, I.V. Ladenkov, A.G. Fefelov. Universal simple weak barrier SL-based broad band tunable sources at any THz?	Tu-1-3
10:30-10:50	I.V. Altukhov, M.S. Kagan, S.K. Paprotskiy, N.A. Khvalkovskiy, I.A. Kohn, I.S. Vasil'evskii, A.N. Vinichenko, N.D. Il'inskaya, A.A. Usikova, A.N. Baranov, R. Teissier. Tunneling conductivity in GaAs/AlAs superlattices with electric domains	Tu-1-4

10:50-11-10	A.A. Dubinov, A.A. Afonenko, D.V. Ushakov, V.Ya. Aleshkin, R.A. Khabibullin. Room temperature terahertz HgCdTe-based quantum cascade laser	Tu-1-5
11:10-11-30	V.G. Popov, V.G. Krishtop, S.G. Chigarev, T.I. Ahmedov, M. Henini. Polarons in semiconductor heterostructures and their possible application in terahertz sources	Tu-1-6
11:30-12:00	**Coffee break**	

Session Tu-2: Excitons & impurities

Chair: S. Morozov

12:00-12:30	A.V. Andrianov, A.O. Zakhar'in. Terahertz photoluminescence from free excitons in silicon. *(invited)*	Tu-2-1
12:30-13:00	V.N. Shastin. Silicon based THz lasing *(invited)*	Tu-2-2
13:00-13:30	S.G. Pavlov, N. Deßmann, A. Pohl, R.Kh. Zhukavin, K.A. Kovalevsky, S.A. Tarelkin, V.S. Bormashov, Yu.Yu. Choporova, S.A. Lynch, K.L. Litvinenko, B. Redlich, N. Stavrias, A.F.G. van der Meer, V.V. Tsyplenkov, N.A. Bekin, V.N. Shastin, B.A. Knyazev, S.A. Terentiev, V.D. Blank, B. Murdin, S. Winnerl, J.M. Klopf, N.V. Abrosimov, H. Riemann, H.-W. Hübers. Dynamics of Terahertz Excitations in Group-IV Semiconductors Doped by Hydrogen-Like Impurity Centers *(invited)*	Tu-2-3
13:30-15:00	**Lunch**	

Session Tu-3: THz spectroscopy

Chair: V. Kachorovskii

15:00-15:30	H.-W. Hübers, T. Alam, T. Hagelschuer, H. Richter, M. Wienold. High resolution spectroscopy with terahertz quantum-cascade lasers *(invited)*	Tu-3-1
15:30-15:50	S.R. Yegiyan, L.N. Alyabyeva, V.I. Torgashev, D.A. Vinnik, S.A. Gudkova, A.S. Prokhorov, M. Dressel, B.P. Gorshunov. Terahertz-infrared spectroscopy of single crystalline M-type hexaferrite $BaTi_xFe_{12-x}O_{19}$	Tu-3-2
15:50-16:10	M. Belyanchikov, M. Savinov, P. Bednyakov, Z. Bedran, V. Thomas, V. Torgashev, V.B. Anzin, A. Loidl, P. Lunkenheimer, E. Zhukova, E. Uykur, M. Dressel, B. Gorshunov. Terahertz dynamics of a network of nanoconfined electric dipoles	Tu-3-3
16:10-16:30	**Coffee break**	
16:30-18:00	**Poster session**	

July 10, 2019 – Wednesday

Session Wed-1: Carbon nanostructures

Chair: A.Dubinov

09:00-09:40	V. Ryzhii, T. Otsuji, M. Ryzhii, V. Leiman, V.E. Karasik, D. Ponomarev, P.P. Matsev, V. Mitin, M.S. Shur. Graphene/black As_xP_{1-x} heterostructures for terahertz and infrared devices *(plenary)*	Wed-1-1
09:40-10:10	G.E. Fedorov, D. Svintsov, D. Bandurin, I. Gayduchenko, G. Goltsman. Graphene based plasmonic interferometer for terahertz radiation detection *(invited)*	Wed-1-2
10:10-10:40	D.V. Fateev, K.V. Mashinsky, I.M. Moiseenko, O.V. Polischuk, V.V. Popov. Excitation of the propagating "nonradiative" plasmon modes in a periodic graphene structures *(invited)*	Wed-1-3
10:40-11:00	S.S. Zhukov, D.S. Kopylova, A.P. Tsapenko, A.V. Mogorychnaia, E.S. Zhukova, A.G. Nasibulin, B.P.Gorshunov. Influence of the length of the CNT and plasma treatment on the terahertz conductivity spectra of CNT films	Wed-1-4
11:00-11:20	M.Yu. Morozov, V.V. Popov. Giant amplification of terahertz plasma waves in tapered heterostructure with active graphene	Wed-1-5
11:20-11:40	Z.V. Gagkaeva, K.A. Motovilov, V. Grinenko, M. Savinov, L.S. Kadyrov, A.A. Pronin, Z.V. Bedran, E.S. Zhukova, A.B. Mostert, B.P. Gorshunov. Broadband dielectric spectroscopy of eumelanin	Wed-1-6
11:40-12:10	**Coffee break**	

Session Wed-2: Graphene & Gyrotrons

Chair: M.Bakunov

12:10-12:40	V. Perebeinos. Plasmonics with graphene nanoribbons *(invited)*	Wed-2-1
12:40-13:10	M.Yu. Glyavin. Gyrotrons for high-power terahertz science and technologies *(invited)*	Wed-2-2
13:10-13:30	G.G. Denisov, A.V. Chirkov, A.P. Fokin, A.N. Kuftin, M.V. Morozkin, M.D. Proyavin, A.S. Sedov, E.M. Tai, A.I. Tsvetkov, M.Yu. Glyavin. Development of CW 527 GHz gyrotron for DNP/NMR spectroscopy	Wed-2-3
13:30-15:00	**Lunch**	
15:00-18:00	**Excursion**	

July 11, 2019 – Thursday

Session Thu-1: THz time-domain spectroscopy

Chair: G. Goltsman

09:00-09:30	D.V. Lavrukhin, I.A. Glinskiy, R.A. Khabibullin, A.V. Arsenin, V.S. Volkov, I.V. Minin, O.V. Minin, K.I. Zaytsev, D.S. Ponomarev. Improving of a terahertz radiation efficiency due to optical light confinement in nanoantennas *(invited)*	Thu-1-1
09:30-10:00	M.I. Bakunov, M.V. Tsarev, A.V. Maslov, E.S. Efimenko, S.A. Sychugin. Optically generated terahertz pulses with high-field DC precursors *(invited)*	Thu-1-2
10:00-10:20	S.B. Bodrov, M.Y. Emelin, Y.A. Sergeev, A.I. Korytin, M.Y. Ryabikin, A.A. Murzanev, A.N. Stepanov. Surface vs bulk second optical harmonic generation from fused quartz in strong terahertz field	Thu-1-3
10:20-10:40	A.A. Gavdush, B. M. Giuliano, B. Müller, G.A. Komandin, M.E. Palumbo, G.A. Baratta, C. Sciré, S.O. Yurchenko, K.I Zaytsev, A.V. Ivlev, P. Caselli. Terahertz time-domain spectroscopy of interstellar and circumstellar ice analogs: Experimental setup and pilot results	Thu-1-4
10:40-11:00	S.B. Bodrov, A.I. Korytin, Y.A. Sergeev, A.N. Stepanov. Terahertz induced optical second harmonic generation from zinc blende crystals	Thu-1-5
11:00-11:20	A.I. Shugurov, E.A. Mashkovich, S.B. Bodrov, M.I. Bakunov Electro-optic sampling of terahertz waves in $LiNbO_3$ with avoided intrinsic birefringence	Thu-1-6
11:20-11:40	I.V. Oladyshkin, D.A. Fadeev, V.A. Mironov. Mechanisms of laser-induced THz response of metallic structures	Thu-1-7
11:40-12:10	**Coffee break**	

Session Thu-2: THz superconductor devices

Chair: V.Vaks

12:10-12:40	S.V. Antipov, N.A. Tovpeko, A.V. Trifonov, N.S. Kaurova, N.A. Titova, A.V. Semenov, G.N. Goltsman. Superconducting hot-electron and normal metal bolometer *(invited)*	Thu-2-1
12:40-13:00	A.M. Klushin, M.A. Galin, V.V. Kurin, V.M. Krasnov, F. Rudau, D. Koelle, R. Kleiner. Low-temperature scanning laser microscopy of niobium Josephson junction arrays	Thu-2-2
13:00-13:20	M.A. Galin, V.M. Krasnov, A.M. Klushin. Mutual Synchronization of Two Stacked Josephson Junction Arrays	Thu-2-3

13:20-13:40 **Closing remarks**

13:40-15:00 **Lunch**

P o s t e r s

A.A. Andronov, V.I. Pozdniakova. THz Dirac gated plasmons in graphene: Landau damping, electron "streaming" and problem of THz amplification — P-1

A.A. Baranova, V.N. Trukhin, P.G. Gavrilova, A.V. Semenova, K.G. Gareev, D.V. Korolev, O.A. Smolyanskaya. Terahertz spectra of drug-laden magnetic nanoparticles — P-2

L. Bovkun, A. Ikonnikov, M. Potemski, M. Orlita, N. Mikhailov, S. Dvoretskii, V. Aleshkin, V. Gavrilenko. Magnetic field induced interband THz absorption in HgTe quantum wells — P-3

R.A. Khabibullin, N.V. Shchavruk, D.S. Ponomarev, D.V. Ushakov, A.A. Afonenko, K.V. Maremyanin, A.A. Dubinov, O.Yu. Volkov, V.V. Pavlovskiy. Operation of THz quantum cascade laser in the region of negative differential resistance — P-4

N.S. Kulikov, A.A. Dubinov, V.Ya. Aleshkin, V.V. Utochkin, S.V. Morozov, M.A. Fadeev, V.V. Rumyantsev, N.N. Mikhailov, S.A. Dvoretsky. Auger recombination thresholds in narrow gap HgTe/CdHgTe QW heterostructures — P-5

K. Nishimura, Y. Omori, T. Hosotani, T. Suemitsu, K. Iwatsuki, T. Otsuji, A. Satou. Integration of UTC-PD structure with InGaAs-HEMT for optical-to-wireless carrier frequency down-conversion — P-6

A.L. Novokovskaya, M.I. Bakunov. Compression of unipolar terahertz pulses at ionization fronts in GaP — P-7

E.L. Odlyanitskiy, M.S. Kulya, N.S. Balbekin, Q. Cassar, O.V. Kravtsenyuk, J.-P. Guillet, P. Mounaix, K.I. Zaytsev, N.V. Petrov, O.A. Smolyanskaya. Terahertz pulse time-domain holography method for phase imaging of breast tissue — P-8

A.A. Razova, V.V. Rumyantsev, M.A. Fadeev, M.S. Zholudev, A.A. Dubinov, V.Ya. Aleshkin, N.N. Mikhailov, S.A. Dvoretsky, V.I. Gavrilenko and S.V. Morozov. Terahertz photoconductivity studies of waveguide HgCdTe structures with quantum wells for long-wavelength lasers — P-9

V.V. Rumyantsev, A.P. Fokin, K.V. Maremianin, A.A. Dubinov, V.I. Malygin, N.N. Mikhailov, S.A. Dvoretsky, V.I. Gavrilenko, M.Yu. Glyavin, and S.V. Morozov. Terahertz radiation obtained by doubling of gyrotron radiation frequency in InP:Fe — P-10

N.V. Shchavruk, A.A. Zaycev, V.G. Babkin, D.S. Ponomarev, R.A. Khabibullin. Nondestructive Acoustic Micro Imaging Analysis of thermocompression bonding for improvement of THz QCL with double metal waveguide based on Au, Cu and Ag — P-11

A.V. Shirokova, A.V. Maslov, M.I. Bakunov. Graphene plasmon transformation at a rapid increase of carrier density — P-12

V.V. Utochkin, S.V. Morozov, M.A. Fadeev, V.V. Rumyantsev, N.N. Mikhailov, S.A. Dvoretsky, T. Komiyama, T. Watanabe, H. Fukidome, A. Satou, T. Otsuji. Terahertz photoluminescence from narrow gap HgTe/CdHgTe heterostructures and multilayer graphene — P-13

International Research Network

“Bright Far-Infrared Optoelectronic Sources to Field-Matter Interaction Studies, Life Sciences and Enviromental Monitoring”

Secondary Emission from the Plasma Generated by Organized Superfilaments

A. Couairon[1], D. E. Shipilo[2,3], D. V. Mokrousova[3], N. A. Panov[2,3], G. E. Rizaev[4], A. V. Shalova[4], E. S. Sunchugasheva[3], A. A. Ionin[3], L. V. Seleznev[3], O. G. Kosareva[2,3]

[1] Centre de Physique Théorique, CNRS, Ecole polytechnique, Université Paris-Saclay, Palaiseau, France
[2] Faculty of Physics and International Laser Center, Lomonosov Moscow State University, Moscow, Russia
[3] Lebedev Physical Institute of Russian Academy of Sciences, Moscow, Russia
[4] Moscow Institute of Physics and Technology, Dolgoprudny, Moscow Region, Russia

E-mail: arnaud.couairon@cpht.polytechnique.fr

Abstract – Third harmonic generation was investigated along four organized filaments obtained by sending a 744 nm ultrashort laser pulse through an amplitude mask with four holes. Experiments show that the third harmonic angular distribution form a square-like pattern, which is reproduced by 3*D* + time numerical simulations. The fusion of the initially separated filaments and the formation of a superfilament arrests the third harmonic yield but enhances self- and cross-phase modulation effects and produces a fourfold increase in the high-frequency wings of the spectra of the fundamental and the third harmonic. THz generation from a single UV and multicolor filaments is now under study with the same setup.

Keywords – superfilamentation, third harmonic, THz generation

When near-infrared laser sources at the fundamental wavelength of 800 nm are used to generate long-range light and plasma filaments [1], the high-frequency wing of the supercontinuum spectrum spans from 800~nm to almost 230 nm thus reaching the third harmonic (266 nm) wavelength [2]. For high-intensity femtosecond pulse propagation in air, the third and higher harmonics originate mainly from the third-order contribution to the anharmonic oscillations of bound electrons [3].

The conversion efficiency of the pulse energy from the fundamental 800 nm wavelength to the third harmonic and to the supercontinuum were studied at the scale of the laboratory using moderate-focusing geometries in noble gases [4] and air [5]. The superfilamentation regime that consists in squeezing a bunch of filaments by geometrical focusing [6] or by telescoping the beam [7] leads to an increase the intensity and the plasma density in the filament. The fusion of several (about 4) filaments combined with their organization by means of amplitude masks helps to control the enhancement of nonlinearity and laser-plasma interaction in air at peak plasma densities of 10^{17}–10^{18} cm^{-3} [8], exceeding values reached within a single filament generated by a Gaussian beam.

We have investigated experimentally and numerically the spatial distribution of the third harmonic generated from organized converging filaments. Experimentally, filaments were initiated by sending a 744 nm laser pulse through an amplitude mask with four-holes and by focusing the resulting beamlets. The third harmonic obtained in the far field was the replica of the mask with four maxima at the positions of the holes (Fig. 1a), while the far-field of the fundamental reveals the bright on-axis emission typical for the superfilamentation regime (Fig. 1b).

3*D* + time numerical simulations with carrier-wave resolution reproduced the results of the experiment and showed an increase in conversion efficiency accompanying the growth of intensity due to the merging of the convergent filaments as well as a broadening of the third harmonic spectrum. In the filament merging zone, the enhanced plasma density suggests a superfilamentation regime. This enhanced plasma with density exceeding 10^{18} cm^{-3} is responsible for the suppression of the on-axis maximum of the third harmonic due to the strong decrease of the coherence length in the plasma. The effect of this enhanced plasma generation on THz yield from organized superfilaments is now under study.

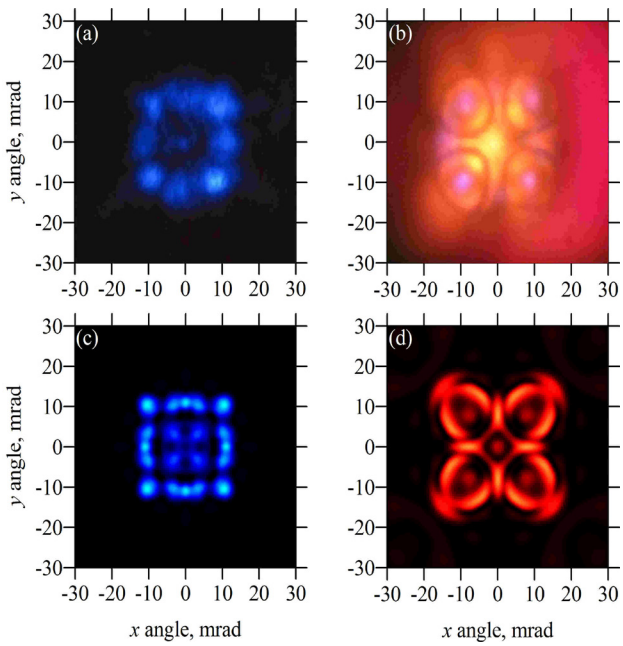

Fig. 1. Far-field photos of (a) the third harmonic distribution and (b) the overall radiation distribution after filamentation. The simulated angular distribution at (c) 248 nm and (d) 744 nm

ACKNOWLEDGMENTS

Russian Foundation for Basic Research (RFBR) (18-02-00954, 18-52-16020, 18-32-01000, 17-02-00722). Programs of the Presidium of the RAS P1.11. The program "UMNIK"' of Foundation of assistance to development of small forms of enterprises in scientific-technical sphere (FASIE) (11522GU/2017). The National key research and development program (2018YFB0504400). D.E.S. acknowledges "Basis" Foundation, Scholarship of Russian Federation President (SP-2453.2018.2), and SPIE Optics and Photonics Education Scholarship.

REFERENCES

[1] A. Couairon and A. Mysyrowicz, *Phys. Rep*. **441**, 47 (2007).

[2] F. Theberge, W. Liu, Q. Luo, and S. L. Chin, *Appl. Phys. B* **80**, 221 (2005).

[3] R. Boyd, *Nonlinear Optics*, 3rd ed. (Elsevier, 2008).

[4] C. W. Siders, N. C. Turner, M. C. Downer, A. Babine, A. Stepanov, and A. M. Sergeev, *J. Opt. Soc. Am. B* **13**, 330 (1996).

[5] A. B. Fedotov, N. I. Koroteev, M. Loy, X. Xiao, and A. M. Zheltikov, *Opt.Commun.* **133**, 587 (1997).

[6] G. Point, Y. Brelet, A. Houard, V. Jukna, C. Milián, J. Carbonnel, Y. Liu, A. Couairon, and A. Mysyrowicz, *Phys. Rev. Lett.* **112**, 223902 (2014).

[7] Q. Luo, S. Hosseini, W. Liu, J.-F. Gravel, O. Kosareva, N. Panov, N. Aközbek, V. Kandidov, G. Roy, and S. Chin, *Appl. Phys. B* **80**, 35 (2005).

[8] D. Shipilo, N. Panov, E. Sunchugasheva, D. Mokrousova, V. Andreeva, O. Kosareva, L. Seleznev, A. Savel'ev, A. Ionin, and S. Chin, *Laser Phys. Lett*. **13**, 116005 (2016).

THz Yield Dependence on the Initial and Local Phase Shift in a Two-Color Filament

O. G. Kosareva[1,2,*], I. A. Nikolaeva[1], D. E. Shipilo[1,2], N. A. Panov[1,2], A. Houard[3], A. Couairon[4], A. P. Shkurinov[1]

[1] Faculty of Physics and International Laser Center, Lomonosov Moscow State University, Moscow, Russia
[2] Lebedev Physical Institute of Russian Academy of Sciences, Moscow, Russia
[3] Laboratoire d'Optique Appliquée, ENSTA ParisTech, CNRS, France
[4] Centre de Physique Théorique, CNRS, Ecole polytechnique, Institut Polytechnique de Paris, France

*E-mail: kosareva@physics.msu.ru

Abstract – For the first time we reproduce the sinusoidal dependence of the terahertz (THz) yield expressed in absolute Joule units on the initial relative phase between the fundamental and the second harmonics by means of 3*D* + time numerical simulations in agreement with the experiment. We have quantitatively justified the optimum phase shift (~50 degrees) between ω – 2ω fields, which should be applied in the initial conditions to maximize two-color THz generation. This optimum phase shift is not preserved locally in the filament, which exhibits a full range of phase variations from –2π to π.

Keywords – two-color filamentation, terahertz generation

Terahertz emission from two-color femtosecond filament in air [1] strongly depends on the relative delay between the fundamental (ω) and the second (2ω) harmonics. First, the temporal overlap between the harmonics is a prerequisite for THz generation. This overlap can be controlled by using a positive initial pulse chirp that allows the group walk-off to be compensated so as to maximize the THz yield [2]. Second, the relative phase between the harmonics, which is governed by the phase walk-off, influences the THz yield due to the degenerate four-wave mixing process 0 = ω + ω – 2ω [3]. The optimal phase between the optical harmonics is π/2, as found from a local in space analysis using a 0*D* + time model based on the transient photocurrent model [4].

In the typical experiment [5], the THz energy maximization is performed through variation of the angle of the frequency-doubling crystal (usually BBO), which results in the change of the 2ω optical path as well as the phase-shift between the optical harmonics. This optimization routine has not been reproduced in 3*D* + time simulations which include not only generation of the THz field [4], but also propagation and space-time couplings. In this paper we study numerically the influence of the initial phase between the optical harmonics on the THz yield in the actual conditions of the experiment [6] using the nonlinear Unidirectional Pulse Propagation Equation [7].

Let the pulse propagate along *z* axis. The initial field at the entrance to air $z = 0$ is

$$E(z = 0) = E_1(r, \tau) \cos \omega\tau + E_2(r, \tau) \cos (2\omega\tau + \varphi), \quad (1)$$

where $E_h(r, \tau) = E_{h0} \exp[-h/2 \times (r^2/R^2 + \tau^2/T^2)]$ is the spatio-temporal shape of the *h*-th harmonic with the amplitude E_{h0}, $h = 1, 2$, the pulse duration at e^{-1} intensity level $2T = 120$ fs, and the beam diameter at e^{-1} intensity level $2R = 3$ mm. The energy of the fundamental pulse is 1.5 mJ and the energy of the second harmonic pulse is 10 μJ. The beam is focused by a lens with a focal length of 15 cm. The phase between the optical harmonics φ will be varied during our numerical experiment.

Figure 1 represents the dependence of the THz energy after filamentation on the initial relative phase φ between the harmonics. Its sinusoidal form is typical and reproduces measurements of the THz yield from the experiment in Ref. [6]. The maximum THz energy in our simulations of 0.25 μJ corresponds to the optical-to-THz conversion efficiency of ~10^{-4} at ~50 degree phase shift between ω – 2ω fields, while the minimum is 30 nJ (conversion efficiency ~10^{-5}). Knowing the initial ω – 2ω phase shift φ from Eq. (1), we also analyzed the actual local phase shift for those positions in the propagation direction and in the local time, where the THz yield reaches its maximum or minimum value. This actual local ω – 2ω phase shift within the particular two-color pulse reveals a continuous phase change from –2π to π. No preferable shift values of 0 or π/2 or any other were found.

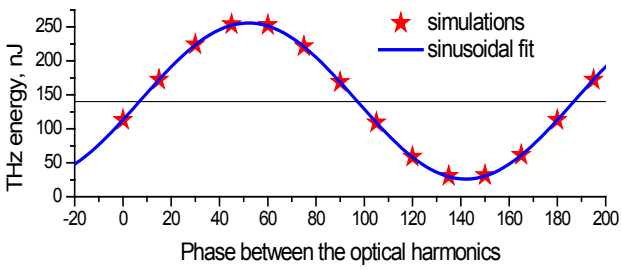

Fig. 1. The dependence of the THz energy after filamentation on the initial relative phase between the harmonics

Thus we reproduced quantitatively the sinusoidal shape of the dependence of the THz energy on the initial ω–2ω phase in 3*D* + time simulations in agreement with the experiment. We have presented the quantitative justification that the traditional π/2 shift is close to the optimum one (~50 degree) to be applied in the initial conditions to maximize THz generation from the two-color THz generation scheme. However, this optimum

shift is not preserved along the propagation since the local phase shift exhibits a full range of phase variations from -2π to π.

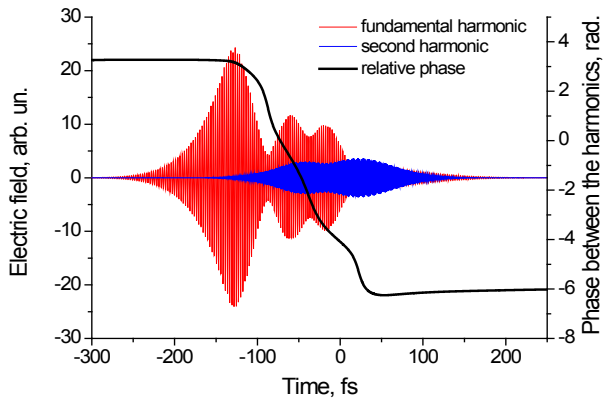

Fig. 2. Fields of the fundamental and second harmonics and relative phase between them in the optimum (~50 degree) phase shift case

ACKNOWLEDGMENTS

Russian Foundation for Basic Research (RFBR) (grant #18-52-16020). D.E.S. acknowledges the program "UMNIK" of Foundation of assistance to development of small forms of enterprises in scientific-technical sphere (FASIE) (11522GU/2017), "Basis" Foundation, Scholarship of Russian Federation President (SP-2453.2018.2).

REFERENCES

[1] D. Cook and R. Hochstrasser, *Opt. Lett.* 25, 1210 (2000).

[2] Zh. Zhang, N. Panov, V. Andreeva, et al., *Appl. Phys. Lett.* 113, 241103 (2018).

[3] J. Dai, X. Xie, and X.-C. Zhang, *Phys. Rev. Lett.* 97, 103903 (2006).

[4] K.-Y. Kim, J. H. Glownia, A. J. Taylor, and G. Rodriguez, *Opt. Express* 15, 4577 (2007).

[5] X.-C. Zhang and J. Xu, Introduction to THz Wave Photonics (Springer, 2010), Vol. 29.

[6] V. Andreeva, O. Kosareva, N. Panov, et al., Phys. Rev. Lett. 116, 063902 (2016).

[7] M. Kolesik and J. V. Moloney, *Phys. Rev. E* 70, 036604 (2004).

THz Radiation Spectra Emitted by a Single-Color Infrared and Ultraviolet Filaments

L. V. Seleznev[1], A. A. Ionin[1], O. G. Kosareva[2,1], Yu. A. Mityagin[1], D. V. Mokrousova[1], N. A. Panov[2,1], G. E. Rizaev[1], S. A. Savinov[1], D. E. Shipilo[2,1]

[1] P.N. Lebedev Physical Institute of the RAS, Moscow, Russia
[2] M.V. Lomonosov Moscow State University, Moscow, Russia

E-mail: seleznev@lebedev.ru

Abstract – We report on the observation of THz radiation spectra emitted by a single-color infrared (IR) and ultraviolet (UV) filaments. THz spectra obtained from the filament are wider and are spread down to the higher frequency components in contrast to UV filament. This may be due to much higher intensity and plasma density in IR filament as compare to UV one.

Keywords – filamentation, ultraviolet, terahertz spectra

I. Introduction

The region THz frequency band is a spectral region with rich possibilities[1] in various fields, for instance, medicine, ecology, security and defense, etc. One of the possible sources of THz radiation is the air filament. Transverse THz emission from filament was observed in Ref.[2]. Later, strong forward conical THz radiation was obtained[3]. To enhance THz emission the electric field[4, 5] and second harmonic[6] are used. Intuitively, the THz radiation parameters should strongly depend on the filament characteristics. Indeed in Ref. [3] it was shown that emission diagrams of THz signal depend strongly on the focusing conditions. In the experiments the filament parameters are extremely sensitive to the geometrical focusing distance. Therefore, if the geometry of experiment varies slightly, there is a threat that several parameters (pulse intensity, plasma density, filament length, etc.) will be changed simultaneously. That is why the purpose of this paper is comparison of THz radiation spectra emitted from IR and UV filaments at the same focusing conditions.

II. Experiment

In our experiments we use Ti:sapphire laser system pulse at the central wavelength of 740 nm and the third harmonic at 248 nm. The pulse duration is about 90 fs with the energy of 1.8 and 0.2 mJ, respectively. The laser pulse is focused by the lens with the focal length of 7 cm. Since the pulse peak power is several times larger than the critical power for self-focusing in air, the filament starts near the geometrical focus of the lens. The spectrum of THz radiation emitted from the filament is measured in air by Fourier transform infrared spectroscopy (FTIR). The THz radiation is collected by a parabolic mirror into the collimated beam and directed to the Fourier interferometer input. Our interferometer operates by the principle of step-by-step scanning of the interference pattern, implemented by moving the mobile mirror using a micrometer screw rotated by the step motor. As a beam splitter, a Mylar film 12.5 μm thick is used. This film provides us with a signal maximum at the frequency of 120 cm^{-1} (3.6 THz). Output radiation is registered by superconducting NbN hot-electron bolometer (HEB), which operates at ~10K, has a time constant of about 1ns and a noise equivalent power (NEP) better than 10^{-13} W/√Hz. The black polyethylene (200 μm), high-density polyethylene cryostat window (2 mm) and cold filter (Zitex G-108) are used to block the laser and background radiation. Signal from HEB low-noise cold preamplifier is accumulated in the gated integrator/boxcar SR250, digitized by the analog-to-digital convertor (ADC) and recorded by the computer, where the obtained interferograms are restored using the Fast Fourier Transform (FFT) algorithm. To observe the angular distribution, the THz radiation is directed to the bolometer immediately after the parabolic mirror. In the experiments a diaphragm is installed before the bolometer with the diameter of 2 mm for IR pulse and 6 mm for the UV pulse.

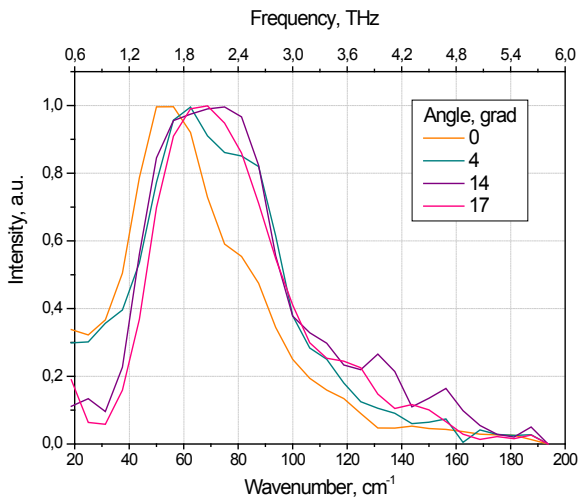

Fig. 1. Terahertz radiation spectra formed in IR filament observed at different angle

For both wavelengths the terahertz radiation is emitted into the cones. Observed terahertz radiation spectra are shown in Figs.1 and 2 for the IR and UV filaments, respectively. The maximum terahertz signal for the IR filament is larger than for the UV one by more than an order of magnitude.

In both IR and UV pulse cases, the spectra on the optical axis (angle is equal to zero) have their longer wavelength components enhanced as compared with the spectra of the pulses propagating in the off-axis direction. These off-axis spectra are similar to each other. At all the directions studied the terahertz radiation spectra for IR pulses are spread towards 5–6 THz in contrast to the spectra of the UV pulse which extend towards ~2.5 THz only.

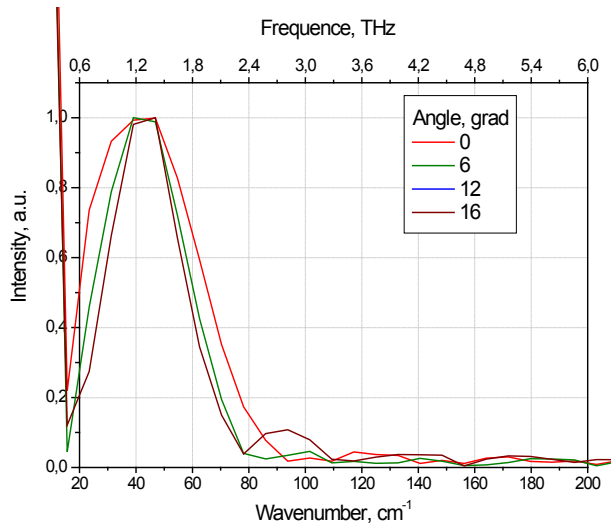

Fig. 2. Terahertz radiation spectra formed in UV filament observed at different angle

III. Discussion

Possible explanation to this phenomenon is that the IR filament is characterized by the larger intensity and plasma density as well as the smaller transverse size as compared with the UV filament[7,8] . This results in the higher transverse gradient of intensity and plasma density in the IR filament. Therefore, the ponderomotive electron acceleration and photo current in the IR filament are larger than in the UV one. Consequently, the IR filament should deliver higher THz signal and larger spectral broadening than the UV filament. This is in agreement with our experimental observation.

Acknowledgments

Russian Foundation for Basic Research (RFBR) (18-02-00954, 18-52-16020, 18-32-01000, 17-02-00722).

References

[1] X. C.Zhang, A.Shkurinov, & Y.Zhang, *Nat. Photonics*, **11**(1), 16 (2017).

[2] S.Tzortzakis, G.Méchain, G.Patalano, Y.-B.André, B.Prade, M.Franco, A.Mysyrowicz, J.-M.Munier, M.Gheudin, G.Beaudin, P.Encrenaz, *Opt. Lett*. **27** (21), 1944–1946 (2002).

[3] C.D'Amico, A.Houard, M.Franco, B.Prade, A.Mysyrowicz, A.Couairon, & V. T.Tikhonchuk, *Phys. Rev. let.*, **98**(23), 235002 (2007).

[4] C.D'Amico, A.Houard, M.Franco, B.Prade, & A.Mysyrowicz, *Opt. Expr.*, **15**(23), 15274-15279 (2007).

[5] A.Houard, Y.Liu, B.Prade, V. T.Tikhonchuk, & A.Mysyrowicz, *Phys. Rev. let.*, **100**(25), 255006 (2008).

[6] V.Blank, M. D.Thomson, & H. G. Roskos, *New J.of Phys*., **15**(7), 075023 (2013).

[7] V. P.Kandidov, S. A.Shlenov, & O. G.Kosareva, *Quant. Electron.,* **39**(3), 205 (2009).

[8] A. A.Dergachev, A. A.Ionin, V. P.Kandidov, L. V.Seleznev, D. V. Sinitsyn, E. S.Sunchugasheva, & S. A. Shlenov, *Quan. Electron.,* **43**(1), 29 (2013).

Generation of Terahertz Radiation from Liquid Nitrogen

A. V. Balakin[1,2], J.-L. Coutaz[3], V. A. Makarov[1,2], I. A. Kotelnikov[4,5], Y. Peng[2], P. M. Solyankin[2,6], Y. Zhu[2], A. P. Shkurinov[1,2]

[1] Faculty of Physics and International Laser Center, Lomonosov Moscow State University, Moscow 119991, Russia
[2] Terahertz Technology Innovation Research Institute, Shanghai Key Lab of Modern Optical System, Terahertz Spectrum and Imaging Technology Cooperative Innovation Center, University of Shanghai for Science and Technology, Shanghai 200093, P. R. China
[3] IMEP-LAHC, UMR CNRS 5130, Universite Savoie Mont-Blanc, Campus scientifique, 73376 Le Bourget du Lac Cedex, France
[4] Budker Institute of Nuclear Physics, Novosibirsk, 630090, Russia
[5] Novosibirsk State University, Novosibirsk, 630090, Russia
[6] Institute on Laser and Information Technologies - Branch of the Federal Scientific Research Centre "Crystallography and Photonics" of Russian Academy of Sciences, Svyatoozerskaya 1, 140700, Shatura, Moscow Region, Russia

E-mail: a.v.balakin@physics.msu.ru

In this paper we present the first observation of terahertz (THz) wave generation by photo-excitation of a liquefied gas – liquid nitrogen (LN). We use double pulse excitation scheme and apply both "single-color" and "dual-color" regimes of LN excitation with high power femtosecond laser pulses. Our experimental results show clearly that under acting of femtosecond laser radiation liquid and air emit THz waves in a very different way. Careful theoretical examination of the results shows that both the ionization of the medium and its nonlinear susceptibility play a considerable role in the generation of THz radiation in LN. We assume that the mobility of ions and electrons in liquid can play an essential role in the THz generation by acting through a quasi-static electric field formed by means of ambipolar diffusion mechanism.

Keywords – Terahertz generation, liquid nitrogen, ambipolar field

I. INTRODUCTION

That is well known that when focusing femtosecond laser pulses into a gaseous medium, it is possible to obtain THz pulsed radiation with fairly high intensity and wide spectral width[1]. There are two experimental schemes normally applied in THz gas photonics for the THz generation from an optically-produced spark in the gaseous medium: so named "single-color" scheme, when only one femtosecond pulse at a fundamental laser frequency ω is used for the conversion into THz radiation, and "dual-color" scheme, when two waves at ω and 2ω frequencies interact and generate the THz pulse. It is considered that origin of the THz generation involves two different mechanisms: due to pulsed transient photo-current produced by free electrons created in the medium through its photo-ionization[2,3] in the first case and due to the nonlinearity of the plasma araised from the contributions of bound and free electrons[4] in the second one. Previously we demonstrated, that these two contributions to the total THz signal sum up effectively and have two different frequency characteristics[5].

Recently[6,7], it was suggested using a liquid medium as a source of THz radiation. Differences between gases and liquids promise higher THz conversion efficiency in liquids, at least because the nonlinear susceptibility of liquid, for instance $\chi^{(3)}$, is three orders higher in comparison with gas. But the origin of THz radiation from optical breakdown in liquids and its possible explanations are still not completely clear and demanding additional efforts to be validated or explained.

In the present work we studied the THz generation from a photo-induced plasma in LN. We chose LN instead of water (like it was in Refs. 6, 7) because, besides exhibiting third-order nonlinearity, this non-polar liquid posses quite weak absorption in the visible and THz frequency ranges. Here we reported on THz generation in LN by two successive lasers pulses versus the time delay between the pulses, and also when LN was excited by the laser pulses at the fundamental and second-harmonic frequencies. We compared these signals with the ones generated in air. We analyzed the observed effects and interpreted them.

II. EXPERIMENTAL SETUP

In our experiments we used setup shown in Figure 1. A femtosecond laser system that included a Ti:Sapphire Mira 900 oscillator and a regenerative amplifier Legend Elite Duo (Coherent, Inc.) was used as a source of femtosecond laser radiation. This system provided 90 fs pulses at 1 kHz repetition rate with 800 nm of central wavelength and energy up to 8.5 mJ. To create two time-delayed laser pulses a Michelson-type interferometer was used in the experimental setup. The time delay between these two pulses was controlled by changing the optical path length of one arm of the interferometer. At the output of the interferometer, the two pulses propagated along the same axis, and then were sent to the sample and then to the detection system. This part of the experimental setup was the similar to the one in our previous work[8].

III. Results

We carried out a series of experimental investigations on the dependence of the THz yield from LN versus the time delay Δt between the two laser pulses and compared it with the one generated in air under the same excitation conditions. Part of the experimental results are presented in Figure 2.

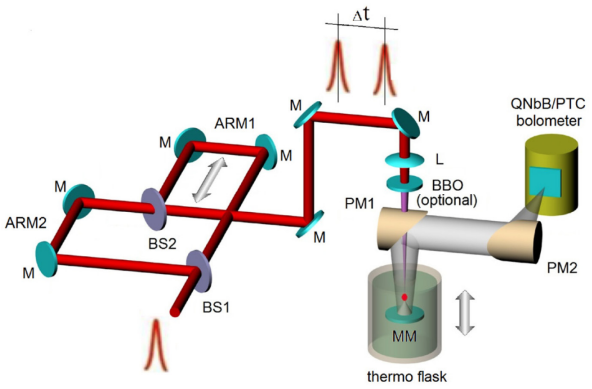

Fig. 1. Experimental setup. M – dielectric mirrors; MM – metallic mirror; BS – beam splitters; L – lens; PM – off-axis parabolic mirrors; BBO – β-barium borate (BBO) crystal

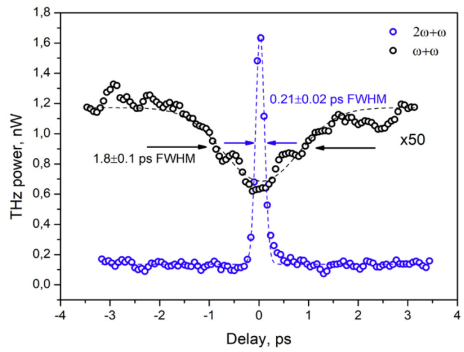

(a)

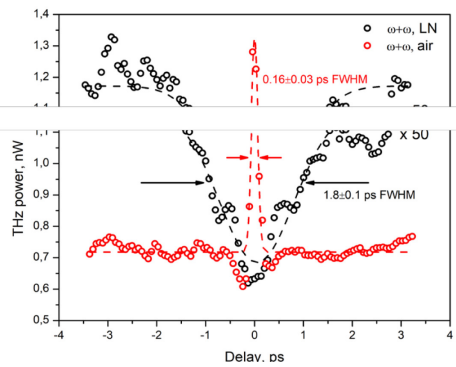

(b)

Fig. 2. The THz signal via the time delay between the laser pulses. (a) LN: single-color (black) and dual-color (blue) schemes; (b) single-color interaction in air (red circles) and in LN (black circles)

IV. Conclusions

We presented the results of research, carried out for the first time, on the generation of THz radiation under the action of single-color and dual-color high power femtosecond laser pulses on LN. In our experiment we used a time-resolved double pulse excitation scheme, in which the second pulse probes the liquid after excitation by the first pulse. Direct comparing of results obtained when THz generation appeared from the plasma created by the optical breakdown in air and from LN showed that liquid and air emit THz waves in a very different way. Careful theoretical interpretation of our experimental results demonstrated that both the ionization of the medium and its nonlinear susceptibility play a considerable role in the generation of THz radiation in LN. We assumed that the mobility of ions and electrons in liquid can play an essential role, forming a quasi-static electric field by means of ambipolar diffusion mechanism. This quasi-stationary field permits the THz generation through a third-order nonlinear effect, which is stronger than second-order effects in quasi center-symmetric media like plasmas.

Acknowledgments

This work was financially supported partially by the Russian Foundation for Basic Research under Grants 18-52-16016, 18-29-20104 and 17-02-01217, partially by the Major National Development Project of Scientific Instrument and Equipment (2016YFF0100503), partially by the National Natural Science Foundation of China (61722111), the 111 Project (D18014), the International Joint Lab Program supported by Science and Technology Commission Shanghai Municipality (17590750300), and partially by the Ministry of Science and Higher Education within the State assignment FSRC "Crystallography and Photonics" RAS.

References

[1] X.-C. Zhang, A. Shkurinov, and Y. Zhang, *Nat. Photonics* **11**, 1–3 (2017).
[2] K. Y. Kim, J. H. Glownia, A. J. Taylor, and G. Rodriguez, *Opt. Express* **15**, 4577–4584 (2007).
[3] V. Balakin, A. V. Borodin, I. A. Kotelnikov, and A. P. Shkurinov, *J. Opt. Soc. Am. B* **27**, 16–26 (2010).
[4] J. Cook and R. M. Hochstrasser, *Opt. Lett.* **25**, 1210–1212 (2000).
[5] V. Borodin, N. A. Panov, O. G. Kosareva, V. A. Andreeva, M. N. Esaulkov, V. A. Makarov, A. P. Shkurinov, S. L. Chin, and X.-C. Zhang, *Opt. Lett.* **38**, 1906–1908 (2013).
[6] Q. Jin, Y. E, K. Williams, J. Dai, and X.-C. Zhang, *Appl. Phys. Lett.* **111**, 071103 (2017).
[7] Q. Jin, J. Dai, Y. E, and X.-C. Zhang, *Appl. Phys. Lett.* **113**, 261101 (2018).
[8] V. Balakin, S. V. Garnov, V. A. Makarov, N. A. Kuzechkin, P. A. Obraztsov, P. M. Solyankin, A. P. Shkurinov and Y. Zhu, *Opt. Lett.*, **43**, 4406 (2018).

Efficient Conversion of Intense Laser Pulses to THz in a Low Pressure Gas

M. M. Nazarov[1], A. V. Mitrofanov[1,2,3], D. A. Sidorov-Biryukov[1,3,4], M. V. Chashin[1], M. Bernier[5], P. M. Solyankin[2,4], A. P. Shkurinov[2,4], A. M. Zheltikov[1,3,4,6], V. Ya. Panchenko[1,2,4]

[1] Kurchatov Institute National Research Center, Moscow, Russia
[2] FSRC "Crystallography and Photonics" of the RAS, Moscow, Russia
[3] Russian Quantum Center, Skolkovo, Moscow Region, Russia
[4] Physics Department and ILC of M.V. Lomonosov Moscow State University, Russia
[5] IMEP-LAHC, Chambery, France
[6] Department of Physics and Astronomy, Texas A&M University, Texas, USA

E-mail: nazarovmax@mail.ru

Abstract – One of the promising ways to obtain intense and short THz pulses is laser excitation of gas plasma. A 2-TW, 30-fs, 800-nm laser radiation is combined with its second harmonic to yield a two-color filament in a loose-focusing geometry inside a low-pressure gas cell. With multiple filamentation and excessive ionization avoided in our experiments through an appropriate choice of the pressure of the gas, as well as focusing conditions. Ten-fold increase of THz yield is observed for 1–50 mbar gas pressure in comparison with normal conditions case. Still THz generation process looks saturated at laser energies above 40 mJ. We compare strong THz pulses obtained with two-color filament and with tilted pulse front in $LiNbO_3$, apply obtained pulses to alter silicon and GaSe instant response.

Keywords – intense pulse, filament, gas pressure

I. Introduction

Terahertz (THz) pulses with electric field above few MV/cm are now required for strong field applications like particles acceleration, short electron bunches measurements, fast controlling of state of the matter. Except the huge free-electron lasers facilities, the only way to get THz radiation of MV/cm field strength is the conversion of high-power femtosecond laser pulses. The terahertz wave generation via two-color laser-induced gas breakdown is free from damage threshold and phase-matching limitations inherent to nonlinear crystals, although its typical conversion efficiency 10^{-5}–10^{-4} is low compared to conversion in nonlinear crystals[1]. For crystals like $LiNbO_3$ conversion efficiency to THz can reach up to 10^{-3}, but input energy of laser pulse is limited by material damage at 1–2 mJ energies in pump pulses. Thus to exceed microjoule level of THz energy we try to convert hundred of mJ, 800 nm pulse into THz one in the two-color, long filament in low pressure gas.

The possibility to scale THz generation in a filament using terawatt laser pulses long been discussed[2–4]. Record values for THz pulse energy in ambient air makes up 2-5 μJ, with a peak field up to 16 MV/cm at 10–50 mJ, 800 nm pumping. To overcome observed saturation loose focusing[4] and pulse stretching[2] were suggested. We go further and optimize pressure. As far as we know, with terawatt pulses in a low pressure gas, experiments on two-color filamentation were not carried out for THz generation. For optimal filament performance, filament parameters should be scaled according to certain rules [5], along with the energy we should increase the beam size, the focus length, as well as to reduce the pressure.

II. Experiment

Laser system "Pulsar 200 TW" based of titan-sapphire and installed in NRC "Kurchatov Institute", capable of generating 25 fs pulses with an energy up to 7 J at 800 nm and 10 Hz was used at "low", <100 mJ power regime. Thus we use 2.5 m focusing mirror and 70 mm beam and 70 mm diameter beam, we double laser radiation in 150 μm, large aperture KDP crystal and launch a 20 cm long, two-color filament in nitrogen, argon and air with 0.1-1000 mbar pressure. For comparison, 1 kHz, 2 mJ laser system with the same 800 nm was used with tilted pulse front THz generation in $LiNbO_3$.

We estimated obtained in filament THz bandwith (<2 THz) by electro-optical detection (provided 0.4 ps pulse duration) and by attenuation of known materials – Si with 10^{14}–10^{17} cm^{-3} carrier concentration, thick polymers, dense paper. In our case most of THz energy, expected at 10–20 THz is blocked by cell output polypropylene window and THz filters. Improving those technical issues one can exceed to get 10^{-4} conversion efficiency level for THz generation at TW pumping.

The optimization of the second harmonic crystal position, the gas pressure and the pulse duration allowed us to obtain a THz pulse of about 1 μJ, with 400 fs duration for 40 mJ, 30 fs, 800 nm pulse at 20 mbar of N_2 pressure. Note, that this is only a low frequency part (<2 THz) of THz pulse, detectable in this case.

THz signal is sensitive to the position of frequency-doubling crystal in converging laser beam. For higher energy we need to use larger crystal area to avoid damage, just moving the crystal away form geometrical focus. That (as well as pressure) changes the relative phase between fundamental and second harmonic in the filament area. This phase slippage is known[6] and it is pronounced as signal oscillations for pressure dependence – Fig. 1, a).

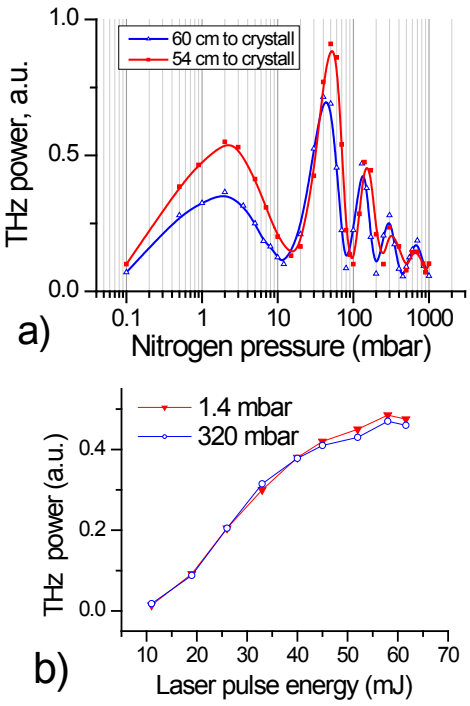

Fig. 1. a) THz yield vs nitrogen pressure for 40 mJ laser pulses at 60 and 54 cm distance from frequency doubling crystal to filament center. b) THz yield vs laser power for 1.4 and 320 mbar nitrogen pressure

In our case, the pressure decrease from ambient to tens of mbar provides a 20-times gain in the THz generation efficiency, see Fig. 1, a). Filling the cell with nitrogen, argon or air does not significantly change the obtained THz signal.

III. Discussion

With 6–60 mJ laser pulses for two-color filamentation we observed an order of magnitude increase of THz emission, when decreasing gas pressure from ambient to tens of mbar. Such strong efficiency increase cannot be explained only by decreasing of phase slippage or plasma density. The known THz generation scenario in filament, which was studied in detail for short focusing and atmospheric pressure[2–4, 6], is not confirmed for this range of parameters. Novel approach should be suggested.

The other open question is the THz yield saturation reason. For transform limited pulses and pressure below 0.3 atm (even at 0.001 atm!), we observe a decrease in the THz efficiency at laser pulse energies above 40 mJ (Fig. 1b)). In this case we detect the broadening of the spectrum not only of fundamental, but also of the second harmonic after the filament and an increase in the pulse duration. We suppose that the reasons for this saturation, besides excessive ionization are self-phase modulation of a powerful pulse in the windows and in the frequency-doubling crystal. It should be taken into account and minimized for further energy increase.

To calibrate the THz detector (Golay cell, Tydex "GC-1P") in the 10 Hz repetition rate, THz signals were compared with the THz radiation obtained with the scheme of tilted pulse front in lithium niobate at 1 mJ, 120 fs also reduced to 10 Hz rep. rate. In both cases we obtain 3–5 V Golay cell response, that corresponds to about 1μJ of THz energy. So far, the received THz pulse energy in plasma from 40 mJ is comparable with that one from lithium niobate with 1 mJ. But THz energy in plasma can be further scaled up, at least with longer focusing.

With estimated peak field of the THz pulse of 0.7 MV/cm we get in the scheme with lithium niobate, non-linear silicon transmission enhancement (figure 2 b) in typical z-scan[1] measurements. It is a convenient method for confirming the generation of strong and short THz fields with good focusing.

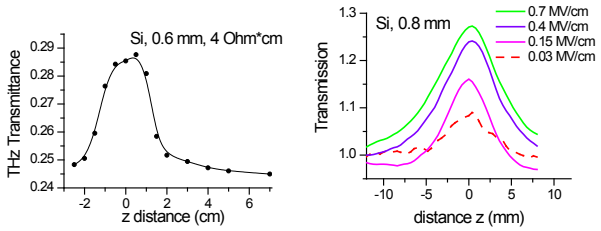

Fig. 2. Z-scan measurements at 1uJ THz pulse . a) filament THz source for 660 um, 4 Ohm*cm Si b) LiNbO3 THz source for 800 um, 12 Ohm*cm Si

Similar, non-linear p-doped silicon transmission enhancement was observed for the case of THz generation in filament. Confirming focusing ability of this radiation from elongated source. We estimate a 0.2 MV/cm field in this case, with measured beam-waist diameter about 0.7 mm.

Finally, with obtained 1 microJoule of THz energy we tried to observe phonon resonance saturation in THz frequency range.

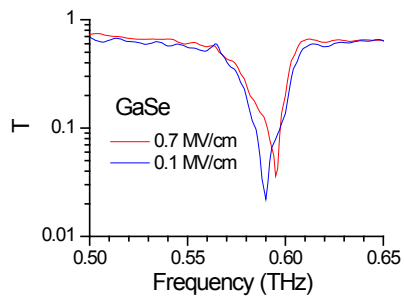

Fig. 3. Fragment of transmission spectra of 6 mm thick GaSe crystal at 0.7 and 0.1 MV/cm THz field amplitudes

We detect (with $LiNbO_3$ THz source) week decreasing of phonon resonance amplitude in GaSe crystal at its narrow absorption band at 0.59 THz, when applying 0.7 and 0.1 MV/cm THz fields – Fig.3

IV. Conclusions

In preliminary experiments with 1–60 mJ laser pulses for two-color filamentation we observed an order of magnitude increase of THz emission, when decreasing

gas pressure from ambient to tens of mbar. Such strong efficiency increase cannot be explained only by decreasing of phase slippage or plasma density as far as we know. The theoretical treatment for the observed pressure dependencies should clear out the way to further increase THz energy for more intense laser pulses. Then it will be possible to generate a more powerful (and short) pulse (several MV/cm) than in nonlinear crystals. This will be enough to work on THz nonlinear optics and on the influence of the powerful THz pulses on the matter.

ACKNOWLEDGMENTS

This work was financially supported by RFBR grants 18-52-16024, and 18-02-40032.

REFERENCES

[1] Chefonov O, Ovchinnikov A, Romashevskiy S, Chai X, Ozaki T, Savel'ev A, Agranat M and Fortov V 2017 Optics letters 42 4889–92

[2] Wang T J, Chen Y, Marceau C, Theberge F, Chateauneuf M, Dubois J and Chin S L 2009 Applied Physics Letters 95 131108

[3] Yoo Y J, Kuk D, Zhong Z and Kim K Y 2017 IEEE Journal of Selected Topics in Quantum Electronics 23, 1–7

[4] Oh, T. I., You, Y. S., Jhajj, N., Rosenthal, E. W., Milchberg, H. M., & Kim, K. Y. (2013). Intense terahertz generation in two-color laser filamentation: energy scaling with terawatt laser systems. New Journal of Physics, 15(7), 075002.

[5] Zhokhov, P. A., & Zheltikov, A. M. (2014). Scaling laws for laser-induced filamentation. Physical Review A, 89(4), 043816.

[6] Rodriguez, G., & Dakovski, G. L. (2010). Scaling behavior of ultrafast two-color terahertz generation in plasma gas targets: energy and pressure dependence. Optics express, 18(14), 15130-15143.

.

Breathomics Applications of IR and Terahertz Spectroscopy and Machine Learning

Yu. V. Kistenev[1], M. Rotger[2], A. Cuisset[3], R. Bocquet[3], A. V. Borisov[1], F. Hindle[3], A. I. Knyazkova[1,4], M. Mouelhi[3], G. Mouret[3], B. Parvitte[2], R. Vallon[2], V. S. Zasedatel[1], V. Zéninari[2], A. A. Karapuzikov[5], D. B. Kolker[6], N. Yu. Kostyukova[5,7], A. A. Boyko[5,6], A. A. Markelov[4,5,7], K. G. Zenov[5]

[1] Tomsk State University, Tomsk, Russia
[2] University of Reims Champagne-Ardenne, Reims, France
[3] Laboratoire de physico-chimie de l'atmosphere, EA-CNRS, Universite Du Littoral Cote d'Opale, Dunkerque, France
[4] Institute of Strength Physics and Materials Science of SB RAS, Tomsk, Russia
[5] Special technologies, Ltd., Novosibirsk, Russia
[6] Novosibirsk State University, Novosibirsk, Russia
[7] Insitute of Laser Physics of SB RAS, Novosibirsk, Russia

E-mail: yuk@iao.ru

Abstract – Analysis of volatile organic compounds (VOCs) in the exhaled air, called breathomics, is a promising approach for operative non-invasive medical screening tests. The report is devoted to applications of molecular spectroscopy and machine learning for evaluation of VOCs profile for medical diagnosis.

Keywords – breathomics, biomarkers, IR and terahertz spectroscopy, machine learning

I. Introduction

Breath air analysis can be used both as a tool in diagnosis and to understand specific biochemical processes. Since most VOCs do not provide sufficient specificity, the metabolite profile approach, called also metabolic fingerprinting, is used to provide diagnosis. The metabolic fingerprinting requires registration of large number of VOCs and pattern recognition technique for data analysis.

Machine learning allows one to discover functional relationships from examples based on features rather than from manual verification of entire experiments. Compared to conventional approaches, these methods are more efficient in handling multi-dimensional data analysis such as distinguishing phenotypes that is defined by a high number of features. The key challenge to use machine learning for medical diagnosis is existence of latent dependences between measured features set and human state variations due to pathological processes. On the other hand, medical diagnostics requires very high sensitivity and specificity of trained classifier which is difficult to achieve because of lack of representativity of training datasets comparing with annotated image sets used by Google, Amazon for face and object recognition.

The scientific problem solved is related to the development of the physical foundations of mid-IR and terahertz (THz) spectroscopy for detection of a large number of VOCs present in the exhaled breaths, which can be suitable for routine measurements, and application of machine learning to create effective classifiers.

II. Results under discussion

We plan to discuss the new generation PA spectrometers specially designed for breathomics applications: the first one will use a widely tunable OPO source in the mid-IR (2–12 μm) and the second one a frequency multiplication chain with excellent delivery power in the subTHz domain (62–620 GHz).

Recently, $BaGa_4S_7$ (BGS) and $BaGa_4Se_7$ (BGSe) chalcogenide crystals have appeared, which are promising for the mid-IR range; the latter crystal has a transparency range of 0.47–18 μm, which potentially allows for the wavelength tuning up to 18 μm. We will analyse generation properties of BGS(e) for optical parametric oscillation.

The photoacoustic (PA) detectors improvement is connected with increasing the quality factor of the acoustic resonator and decreasing the level of background noise.

Acknowledgments

This work was partially funded by RFBR (grant No.17-00-00186) and the Fundamental Research Program of the State Academies of Sciences for 2013-2020, line of research III.23.

Interaction of Terahertz Radiation with Bio-Like Objects: Theoretical and Numerical Modelling, Real Objects and Phantom Experiments

O. A. Smolyanskaya[1], M. S. Kulya[1], Q. Cassar[2], O. V. Kravtsenyuk[1], E. L. Odlyanitskiy[1], P. Mounaix[2], J.-P. Guillet[2], K. I. Zaytsev[3,4], N. V. Petrov[1]

[1] ITMO University, Saint-Petersburg, Russia
[2] Bordeaux University, IMS Laboratory, Bordeaux, France
[3] Bauman Moscow State Technical University, Moscow, Russia
[4] Prokhorov General Physics Institute of the Russian Academy of Science, Moscow, Russia

smolyanskaya@corp.ifmo.ru

I. Introduction

New biomedical devices require test objects to check their performance and periodic calibration to monitor the system efficiency over the time. A phantom is a bio-like object mimicking the intrinsic real-tissue properties that serves as a test object. A variety of phantoms are commercially available. Phantoms are already used in spectroscopy within various spectral range. However, currently, the THz frequency range suffers from a lack of investigations in this direction. Only the first steps have been performed [1]. In the present work, we investigate interaction of submillimeter radiation with the breast-mimicking skin-mimicking phantoms. Results for breast-mimicking phantom were compared with numerical models based on a double-Debye model of the dielectric permittivity for different content of fat, fibrous and cancerous tissue. The wave front propagation using the angular spectrum representation was used to simulate the theoretical response of breast-mimicking phantoms.

II. Model of wavefront propagation

Electromagnetic fields can be represented in various ways. The angular spectrum representation is a numerical technique describing optical fields in a homogeneous media [2]. Optical fields are described as a superposition of plane waves and evanescent waves. A useful approach to describe optical field diffraction is to conduct the Fourier analysis at a given plane so that the different Fourier components of the field distribution are identified as plane waves propagating away from that plane in different directions. Thus taking less computation time for numerical reconstruction. This technique is preferable for the analysis of light diffraction by histological slides [3]. Angular spectrum representation consists of the following stages: (i) the representation of the field through the angular spectrum of 2D waves (Eq.1); (ii) multiplication by the transfer function that contains a complex refractive index of the object (Eq.2); (iii) the back transition from plane waves to the wave field in the calculated z-plane (Eq.3).

$$C\left(f_x, f_y, \nu\right) = \int_{-\infty}^{\infty}\int_{-\infty}^{\infty} G\left(\tilde{x}, \tilde{y}, \nu\right)_{z=0} \exp\left(-2\pi i\left(\tilde{x} f_x + \tilde{y} f_y\right)\right) d\tilde{x} d\tilde{y}$$

$$g_{x,y}\left(f_x, f_y, \nu, z\right) = C\left(f_x, f_y, \nu\right) \exp\left(-i\frac{2\pi\nu n(\nu)}{c}\sqrt{1-\left(\frac{f_x \cdot c}{\nu n(\nu)}\right)^2 - \left(\frac{f_y \cdot c}{\nu n(\nu)}\right)^2} \cdot z\right)$$

$$G\left(x, y, \nu, z\right) = \int_{-\infty}^{\infty}\int_{-\infty}^{\infty} g_{x,y,z}\left(f_x, f_y, \nu, z\right) \exp\left(2\pi i\left(x f_x + y f_y\right)\right) df_x df_y$$

where $n\left(\tilde{x}, \tilde{y}, \nu\right) = n_{re}\left(\tilde{x}, \tilde{y}, \nu\right) + i \cdot n_{im}\left(\tilde{x}, \tilde{y}, \nu\right)$ is the spatial and frequency distribution of the complex index of refraction.

III. Materials and methods

A. Sample preparation

We have used three-component phantoms made of fat, protein and water of different content. Vegetable oil (10–75%), soya (13–75%) and water (0–70%) were homogenized to generate an emulsion. Then, the phantoms were deposited into vacuum packages.

B. THz-Spectrometer

The commercially available TPS 4000 (Teraview Ltd, UK) spectrometer working in reflection mode was used. The spectral range of the system is from 0.06 to 4.50 THz. The entire system was under an air-dried dome to limit the interaction of water molecules with generated pulses. Samples were mounted on a sapphire substrate during measurement. The sapphire cut was chosen not to exhibit a birefringence that would disrupt results of measurements [4]. Each sample was measured 5 times, independently, *i.e.* the sample was removed and replaced again into system.

C. Numerical modelling

A double-Debye model of the dielectric permittivity was used to compare optical properties of the three-component phantoms and some biological tissue (adipose, fibrous and cancerous) taken from our previous paper [5].

IV. RESULTS AND DISCUSSION

The propagation dynamics of the pulsed THz radiation through a tissue sample was numerically simulated in the temporal and spectral domains. The index of refraction, n_{re}, absorption coefficient, α, as well as real, ε_{re}, and imaginary, ε_{im}, part of dielectric permittivity was calculated from the experimentally obtained data. We have obtained the time-domain spatial evolution of the THz pulse. Agreement between measured and simulated THz waveforms is confirmed by the comparison was shown. The spectral dependences of the absorption coefficient of the three-component phantoms consisting of fat, protein and water are depicted. It is shown that within the spectral window, the absorption coefficient of phantoms containing water exceeds the absorption coefficient of phantoms free of water. This is due to the fact, that water molecules, which strongly absorb THz radiations, are replaced by low absorbing components (fat and protein). Our results were compared with simulated signals of adipose, fibrous and cancerous tissues taken from our previous paper [5].

V. CONCLUSION

To overcome the lack of knowledge on tissue-mimicking phantoms within the submillimeter spectral range, we conducted preliminary studies on skin- and breast tissue-mimicking samples. Simulations performed for skin-mimicking phantoms have match the experimental spectral data. Thus demonstrating advantages of the technique used in this study. The spectral dependences of absorption coefficient extracted from measurements for breast-mimicking phantom are clearly differentiated into two distinct groups. One for phantoms containing water and those being water-free. Such a discrimination is also shown via the double-Debye model of the dielectric permittivity. Thus, finding of a proper composition of tissue phantom is possible by an appropriate matching of model and experimental data, in particular for prediction of impact on THz radiation probing depth of tissue reversible dehydration using hyperosmotic optical clearing agents [3]. Deeper investigations are however still required to fulfill a set of phantoms that could be used to perform tissue measurement within the THz-range. Such a set would be profitable to design new medical THz-devices without human biopsy.

ACKNOWLEDGMENTS

The reported study was funded by RFBR and CNRS according to the research project №18-51-16002, and by the Government of the Russian Federation (Grant 08-08).

REFERENCES

[1] *E Liakhov, O Smolyanskaya, A Popov, E Odlyanitskiy, N Balbekin, M Khodzitsky,* Fabrication and characterization of biotissue-mimicking phantoms in the THz frequency range // Journal of Physics: Conference Series. 2016. No. 735. P. 012080.

[2] *Petrov, N. V., Kulya, M. S., Tsypkin, A. N., Bespalov, V. G., & Gorodetsky, A.* Application of terahertz pulse time-domain holography for phase imaging // IEEE Transactions on Terahertz Science and Technology, 2016, V. 6, No. 3, P. 464-472.

[3] *O. A. Smolyanskaya, I. J. Schelkanova, M. S. Kulya, E. L. Odlyanitskiy, I. S. Goryachev, A. N. Tcypkin, Ya V. Grachev, Ya G. Toropova, and V. V. Tuchin* // Glycerol dehydration of native and diabetic animal tissues studied by THz-TDS and NMR methods // Biomedical Optics Express, 2018, V. 9, No. 3, P. 1198-1215.

[4] *Q. Cassar, A. Al-Ibadi, la. Mavarani, Ph. Hillger, J. Grzyb, G. Macgrogan, Th. Zimmer, U.R. Pfeiffer, J.-P. Guillet, P. Mounaix* Pilot study of freshly excised breast tissue response in the 300 – 600 GHz range // Biomed Opt Express. 2018. V. 9 No. 7. P. 2930–2942.

[5] *A. J. Fitzgerald, E. Pickwell-MacPherson, and V. P. Wallace,* Use of finite difference time domain simulations and Debye theory for modelling the terahertz reflection response of normal and tumour breast tissue // Plos One **9**, 1-9 (2014)

Research and Development of Effective Optical Technologies for Diagnostics in Dermatology

V. V. Tuchin[1,2,3], E. A. Genina[1,2], A. N. Bashkatov[1,2], E. N. Lazareva[1,2], D. K. Tuchina[1,2], I. Yu. Yanina[1,2], V. V. Nikolaev[3], A. V. Borisov[3], D. D. Yakovlev[1], M. E. Shvachkina[1], A. B. Pravdin[1], Yu. V. Kistenev[3], M. Amouroux[4], V. I. Kochubey[1,2], W. Blondel[4]

[1] Research-Educational Institute of Optics and Biophotonics, Saratov State University, Saratov, Russia
[2] Interdisciplinary Laboratory of Biophotonics, Tomsk State University, Tomsk, Russia
[3] Institute of Precision Mechanics and Control of the Russian Academy of Sciences, Saratov, Russia
[4] Université de Lorraine, CNRS, CRAN UMR 7039, Vandoeuvre-Lès-Nancy, France

E-mail: tuchinvv@mail.ru

Abstract – A set of fundamental researches targeting valuable optical technologies for diagnosis in dermatology are presented. Theoretical and experimental results demonstrated that these technologies based on tissue optical properties control are effective in a wide spectral range from visible/NIR to MIR/THz.

Keywords – optical methods, visible/NIR, MIR/THz, dermatology, diagnostics

I. Introduction

The present contribution was to develop the physical basis for increasing the informativity of optical spectroscopy and imaging of skin pathologies through its temporal and reversible dehydration due to the use of hyperosmotic agents and compression.[1] These basic results received for the visible/NIR and terahertz spectral ranges are expected to allow us to propose a set of complementary photodiagnostic methods in dermatology.

The controllable changes in absorption and scattering of radiation that is, in probing biological tissue, are intended to improve the skin diagnostic efficiency. One of the key point is to investigate the correlation between THz data and multimodal spectroscopy and imaging in the visible/NIR, including the analysis of reflection and fluorescence spectra, as well as OCT images of the skin under the action of hyperosmotic Optical Clearing Agent (OCA) and tissue compression.

II. Skin Fractional Laser Microablation

Fractional laser microablation (FLMA) was implemented to enhance the diffusion of OCA through *in vivo* white rat skin. An Er: YAG StarLux/Lux2940 laser (Palomar Medical Technologies Inc., Burlington, MA, USA) was used (wavelength 2940 nm, pulse energy 1 J, pulse duration 200 µs). It provided 64 microchannels in the skin of 100–150 µm depth and ~100 µm diameter on the skin surface, and spaced of 500 µm. Figure 1 (a) shows the OCT images of intact *in vivo* rat skin. Dotted lines indicate the boundaries of the analyzed zones. In Fig. 1 (a–d), it is clearly seen that immediately after FLMA, illumination of the upper layer of the dermis is increased. In zone II, the signal is also increased. Throughout the OCA PEG-300 delivery via the microchannels, the local scattering coefficient μ_s of zone I and II is observed to decrease during the first 15–20 min and then to rise (Fig. 1(e)).

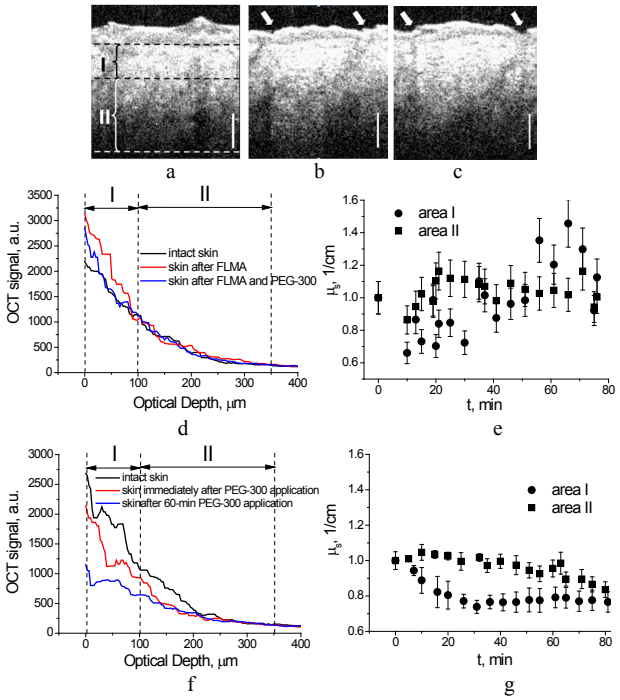

Fig. 1. *In vivo* OCT images of rat skin: (a) intact skin; (b) skin after FLMA; (c) 1 hour after FLMA and application of PEG-300; (d) the averaged OCT A-scans corresponding to the (a–c) images; (f) the dermal layers of intact skin before PEG-300 application, immediately, and in 60 min after; and (e, g) the kinetics of the normalized scattering coefficient in the analyzed areas I and II, corresponding to the signals presented in (d, f), respectively. In (a, b, c), the arrows point the microchannels visible in the epidermis. Dotted lines indicate the boundaries of the area I (from 50–70 µm to 150–170 µm) and area II (from 150–170 µm to 350–400 µm). Bars correspond to 100 µm

This may be due to the hygroscopicity of PEG-300, which permeates directly into dermis through the microchannels and induces water diffusion from the deeper layers of the dermis. From Fig. 1 (f, g) it follows that the OCT signal of intact (not perforated) skin was significantly reduced in the zone I, which corresponds to

the optical clearing of the upper part of the dermis. At a depth of 150–400 μm (zone II), the decrease in μ_s appears much slower. After approx. 1.5 h, the relative μ_s values in both zones were equalized.

III. THE DEHYDRATION OF THE SKIN *EX VIVO*

The degree of dehydration for *ex vivo* rat skin was estimated by measuring the weight of skin samples before and during (every 5 min) their immersion in the OCA, consisting of an aqueous-alcohol 50%-fructose solution (refractive index (RI) is 1.4087). Figure 2 shows the evolution of the skin sample weight as a function of immersion time in OCA, normalized to the initial values of skin weight and averaged over all the samples divided into two separate groups.

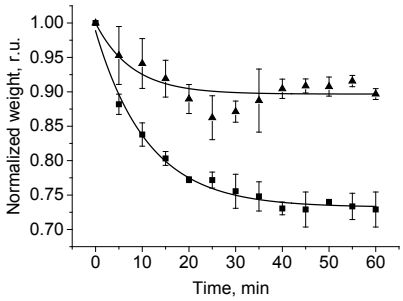

Fig. 2. Kinetics of weight of rat skin samples throughout their immersion into OCA water-alcohol 50%-fructose solution (two groups of samples with different dehydration degree)

It can be seen in Fig. 2 that the weight of the skin samples starts to decrease just after the samples were immersed in the OCA. This results from the interaction of the latter with the tissue via osmotic pressure, leading to sample dehydration. In one group of samples taken from different animals, the weight curve continues to decrease during 1 h of immersion, while in another group, after tissue shrinkage during 30 min, some swelling-like phenomenon happened, which can be related to intensive diffusion of OCA molecules into the skin and rehydration. Skin pH alterations may also play a role in this complex kinetics. These differences in temporal behavior may probably due to the inter-individual skin features between animals. To assess the degree and characteristic time of dehydration of skin samples, an approximation of the temporal dependences of the weight of the skin samples immersed in a water-alcohol solution of fructose was done (Table 1).[2]

Table 1. The approximated parameters of the time dependences for the weight of rat skin samples immersed into OCA water-alcohol 50%-fructose solution (two groups of samples with different dehydration degree).

Group	Dehydration degree, %	Dehydration characteristic time, min
I	26 ± 1	11 ± 1
II	10 ± 1	8 ± 1

The results may be useful for further studies of the skin optical clearing, development of optical methods of treatment and diagnosis in dermatology. Quantifying the degree of tissue dehydration is important for providing controlled conditions to enhanced transmission of tissue for terahertz radiation, due to less absorption and to less Fresnel reflection at the air-tissue interface reducing the RI at dehydration.[3] The diffusivity of exogenous agent (OCA) in tissues measured from kinetic curves could also serve as a biomarker of organ pathology associated with change of tissue permeability, such as malignant tumors[4] or diabetes mellitus.[5]

Ex vivo rat skin dehydration by an OCA was also estimated using a multi-wavelength refractometry for the visible and NIR (Abbe refractometer DR-M2/1550 (Atago, Japan); 486 nm - 1300 nm). Skin samples were placed into a closed sealed container with 2 ml of 70%-glycerol solution or 40%-glucose solution. Measurements of the RI of OCAs were carried out during 60 min of their interaction with a sample. It was found that OCA RI decreased, indicating tissue dehydration and making it possible to quantify the volume of fluid (mostly free water) extracted from the tissue using the modified Gladstone-Dale equation. The 70%-glycerol led to a greater dehydration of the skin (8.11%), compared with the 40%-glucose (2.02%).[6]

IV. THE THERMAL DEHYDRATION OF THE PORCINE SKIN: THZ MEASUREMENTS

THz spectral measurements were made using a T-SPEC terahertz real-time spectrometer (EKSPLA, Lithuania) in the frequency range 0.25-1THz and software THzSpectrometer 2D. The transmittance spectra of porcine abdominal adipose tissue samples of ~0.5 mm in thickness were obtained at various temperatures (26–70°C) and the temperature dependency of optical density (OD) at a frequency of 1 THz was measured. In Fig. 3, the latter OD is seen to decrease as temperature increases, which can be associated mostly with the dehydration of the sample. However, some inclusion of THz wave scattering suppression into OD decrease at RI matching by free fatty acids released from adipocytes caused by thermally induced cell lipolysis can be expected.

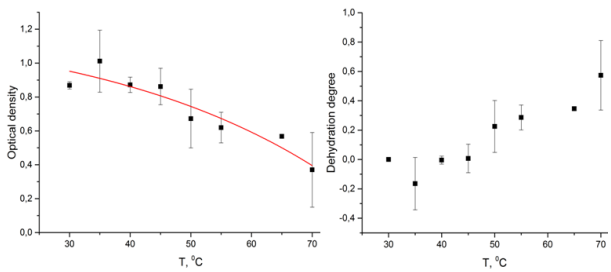

Fig. 3. Temperature dependences of optical density (a) at a frequency of 1 THz and the calculated average value of dehydration of samples (6) of porcine adipose tissue

V. Modeling of Scattering and Fluorescence in Tissues

A computationally efficient and reliable method for calculating the scattering and fluorescence characteristics of layered models of tissues with oblique incidence of light was developed. The method is based on solving one-dimensional transport equations in a form discretized in angular variables for radiation with an arbitrary angular distribution. To calculate the matrix operators characterizing the action of the layers with coordinate-independent scattering and fluorescence parameters, a mode representation of the radiation characteristics and an adding algorithm similar to that presented in Ref. [10] were used. Figure 4 shows the calculated dependence of the scattering signal (P_{ex}) and the fluorescence signal (P_{fl}) on the scattering coefficients $\mu_{fl\text{-}s}$ and $\mu_{ex\text{-}s}$ at the wavelengths of fluorescence excitation (λ_{ex} = 365 nm) and emission (λ_{fl} = 480 nm). The angle of incidence of the exciting radiation was α_{inc} = 28°. Radiation within a solid angle of $3.4\cdot10^{-2}$ sr around the normal direction was recorded. In the calculations, the ratio $\eta = \mu_{ex\text{-}s}/\mu_{ex\text{-}s0} = \mu_{fl\text{-}s}/\mu_{fl\text{-}s0}$ was varied, with $\mu_{ex\text{-}s0}$ and $\mu_{fl\text{-}s0}$ the initial values of $\mu_{fl\text{-}s}$ and $\mu_{ex\text{-}s}$.

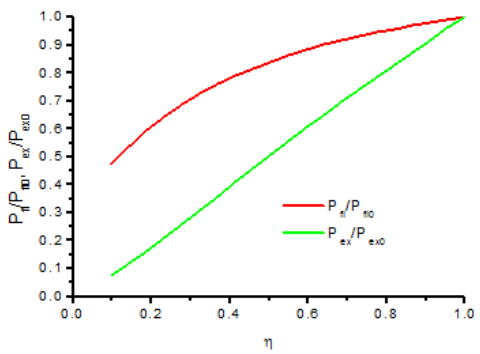

Fig. 4. Calculated dependencies P_{ex}/P_{ex0} and P_{fl}/P_{fl0} on η. P_{ex0} and P_{fl0} correspond to $\eta = 1$; $\mu_{ex\text{-}s0}$= 227 cm^{-1} and $\mu_{fl\text{-}s0}$ = 205 cm^{-1}. Parameters g_{ex}, g_{fl}, $\mu_{ex\text{-}s0}$, $\mu_{fl\text{-}s0}$, and $\mu_{fl\text{-}a0}$ were taken as for skin dermis [1]

A series of phantoms with different in depth location of fluorescent layer were made. The sequence of fluorescence spectra was measured on each phantom. The obtained experimental results on the kinetics of fluorescence signal from layered "tissue" under optical clearing were interpreted with reference to computer simulations.

VI. Conclusion

We conducted complex fundamental research aimed at creating effective optical technologies for diagnosis in dermatology. These technologies are effective in a wide spectral range from visible/NIR to MIR/THz and based on tissue optical properties control.

Acknowledgments

This work was financially supported by RFBR grant 18-52-16025 NTSNIL_a

References

[1] V.V. Tuchin, *Tissue Optics: Light Scattering Methods and Instruments for Medical Diagnostics*. 3rd ed. (SPIE press, Bellingham, 2015).

[2] D.K. Tuchina, A.N. Bashkatov, E.A. Genina, V.V. Tuchin Investigation of the impact of immersion agents on the weight and geometric parameters of myocardial tissue in vitro, *Biofizika* **63** (5), 989–996 (2018).

[3] O.A. Smolyanskaya, N.V. Chernomyrdin, A.A. Konovko, et al., Terahertz biophotonics as a tool for studies of dielectric and spectral properties of biological tissues and liquids, *Progr. Quant. Electron.* **62** 1–77 (2018).

[4] S. Carvalho, N. Gueiral, E. Nogueira, R. Henrique, L. Oliveira, V.V. Tuchin, Glucose diffusion in colorectal mucosa—a comparative study between normal and cancer tissues, *J. Biomed. Opt.* **22**(9) 091506 (2017).

[5] D.K. Tuchina, A.N. Bashkatov, A.B. Bucharskaya, V.V. Tuchin, Exogenous agent diffusivity in tissues as a biomarker of diabetes mellitus pathology, *Proc. SPIE* **10877**, 108770X (2019).

[6] Yu.V. Kistenev, V.V. Tuchin, A.V. Borisov, et al., Medical diagnosis using NIR and THz tissue imaging and machine learning methods, *Proc. SPIE* **10877**, 108770J (2019).

[7] N. V. Chernomyrdin, A. S. Kucheryavenko, G. S. Kolontaeva, et al., Reflection-mode continuous-wave 0.15 λ -resolution terahertz solid immersion microscopy of soft biological tissues, *Applied Physics Letters* **113**(11) 111102 (2018).

[8] I. N. Dolganova, K. I. Zaytsev, S. O. Yurchenko, V. E. Karasik, V. V. Tuchin, Scattering in quasi-ordered structures for terahertz imaging: local order can increase an image quality, *IEEE Trans. Terahertz Sci. Technol.* **8** (4),403–409 (2018).

[9] J. W. Bowen, T. Owen, J. B. Jackson, et al., Cyclododecane as a contrast improving substance for the terahertz imaging of artworks, *IEEE Trans. Terahertz Sci. Technol.* **5**(6) 1005–1011 (2015).

[10] S. Leyre, G. Durinck, B. Van Giel, et al., Extended adding-doubling method for fluorescent applications, *Opt. Express* **20**, 17856–17872 (2012).

Spectroscopy of Pre-Cancer States with Using THz Emitters Based on Superlattices

V. L. Vaks[1], V. A. Anfertev[1], M. B. Chernyaeva[1], E. G. Domracheva[1], A. Baranov[2], R. Teissier[3]

[1] Terahertz spectrometry department of IPM RAS, IAP RAS, Nizhny Novgorod, Russia
[2] Institute of Electronics and Systems (IES), UMR 5214 CNRS - University of Montpellier, France

E-mail: vax@ipmras.ru

Abstract – The results of development of radiation sources such as THz emitters based on quantum cascade lasers and multipliers based on superlattices as well as investigation of their characteristics were presented.

Keywords – quantum cascade laser, continuous and pulse modes, semiconductor superlattice, terahertz frequency range, spectrum, pre-cancer state, gas-marker.

I. Introduction

The main problem of high precise spectroscopy and its applications is development of high-stable tunable coherent sources of terahertz radiation. The modern spectroscopic requirements to THz radiation sources are frequency stabilization with accuracy ~10^{-8}–10^{-10} from carrier frequency, Doppler resolution (10^{-6} from carrier frequency), high spectral purity and smooth tuning of frequency in wide frequency range.

The aim of work is the elaboration of new semiconductor radiation sources and the development of physical basis of THz nonstationary spectroscopy for fast qualitative and quantitative analysis of various biomarkers concerned with cancer disease for its early diagnostics and analysis of chemical substances produced in human organism (which called as metabolites) allowing to control and verify the efficiency of therapy or its combinations.

The development of radiation sources such as THz emitters based on quantum cascade lasers (QCL) of THz frequency range (3–4 THz) with frequency multiplying for the developing the inaccessible part of THz range over 5 THz is proposed. Besides the subTHz radiation source (500–700 GHz) based on semiconductor generator with frequency multiplying will be used for verification of method. The multiplier based on semiconductor superlattices (SL) operated from 0.1 to 10 THz will be used.

II. QCL on the base of GaAlAs/GaAs and superlattices (IES)

The initial progress in the QCL performances was provided by the design improvements. The three-well diagonal scheme with resonant LO-phonon depopulation of the bottom transition level was demonstrated to be very promising for high temperature operation with T_{max} = 175 K achieved in lasers employing an Au-Au double-metal waveguide [2]. Further improvements aimed essentially at the optimization of the transition diagonality and particularly the use of Cu-Cu double-metal waveguides allowed increasing T_{max} up to 186 K [3] and later to almost 200 K [4] This very reliable design was chosen to fabricate QCLs for the goals of these work. Theoretical calculations of the conduction band diagram and squared modules of the wavefunctions of the investigated structure calculated for an electric field corresponding to the lasing threshold at 80 K were carried out. The band bending due to the charge of ionized donors was taken into account in these calculations. The lasing transitions are e4-e2 and e3-e2. The last well of structure is isolated from the next period of the structure for better visibility of the extraction gap and the distance e1-e0 is equal to the GaAs LO-phonon energy to provide efficient removal of electrons from the bottom transition level. The ground level e0 is in fact splitted and corresponds to the levels e3 and e4 in the previous wide well in the considered portion of the structure.

Each stage of the GaAlAs/GaAs active zone of our devices is based on the following layer sequence, in Å starting from the injection barrier: 48/85/28/85/15/12/15/164 where the $Ga_{0.85}Al_{0.15}As$ barriers are indicated in bold, the underlined layer is $Ga_{0.85}Al_{0.15}As$ doped with Si to 4×10^{17} cm^{-3}. In order to increase the output power and improve the beam quality the number of stages was increased from 222 in the original structure to 300. The wafer was grown by molecular beam epitaxy in a RIBER 412 solid source machine on an undoped (100) GaAs substrate. A 0.6-µm-thick GaAs bottom contact layer doped with Si to n = 5×10^{18} cm^{-3} was grown before the laser active zone and a 50-nm-thick GaAs top contact layer with the same doping level terminated the structure. The grown wafer was processed into (1–3)-mm-long lasers with a double-metal (DM) and simple plasmon (SP) waveguides. The DM devices with an Au-Au waveguide were characterized in order to compare their performances with the published results whereas the SP lasers providing much better beam quality were mainly used for spectroscopy experiments. To fabricate SP lasers the structure was etched down to the bottom contact layer. Both contact layers were metallized with Cr/Au without annealing. To provide efficient lateral current injection the bottom contact was wire bonded from both sides of the laser ridges. The lasers were soldered epi-side up on copper heatsinks.

The fabricated lasers exhibited threshold current densities about 0.8 and 1.2 kA/cm^2 for the devices with a DM and SP waveguide, respectively, at 80 K. The DM

lasers operated in pulsed mode up to T_{max} = 181 K which corresponds to the best published results for THz QCLs with the Au-Au waveguide. Efficient collection of the output power of the DM lasers is difficult because of the diffraction effects due to the very thin waveguide with a thickness smaller than the emission wavelength. In the SP QCLs the optical mode penetrates into the substrate thus increasing the output aperture which, in turn, significantly improves the beam quality. In our characterization setup the collected optical power of the SP lasers was more than 50 times higher than for the DM devices. On the other hand, the maximum operation temperature of the SP lasers is lower with T_{max} = 125 K for the investigated devices.

Spectral measurements were performed using a Bruker Vertex 70 Fourier transform infrared spectrometer (FTIR) equipped with a pyroelectric photodetector. Emission spectra of the fabricated lasers were quite similar for the DM and SP devices. The emission frequency shifted from about 2.9 THz to 3.8 THz with increasing current and temperature. It is necessary to point out a gap around 3.5 THz between two observed groups of longitudinal modes. To explain and predict the behavior of the emission spectra we calculated positions of the electron levels in the structure as a function of applied electric field. These results show that the low frequency emission at 2.9–3.3 THz is due to the e3-e2 transition. At higher electric fields, the population of the e4 level and the oscillator strength of the e4-e2 transition increase and this process dominates at high currents. The gap around 3.5 THz is due to the anticrossing of the levels e4 and e3.The e3-e2 separation increases faster with electric field than the e4-e2 energy, which explains the larger shift of the low frequency modes with current. At elevated temperatures, the QCL operates at high electric field and the modes at 3.7–3.8 THz dominate.

The obtained results show that the three well resonant phonon design is well suited for the development of THz QCLs for spectroscopic applications. It provides low threshold operation above the liquid nitrogen temperature and a large spectral range that can be covered by varying the laser current and temperature. The design should nevertheless be modified to obtain emission in the anticrossing gap and at frequencies below 2.9 and above 3.8 THz. This will be done if necessary later.

An GaAs/AlAs SL was grown to fabricate frequency multipliers. The sample contained 18 periods of the layer sequence composed of 51 Å of GaAs doped with Si to 2×10^{18} cm^{-3} and 12 Å of AlAs. The SL was sandwiched between the Si-doped 0.5-µm-thick GaAs layers. The structure was grown on an undoped (100) GaAs substrate.

III. INVESTIGATION OF SEMICONDUCTOR DEVICES (IPM RAS)

Spectral distribution of radiation of some pulse QCLs (GaAs/AlGaAs, with resonance photon design based on 3 quantum wells) grown at Montpellier University (France) by group of Prof. A. Baranov was investigated. The experimental setup for investigation of QCL spectra was designed. The QCL sample with single mode generation and sufficiently large power was chosen from the QCL sample series. The precise QCL frequency value which was equal to 3.77 THz (the value of 3.78 THz was obtained by French group with using the Fourier spectrometer) was measured. The features of QCL frequency tuning including the frequency tuning range (which is equal to 2 GHz), the speed of QCL frequency downward tuning within the pulse duration (which is equal to 500 MHz/µs) and other were determined. The frequency upward tuning is possible with greater speed at the large currents.

The optimization of SL operation as frequency multiplier at low (2, 3) harmonics numbers was carried out. The possibility of SL multiplier use for pumping and bringing the hot-electron bolometer (HEB) to heterodyne mode was studied. Experimental results show that the power of the third and fifth harmonics containing the main part of radiation power is enough for HEB pumping to the mixer mode. Besides the possibility of making the THz heterodyne receiver based on HEB mixer, high-stable synthesizer and SL generator of harmonics was studied. It is established that SL multiplier harmonics power is enough to bring the HEB mixer to the operation mode.

An experiment on studying the SL harmonics power change at cryogenic temperatures was carried out. The total power of harmonics of SL multiplier was equal to 0.42 µW (at the room temperature), 0.15 µW (at liquid nitrogen temperature) and 0.3 µW (at liquid helium temperature). The radiation power dependence of SL multiplier harmonics on given power and diode bias for various frequencies was investigated and current-voltage characteristics of SL diodes in dependence with radiation influence were measured.

The development and realization of power supply for QCL with changed operation parameters which operates in pulse or continuous modes were carried out. The dependences of various power-frequency characteristics on supply mode (voltage, current, supply pulse duration) were investigated for studying the THz QCL features. It is enough to use the laboratory stable current source for providing the possibility of QCL continuous generation. The pulses driver based on the field transistor which has sufficient speed was elaborated for pulsed QCL. In future the pulse current source will be planned.

The works for elaboration of QCL frequency stabilization system with using the high-stable signal of reference source were carried out. A QCL sample with frequency of 2.02 THz and possibility of pulse and continuous operation modes was used for development of QCL frequency stabilization system Dependences of radiation power and current-voltage characteristics on duty cycle, dependences of radiation power on current were investigated. The images of QCL collimated beam profile at duty cycle of 10% for various currents were obtained. The QCL quasi-parallel beam profile images were obtained for various currents for investigation of

QCL continuous operation mode. An experiment on mixing the QCL radiation with signal of BWO based synthesizer (120-170 GHz) as a reference source, which was preliminary multiplied with using SL multiplier (13th harmonics). An estimation of QCL linewidth was about 1 MHz. The tuning frequency range was about 700 MHz. QCL is shown to have monotonic tuning from control current hat is acceptable for elaboration of phase-lock loop (PLL) system. The PLL unit containing the phase detector (for comparison of phases of signal of reference generator and signal of intermediate frequency (IF) between QCL and BWO harmonics), loop filter (the 3rd order) (to cut off the high sideband components after phase detector) and control load was elaborated and realized. The test bench realizing the radiation source at the frequency of 2.02 THZ with spectral linewidth of some tens kHz was developed and realized.

The possible continuous QCL radiation modulation modes were analyzed and one providing the maximal sensitivity of spectrometer was chosen. Spectrometers based on detection of electromagnetic radiation transmitted through the gas cell use three variants of modulations (frequency modulation by sin signal, frequency manipulation by rectangular signal and phase manipulation). The comparison of three modulation methods allows concluding the phase manipulation to be more preferable for realization in spectrometer with continuous QCL as a radiation source with stabilized frequency. The phase manipulation allows to achieve the maximal spectrometer sensitivity, interference suppression using the digital methods, a simplicity of receiving part of spectrometer, a possibility of using the broadband and narrowband QCL PLL.

The test bench composed of radiation source (BWO based synthesizer with SL multiplier), measuring cell, vacuum exhaust unit and receiving unit was built for measuring the absorption spectra of exhaled breath samples in frequency range of 500–700 GHz. The measurements of absorption spectra of exhaled breath and biological liquids samples were carried out for developing the method of determination of potential cancer diseases gas-marker. These measurements were carried out as in mode of continuous pumping the measuring cell as in stationary mode without permanent pumping after sample injection in gas cell. Besides the measurements in two operation modes of test bench (frequency scanning mode for determination of analytical absorption lines of substances and mode of record at assigned analytical line frequency) were carried out. Such potential markers of endogenous intoxication at cancer diseases, as nitric oxide and ammonia were detected in investigated samples using their analytical absorption lines.

IV. CONCLUSIONS

The radiation sources (THz emitters) based on THz quantum cascade lasers (3–4 THz) with multiplying the frequency for development of inaccessible THz domain (5–8 THz) are developed and realized. The next stages of work will be devoted to development of radiation receiver of 5-8 THz frequency range with using harmonic mixer and continuation of wideband measurements in 500–700 GHz, 3–4 THz and over 5 THz frequency ranges with using the THz high resolution spectroscopy method in the samples of exhaled breath and vapors of biological liquids for medical diagnostics of pre-cancer states.

ACKNOWLEDGMENTS

This work was financially supported by RFBR grant N 18-52-16017 NCNIL-a

REFERENCES

[1] R. Köhler, et al, *Nature* **417**, 156 (2002).
[2] M. A. Belkin et al. *Opt. Express* **16**, 3242 (2008).
[3] S. Kumar et al. *Appl. Phys. Lett*. **94**, 131105 (2009).
[4] S. Fathololoumi et al. *Opt. Express* **20**, 3866 (2012).

Theoretical and Experimental Analysis of the Mechanisms of the Interaction of Terahertz Radiation with Neurons

A. S. Ratushniak[1], T. A. Zapara[1], A. L. Proskura[1], A. S. Kozlov[2], D. S. Serdyukov[3], O. P. Cherkasova[3], J. P. Guillet[4], P. Mounaix[4]

[1] Institute of Computational Technologies of SB RAS, Novosibirsk, Russia
[2] Institute of Chemical Kinetics and Combustion of SB RAS, Novosibirsk, Russia
[3] Institute of Laser Physics of SB RAS, Novosibirsk, Russia
[4] IMS – Bordeaux University, France

E-mail: o.p.cherkasova@gmail.com

Abstract – The aim of the work is to study the mechanisms of THz radiation influence on membranes and neural signaling pathways, which alters intermolecular interactions, including the permeability of cell membranes.

Keywords – THz radiation, neurons, membrane permeability

I. INTRODUCTION

At present, there is evidence pointing to the interaction of terahertz (THz) radiation with biological objects of different levels of organization, from simple molecules, such as water [1], to complex biopolymers, such as sugars, proteins, DNA [2], respectively, to cells, tissues [3], and the body as a whole [4]. The analysis of the mechanism of the primary physical action of THz radiation on biological objects is confronted with the problems of explaining its transmission to membrane structures, signaling pathways and the genetic apparatus of the cell [5]. Currently, these problems are not fully resolved. The project aims to study the mechanisms of influence of THz radiation on the membrane and signal structures of nerve cells, which changes the intermolecular interactions, including the permeability of cell membranes. Transmembrane delivery of pharmacological or other means to cells in neuro-induced pathological conditions is one of the most important tasks of finding new ways to correct these conditions. In this regard, the search and development of effective and safe methods and technologies that make it possible to facilitate the delivery of such agents through membrane structures that are both sufficiently efficient, able to localize the delivery zone and sufficiently safe for the organism remain relevant. Therefore, the development of methods for influencing the reversible permeability of the membranes of nerve cells seems quite promising.

II. RESULTS

The project will carry out a comprehensive experimental assessment of the possibility of a controlled change in the permeability of membranes using non-ionizing electromagnetic radiation in the terahertz frequency range. A method will be developed for diagnosing changes in cell membrane permeability under the action of THz radiation using THz-TDS [6]. A theoretical-experimental analysis of the mechanisms of the action of electromagnetic radiation in this range on biological systems will be carried out [7]. An experimental selection of the most effective frequencies, energies and other parameters and modes of exposure will be conducted. The safety of such effects will be investigated and the necessary conditions and characteristics of the radiation will be identified. All this will allow, on the one hand, to identify and clarify known mechanisms for the formation of transmembrane pores, and, on the other hand, to develop new physical tools for efficient cell transfection, targeted delivery of drugs and other (especially hydrophobic) biologically active compounds; which, in turn, will improve the efficiency of targeted correction of a wide range of pathologies. This project will greatly improve the knowledge of the interaction of THz waves with cells and the surrounding medium and the influence of the intracellular protein composition of cells. Also the permeabilization of neurons or other targeted cells under chemical agent will be studied.

REFERENCES

[1] [O. Smolyanskaya, N. Chernomyrdin, A. Konovko et al, *Progress in Quantum Electronics*, **62**, 1–77 (2018).
[2] X. Yang, X. Zhao, K. Yang et al, *Trends in Biotechnology*, **34** (10), 810–824 (2016).
[3] I. Il'ina, D. Sitnikov, and M. Agranat, *High Temperature*, **56** (5), 789–810 (2018).
[4] V. Fedorov and N. Weisman, *Biophysics*, **62** (3), 460–465 (2017).
[5] V. Fedorov, D. Serdyukov, O. Cherkasova, S. Popova, E. Nemova, *Journal of OpticalTechnology*, **84** (8), 509–514 (2017).
[6] J.-B. Perraud, J.-P. Guillet, O. Redon, M. Hamdi, F. Simoens, P. Mounaix, *Opt. Lett.*, **44** (3), 483 (2019).
[7] E.A. Ananko, N.L. Podkolodny, I.L. Stepanenko et al. *Nucleic Acids Res,* **33**, 425–427 (2005).

Controllable Synthesis of DAST Submicron Crystals and Their Microstructuration by Direct Laser Writing

T. N. Pogosian[1,2], I. Yu. Denisyuk[1], N. D. Lai[2]

[1] International Laboratory of Nonlinear Optical Molecular Crystals and Microlasers, ITMO University, St. Petersburg, Russia

[2] Laboratoire de Photonique Quantique et Moléculaire, UMR 8537, ENS Paris-Saclay, Centrale Supélec, CNRS, Université Paris-Saclay, France

E-mail: denisiuk@mail.ifmo.ru

Abstract – We report on a synthesis of DAST submicron crystals in polymer matrix and their microstructuration for nonlinear optical application. The DAST crystals sizes were controlled by viscosity of the initial mixing solution. The optimum concentrations of DAST/PMMA (mass ratio = = 2/100) in chloroform are about 3 to 8%, which resulting in DAST crystals with sizes ranging from 150 nm to 1000 nm. The DAST crystals were demonstrated to be easily bleached by a focused green laser beam. Fast optical heating and cooling turn DAST crystals into an amorphous form hence provoking loss of their nonlinear properties. By scanning the DAST submicron crystals in polymer matrix with a continuous-wave laser (532 nm) with a modest laser power of 10 mW and a scanning speed of about 35 µm/s, well-defined microstructures of DAST crystals were obtained. These nonlinear structures are very promising for nonlinear frequency conversion via quasi-phase matching technique as well as for applications in THz domain.

Keywords – nanoparticles, DAST, direct laser writing, nonlinear optics

I. Introduction

Quasi-phase-matching (QPM) structures allow dramatically extending the interaction length between terahertz and optical pulses. QPM is used for optical-to-terahertz conversion by optical rectification[1] (OR) or by difference frequency generation[2] (DFG).

Highly nonlinear optical 4-(4-dimethylaminostyryl)-1-methylpyridinium tosylate (DAST) crystal is one of the promising materials for applications in THz domain[3,4]. We propose an efficient method to realize QPM nonlinear structures by synthesis of DAST nanocrystals in PMMA matrix and photobleaching these crystals by a direct laser writing (DLW) method[5].

II. Controllable Synthesis of DAST Nanocrystals

Using the method presented in Ref. 6, we prepared following solutions and studied the influence of the viscosity of these solutions on the size of final DAST crystals. DAST powder (CAS:80969-52-4 Genolite biotek) was dissolved in methanol (322415 Aldrich) according to solubility limit from Ref. 7 at room temperature. PMMA (Plexiglas® V045) was dissolved in chloroform (CL0218 Scharlau). These two solutions were mixed together without loss of homogeneity. The DAST mass is equal 2% of the PMMA mass. The concentration of PMMA in chloroform was changed to vary the viscosity of solutions. We prepared six solutions with 1, 3, 5, 8, 10, and 15% of (DAST/PMMA) in chloroform.

The DAST/PMMA films were formed by two-step centrifuging (100 and then 1500 rpm for 10 s). The samples were annealed by a hot plate at 180°C using different annealing time for different films thicknesses.

Fig. 1 shows the influence of viscosity (hence thickness) of films on the size and form of DAST crystals. An increase in the viscosity leads to an increase of crystals size and loss of shape similarity. In order to examine real size and shape of DAST crystals, the PMMA layer of samples was removed by a pure toluene leaving only DAST crystals on glass substrate. The samples were then covered by a thin gold layer and imaged scanning electron microscope (SEM). Fig. 1 presents set of films characterizations, such as annealing time, thickness, range of crystals size, second-harmonic generation (SHG) intensity and nonlinear optical coefficient. The SHG signal was exited by CryLas laser emitting a wavelength at 1064 nm and was measured by an Ocean Optics USB2000+ spectrometer. The nonlinear optical coefficient was calculated as the square root of the ratio of the SHG intensity to the film thickness.

III. Structuration by Direct Laser Writing

We demonstrated that it was possible to realize microstructures of DAST films by bleaching DAST crystal with a focused laser beam. The DLW based on low one-photon absorption (LOPA) setup is fully presented in Ref. 5. A continuous-wave 532 nm laser (Oxxius frequency-doubled Nd-YAG laser) was used to bleach DAST crystals because this wavelength belongs to the pick of DAST absorption spectrum. High laser intensity (power of about 10 mW) at the focusing spot allowed us bleaching the DAST crystals meaning local destroying of fluorescence and nonlinear optics properties of material. By using very weak laser beam (power of about 1 microWatt), the same laser setup allowed us to scan the same sample area and collecting fluorescence image. This signal was detected by the avalanche photodiode (SPCM-AQRH-13 Perkin Elmer). A Nd:YAG

laser beam (wavelength of 1064 nm) was also added to the LOPA-DLW system, in perfectly alignment with the 532 nm beam, to test the SHG of the DAST microstructures. We note that for this experiment, we chose samples with 5% of DAST/PMMA concentration without loss of generality.

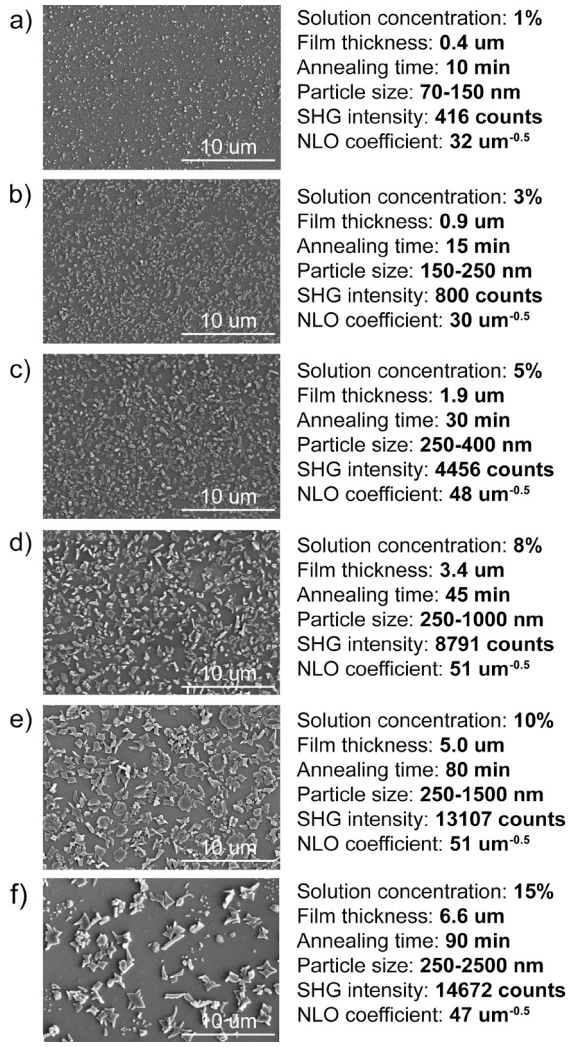

Fig. 1. SEM images of samples prepared from solutions with concentrations of (a) 1, (b) 3, (c) 5, (d) 8, (e) 10, and (f) 15% and their corresponding characteristics

We observed disappearance of DAST luminescence without formation of visible damages of PMMA layers. The mechanism of DAST crystal bleaching can be explained as following. Due to the fast heating and fast cooling, the molecular crystals of DAST pass into an amorphous form which has a quantum yield of luminescence around 0.2%. It is much smaller in comparison with that of an original DAST crystal form, which shows a luminescence quantum yield of around 14–20%.We tested photo-destruction by writing a 2D grating (5 x 5 lines), as shown in Fig. 2. The distance between lines was fixed at 15 µm. We have investigated in detail the dependence of bleaching effect on laser power (1–10 mW) and writing speed (5–35 µm/s). Fig. 2 presents results obtained with a writing speed of 35 µm/s and a laser power of 10 mW. It is obvious that the DAST crystals were bleached and the nonlinear microstructure is well created, with a width of less than 1 µm. Fig. 2a shows a fluorescence image obtained by scanning with a 532 nm laser (with a laser power of about 0.1 µW). Figs. 2 (b, c) show optical microscope images of corresponding structure, where we can clearly observe the absence of DAST crystals.

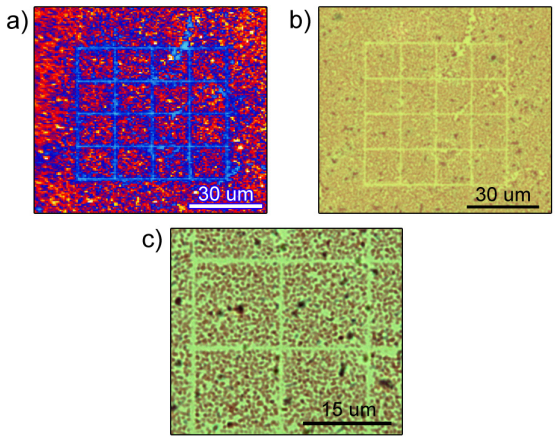

Fig. 2. a) Fluorescence image obtained by scanning with a 532 nm laser, b) optical microscope image of corresponding sample, c) enlarged optical microscope image of corresponding sample

IV. Conclusions

We demonstrated that DAST crystals with different submicrometer sizes can be synthesized by controlling the viscosity of used solution. The best DAST crystals for fabrication of nonlinear DAST microstructures by DLW technique is obtained with samples having 3 to 8% of DAST + PMMA concentrations in solvent. The bleaching effect of DAST by a focused laser beam is due to the fast heating and cooling during light exposure, which turns DAST crystals into an amorphous form resulting in a loss of their nonlinear properties. DLW allowed thus create desired DAST microstructures by appropriate laser power and writing speed. We expect that these nonlinear structures will be useful for nonlinear optical effect, such as high conversion efficiency THz frequency generation...

Acknowledgments. This work was financially supported by Russian Foundation for Basic Research project № 18-52-16014.

References

[1] K. L. Vodopyanova, M. M. Fejer, X. Yu, J. S. Harris, Y.-S. Lee, W. C. Hurlbut, V. G. Kozlov, D. Bliss and C. Lynch, *Appl. Phys. Lett.* **89**, 141119 (2006).

[2] Y. Sasaki, Y. Avetisyan, H. Yokoyama and H. Ito, *Opt. Lett.* **30**, 2927 (2005).

[3] P. Y. Han, M. Tani, F. Pan and X.-C. Zhang, *Opt. Lett.* **25**, 675 (2000).

[4] B. Pradarutti, G. Matthäus, S. Riehemann, G. Notni, S. Nolte and A. Tünnermann, *Opt. Commun.* **281**, 5031 (2008).

[5] Q. Li, M. T. Do, I. Ledoux-Rak and N. D. Lai, *Opt. Lett.* **38**, 4640 (2013).

[6] M. L. Zheng, W. Q. Chen, K. Fujita, X. M. Duan, and S. Kawata, *Nanoscale* **2**, 913 (2010).

[7] T. Thomas, J. V. Ramaclus, F. P. Mena, E. Mosquera, P. Sagayaraja, and E. A. Michaelb, *CrystEngComm* **17**, 1989 (2015).

Co-crystal 4-aminopyridine-4-nitrophenol-4-nitrophenolate for Terahertz Applications

I. Denisyuk[1], M. Fokina[1], A. Sinko[2], I. Ozheredov[2], E. Sheklanova[1], K. Zhevaikin[1], I. Ledoux-Rak[3]

[1] ITMO University, St. Petersburg, Russia
[2] Lomonosov MSU, Moscow, Russia
[3] ENS, Paris-Soclay, France

Email: denisiuk@mail.ifmo.ru

Abstract – Optical and terahertz properties of new co-crystal 4-aminopyridine-4-nitrophenol-4-nitrophenolate were measured. This material having low absorption in terahertz range and photo bleaching proprieties is suitable for producing of the periodic lattice. We discuss of its further applicability for terahertz applications.

Keywords – Organic crystals, nonlinear optics, terahertz applications

I. INTRODUCTION

Organic nonlinear-optical (NLO) molecular crystals have attracted consistent attention because of the advantages offered by organic systems including high electric susceptibilities, fast response time, good optical threshold for laser power, and relative ease of devise processing. Such materials can find wide applications in laser frequency conversion, optical data storage, terahertz (THz) generation, optical modulation, optical waveguides, etc. [1].

This study presents preparation, crystals grown and measurements of optical and THz properties of new co-crystal 4-aminopyridine-4-nitrophenol-4-nitrophenolate. Single crystal of a good quality was grown by slow evaporation technique using isopropanol as a solvent. Optical transparency in visible and infrared regions was found to be suitable for different wavelength pumping for THz generation. This co-crystal shows low absorption in THz range and is suitable for THz generation via optical rectification in periodic lattice made by photo bleaching.

II. CRYSTAL GROWTH

Co-crystal 4-aminopyridine-4-nitrophenol-4-nitrophenolate (4AP4N) was grown by slow evaporation technique at a fixed temperature (25 ^{o}C). Melting point was equal to 149 ^{o}C. High purification level of synthesized compounds was achieved by successive recrystallization of obtained crystal in the same solvent.

III. OPTICAL PROPERTIES

Transparency of the co-crystal was studied with Shimadzu UV-1800 spectrophotometer in the range 190 – 1100 nm to show absence of light dispersion by threshold of absorption value near to crystalline absorption edge 480 nm and high transmittance in transparent area.

Obtained spectrum (Fig. 1) shows that co-crystal has wide and uniform transmittance of about 80 % from cut-off wavelength 480 nm (also observed in [2]) up to 1100 nm. The homogeneity of the co-crystal is confirmed by the optical transmittance spectrum too - there is no monotonic increase in transmittance with an increase of the wavelength in the visible region, which indicates the absence of scattering by heterogeneities.

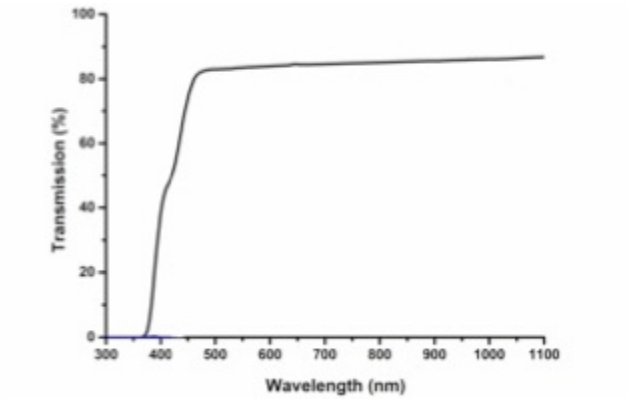

Fig. 1. Transmission spectrum of 4AP4N

Second harmonic generation (SHG) conversion efficiency of the obtained single crystalline sample was measured by comparative SHG technique presented in [2]. An estimation of the nonlinear optical coefficient magnitude (d) (at $\lambda = 1064$ nm, $\tau = 10$ nc, $E = 10$ mJ) considering the thickness of the sample and the disordering of the crystalline regions that fall into the laser beam, gives value near 0.6 ± 0.1 pm/V, which allows to consider this co-crystal as a material with high nonlinear optical parameters. This value of nonlinear coefficient of the co-crystal is quite sufficient for THz generation via optical rectification method.

Phase-matching conditions in the organic crystals can be realized by taking into accout 2D periodical lattice and sutisfying the quasi-phase-matching conditions. Formation of 2D lattice in 4AP4N could be done by photo bleaching by UV irradiation using photo mask (Fig. 3).

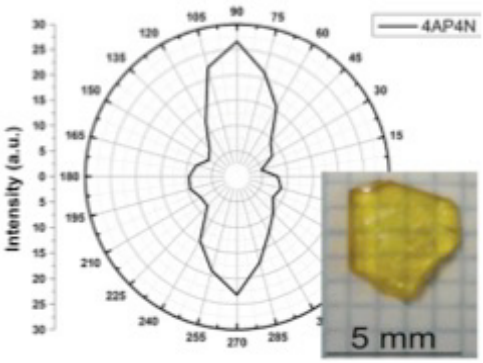

Fig. 2. SHG signal versus angle of rotation around an axis perpendicular to the incoming laser beam.
Inset: photo of 4AP4N sample

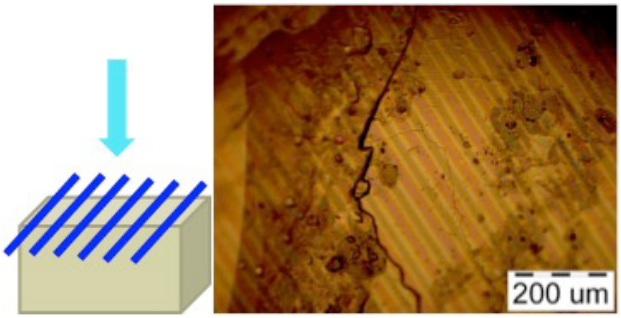

Fig. 3. Schematic representation of the UV irradiation using photo mask for cration of the 2D perodic lattice (Left) and interference contrast microscopy image of 4AP4N co-crystal after UV exposition through the mask (Right)

As a result of UV exposure of the co-crystal we obtained the change of SHG signal value dropping from 75–90 arb. units (before exposure) down to 30–45 arb. units (after the photo bleaching).

III. Terahertz properties

For studies of THz transmission properties of 4AP4N co-crystal we used a THz time-domain spectrometer. Its scheme might be found elsewhere [3]. The spectrometer allows one to study the THz absorption and refraction properties of the co-crystals. In this spectrometer, the THz radiation is generated when a femtosecond pulse from a Ti:Sapphire laser (Spectra Physics Tsunami, $\lambda = 797$ nm, $\tau = 120$ fs, $f = 80$ MHz) irradiates GaAs crystal [3]. THz radiation is collimated and focused into free space using a pair of parabolic mirrors. For spectroscopic measurements the co-crystalline sample is placed in the THz beam waist. After passing the sample THz radiations is collimated again and refocused into the detector crystal using two off-axis parabolic mirrors. For detection of THz radiation we use a 2-mm thick ⟨110⟩ ZnTe crystal and traditional electro-optical method. The signal from the balanced detector is sent to lock-in amplifier for increasing the signal-to noise ratio. The pump beam is modulated at frequency 1.3 kHz with a chopper, and this frequency is used as reference for the lock-in amplifier.

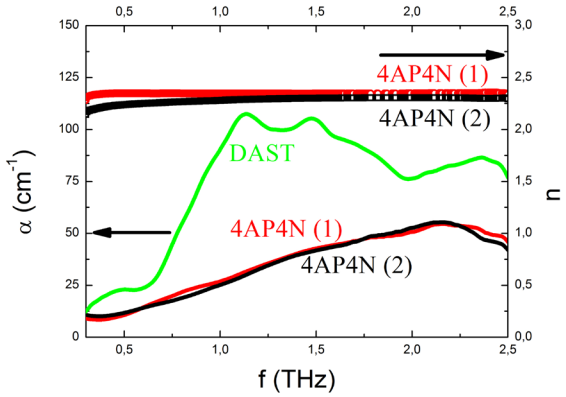

Fig. 4. Absorption coefficients for THz radiation for two samples of 4AP4N crystals and DAST crystal as well as refractive indices in the THz range

The averaged THz absorption spectra of two samples of co-crystals 4AP4N are shown in Fig. 4 along with their THz refraction coefficients. For comparison, the Fig. 4 also shows the absorption spectrum of a DAST crystal, measured under the same conditions. It is clearly seen that THz absorption in 4AP4N crystal is substantially lower than in DAST.

IV. Conclusions

We have synthesized and grown new co-crystal 4-aminopyridine-4-nitrophenol-4-nitrophenolate (4AP4N). Its optical properties demonstrated the suitability for producing of the periodic lattice. Optical, infrared and THz transparency, as weel as reasonably high value of nonlinar optical succeptibility make such crystal good candidate for THz applications.

Acknowledgments

This work was financially supported by Russian Foundation for Basic Research project № 18-52-16014.

References

[1] E. Garmine, *Opt. Express* **21**, 30532 (2013).
[2] I.M. Pavlovetc, S. Draguta, M.I. Fokina, T.V. Timofeeva, I.Y. Denisyuk, *Opt. Comm.* ***362***, *64* (2016).
[3] A.A. Angeluts, A.V. Balakin, M.G. Evdokimov, M.N. Esaulkov, M.M. Nazarov, I.A. Ozheredov, D.A. Sapozhnikov, P.M. Solyankin, O.P. Cherkasova, A.P. Shkurinov, *Quantum Electronics* ***44***, 614 (2014).

Numerical Study of $ZnGeP_2$ and GaSe Crystals for CO Laser Down-conversion into the THz Range

A. A. Ionin[1], I. O. Kinyaevskiy[1], Yu. M. Klimachev[1], Yu. M. Andreev[2,3], A. M. Sagitova[1]

[1] P.N. Lebedev Physical Institute of the Russian Academy of Sciences, Moscow, Russia,
[2] Institute of Monitoring of Climatic and Ecological Systems of the Siberian Branch of Russian Academy of Sciences, Tomsk, Russia
[3] Siberian Physical Technical Institute of Tomsk State University, Tomsk, Russia

E-mail: aion@sci.lebedev.ru

Abstract –Difference frequency generation of multiline Q-switched CO laser radiation in $ZnGeP_2$ and GaSe crystals was numerically studied. Phase-matching conditions of the crystals and CO laser spectrum make it possible to obtain about 10^3 narrow lines in the wavelength range from 50 µm (6 THz) to 3000 µm (0.2 THz). Energetic and spectral characteristic of frequency converted THz radiation were estimated in an experiments simulation.

Keywords – THz range, CO laser, nonlinear crystals

I. INTRODUCTION

At the moment, intensive researches have been carried out all over the world to develop high-power frequency-tunable terahertz (THz) laser sources. One of promising THz laser applications is atmosphere sensing due to a number of favorable factors. The first is atmosphere transparency windows in THz shortwave part and an absence of the water vapor absorption, as a main perturbation factor in the long-wave part. The long wavelength of THz radiation minimizes the scattering on dust particles and active weather. Also the THz radiation is safe for living organisms that allows wide using of such laser systems in practice.

A lot of THz generators of femtosecond and picosecond pulses based on nonlinear crystals pumped by powerful Ti: Sapphire laser systems (for example [1]) were developed, but they did not allow us to enter kilometer measurement distance. A demonstration of small atmospheric components measuring and a creation of a constructively simple, convenient device for atmosphere sensing were not achieved [1]. Therefore in this work we considered another way to create powerful reliable and constructively simple THz source based on down-conversion of powerful molecular gas lasers in mid-IR nonlinear crystals.

A choice of a down-conversion process (a type of three ways mixing) and a nonlinear crystal is the key factor determining an efficiency of the THz laser source. Limit of down-conversion efficiency is determined by the Manley-Row relation, i.e. the ratio of the energies of frequency-converted (THz) radiation quantum to pump light quantum [2]. This means that an application of high-power mid-IR molecular gas lasers (CO_2 and CO lasers) should be more effective for obtaining THz radiation than with near-IR lasers. As frequency converter we considered the most effective mid-IR nonlinear crystals $ZnGeP_2$ and GaSe which applicable for THz radiation generation [3].

II. SIMULATION RESULTS

At first, we calculated phase-matching angles θPM for difference frequency generation (DFG) in $ZnGeP_2$ and GaSe crystal. Refractive index dispersion equations were taken from [3] for GaSe crystal. Dispersion equations of $ZnGeP_2$ crystal were taken from [3] for the middle infrared band and from [4] for the THz band. The calculation method is described elsewhere, for example in [5]. In the calculation one CO laser wavelength was locked at 5.5 µm, second one was variable form 5 to 6 µm, DFG wavelength was in interval from 50 µm (6 THz) to 3000 µm (0.2 THz).

The calculation shows that two types of collinear phase matching are possible in the both ZGP and GaSe crystals. The dependence of calculated phase-matching angles on DFG radiation frequency for both interaction types are presented in Fig. 1. An angles difference between Type I and type II phase-matching was small and curves in Fig. 1a was merged. Also Fig. 1 depictures the transmittance of the $ZnGeP_2$ and GaSe crystals taken in the Ref. [6] and Ref [7], respectively.

The calculation indicates that DFG of CO laser radiation is possible in $ZnGeP_2$ and GaSe crystals in wide range from 50 µm (6 THz) to 3000 µm (0.2 THz). Phase-matching angles in this case are in the range 15 – 40 deg and 0 – 20 deg for, respectively. However the transmittance of the crystals limits the DFG spectral range. It was from ~70 µm to ~500 µm for $ZnGeP_2$ crystal and from ~70 µm to ~800 µm for GaSe crystal.

The next step of the study was a numerical simulation of the DFG for multi-line Q-switched CO laser in $ZnGeP_2$ and GaSe nonlinear crystals. The crystals length was 10-mm. The crystals were optimized for I type of three-wave mixing. CO laser pulse contained 150 lines within 5.0–7.5 µm wavelength interval [5]. The simulation was conducted in a plane-wave approximation and low efficiency of frequency conversion. The Fresnel losses at the crystals facets were not considered in our calculations due to possible antireflection coating.

For $ZnGeP_2$ crystal CO laser intensity was 78 MW/cm^2 which is quite close to the optical damage threshold [3]. If THz radiation absorption was not considered, the maximum power of the DFG radiation (integral over the spectrum) in the THz range was observed at phase-matching angle ~45° (Fig. 1a). In this case the most powerful DFG emission line was ~70 µm (emission frequency about 4 THz). The conversion efficiency was up to $3\cdot10^{-2}$ %. The DFG power is 2 times lower from the maximum at phase-matching angles of 35° and 60°. It corresponds to DFG frequency of 2.5 THz and 5 THz, respectively. When the crystal absorption in THz range was considered, DFG spectrum of CO laser lines was shifted to lower frequencies. Optimal phase-matching angle was about ~25° that corresponded to DFG radiation frequency of 1.5 THz. Frequency conversion efficiency decreased an order of magnitude due to absorption.

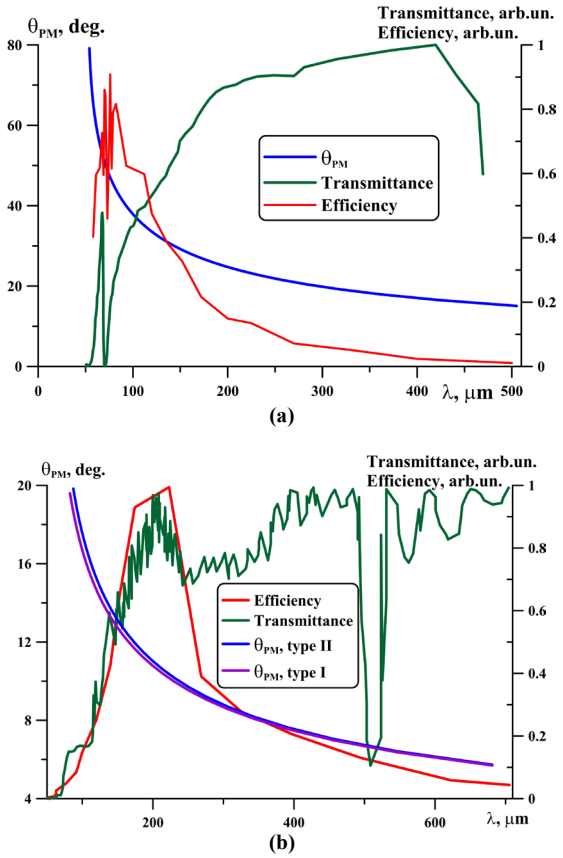

Fig. 1. The dependence of calculated phase-matching angles, transmittance and calculated efficiency on DFG radiation wavelength for multiline CO laser down conversion in $ZnGeP_2$ (a) and GaSe (b) crystals

Similar results of experiment simulation were obtained for GaSe crystal (Fig. 1b). For GaSe crystal CO laser radiation intensity was 30 MW/cm^2 which is quite close to the optical damage threshold [3]. The highest conversion efficiency was up to $1\cdot10^{-2}$ % which less then one for $ZnGeP_2$ crystal due less optical damage threshold. When the crystal absorption in THz range was considered, DFG spectrum was shifted to lower frequencies as well as for $ZnGeP_2$ crystal, and frequency conversion efficiency decreased an order of magnitude due to absorption. Calculated conversion efficiency for GaSe presented in Fig. 1b taken into account the crystal absorption. Fig 1b illustrate that the influence of DFG to THz range was significant.

It should be noted that CO laser frequency conversion efficiency can be increased for high-power nanosecond CO laser systems [8, 9]. For example second harmonic generation efficiency of short train of nanosecond CO laser pulses was 37% [8] versus 6.5% for microsecond pulses [5]. Our estimations indicate that for high-power nanosecond CO lasers (such as reported in [8, 9]) the conversion efficiency may rich 10^{-2} % at kW-range THz radiation power.

III. Conclusions

Thus, the numerical study of difference frequency generation (down-conversion) between rotational-vibrational transitions of multi-line Q-swithed CO-laser in $ZnGeP_2$ and GaSe crystals was performed. This technique allows to get about one thousand narrow lines in THz range from ~100 µm (3 THz) to ~1000 µm (0.3 THz). Conversion efficiency taking into account the crystal absorption was ~10^{-3} %. However for high-power nanosecond CO lasers (such as reported in [12]) the conversion efficiency may rich 10^{-2} % at kW-range THz radiation power.

Acknowledgments

The research was supported by the RFBR (Project No. 18-52-16019)

References

[1] G.-R. Kim, T.-I. Jeon, D. Grishkowsky, *Optics Express*, **25**, 25422 (2017)
[2] F. Zernike, J.E. Midwinter, *Applied nonlinear optics* (John Willey & Sons, N.Y. 1973), p. 213
[3] V.G. Dmitriev, G.G. Gurzadyan, D.N. Nikogosyan, *Handbook for nonlinear optical* crystals, 3d ed (Springer, Berlin, 1999), p. 413
[4] P. Kumbhakar, T. Kobayashi, and G.C. Bhar, *Appl. Opt.*, **43**, 3324 (2004)
[5] Yu.M. Andreev, A.A. Ionin, I.O. Kinyaevskiy et al., *Quantum Electronics*, **43**, 139 (2013)
[6] K. Zhong, C. Liu, M. Wang et al., *Opt. Mater. Express*, **7**, 3571 (2017)
[7] C.-W. Chen, T.-T. Tang, S.-H. Lin, *J. Opt. Soc. Am. B*, **26**, A58 (2009)
[8] Yu.M. Andreev, O.V. Budilova, A.A. Ionin, Iet al., *Opt. Lett.*, **40**, 2997 (2015)
[9] A.A. Ionin, I.O. Kinyaevskiy, Yu.M. Klimachev et al., *Infrared Ph. & Tech.*, **85**, 347 (2017)

Towards Sub-wavelength THz Imaging through Nonlinear Optical Techniques

G. Soylu, E. Herault, F. Sanjuan*, G. Gaborit and J.-L. Coutaz

IMEP-LAHC, UMR CNRS 5130, University Savoie Mont Blanc, 73376 Le Bourget du Lac cedex, France

E-mail: coutaz@univ-savoie.fr

Abstract – We present experimental results achieved in view of recording sub-wavelength THz images by performing optical rectification in the samples excited by a femtosecond laser beam that is scanned over the sample.

Keywords – Terahertz, imaging, optical rectification

I. Introduction

Recording images with a sub-wavelength lateral resolution requires to break the diffraction limit. In the THz domain, this has mainly been achieved with near field techniques, in which enhanced diffraction of the THz beam occurs between a nanometer tip and the sample [1], or by performing super transmission through sub-wavelength holes [2]. Another possibility is to generate THz at the sample surface by optical rectification (OR). This has been demonstrated with semiconductor samples, in which the THz signal is radiated through the acceleration of photo-excited carriers [3]. More recently, the physical properties of ferroelectric domains have been observed in hydrogen-bonded supra-molecular ferroelectrics by OR [4].

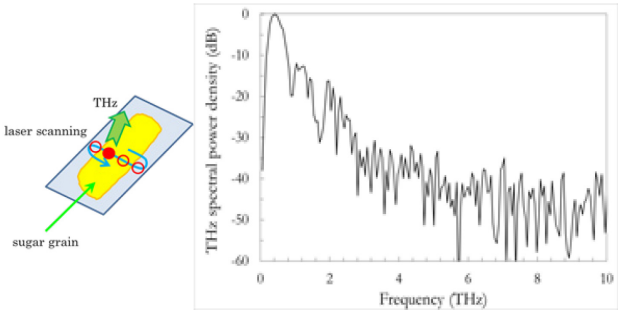

Fig. 1. Left: THz-OR measurement principle;
Right: Typical spectrum of the THz signal generated by OR in the sugar grain

We are presently leading research in view of recording a THz image, with a sub-wavelength lateral resolution, of a heterogeneous sample by performing OR at its surface. The basic idea is that the THz signal is generated only in the illuminated area, whose size is determined by the laser beam focusing, and could be as small as the laser wavelength. The illuminated part of the sample acts as a THz punctual source, and the THz image (we call it hereafter THz-OR image) is obtained by scanning the sample in the laser beam (Fig. 1 left). The so-achieved image gives a map of the nonlinearity of the sample, which depends on both its crystallinity and composition. Indeed, because OR is a second order nonlinear effect, it occurs only in non-centro-symmetric media. Also, absorption at both laser and THz frequencies and sample thickness could modify the THz signal strength. The weak efficiency of visible-to-THz OR obliges to use a femtosecond pulsed laser, with a high peak power and a relatively moderate mean power. The advantage of such lasers is the possibility of addressing the THz range and performing time-equivalent sampling in detection, and thus to get the temporal shape of the THz pulse. Then a Fourier transform gives the related spectra over the whole THz range.

II. Samples and Experimental Setup

We study either grains of brown caster sugar supplied by a local grocery [5], or slivers of [111] ZnTe crystal [6]. We chose sugar as it is known to be a relatively efficient and cheap nonlinear material, and grains are highly crystalline. Moreover, it is a real-life material, which demonstrates our technique could be applied to any common material, maybe like biological tissues in the future. Slivers of ZnTe are more efficient and thus deliver a stronger signal, which allows us to easily record THz waveforms at each point of the sample, and thus to get spectral information.

The experimental setup for recording THz-OR images is based on a classical THz time-domain spectroscopy setup, in which the emitting antenna is substituted by the sample. When studying sugar samples, we used an amplified Ti-Sa laser at 800 nm (5 mJ/pulse maximum, 1 kHz repetition rate, 50 fs pulse duration). For the ZnTe sample, a non-amplified oscillator (800 nm, 15 fs, 80 MHz repetition rate, 130 mW) was sufficient to achieve a good signal-over-noise ratio. The pumping laser beam is focused at the sample location, and the sample is mechanically moved perpendicularly to the laser beam. The THz signal is more or less divergent, depending of the size of the emitting area, i.e. of the laser spot. To collect most of this radiated THz signal, a large aperture dielectric lens is placed nearby the sample, which makes the THz beam parallel. This THz beam is received by an electro-optic detector (sugar experiment) or a LT-GaAs photo-conducting antenna (ZnTe experiment). The detector is triggered with a laser pulse that is time-delayed as compared to the emission.

III. THz-OR picture of a sugar grain [5]

Fig. 1 (right) shows a typical THz spectrum obtained for a sugar grain (thickness ~0.8 mm). The spectrum is maximum around 0.5 THz. Similar spectra are recorded while changing the mean laser power from 56 µW up to 3.65 mW. As the laser spot diameter is 30 µm, the corresponding peak power densities at the sample range from 0.18 to 10 TW/cm^2. As well, we have got similar spectra with grains of different thicknesses. Therefore the peak amplitude of the waveforms supplies us with the relevant information, and recording only it reduces strongly the image acquisition time. Fig. 2 shows a photography as well as the THz-OR image of a sugar grain. Here the lateral resolution of the THz image is 50 µm (Rayleigh criterion), i.e. $\lambda/12$ assuming the THz spectrum is maximum at 0.5 THz.

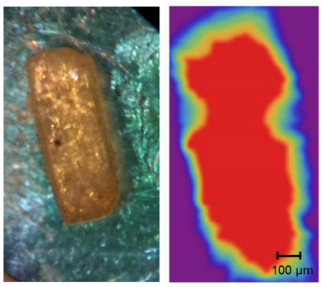

Fig. 2. Photography (left) and THz-OR image (right) of the sugar grain

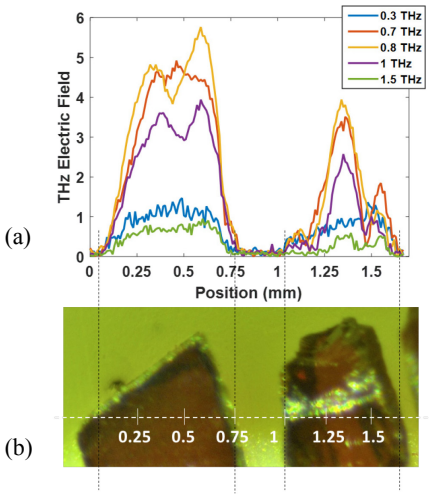

Fig. 3. a) THz field vs position at different frequencies (0.3, 0.7, 0.8, 1 and 1.5 THz); b) Photography of the sample: the white dashed line is the scanning axis

IV. Hyperspectral THz-OR image of a ZnTe crystal sliver

Here the samples are slivers made from a [111] ZnTe wafer that are stick side-by-side on a rubber tape. The thickness of the slivers is about 300 µm, while their lateral dimensions are in the order of millimeter. Fig. 3b shows a picture of the slivers together with the line along which the laser beam has been scanned. A full waveform is recorded at each spatial point.

Then the waveforms are Fourier-transformed, and the THz signal profiles at different frequencies are plotted in Fig. 3a. One sees that the THz signal is generated only in the slivers, and that the size of the slivers is retrieved whatever is the frequency. As expected, this demonstrates that the sub-wavelength resolution of the THz-OR images is limited by the laser spot size but not by the THz wavelength.

Moreover, some oscillations are seen in the THz profiles around the center of the slivers. The amplitude and position of these features depend on the frequency, and thus they could be more likely explained by THz interference effects inside the sample (Fabry-Pérot resonances).

V. Conclusion

THz-OR technique delivers sub-wavelength images of samples which exhibit a second order nonlinearity. Such images supply information on the map of the nonlinear optics-THz conversion efficiency of the sample, which depends on several parameters, mainly its crystallinity, absorption at both optical and THz frequencies, thickness, and so on. The limit of this technique, in terms of lateral resolution δ, arises from a compromise between sample damage threshold and detector sensitivity. Indeed, the signal to be detected should be over the detector noise equivalent power (NEP), and the laser power density at the sample should remain weaker than the sample damage threshold D_{damage}. One can demonstrate that δ obeys the following expression [5]:

$$\delta \propto \frac{1}{\chi D_{damage}} \sqrt{\frac{\mathrm{NEP}}{\Omega_{lens}}}$$

Here χ is the nonlinear tensor of the material, and Ω_{lens} is the solid angle of the collecting optics. Therefore the resolution depends on the sample properties (nonlinearity, damage threshold) and on the detector sensitivity. Using low-NEP detectors, like cryogenic KID [7], HEB, CSIP, etc., may allow one to achieve a sub-micronic resolution.

Acknowledgments

This research is supported by the French Research Agency (ANR) through the LabEx FOCUS ANR-11-LABX-0013 project.

* Present affiliation: LFCR, UMR CNRS 5150, University Pau et des Pays de l'Adour, 64012 Pau cedex, France

References

[1] A. Adam, *J. Infra. Millim. THz Waves* **32**, 976 (2011).
[2] U. Schade et al., *Appl. Phys. Lett.* **84**, 1422 (2004).
[3] T. Kiwa et al., *Opt. Lett.* **28**, 2058 (2003).
[4] M. Sotome et al., *ACS Photonics* **2**, 1373 (2015).
[5] F. Sanjuan et al., *Scient. Rep.* **8**, 13492 (2018).
[6] G. Soylu et al., submitted to *IRMMW* (2019).
[7] G. Soylu et al., *J. Infra. Millim. THz Waves* **40**, 31 (2019).

THz Cyclotron Emission from HgCdTe Alloys with Dirac-like Band Structure

D. B. But[1,2], C. Consejo[1], N. Dyakonova[1], S. Krishtopenko[1,3], V. I. Gavrilenko[3], N. N. Michailov[4], F. Teppe[1] and W. Knap[1,2]

[1] Laboratory Charles Coulomb, University of Montpellier&CNRS, Montpellier, FR-34095, France
[2] International Research Agenda CENTERA, Institute of High Pressure Physics PAS, Warsaw, Poland
[3] Institute for Physics of Microstructures RAS, GSP-105, 603950, Nizhny Novgorod, Russia
[4] Institute of Semiconductor Physics, Siberian Branch RAS, 630090, Novosibirsk, Russia

E-mail: knap@univ-montp2.fr

Abstract – Recent emergence of extremely high crystalline quality MBE grown HgCdTe alloys with extremely narrow band gap and even Dirac-like linear energy spectra rises the question about mechanisms of electron heating and possibility of THz cyclotron emission with high efficiency and tuneability. This work shows the first experimental results on cyclotron resonance emission from CdHgTe alloys of different composition.

Keywords – Terahertz emission, Cyclotron resonance, Dirac matter.

I. Introduction

Effect of carriers heating and terahertz (THz)/Far infrared (IR) magnetically tunable emission were subject of intense studies for decades [1, 2]. Impressive results have been obtained using GaAs and InSb semiconductors leading to the design of cyclotron emitters based THz/Far-IR spectrometers [3]. Recent emergence of extremely high crystalline quality MBE grown HgCdTe alloys with extremely narrow band gap and even Dirac-like linear energy spectra rises the question about mechanisms of electron heating and possibility of THz cyclotron emission with high efficiency and tuneability [4]. Indeed, decrease of the cyclotron mass may lead to magnetic field tunability, greater by an order of magnitude than the one in GaAs or InSb semiconductors and non-equidistant LLs may help in decreasing of the self-absorption phenomena. [3].

II. Results

In this work we present the first experimental results on magnetically tunable THz emission from $Hg_{0.81}Cd_{0.19}Te$ bulk layers with a band gap of about 40 meV or smaller. Our samples were MBE grown on (013) semi-insulating GaAs substrate covered by thick CdTe buffer. The film was sufficiently thick (≈3.2 μm) to be considered as a bulk material. Figure 1a shows an example of LLs energies in conduction band for zero quasimomentum k_z along the z-axis as a function of magnetic field, calculated by using Kane Hamiltonian [5]. The z-axis coincides with the growth direction and orientation of magnetic field. The arrows indicate cyclotron resonance (CR) transitions from two lowest LLs. For details of LLs notations see [5]. Nonlinear behavior of LLs is attributed to the nonparabolicity of conduction band.

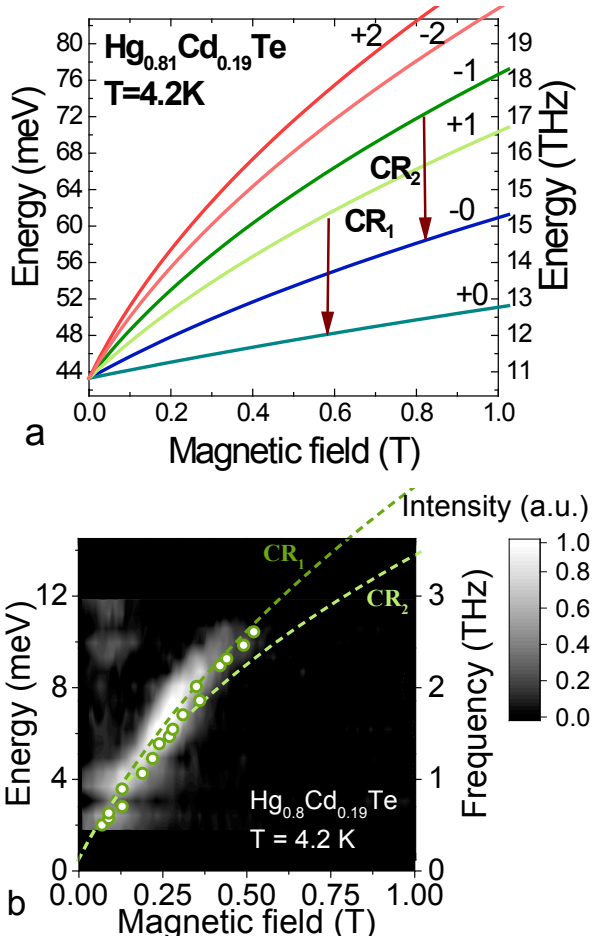

Fig. 1. a) Landau levels fan chart at kz =0 in the conduction band of one of the HgCdTe samples. The magnetic field is oriented along the growth direction. Zero energy corresponds to the top of valence band. b) Grey scale map for emission spectra at different magnetic fields. The white region corresponds to the maximum intensity of THz emission

Our experimental setup contains two independent 8 T and 14 T superconducting coils placed in one cryostat. The sample, excited with electric field pulses was inserted into the first coil, while a magnetically tunable InSb photoconductive detector was placed in the second

one. The measurements were performed at 4.2 K. THz radiation from the sample was guided to the detector by a copper light pipe. The carrier, concentration n_V and mobility μ values were obtained from magnetotransport measurements.

Figure 1b presents emission spectra at different values of magnetic field plotted as a grey-scale map. The open symbols correspond to the maximum intensity in a given magnetic field. Dashed curves describe theoretical CR energies from the two lowest LLs (see Fig. 1a). A good agreement between theoretical curves and experimental results demonstrates that emission from our sample is indeed attributed to the CR excitations from LLs in the conduction band.

III. Conclusion

Our results pave the way towards new cyclotron emission THz spectrometers of high sensitivity based on HgCdTe films. We discuss also the mechanism of the electron heating and recombination in HgCdTe alloys with Dirac-like energy versus momentum dispersion.

References

[1] W. Müller, F. Kohl, E. Gornik, *Infrared Physics*, **18**, 691 (1978).
[2] W. Zawadzki, C. Chaubet, D. Dur, W. Knap, A. Raymond, *Solid-State Electronics*, **37**, 1213 (1994).
[3] W. Knap et al., *Rev. Sci. Instrum.*, **63**, 3293 (1992).
[4] F. Teppe et al., *Nat. Commun.*, **7**, 12576 (2016).
[5] M. Zholudev et al., *Phys. Rev. B* **86**, 205420 (2012).

THz Excited State Level Spacing in Encapsulated Graphene Quantum Dots

E. Riccardi, S. Massabeau, F. Valmorra, M. Rosticher, J. Tignon, T. Kontos, S. Balibar, S. Dhillon, R. Ferreira, J. Mangeney

Laboratoire de Physique de l'Ecole normale supérieure, ENS, Université PSL, CNRS, Sorbonne Université, Université Paris-Diderot, Sorbonne Paris Cité, Paris, France
E-mail: juliette.mangeney@ens.fr

Abstract – We report a high-quality encapsulated graphene quantum dot that exhibits stable Coulomb diamonds and excited states in the THz energy range (~0.5 THz). The quantum dot is connected to a bow tie antenna for measurements under THz illumination at temperature T < 200 mK.

Keywords – terahertz, grapheme, quantum dots

I. Introduction

Owing to its unique properties, graphene has been receiving considerable interest for fundamental studies and application in the THz spectral range. A related emerging material system are large graphene quantum dots that are very appealing for quantum technology at THz technology, single photon THz emitter and for the investigation of light-matter interaction. Main of the studies performed in the last years on large graphene quantum dots have been based on transport measurements [1] and the potential of graphene quantum dots for photonic THz devices is largely unexplored.

II. Results

Here we report a high-quality encapsulated graphene quantum dot with stable Coulomb diamonds and excited states in the THz energy range. Encapsulating graphene with hexagonal Boron Nitride (hBN) layers provides reduced disorder by preserving the graphene from chemical contamination during technological process and also by a weak perturbation of the substrate [2]. The device is connected to a bow tie antenna and is placed in a dilution cryostat operating at temperature T < 200mK with optical access at THz frequencies.

We will present transport measurements (Fig. 1) showing pronounced and stable Coulomb diamonds and multiple energy levels in the THz range (~2 meV). We will also report current measurements under THz illumination.

Our configuration is a unique probe of the light-matter interaction at THz frequencies in single large GQD. Such graphene quantum dots are promising for fundamental physics such as investigating Kondo effect as well as for application as active materials for THz emitters and detectors. Further experiments will be performed under THz illumination.

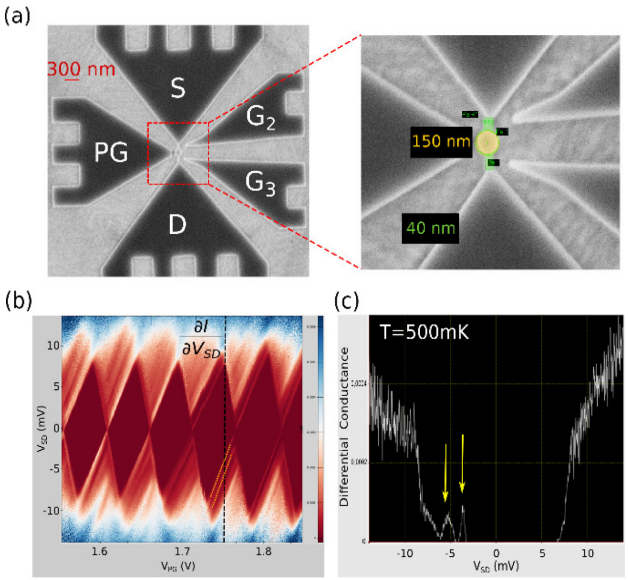

Fig. 1. (a) Scanning electron microscope (SEM) images of the encapsulated graphene quantum dot. (b) Differential conductance in the function of source-drain voltage VSD and of the plunger gate voltage VPG, exhibiting Coulomb diamonds. The resonances parallels to the edges of the diamonds are clearly seen. (c) Differential conductance in the function of VSD at VPG=1.75 V (cut along the dashed line in (b)) showing the profile of the excited states (yellow arrows) at T = 500 mK

References

[1] J. Güttinger, F. Molitor, C. Stampfer, S. Schnez, A. Jacobsen, S. Droscher, T. Ihn and K. Ensslin, *Rep. Prog. Phys.* **75**, 126502 (2012).

[2] S. Engels, A. Epping, C. Volk, S. Korte, B. Voigtländer, K. Watanabe, T. Taniguchi, S. Trellenkamp, and C. Stampfer, *App. Phys. Lett.* **103**, 073113 (2013).

Terahertz Emission from HgCdTe Quantum Wells under Long-Wavelength Optical Pumping

V. V. Rumyantsev[1,2], V. I. Gavrilenko[1,2], A. A. Dubinov[1,2], M. A. Fadeev[1,3], V. V. Utochkin[1,2], N. S. Kulikov[1,2], V. Ya. Aleshkin[1,2], N. N. Mikhailov[4,5], S. A. Dvoretskii[4], F. Teppe[3], S. V. Morozov[1,2], Z. F. Krasilnik[1], C. Sirtori[6]

[1] Institute for Physics of Microstructures of Russian Academy of Sciences, Nizhny Novgorod, Russia
[2] Lobachevsky State University, Nizhny Novgorod, Russia
[3] L2C, UMR CNRS 5221, Montpellier University, Montpellier, France
[4] A.V. Rzhanov Institute of Semiconductor Physics, Siberian Branch of Russian Academy of Sciences, Novosibirsk, Russia
[5] Novosibirsk State University, Novosibirs, Russia
[6] Laboratoire de Physique de l'Ecole Normale Supérieure, Paris, France

E-mail: rumyantsev@ipmras.ru

Abstract – The report reviews recent advances in the field of stimulated middle and far infrared radiation generation from HgTe/CdHgTe QW heterostructures.

Keywords – terahertz, QCL, HgCdTe

I. INTRODUCTION

The mid-IR region (that can be roughly defined as the 2.9–24 μm wavelength interval) is the well- known molecular "fingerprint region," where the strongest fundamental ro-vibrational bands, that allow to distinguish specific molecules and isotopomers, lie. In the far-infrared region, instead, rotational transitions can be excited for molecules possessing a permanent dipole moment. The intensity of such transitions can be comparable with the strongest ro-vibrational transitions in the mid-IR. Despite of the importance of both far-IR and mid-IR regions, this spectral range still lacks cheap and efficient sources of radiation. Contrary to the near-IR region, where the most common lasers are based on diode structures, the main sources of the mid-IR and far-IR regions of spectrum are unipolar quantum cascade lasers. Despite the great achievements of QCLs, there is still a frequency range from 5 to 12 THz, which is not covered by this type of devises. Within this range the energies of optical phonons of conventional QCL materials such as AlGaAs, GaAsSb and InGaAs lie, which causes strong lattice absorption. Thus creating QCLs for the abovementioned spectral range is generally possible but the usage of new materials with different phonon frequencies is needed. In HgCdTe, the phonon frequencies are low enough to enter 20–60 μm spectral region, while $Hg_{1-x}Cd_xTe/Cd_yHg_{1-y}Te$ quantum wells (QWs) allow bandgap tuning in a wide range from several hundred of meV down to less than 10 meV.

II. RESULTS

Various designs of HgTe/CdHgTe quantum well heterostructures for lasers emitting in the wavelength range of 10–25 μm were examined both theoretically and experimentally, and optimal designs of such structures were identified for different emission wavelengths. In optimized HgCdTe/CdHgTe QW laser heterostructures, suppression of nonradiative Auger recombination of nonequilibrium carriers in the QWs was demonstrated. For a given energy of interband radiative transitions, designs with the narrowest QWs of the purest possible (with a small fraction of residual Cd) HgTe are optimal from this point of view. In addition, the radiative recombination rate also increases as the QW width decreases; thus, it is possible to achieve the predominance of radiative recombination over nonradiative processes both by the Auger mechanism and Shockley-Read-Hall mechanism. The above factors are crucial for realization of stimulated emission (SE) in the far-IR HgTe/CdHgTe based lasers and greatly enhance their performance, lowering the SE threshold and increasing the operating temperature at which SE can be realized.

It has been demonstrated that tuning of pump radiation wavelength towards lower photon energies from near-IR (2.3 μm) to mid-IR (10.6 μm using CO_2-laser) benefits the emission characteristics of HgTe/CdHgTe QW laser heterostructures due to reduced heating of non-equilibrium charge carriers by the pump radiation. This decrease in the effective carrier "temperature" reduces the rate of Auger recombination (which is a threshold process with respect to carrier energy), favoring radiative recombination. Under near-IR pumping, we observed quenching of SE from HgTe/CdHgTe QW laser structures as the pump increased further beyond the SE threshold; we attribute this effect to the excessive carrier "heating" leading to activation of Auger processes. Switching to mid-IR pumping allowed us to avoid the SE quenching and resulted into much better output characteristics of the laser structures in the wavelength range from 14 to 20 μm. At shorter wavelengths $\lambda \sim 10$ μm the excitation threshold power ($\lambda_{exc} \sim 2.3$ μm) was shown to be as low as 120 W/cm^2 and the SE was obtained even at CW excitation ($\lambda \sim 0.9$ μm). Under low-power cw QCL pumping (8 μm) photoluminescence signal was found in HgTe/CdHgTe heterostructures up to

20 μm. We suggest that it is possible to achieve SE in cw pumping at the wavelengths above 10 μm at higher pumping intensity.

III. Conclusions

Summing up, SE under optical pumping was obtained in HgTe/HgCdTe quantum well heterostructures in the spectral range up to 25 μm for dielectric waveguide and up to 31 μm for "Reststrahlen band mode localization". It was shown that longer pumping wavelengths reduce carrier heating and provide better performance. At 10 μm SE was obtained at cw pumping. These results demonstrate that HgCdTe heterostructures are promising candidates for far-IR lasers and optical converters from mid-IR QCLs to far-IR region.

Acknowledgments

This work was financially supported by the Russian Foundation of the Basic Research (#18-52-16013).

Terahertz Quantum Cascade Laser with Non-Resonant Depopulation Temperature

A. N. Baranov[1], H. Nguyen-Van[2], Z. Loghmari[1], M. Bahriz[1], and R. Teissier[1]

[1] IES, Univ. Montpellier, CNRS, Montpellier, France
[2] currently with Univ. Nagoya, Japan

E-mail: baranov@umontpellier.fr

Abstract – To improve the maximum operating temperature of THz quantum cascade lasers (QCLs) we propose to modify the three-well resonant phonon design by increasing the energy of the separation between the bottom transition levels and the ground states, which is usually adjusted to the LO phonon energy in GaAs. Devices with Au-Au double-metal waveguide based on this design with non-resonant depopulation of the bottom transition level operated in pulsed mode up to T_{max}=190 K, which favorably compares with T_{max}=181 K obtained for QCLs employing resonant electron extraction. The performed analysis showed that the achieved improvement could be explained by the proposed design modification.

Keywords – terahertz, quantum cascade lasers

I. Introduction

Low operating temperatures is the main drawback of THz QCLs and much effort has been put into increasing their maximum operating temperature Tmax. The three-well diagonal scheme with resonant LO-phonon depopulation of the bottom transition level was demonstrated to be the best suited for high temperature operation with T_{max} = 168 K achieved in lasers employing an Au-Au double metal waveguide [1]. A Cu-Cu waveguide was proposed in the same publication in order to decrease losses in THz QCLs, which allowed the authors to reach T_{max}=178 K [1]. Different variants of the three-well design were examined to further improve Tmax. In particular, the design was modified to increase the upper-level lifetime in order to obtain a higher gain and reduced parasitic leakage current [2] or to maximize the population inversion at high temperatures [3]. In combination with the Cu-Cu double metal waveguide these improvements resulted in the increase of Tmax up to 186 K [2] and later to almost 200 K [3].

One of the reasons of degradation of QCL performances at elevated temperatures is thermal population of the bottom transition level. The specific feature of the THz QCLs with resonant phonon depopulation consists in a fixed gap for this excitation, equal to the LO-phonon energy in GaAs (E_{LO} = 36 meV), which is necessary for fast electron extraction since any deviation from this value increases the bottom level lifetime. On the other hand, if this extraction gap is larger the thermal backfilling can be reduced. In this work we present a study of a THz QCL based on the three-well design with the extraction energy gap exceeding the LO-phonon energy.

II. QCL design

We modified the three-well resonant phonon design from [2] by increasing the extraction gap by 5 meV, up to 41 meV, while keeping the same shape of electron wavefunctions. Figure 1 presents the conduction band diagram and squared moduli of the wavefunctions computed using the in-house QCL simulation tool based on a one-band Shrödinger-Poisson solver.

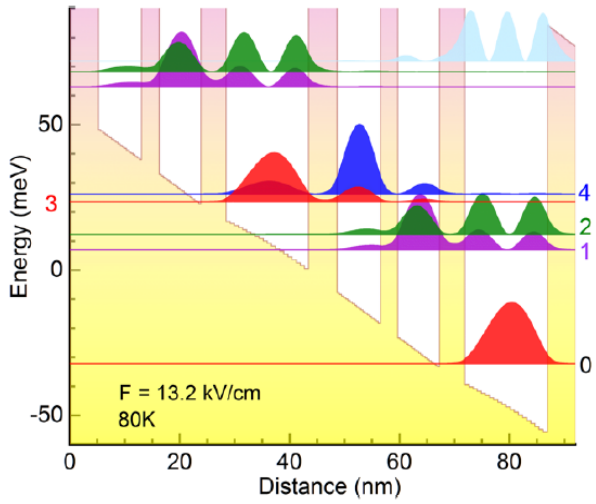

Fig. 1. Conduction band diagram and square moduli of electron wavefunction of the QCL design. The last quantum well is isolated from the next period of the structure for better visibility of the extraction gap e1-e0

The last well in the diagram is isolated from the next period of the structure for better visibility of the extraction gap. In the original design [2] the distance 1-0 corresponds to the GaAs LO-phonon energy of 36 meV. The ground level 0 is in fact splitted corresponding to a combination of the levels 3 and 4 of the previous wide well in the considered portion of the structure. We expect that the increase in the depopulation energy in our structure should result in reduction of the thermal backfilling. It can therefore be helpful for increasing the QCL operation temperature, provided the efficiency of the carrier extraction from the bottom transition level does not degrade much because of the deviation of the distance to the ground transition state from the LO-phonon energy. The goal of this work was to verify this assumption.

III. Device Fabrication

The GaAs/AlGaAs active zone of the QCL consisted of 300 repetitions of the following layer sequence **5.2**/7.85/**3.2**/7.6/**4.6**/15, in nm starting from injection barrier, $Al_{0.15}Ga_{0.85}As$ barriers in bold. A 1.2-nm-thick layer in the middle of the underlined barrier was doped with Si resulting in a sheet carrier density $N_s = 3\times10^{10}$ cm^{-2} per period. The structure was grown by molecular beam epitaxy in a RIBER 412 solid source machine on an undoped (100) GaAs substrate. The growth was started with a 300-nm-thick $Al_{0.55}Ga_{0.45}As$ stop etch layer. A 100-nm-thick GaAs bottom contact layer doped to n = =5×10^{18} cm^{-3} was grown before the laser active zone, and a 50-nm-thick GaAs top contact layer with the same doping level terminated the structure. The grown wafer was processed into (1-3)-mm-long and (120-150)-µm-wide ridge lasers with a double metal Au-Au waveguide.

IV. Results and Discussion

Voltage-current and light-current characteristics of a fabricated QCL measured in pulsed mode are shown in Fig. 2. At 80 K the emission frequency shifted with current from 2.9 to 3.7 THz. For the best device, lasing was observed up to T_{max} = 190 K (185-188K, typically). The threshold current density of the laser was 0.8 kA/cm^2 at 80 K and increased up to 1.6 kA/cm^2 at the maximum operating temperature.

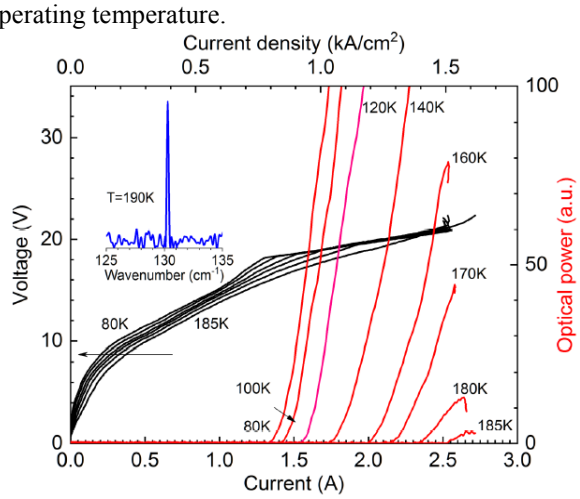

Fig. 2. Voltage-current and light-current characteristics of a QCL measured at different temperatures in pulsed mode. Inset shows an emission spectrum measured at T = T_{max}

The lasers were compared with QCLs based on the traditional resonant-phonon design [2] fabricated in the same way. These reference devices exhibited similar performance at low temperature except the voltage that was about 2V lower at threshold in the lasers with the original design due to the smaller extraction gap. Above 140 K the threshold current density of the reference laser grows faster and the operation temperature of the best devices is limited at 181 K (175-178 K, typically).

To estimate the effect of the design modification on T_{max} we compared the change in the carrier density in the bottom transition level 2 in the modified design due the increase in the electron lifetime because of the deviation from the phonon resonance and, on the other hand, reduced thermal backfilling. For simplicity we can consider that the level 0 (Fig. 1) is the ground state that accumulate electrons with the density N_s. Using the Boltzmann factor the change in thermal population in the level 2 due to the larger extraction gap can be estimated as $\Delta n_{2th} = -7 \times 10^8$ cm^{-2} at T = 200 K for the original design and the modified one, respectively. The electron concentration in the level 2 due to scattering from the upper levels 3 and 4 can be written as:

$$n_{2sc} = \frac{J}{q}\frac{\tau_{up}}{\tau_{up\to 2}}\tau_2,$$

where J is the current density, τ_{up} is the combined lifetime in the levels 3 and 4, $\tau_{up\to 2}$ is the lifetime of the transition between the combination 3–4 and 2, and q is the charge of electron. Considering that $\tau_{up}/\tau_{up\to 2} < 1$ one can conclude that $n_{2sc} < \frac{J}{q}\tau_2$. Calculated values of τ_2 at 200 K are 0.30 and 0.33 ps for the modified and original structures, respectively. Finally, for the threshold current density of 1.8 kA/cm^2 at T = T_{max} we can deduce that the additional population of the level 2 due to the increase of its lifetime in the modified design Δn_{2up} is not greater than 3.4×10^8 cm^{-2}. Comparing Δn_{2th} and Δn_{2sc} and considering the assumptions made one can conclude that in the investigated structures the larger extraction gap can provide an improvement in the population inversion at elevated temperatures close to T_{max}. A more detailed analysis performed using our QCL simulation tool qualitatively confirmed this conclusion.

V. Conclusions

To summarize, we proposed to modify the three well resonant phonon design by increasing the energy of the separation between the bottom transition levels and the ground states above the energy of the GaAs LO-phonon in order to improve the population inversion at elevated temperatures and thus to increase the QCL operation temperature. The fabricated devices based on such design with non-resonant depopulation of the bottom transition level operated in pulsed mode up to 190 K, which compares favorably with T_{max} = 181 K of the devices fabricated on the base of a conventional three-well design with resonant depopulation. The performed analysis showed that the achieved improvement could be explained by the proposed design modification.

References

[1] M. Belkin at al., *Optics Express* **16**, 3242 (2008).
[2] S. Kumar, Q. Hu and J. Reno, *Appl. Phys. Lett.* **94**, 131105 (2009).
[3] S. Fathololoumi at al., *Optics Express* **20**, 3866 (2012).

Molecular THz Lasers Pumped by Mid-Infrared Quantum Cascade Lasers

J. Turut[1], S. Eliet[1], J. Hesler[2], S. Barbieri[1], J.-F. Lampin[1]

[1] Terahertz Photonics Group, Institute of Electronics Microelectronics and Nanotechnology (IEMN) UMR CNRS 8520, Lille University, Villeneuve d'Ascq, France
[2] Virginia Diodes Inc., Charlottesville, VA, USA

E-mail: jean-francois.lampin@univ-lille.fr

Abstract – We have demonstrated a new approach to realize a continuous wave room temperature THz laser source: a low-pressure molecular gas is optically pumped by a solid-state mid-infrared source. A tunable quantum cascade laser allows to have access to transitions that are not accessible to CO_2 lasers. Here we present our last results concerning NH_3: pure inversion transitions allows emission around 1 THz. At 1.073 THz a new cavity design is used and a power of 0.67 mW is obtained with a high differential efficiency of 6.4 mW/W. This improved output power will permit imaging and local oscillator applications.

Keywords – Terahertz, Molecular Laser, Quantum Cascade Laser

I. Introduction

Terahertz sources around 1 THz and above are still expensive and/or bulky despite investigations and progress. Optically pumped terahertz lasers (OPTL) are based on a polar molecular gas optically pumped by a CO_2 discharge laser. They are bulky, need high voltage, have a small tunability but they are also powerful and operate at room temperature[1–3].

Ammonia (NH_3) has a high permanent electric dipole, a high rotational constant and a fast relaxation rate, it was identified as a "winner molecule"[2] in the 80s but due to the lack of coincidence with the CO_2 laser lines, only one line is accessible thanks to N_2O laser pumping[4].

We have demonstrated for the first time an OPTL[5,6] pumped by a solid-state mid-IR quantum cascade laser (QCL). The main advantage of the QCL is its continuous tunability compared to CW CO_2 lasers. It allows a larger degree of freedom in the choice of the molecule and of the transition that is resonantly pumped. Small molecules with large electric dipoles are good candidates to realize high efficiency and compact OPTL. They are pumped from the ground state to an excited state thanks to a vibrational transition. Population inversion is then generally created between rotational states.

Here, the active medium of the laser is made of low-pressure NH_3 gas enclosed in a cavity. NH_3 is also known for a particular phenomenon: the so-called inversion quantum phenomena. A splitting of the energy levels comes from the fact that the N atom is able to tunnel through the potential barrier formed by the three H triangle. In the first excited vibrational state ($\nu_2 = 1$) the inversion splitting is about 1 THz. Two kinds of THz transitions in the excited state can occur: pure inversion transitions (close to 1 THz) and rotation-inversion transitions. Here we demonstrate Q-branch transitions pumping around 965 cm^{-1} and lasing on pure inversion transitions. Fig. 1 shows an example with the $J = K = 3$ transition.

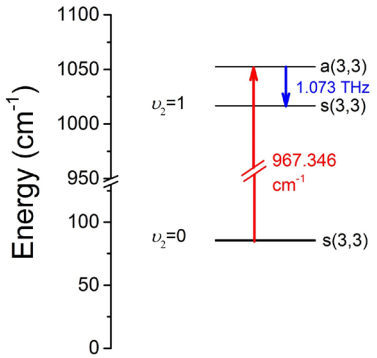

Fig. 1. Simplified energy diagram of the NH_3 molecule. The red arrow illustrates the MIR pump transition *saQ*(3,3) and the blue arrow shows the THz laser emission (pure inversion transition)

II. Experiments

The laser cavity is based on a cylindrical metallic waveguide closed by two flat mirrors. The pump beam comes from a mid-IR distributed feedback (DFB) or an external cavity QCL (both at room temperature). The beam is focused thanks to a ZnSe lens through a hole drilled in the input mirror. The THz output power is measured using a pyroelectric detector calibrated by the PTB (Sensor und Lasertechnik, model THz 10) and the THz spectrum is measured thanks to a GaAs Schottky diode subharmonic mixer (Virginia Diodes WR1.0SAX) and an electrical spectrum analyzer.

Fig. 2 shows the different spectra of the laser emission obtained by tuning the QCL to the various *saQ*(*J*, *K*) transitions. Each spectrum appears as a vertical line because the linewidth is close to 100 kHz. The laser frequency goes from 979.6 GHz (5,3) to 1166.2 GHz (8,8). The most powerful lines are the (3,3) at 1073.0 GHz, the (4,4) at 1082.6 GHz and the (6,6) transition at 1115.1 GHz. Fig. 3 shows the measured THz power versus the pump power for the (3,3) transition. The threshold is very low (few mW). For a pump power of 105 mW we measure an output power of 0.67 mW. The differential efficiency is 6.4 mW/W.

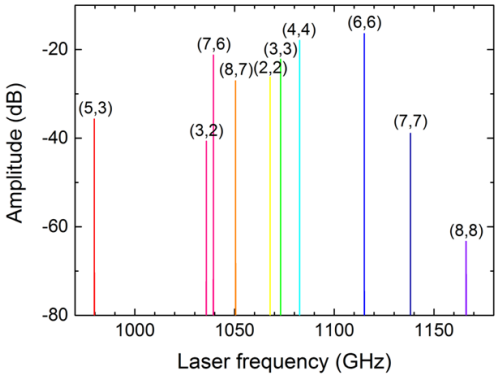

Fig. 2. Spectra of the different pure inversion laser lines that has been measured at the output of the NH_3 laser, each laser transition is identified by its quantum numbers (*J, K*)

The theoretical limit for the optical conversion efficiency, assuming a rapid vibrational relaxation, a lossless cavity, and an ideally coupled laser is given by $\eta_{opt} = 1/2(\nu_{THz}/\nu_{pump}) = 18.5$ mW/W. The measured efficiency corresponds to 35 % of the theoretical maximum. This value is slightly higher than the highest reported for a CO_2-pumped OPTL but at a lower frequency[7].

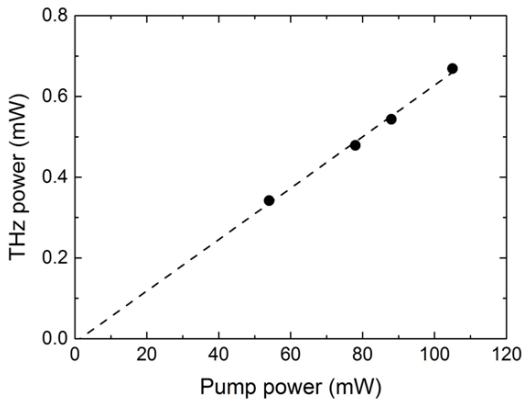

Fig. 3. Measured THz output power of the (3,3) transition at 1.073 THz versus MIR pump power at 967.346 cm^{-1}

III. Conclusions

We have demonstrated that QCL pumping of an OPTL allows to realize an efficient and compact CW THz source. The transitions of the ammonia molecule are highly efficient but are not accessible to CW CO_2 lasers. They are now accessible to QCL and an efficiency of 6.4 mW/W (35 % of the theoretical maximum) is demonstrated for the (3,3) transition at 1.073 THz. Other pure inversion transitions can also be pumped. A maximum output power of 0.67 mW is obtained limited by the pump power. There is no doubt that powers of a few mW can be obtained if a more powerful pump laser is available. This ammonia laser can be used for imaging and local oscillator applications.

Acknowledgments

This work benefited from the facilities of the ExCELSiOR Nanoscience Characterization Center (http://www.excelsior-ncc.eu), the RENATECH network and was financially supported by the ANR-16-CE30-0020 project “HEROES”.

References

[1] Reviews of infrared and millimeter waves, vol. 2, *Optically pumped far-infrared lasers*, edited by K. J. Button, M. Inguscio and F. Strumia (Plenum Press, New-York, 1984).

[2] Infrared and millimeter waves, vol. 7, *Coherent sources and applications, Part II*, edited by K. J. Button, Chapter 1, (Academic Press Inc., New-York, 1983).

[3] S. D. Ganichev and W. Prettl, *Intense terahertz excitation of semiconductors* (Oxford University Press, New-York, 2006).

[4] G. N. Grachev, V. F. Zakhar’yash, V. M. Klement’ev, A. G. Khamoyan, *Quantum Electronics* **29**, 704 (1999).

[5] A. Pagies, G. Ducournau, and J.-F. Lampin, *Appl. Phys. Lett. Photon.* **1**, 031302 (2016).

[6] A. Pagies, G. Ducournau, and J.-F. Lampin, *Progress in continuous wave THz molecular laser optically pumped by a quantum cascade laser*, 42nd International Conference on Infrared, Millimeter and Terahertz Waves (IRMMW-THz), Cancun, Mexico, September 2017.

[7] E. J. Danielewicz, T. A. Galantowicz, F. B. Foote, R. D. Reel, and D. T. Hodges, “High performance at new FIR wavelengths from optically pumped CH_2F_2,” Optics Letters **4**, pp. 280-282, 1979.

Fundamental Principles for the Development of New Functional Nanocomposite Materials Based on Oxide 3D Nanostructures for Applications in THz Optics and Information Transfer

A. Kanaev[1], A. N. Khodan[2], K. I. Zaytsev[3], V. N. Kurlov[4]

[1] Laboratoire des Sciences des Procédés et des Matériaux (LSPM), CNRS, Université Paris 13, Villetaneuse, France
[2] Frumkin Institute of Physical Chemistry and Electrochemistry (IPCE), RAS, Moscow, Russia
[3] Prokhorov General Physics Institute (GPI), RAS, Moscow, Russia
[4] Institute of Solid State Physics (ISSP), RAS, Chernogolovka, Russia

E-mail: andrei.kanaev@lspm.cnrs.fr; anatole.khodan@gmail.com

Abstract – The purpose of this work is development of the solid-state materials possessing a small absorption combined with sufficient refraction index in the THz range. The main criteria, which were used for the material selection, were quite simple: inorganic compound with strong chemical bonds, stoichiometric composition, small concentration of delocalized charge carriers and sufficient polarizability over THz frequency range. It is obvious, that inorganic materials match these criteria in the greatest degree and, first of all, stable oxides with a high fusion temperature: Al_2O_3, SiO_2. In this work we studied monolithic nanofibrous alumina for the THz frequency range, which synthesis process was previously developed [1-5].

Keywords – nanomaterials, 3D nanostructure, mesoporous materials, aluminium oxyhydroxides, ultraporous alumina, nanocomposites, dielectric properties, THz optics

I. Introduction

The choice of materials for THz optics is rather limited, only some polymer materials even porous are used now for this purpose: polyethylene, polytetrafluoroethylene, polypropylene and others. The most common disadvantage of polymer systems is their rather high absorption over the THz frequency range, caused by singularities of chemical composition and intra- and intermolecular hydrogen bonds. The presence of the unshared electronic pairs in a substance, as well as equal availability of the molecular water, and free and loosely coupled charge carriers; all this a priori should enhance the interaction with an electromagnetic radiation and lead to the increment of losses. Probably, it is the reason of why the metallic mirrors are still used for low-loss optical systems in the THz frequency range.

Currently, there are no systematic studies of dielectric properties of porous 3D nanostructures based on hydroxides and oxides of aluminum in the THz range. In this work we report on first studies of monolithic nanofibrous alumina in the THz frequency range.

II. Experimental

New functional materials and nanocomposites were developed on the basis of the original laboratory technology (LT), which has been developed for more than 20 years in the framework of scientific cooperation between LSPM CNRS and IPCE RAS [1-5]. Currently LT allows to obtain highly porous monolithic blocks (PMOA), having a shape with a given cross-section from ~ 1 cm² to < 100 cm² and a height from 0.5 cm to 20 cm. The 2D structure of PMOA consists of alumina nanofibrils of a diameter ~4 – 7 nm and a length of ~120 – 250 nm. Annealing of PMOA in the temperature range of 400 – 1700 °C leads to the isotropic dimensions reduction while samples are not destroyed and retain the porous structure. By varying the annealing conditions, one can control the material mass density in the range from 0.02 to 3 g/cm^3, specific surface area from 300 to 1 m^2/g, and open porosity from 99.3 to 25% (Fig. 1a). To describe the evolution of the 3D structure of PMOA during the annealing process, we proposed a physical model that describes the experimental results for annealing temperatures from 100 ° C to 1700 ° C with a good quantitative agreement [5].

The simplest effective media models using Maxwell-Garnett, Bruggeman and Landau-Lifshitz-Looyenga equations was applied to describe the optical properties of the PMOA materials in the THz range, and good agreement with the experimental results was achieved.

Presently we are conducting exploratory joint studies with the participation of laboratories of the GPI RAS and ISSP RAS on novel functional materials based on 3D oxide nanostructures and nanocomposites. The general goal is developing materials with given and controlled electrodynamic properties for the GHz, THz, IR optics and devices.

An important area of the current research is the development of methods for creating functional 3D hybrid nanostructures and nanocomposites by chemical

modification of PMOA surface. The surface modification of PMOA can be carried out from both gas and liquid media. With the purpose of functionalization of the materials properties, various methods of the structural and chemical modification have been developed: by applying of metalorganic compounds (siloxanes, phthalocyanines, oxyquinolinates), impregnation with nanoparticles <10 nm of TiO_2, ZrO_2, NiO_2, CeO_x, etc. [6–7]. A particulat attention was paid to the interdisciplinary studies of functional heterostructures based on PMOA –monophthalocyaninates of transition metals and sandwich complexes of rare-earth elements [8]. The IPCE RAS has accumulated a vast experience in the synthesis and study of properties of supramolecular materials, establishing patterns of complex formation reactions, which allow high-yield complexes of a given structure with desirable functional characteristics. Original results have been obtained indicating an enhancement of the nonlinear optical properties of supramolecular ensembles, which opened up prospects for creating new materials for optical limiting, dynamic holography, telecommunication, etc.

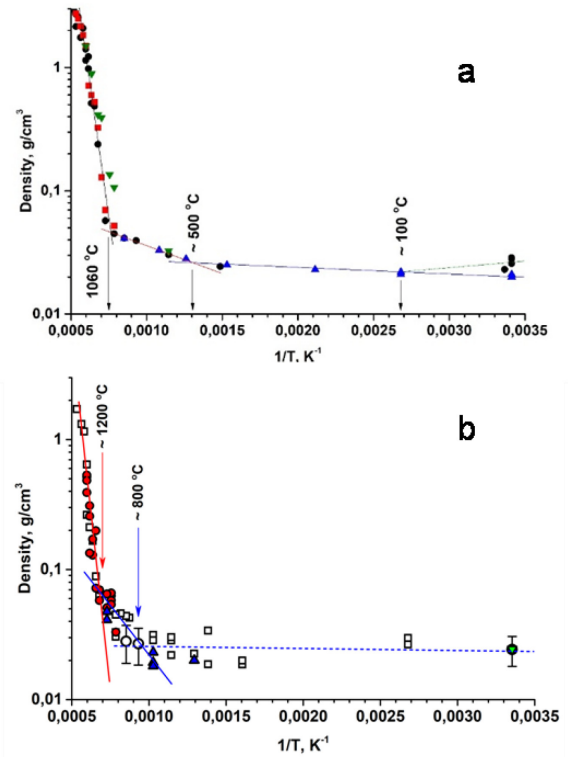

Fig. 1. Density of the samples as a function of the annealing temperature (isochronous annealing time 4 hours). The different series of measurements are indicated with different markers: a) NOA samples [7]; b) NOAM samples

Our systematic studies of the dielectric properties of samples of monolithic highly porous aluminium oxyhydroxides and composite nanostructures began in 2018. Samples in form of plane-parallel plates were studied using THz pulse spectroscopy methods and original THz pulsed spectrometer, developed and assembled in the Laboratory of Submillimeter Dielectric Spectroscopy of GPI RAS [9].

The spectroscopic studies of PMOA samples were carried out using the passage of short THz pulses through a sample with different orientations of the THz electric field relative to the direction of growth of PMOA, along which the texture formation is associated with the predominant growth of alumina nanofibrils. Based on the analysis of the complex amplitude of the THz field passing through a sample and empty cell in the spectrometer (Fig. 2), the complex dielectric constant and complex refractive index were restored, for which an original method of analysis and related software were described in Refs [10-13]. The results in Fig. 3 indicate that PMEA materials are characterized by rather low absorption of THz radiation in a wide frequency range. Its effective refractive index is significantly lower than that of the homogeneous sapphire [13], which is due to a high porosity of the material. Considering two orthogonal polarizations of the THz radiation relative to the direction of orientation of the sapphire nanowires, one can note a significant anisotropy of the optical properties about 10... 40%, depending on structural properties of samples and frequency of electromagnetic radiation.

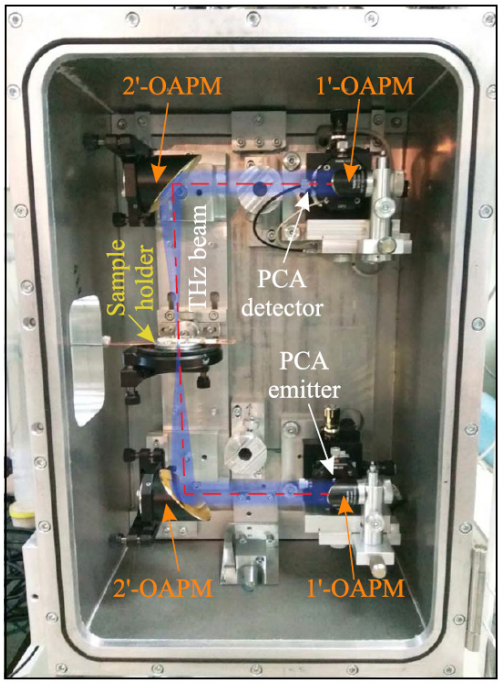

Fig. 2. Laboratory spectrometer using generation and detection of THz pulses in LT – GaAs based photoconductive antennas and equipped with a vacuum measuring chamber (pressure 10^{-3} mbar). Operating frequency range: 0.05 to 4.5 THz, spectral resolution 0.005 THz [8]

The results of preliminary studies indicate a promise of the chosen direction related to a principal possibility of creating novel PMOA based materials for THz optics. Such porous media and nanocomposites are extremely interesting objects for dielectric spectroscopy studies. The most important stages of the related research towards novel materials for THz optics and information transfer devices [12] include studies of elementary electromagnetic dipole excitations of a porous medium,

establishing correlations between the dielectric response and structure of the material and, consequently, the relations with key parameters of the technological process of its manufacturing.

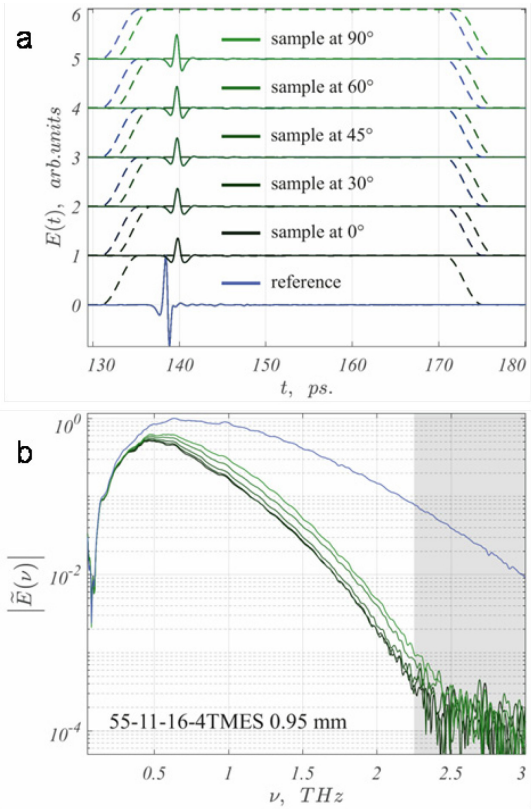

Fig. 3. Results of THz pulsed spectroscopy of porous Al_2O_3: reference THz pulse transmitted through the empty cell of the spectrometer, and THz pulses transmitted through the sample with different polarization of the incident radiation (a) and amplitude of the Fourier spectra of these pulses (b)

We notice an importance of studies of mechanical properties of functional materials based on PMOA. A successful use of highly porous functional 3D nanomaterials in technical devices is impossible without studying their strength and resistance to external factors under operating conditions. This work will be conducted in Derzhavin TSU in the "Nanotechnologies and Nanomaterials" Research and Education Center, which has accumulated vast experience in the field, using traditional and original patented methods of studying fine features of the materials structure, crystalline phase, mechanical and thermal properties.

III. Conclusions

The new nanocomposite oxide systems were developed with properties designed for applications in the THz-GHz optics. The materials based on monolithic nanofibrous alumina open up the possibility for linear and non-linear optics, heterogeneous macro-ordered materials and metamaterials.

Acknowledgments

This work was financially supported by Franco-Russian collaboration exchange program CNRS - RFFI (PRC 1523).

References

[1] T. di Costanzo, A. A. Fomkin, C. Frappart, A. N. Khodan, D. G. Kuznetsov, L. Mazerolles, D. Michel, A. A. Minaev, V. A. Sinitsin and J. L. Vignes, Mater. Sci. Forum **453-454**, 315-320 (2004).

[2] P. N. Martinov, R. Sh. Askhadullin, P. A. Yudintzev and A. N. Khodan, New Industr. Technol. **4**, 48-52 (2008) (in Russian).

[3] J. L.Vignes, L. Mazerolles and D. Michel, *Key Eng. Mater.* **132-136**, 432-435 (1997).

[4] J. L. Vignes, C. Frappart, T. Di Costanzo, J. C. Rouchaud, L. Mazerolles and D. Michel, *J. Mater. Sci.* **43**, 1234-1240 (2008).

[5] A. N. Khodan, T. H. N. Nguyen, M. Esaulkov, M. R. Kiselev, M. Amamra, J.-L. Vignes and A. Kanaev, J. Nanoparticle Res. **20**, 194-204. (2018).

[6] M. Bouslama, M. C. Amamra, S. Tieng, O. Brinza, K. Chhor, M. Abderrabba**,** J.-L. Vignes, A. Kanaev, Appl. Catal. A 402 (2011) 156-161.

[7] M. Bouslama, M. C. Amamra, Z. Jia, M. Ben Amar, O. Brinza, K. Chhor, M. Abderrabba**,** J.-L. Vignes, A. Kanaev, ACS Catal. 2 (2012) 1884-1892.

[8] A. G. Martynov, A. V. Bykov, Yu. G. Gorbunova, A. N. Khodan, A. Yu. Tsivadze, Protection Metals Phys. Chem. Surf. 54 (2018) 1-8.

[9] D.V. Lavrukhin, A. E. Yachmenev, A. Yu. Pavlov, R. A. Khabibullin, Yu. G. Goncharov, I. E. Spektor, G. A. Komandin, S. O. Yurchenko, N. V. Chernomyrdin and K. I. Zaytsev, *Semiconductor Sci. Technol.* **34**, 034005 (2019).

[10] K. I. Zaytsev, A. A. Gavdush, V. E. Karasik, V. I. Alekhnovich, P. A. Nosov, V. A. Lazarev, I. V. Reshetov, and S. O. Yurchenko, *J. Appl. Phys.* **115**, 193105 (2014).

[11] G. R. Musina, I. N. Dolganova, K. M. Malakhov, A. A. Gavdush, N. V. Chernomyrdin, D. K. Tuchina, G. A. Komandin, S. V. Chuchupal, O. P. Cherkasova, K. I. Zaytsev and V. V. Tuchin, Proc. SPIE 10800 (2018).

[12] A. A. Gavdush, N. V. Chernomyrdin, K. M. Malakhov, S. I. T. Beshplav, I. N. Dolganova, A. V. Kosyrkova, P. V. Nikitin, G. R. Musina, G. M. Katyba, I. V. Reshetov, O. P. Cherkasova, G. A. Komandin, V. E. Karasik, A. A. Potapov, V. V. Tuchin and K. I. Zaytsev, *J. Biomed. Opt.* **24**, 027001 (2019).

[13] D. Grischkowsky, S. Keiding, M. van Exter and Ch. Fattinger, *J. Opt. Soc. Am. B* **7**, 2006-2015 (1990).

[14] O. Stepanenko, A. Tartari, M. Amamra, T. H. N. Nguyen, M. Piat, I. Favero, S. Ducci, A. Khodan, L. B. Boinovich, A. M. Emelyanenko, A. Kanaev and G. Leo, *Adv. Device Mater.* **1**, 93-99 (2015).

Experimental Study and Modeling of the Spectral Line Shape and Continuum Absorption by Atmospheric Molecules in the THz Range

M. Yu. Tretyakov[1] and P. Roy[2]

[1] Institute of Applied Physics, Russian Academy of Sciences, Nizhniy Novgorod, Russia
[2] AILES beamline, SOLEIL Synchrotron, Saint-Aubin, France

E-mail: trt@ipfran.ru

Abstract – We report on the current status and the perspectives of our international project. The most important result includes independent experimental confirmation of dominant role of water dimers in the water vapor component of the atmospheric continuum in the millimeter-wave spectral range. We also obtained broad-band spectral recordings of water vapor continuum filling the gap between 6.7 and 12 THz, which was never studied before. Preliminary results of broad-band study of CO rotational spectrum in a mixture of carbon monoxide with argon at atmospheric pressures including experimental observation of subtle line shape effects are presented.

Keywords – atmospheric molecules, continuum, bimolecular absorption, line shape, Terahertz range

I. INTRODUCTION

Our work contributes to the solution of the long standing and one of the most complicated problems of molecular and atmospheric spectroscopy – the problem of non-resonance or continuum radiation absorption in gases. In particular we aim at developing general physically based method of calculating the continuum and collision-induced absorption in the range of rotational-translational spectra of molecules in pure gases and gas mixtures including the problem of resonance line shape modeling at large detuning from the line center. The main motivation is that the radiation balance of all planetary atmospheres having a significant density is largely, if not completely, determined by the relatively weak continuum arising from the collisional interaction of molecules in real gases. Within the project we obtain and analyze broad band high resolution spectra of atmospheric molecules. Analysis of experimental observations is supported by quantum chemical calculations of bimolecular interaction potential and classical trajectories method for calculating the dynamics of collisional interaction of molecules and their spectral manifestations.

Section I presents our recent results on water vapor continuum study, which is very difficult object for theoretical calculations but is of importance for many spectroscopic applications. Section II gives an overview of our work on spectra of carbon monoxide in a mixture with argon at pressures close to atmospheric.

II. WATER VAPOR CONTINUUM

New measurements of the water vapor continuum absorption were performed in the range covering most of the pure rotational spectrum of water molecule from 0.3 up to 23 THz. The continuum absorption was derived from the broad band water vapor spectra recorded at high resolution by Fourier transform spectrometer equipped with the 151-m multipass gas cell at the AILES beam line of the SOLEIL synchrotron. To cover the frequency range, the coherent (0.3–1 THz) and standard (1.3–23 THz) radiation modes of the synchrotron were used. Recordings at several water vapor pressures ranging from 2 up to 16 mbar were used to check the expected quadratic pressure dependence of the continuum.

The new data considerably extend and supplement results of previous measurements of the continuum filling, in particular, the gap between 6.7 and 12 THz, which was never studied before. Analysis of spectra obtained by using coherent synchrotron mode confirmed existence of water dimer spectral future near 0.5 THz which has been predicted in this region by *ab initio* and classical calculations. Our data confirm that the MT-CKD empirical continuum model widely used in atmospheric applications, does not account for the frequency dependence of water vapor continuum in the range of this feature and overestimates the continuum magnitude by about 30% in the whole range of the rotational band of water molecule.

The observed irregular frequency dependence of the retrieved continuum is tentatively interpreted as due to uncertainties on the resonance lines of the water monomer spectrum which is subtracted from the recorded spectra. On the basis of spectra simulations, the inadequate description of the line shapes in the range of the intermediate wings (detuning of 0.2–0.3 THz from line center) and the uncertainties on the self-broadening coefficients of water monomer lines are identified as possible mechanisms responsible for the observed irregular fluctuations. Details of this work are reported in Ref. 1.

III. SPECTRA OF CO – AR MIXTURE

Regular and almost equidistant rotational spectrum of diatomic polar molecule of carbon monoxide is one of the

most studied within the impact approximation and very often is used for spectrometer calibration purposes. So theoretical modeling of the spectrum at low pressures is straight forward. However, to the best of our knowledge no high quality recordings of the spectrum were made at elevated pressures when spectral lines profiles are overlapped and the continuum absorption can be retrieved from experimental data by subtracting calculated spectrum of the CO molecule.

The project within the FIR-LAB framework allows us to perform studies of the CO rotational spectrum by using two broadband high sensitive spectrometers with complementary abilities.

The resonator spectrometer [2] is employed for detailed analysis of the absorption within the range 0.1 – 0.2 THz where the resonance line corresponding to the first rotational transition and the low line wing of the second rotational transitions of CO molecule are located. The spectra of CO and Ar mixture are recorded at pressures up to two atmospheres. High signal to noise ratio (up to 3000) in the spectra allowed first retrieval of the line mixing effect manifestation and determination of its parameters. The effect of speed dependence of collisional relaxation on the line shape is also observed and quantified. The continuum absorption is observed underneath the resonant spectrum.

The Fourier transform spectrometer with the 151-m multipass gas cell at the AILES beam line of the SOLEIL synchrotron operating at the standard radiation modes is going to be used for the spectrum recordings in the 1.3–7 THz range at room temperature and pressures up to one atmosphere. Such spectral interval includes most lines of CO rotational spectrum and experimental conditions ensure that the absorption in gaps between lines is significant. This work is scheduled for the end of May, 2019. Preliminary results of the spectrum analysis will be reported at the meeting.

ACKNOWLEDGMENTS

We express our deep gratitude to all members of our international team contributing to this research: O. Pirali, A. Campargue, T.A. Odintsova, E.A. Serov, M.A. Koshelev, A.A. Balashov, A.O. Zibarova and I.N. Vilkov. This work was financially supported by CNRS-RFBR project 16-55-16006.

REFERENCES

[1] T. A. Odintsova, M. Yu. Tretyakov, A. O. Zibarova, O. Pirali, P. Roy, A. Campargue, *J. Quant. Spectrosc. Radiat. Transfer.* **227**, 190 (2019).

[2] M. A. Koshelev, I. I. Leonov, E. A. Serov, A. I. Chernova, A. A. Balashov, G. M. Bubnov, A. F. Andriyanov, A. P. Shkaev, V. V. Parshin, A. F. Krupnov, M. Yu. Tretyakov, Lee, New frontiers of modern resonator spectroscopy, *IEEE Trans. on Terahertz Sci. Technol.* **8(6)** 773 (2018).

Rovibrational Spectroscopy of the Ground-State and some Fundamental Bands of SO_2F_2

M. Rotger[1], F. Hmida[1,2], B. Grouiez[1], T. Cours[1], L. Manceron[3], V. Boudon[4], H. Aroui[2]

[1] GSMA, UMR 7331 CNRS, University of Reims Champagne Ardenne, Moulin de la Housse, B.P. 1039, 51687, Reims Cedex 2, France
[2] LSDM, ENSIT, University of Tunis, 5 Av. Taha Hussein, 1008 Tunis, Tunisia
[3] Synchrotron Soleil Ligne AILES, B.P. 48, 91192 Gif-sur-Yvette Cedex, France and MONARIS, UMR 8233 CNRS-UPMC, case 49, 4, Place Jussieu, 75252 Paris Cedex, France
[4] Lab. ICB, UMR 6303 CNRS, University Bourgogne Franche-Comté, 9 Av. Alain Savary, B.P. 47870, 21078 Dijon Cedex, France

E-mail: maud.rotger@univ-reims.fr

Abstract – Sulfuryl fluoride is an industrial chemical compound released into the atmosphere in significant quantities. It is used increasingly as a fumigant of timber, buildings and construction materials. SO_2F_2 is also used in agriculture and food processing as a replacement for CH_3Br. Modeling its absorption spectrum is thus essential both for atmosphere concentration measurements and for theoretical aspects related to quasi-spherical tops. The spectroscopy of the fundamental bands of this molecule is quite unknown. In a first time, line positions analysis has been investigated on the ground-state and on some of the fundamental bands of this molecule. In a second time, we have performed an intensity analysis only on the n_2 band (around 850 cm^{-1}) of this molecule. The infrared cross-section of this band has also been evaluated and compared with *ab initio* values. This position and intensity analysis has been performed thanks to the tensorial formalism adapted to quasi-spherical tops and developed in Dijon. A series of programs called C_{2v}TDS (C_{2v} Top Data System) has been used to analyze these rovibrational spectra.

Keywords – molecular spectroscopy, tensorial formalism, sulfuryl fluoride, cross-section

I. INTRODUCTION

Sulfuryl fluoride (SO_2F_2) is an industrial chemical released into the atmosphere in significant quantities [1]. It is used increasingly as a fumigant of timber, buildings and construction materials. SO_2F_2 is also used in agriculture and food processing as a replacement for CH_3Br [2]. Modeling its absorption spectrum is thus essential both for atmospheric concentration measurements and for theoretical aspects of spectroscopy, since SO_2F_2 is close to a spherical rotor and can be considered as derived from the tetrahedral SO_4^{2-} sulfate ion by substitution of two ligands. It means that the vibrational structure of sulfuryl fluoride can be correlated to that of the sulfate ion.

The spectroscopy of sulfuryl fluoride is still quite unexplored. Only quite a limited number of spectroscopic works exist for this rather heavy molecule which is one of the few quasi-spherical species [3–11]. Existing studies have been devoted to investigate line positions in the pure rotation and fundamental band spectra of SO_2F_2. No absolute line intensity experimental study existed up to now. Only two room temperature IR cross section studies exist [12, 13] and a computational quantum chemical study reported prediction of band intensities [14].

The band of interest for intensity analysis, namely the n_2 fundamental band, has been the subject of two previous studies. The first one has been performed by Merke *et al.* [8] who has analyzed this band at room temperature. Using rotational and rovibrational data, parameters up to the sextic centrifugal distortion constants have been determined with Watson's Hamiltonian in *S*-reduction. For IR-transitions, the standard deviation was about 0.40×10^{-3} cm^{-1}. This result was obtained by using about 1900 lines with rotational quantum number up to $J = 68$. This study showed that the n_2 band can be treated as isolated. The second one has been performed by Hmida *et al.* [10] using an oriented tensorial formalism in the $O(3) \supset T_d \supset C_{2v}$ group chain adapted to XY_2Z_2 asymmetric tops close to spherical symmetry. This formalism has been developed by Rotger *et al.* [15] and has been derived from the formalism developed for tetrahedral (T_d) XY_4 molecules [16, 17]. This tensorial model uses the so-called vibrational extrapolation, which makes global analyses much easier and enables studying any rovibrational band or polyad with a systematic development of all rovibrational interactions.

II. TENSORIAL FORMALISM

The theoretical model used is based on the tensorial formalism specific to an XY_2Z_2 asymmetric top close to spherical symmetry and the vibrational extrapolation method developed in Dijon [17, 24]. The tensorial formalism adapted to XY_2Z_2 asymmetric molecules has been developed by Rotger *et al.* [15] as a reorientation of the T_d formalism [25] into the C_{2v} subgroup. It means that the vibrational structure of sulfuryl fluoride can be correlated to that of the tetrahedral sulfate ion. The basic

idea is the use of the $O(3) \supset T_d \supset C_{2v}$ group chain in order to unambiguously label molecular states. This approach follows closely the same steps as those used for C_{4v} and C_{3v} molecules [26–29]. This model, which allows a systematic expansion of the Hamiltonian and dipole moment operator by including all possible interactions for a given rovibrational polyad scheme, has been described in Refs. [6, 7, 15, 17, 30]. We just briefly recall in this presentation the basic principles of this formalism.

III. ANALYSIS

We present the numerous position analysis on the ground state and on some rovibrational fundamental bands of the SO_2F_2 molecule. The lower dyad of this molecule has never been analyzed due to the poor quality of the spectrum and to the fact that the Watson's model seems not adapted to the analysis of this polyad. Two triads have been already investigated, one is still under study. Only the n_2 rovibrational band has been analyzed both in position and in intensity. An integrated band intensity has been calculated and compared to *ab initio* calculations.

IV. CONCLUSIONS

We have conducted an overview of the analysis mainly in position of quite all the fundamental bands of SO_2F_2. One intensity analysis on the n_2 fundamental band is presented and an estimation of the integrated band intensity is compared with *ab initio* calculations [31].

ACKNOWLEDGMENTS

We gratefully thank Dr. J. Vander Auwera (ULB, Bruxelles). This work was financially supported by the french research group named GDR SpecMo (GDR CNRS 3152).

REFERENCES

[1] J. Mülhe *et al.*, Sulfuryl fluoride in the global atmosphere, *J. Geophys. Res.*, 2009; **114** :DO5306.

[2] United Nations Environment Program, Handbook for the Montreal Protocol Substances that Deplete the Ozone Layer 2006.

[3] H. Bürger, H. Ruland, I. Merke, K. Sarka, L. Margulès and J. Demaison, Microwave, Submillimeter-Wave, and High-Resolution FTIR Study of SO_2F_2 in the n_8 State. *J. Mol. Spectrosc.* 2000;**203**:268–272.

[4] K. Sarka, J. Demaison, L. Margulès, I. Merke, N. Heineking, H. Bürger and H. Ruland, Centrifugal Distortion Analysis of a Near-Spherical Top, SO_2F_2: The First Determination of All Six Quartic Centrifugal Distortion Constants for an Asymmetric Top. *J. Mol. Spectrosc.* 2000;**200**:55–64.

[5] H. Bürger, J. Demaison, F. Hegelund, L. Margulès and I. Merke, Microwave, millimeter-wave, and high-resolution FTIR study of SO_2F_2: the n_3, n_7, n_9 triad at 550 cm^{-1}. *J. Mol. Struct.* 2002;**612**:133–141.

[6] M. Rotger, V. Boudon, M. Loëte, L. Margulès, J. Demaison, H. Mäder, G. Winnewisser and H.S.P. Müller, The ground-state rotational spectrum of SO_2F_2. *J. Mol. Spectrosc.* 2003;**222**:172–179.

[7] M. Rotger, V. Boudon, M. Loëte, N. Zvereva-Loëte, L. Margulès, J. Demaison, I. Merke, F. Hegelund and H. Bürger, The bending triad of the quasi-spherical top molecule SO_2F_2 in the 550 cm^{-1} region. *J. Mol. Spectrosc.* 2006;**238**:145–157.

[8] I. Merke, N. Heineking, F. Hegelund, J. Demaison, L. Margulès and H. Bürger, Microwave, millimeterwave, and high-resolution FTIR study of the n_2 = 1 state of SO_2F_2. *J. Mol. Struct.* 2006;**795**:185–189.

[9] L. Margulès, A. Perrin, J. Demaison, I. Merke, H. Willner, M. Rotger, V. Boudon, Breakdown of the reduction of the rovibrational Hamiltonian: The case of $S^{18}O_2F_2$. *J. Mol. Spectrosc.* 2009;**256**:232–237.

[10] F. Hmida, B. Grouiez, M. Rotger, M. Faye, L. Manceron, V. Boudon, and H. Aroui, Line position analysis of the n_2 band of SO_2F_2 using the C_{2v}Top Data System. *J. Mol. Spectrosc.* 2016;**325**:29–34.

[11] F. Hmida, B. Grouiez, M. Rotger, M. Faye, L. Manceron, V. Boudon, and H. Aroui, Line position analysis of the (n_3, n_7, n_9) bending triad of SO_2F_2 using the C_{2v} Top Data System. *J. Mol. Spectrosc.* 2017;**339**:23–30.

[12] V. C. Papadimitriou, R. W. Portmann, D. W. Fahey, J. Mühle, R. F. Weiss, J. B. Burkholder, Experimental and Theoretical Study of the Atmospheric Chemistry and Global Warming Potential of SO_2F_2. *J. Phys. Chem. A* 2008;**112(49)**:12657–12666.

[13] T. J. Dillon, A. Horowitz, J. N. Crowley, Direct detection of OH formation in the reactions of HO_2 with $CH_3C(O)O_2$ and other substituted peroxy radicals. *Atmos. Chem. Phys.* 2008;**8**:1547.

[14] A. T. Kowal, First-principles computation of the anharmonic vibrational spectra of sulfuryl halides SO_2X_2 (X = F, Cl, Br). *Chem. Phys.* 2006;**324(2-3):**359–366.

[15] M. Rotger, V. Boudon and M. Loëte, Spectroscopy of XY_2Z_2 (C_{2v}) Molecules: A Tensorial Formalism Adapted to the $O(3) \supset T_d \supset C_{2v}$ Chain. Application to the Ground State of SO_2F_2. *J. Mol. Spectrosc.* 2002;**216**:297–307.

[16] J.-P. Champion, M. Loëte and G. Pierre, « Spherical top spectra in Spectroscopy of the Earth's Atmosphere and Interstellar Medium » (K. N. Rao and A. Weber, Eds.), Academic Press, Inc., San Diego, 1992, pp. 339–422.

[17] V. Boudon, J.-P. Champion, T. Gabard, M. Loëte, F. Michelot, G. Pierre, M. Rotger, Ch. Wenger, and M. Rey, Symmetry-adapted tensorial formalism to model rovibrational and rovibronic spectra of molecules pertaining to various point groups. *J. Mol. Spectrosc.* 2004;**228**:620–634.

[18] Ch. Wenger, M. Rotger and V. Boudon, C_{2v} Top Data System (C_{2v}TDS) software for infrared spectrum simulation of XY_2Z_2 asymmetric molecules: some improvements to the TDS packages. *J. Quant. Spectrosc. Radiat. Transfer* 2005;**93**: 429–446.

[19] P. Roy, M. Rouzières, Z. Qi, O. Chubar, The AILES Infrared Beamline on the third generation Synchrotron Radiation Facility SOLEIL. *Infrared. Phys. Technol* 2006;**49**:139–146.

[20] M. Faye, M. Bordessoule, B. Kanouté, P. Roy, L. Manceron, Improved mid infrared detector for high spectral or spatial resolution and synchrotron radiation use. *Review of Scientific Instruments* 2016; **87(6)**: 063119.

[21] OPUS spectroscopy software version 6.5. Bruker GmbH, Ettlingen, Germany (www.bruker.com)

[22] I.E. Gordon, L.S. Rothman, C. Hill, R.V. Kochanov, Y. Tan, P.F. Bernath, M. Birk, V. Boudon, A. Campargue, K.V. Chance, B.J. Drouin, J.-M. Flaud, R.R. Gamache, J.T. Hodges, D. Jacquemart, V.I. Perevalov, A. Perrin, K.P. Shine, M.-A.H. Smith, J. Tennyson, G.C. Toon, H. Tran, V.G. Tyuterev, A. Barbe, A.G. Császár, V.M. Devi, T. Furtenbacher, J.J. Harrison, J.-M. Hartmann, A. Jolly, T.J. Johnson, T. Karman, I. Kleiner, A.A. Kyuberis, J. Loos, O.M. Lyulin, S.T. Massie, S.N. Mikhailenko, N. Moazzen-Ahmadi, H.S.P. Müller, O.V. Naumenko, A.V. Nikitin, O.L. Polyansky, M. Rey, M. Rotger, S.W. Sharpe, K. Sung, E. Starikova, S.A. Tashkun, J. Vander Auwera, G. Wagner, J. Wilzewski, P. Wcislo, S. Yu, E.J. Zak, The HITRAN2016 Molecular Spectroscopic Database. *Journal of Quantitative Spectroscopy and Radiative Transfer* 2017, **203**,3-69, ISSN 0022-4073, DOI 10.1016/j.jqsrt.2017.06.038

[23] M. R. Carleer, a Windows program to accurately measure the line intensities of high-resolution Fourier transform spectra,

Remote sensing of clouds and the atmosphere V 2001; **4168**:337–343.

[24] N. Cheblal, M. Loëte, V. Boudon, Development of the Dipole Moment and Polarizability Operators of Octahedral Molecules. *J. Mol. Spectrosc*. 1999;**197**:222–231.

[25] Ch. Wenger, J.-P. Champion, Spherical top data system (STDS) software for the simulation of spherical top spectra. *J. Quant. Spectrosc. Radiat. Transfer* 1998;**59**:471–480.

[26] M. Rotger, V. Boudon and M. Loëte, Spectroscopy of XY_5Z (C_{4v}) Molecules: A Tensorial Formalism Adapted to the $O(3) \supset O_h \supset C_{4v}$ Chain. *J. Mol. Spectrosc*. 2000;**200**:123–130.

[27] M. Rotger, V. Boudon and M. Loëte, Spectroscopy of XY_5Z (C_{4v}) Molecules: Development of the Hamiltonian and the Transition Moment Operators Using a Tensorial Formalism. *J. Mol. Spectrosc*. 2000;**200**:131–137.

[28] A. El Hilali, V. Boudon and M. Loëte, Spectroscopy of XY_3Z (C_{3v}) molecules: A tensorial formalism adapted to the $O_h \supset C_{\infty v} \supset C_{3v}$ group chain. *J. Mol. Spectrosc*. 2005;**234**:113–121.

[29] A. El Hilali, V. Boudon and M. Loëte, Development of the Hamiltonian and transition moment operators of symmetric top molecules using the $O_h \supset C_{\infty v} \supset C_{3v}$ group chain. *J. Mol. Spectrosc*. 2005;**234**:176–181.

[30] V. Boudon, M. Rotger, N. Zvereva-Loëte and M. Loëte, The SO_2F_2 quasi-spherical top: Correspondence between tensorial and Watson's formalisms *J. Mol. Struct*. 2006; **780-781**:124–133.

[31] F. Hmida *et al*., Line position and intensities in the n_2 fundamental band of Sulfuryl fluoride using the C_{2v}Top Data System, *Journal of Quantitative Spectroscopy and Radiative Transfer*, 2019;**227**, 63–71.

8th Russia-Japan-USA-Europe Symposium on Fundamental & Applied Problems of Terahertz Devices & Technologies

Plasmonic Helicity-Driven Detector of Terahertz Radiation

V. Yu. Kachorovskii[1], I. Gorbenko[1], M. Shur[2]

[1] A. F. Ioffe Physico-Technical Institute, St. Petersburg, Russia
[2] Rensselaer Polytechnic Institute, NY, USA

E-mail: kachor.valentin@gmail.com

Abstract. A theory of the helicity-driven plasmonic dc response of a gated two dimensional lectron gas to terahertz (THz) radiation is developed. A general diagram of a plasmonic detector operating in different regimes is found and analytical equations describing all these regimes are derived. It is demonstrated that the helicity-sensitive part of the response dramatically increases in the vicinity of the plasmonic resonances and oscillates with the phase shift between the excitation signals on the source and drain. The resonance line shape is an asymmetric function of the frequency deviation from the resonance. In contrast, the helicity-insensitive part of the response is symmetrical. These properties yield significant advantage for using plasmonic detectors as helicity-sensitive THz and far infrared spectrometers and interferometers.

Keywords – detectors of THz radiation, helicity, plasmonics, interferometers, spectrometers

I. Introduction

The TeraFETs – the devices converting the impinging THz radiation into a dc current by using the excitation of overdamped or resonant plasma oscillations have been implemented in Si, GaAs, GaN, graphene, and other materials systems. The TeraFETs are now being commercialized as tunable and fast detectors of sub-THz and THz radiation. The underlying physical mechanism proposed in Refs [1, 2] is based on the rectification of plasmonic oscillations enabled by the device nonlinearity and the asymmetry of the setup. The latter determines the direction of the dc current response (or the sign of the induced dc voltage). One of the possible ways to introduce the asymmetry is to impose different boundary conditions on the source and drain of the device. In particular, when the source-gate input is excited by a signal with amplitude U_a, while the drain current is fixed the generated open circuit dc voltage is

$$V \propto U_a^2. \qquad (1)$$

Such drain boundary condition implicitly implies that the external circuit is connected to the drain via an antenna or a contact pad with an infinite inductive impedance. Another option is to use identical antennas but apply signals with the different amplitudes U_a and U_b at the source and drain, respectively. For such a setup, the induced dc current is proportional to the difference of the squared voltages at the source and drain (assuming that these signals have the same phase) [3]

$$V \propto U_a^2 - U_b^2. \qquad (2)$$

Importantly, a strong asymmetry can be also induced by the phase shift between the THz signals at the source and drain. For equal amplitudes of signals on the source and drain $U_a = U_b$ nonzero phase shift θ between signals induces the dc voltage [4-7]

$$V \propto U_a^2 \sin\theta. \qquad (3)$$

Such a phase shift can be induced by circularly-polarized radiation [4–7]. Remarkably, this shift depends very weakly on L/λ (here L is the channel length and λ is the THz radiation wavelength) and remains finite even in the limit of a homogeneous field. In this limit, the phase shift is simply given by geometrical angle $\pm\theta$ [see Fig. 1] with the sign being determined by the clockwise or counterclockwise helicity.

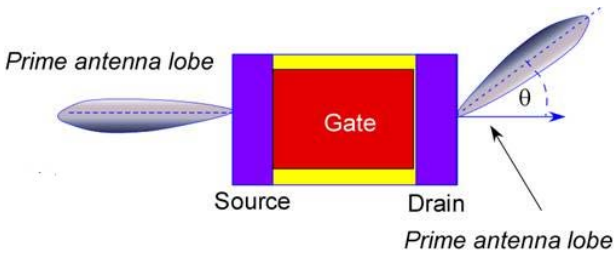

Fig. 1. Asymmetry of external antennas leads to helicity-sensitive response

In the papers [4, 5], helicity-driven effects were discussed in the non-resonant regime. They were predicted to be absent for zero loading impedances. Here, we use hydrodynamic approach to study the resonant regime of helicity-driven TeraFET operation (we follow Refs. [6–7]). We demonstrate that in this regime, the intrinsic FET channel shows the helicity-driven response.

II. Research methods

We start with the hydrodynamic equations describing electron liquid in the channel of FET:

$$\begin{cases} \frac{\partial v}{\partial t} + v\frac{\partial v}{\partial x} + \gamma v = -\frac{e}{m}\frac{\partial U}{\partial x}, \\ \frac{\partial U}{\partial t} + \frac{\partial (Uv)}{\partial x} = 0. \end{cases} \qquad (4)$$

Here, v is the electron liquid velocity, U is the local value of the gate-channel voltage, e and m are the electron charge and mass, γ is the inverse momentum

relaxation time. We use the following boundary conditions (BC)

$$\begin{cases} U(0) = U_g + U_a \cos(\omega t + \theta), \\ U(L) = U_g + V + U_b \cos(\omega t). \end{cases} \quad (5)$$

Here U_g is the voltage between the gate and the channel, U_a and U_b are the amplitudes of the THz signals on the two antennas, θ is the phase shift due to asymmetry of the setup (see Fig. 1), and V is the optically induced voltage drop on the sample which has to be found.

We search solutions of Eq. (4) in the following form

$$\begin{cases} v = v_0(x) + [v_1(x)e^{-i\omega t} + v_{-1}(x)e^{i\omega t}]/2 + \cdots, \\ n = n_0(x) + [n_1(x)e^{-i\omega t} + n_{-1}(x)e^{i\omega t}]/2 + \cdots. \end{cases} \quad (6)$$

where n_1 and v_1 are the amplitudes of radiation-induced plasma oscillations of density and velocity. Taking into account rectification effects after some algebra we find

$$\frac{V}{U_g} = \frac{\gamma}{4s^2}\int_0^L dx\left(n_1 v_{-1} + n_{-1} v_1 - \frac{d[v_1(x)v_{-1}(x)]}{\gamma\, dx}\right) \quad (7)$$

Amplitudes n_1, v_{-1}, n_{-1}, v_1 are found from linearized Eq. (4)

$$(\gamma - i\omega)v_1 + s^2\frac{\partial n_1}{\partial x} = 0, \quad (8)$$

$$-i\omega n_1 + \frac{\partial v_1}{\partial x} = 0. \quad (9)$$

which were solved by taking into account the BC (5) These amplitudes vary in space with the wave vector

$$k = \frac{\sqrt{\omega(\omega + i\gamma)}}{s} = \frac{\Omega + i\Gamma}{s}, \quad (10)$$

Where

$$s = \sqrt{\frac{eU_g}{m}} \quad (11)$$

the plasma waves velocity, which is controlled by the gate voltage U_g. Calculations yield

$$V = \frac{\omega}{\sqrt{\omega^2+\gamma^2}}\frac{\alpha(U_a^2 - U_b^2) + \beta U_a U_b \sin\theta}{4U_g|\sin(kL)|^2}, \quad (12)$$

where

$$\alpha = \left(1 + \frac{\gamma\Omega}{\Gamma\omega}\right)\sinh^2\left(\frac{\Gamma L}{s}\right) - \left(1 - \frac{\Gamma\gamma}{\Omega\omega}\right)\sin^2\left(\frac{\Omega L}{s}\right), \quad (13)$$

$$\beta = 8\sinh\left(\frac{\Gamma L}{s}\right)\sin\left(\frac{\Omega L}{s}\right). \quad (14)$$

III. Results

Equation (12) was analyzed in different limiting cases. Below we consider two most interesting regimes.

High frequency regime: $\omega_0 \ll \gamma \ll \omega$, where $\omega_0 = \pi s / L$ – frequency of plasma oscillations. In this case $\Omega \approx \omega, \Gamma \approx \gamma / 2$, and the response looks

$$V = \frac{3(U_a^2 - U_b^2)}{4U_g} + \frac{4U_a U_b e^{-\gamma L/2s}\sin(\pi\omega/\omega_0)\sin\theta}{U_g}. \quad (15)$$

We see that phase-dependent term is periodical in frequency.

Resonance case: $\omega \gg \gamma, \omega_0 \gg \gamma$.

In the vicinity of the resonant frequencies, $\omega \approx N\,\omega_0$, the response has a very sharp (resonant) dependence on the radiation frequency:

$$V = \frac{(U_a^2 - U_b^2)(3\gamma^2/4 - \delta\omega^2) + 4U_a U_b(-1)^N \delta\omega\gamma\sin\theta}{4U_g(\delta\omega^2 + \gamma^2/4)} \quad (16)$$

$$\delta\omega = \omega - \omega_N, \quad \omega_N = \pi N s/L, \quad (17)$$

where ω_N – resonance frequency.

Remarkably, the resonant response is a nontrivial function of $\delta\omega$. It is given by the sum of two terms: symmetrical and asymmetrical with respect to $\delta\omega$. This is illustrated on Fig. 2, where the response is shown at different phase shifts: $0 < \theta < \pi/2$.

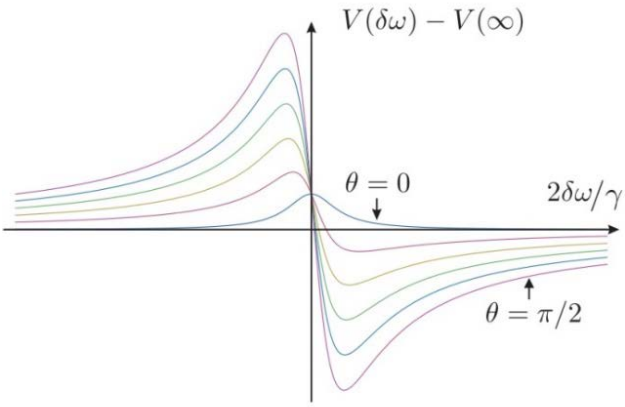

Fig. 2. Dependence of the voltage response on frequency [see Eq. (16)] at different phase shifts θ

IV. Conclusions

To conclude, the theory of nonlinear resonant plasmonic response of the gated 2D electron gas subjected to THz radiation with a given helicity shows that the helicity-driven contribution ramatically increases in the vicinity of the plasmonic resonances. This contribution is a harmonic function of the phase shift and shows an asymmetric dependence on the excitation frequency in the vicinity of the resonances. Hence it can be easily separated from the conventional symmetric contribution, which is not sensitive to the radiation polarization. This result can be directly used for implementation of the helicity-sensitive THz spectrometers and interferometers. The helicity-sensitive contribution can also be observed in the non-resonant regime. Although it is small in this case as compared to the polarization insensitive part of the response, it has different frequency dependence and, therefore, can be experimentally separated.

Acknowledgments

The work was supported by RFBR (Grant No. 17-02-00217) and by Foundation for the Advancement of Theoretical Physics and Mathematics “BASIS”.

REFERENCES

[1] M. Dyakonov and M. S. Shur, "Shallow water analogy for a ballistic field effect transistor: New mechanism of plasma wave generation by dc current", Phys. Rev. Lett. **71**, 2465-2468 (1993).

[2] M. Dyakonov and M.S. Shur, "Detection, mixing, and frequency multiplication of terahertz radiation by two-dimensional electronic fluid", IEEE Transaction on Electron Devices **43**, 380-387 (1996).

[3] D. Veksler, A. Muraviev, V.Yu. Kachorovskii, T. Elkhatib, K. Salama, X.-C. Zhang, M. Shur, Solid-State Electronics, "Imaging of field-effect transistors by focused terahertz radiation", **53**, 571-573 (2009).

[4] C. Drexler, N. Dyakonova, P. Olbrich, J. Karch, M. Schafberger, K. Karpierz, Yu. Mityagin, M. B. Lifshits, F. Teppe, O. Klimenko, Y. M. Meziani, W. Knap, and S. D. Ganichev," Helicity sensitive terahertz radiation detection by field effect transistors", J. Appl. Phys., **111**, 124504-124510 (2012).

[5] K. S. Romanov and M. I. Dyakonov, "Theory of helicity-sensitive terahertz radiation detection by field effect transistors", Applied Phys. Lett., **102**, 153502-153505. (2013).

[6] I. V. Gorbenko, V. Yu. Kachorovskii, and M. S. Shur, "Plasmonic Helicity-Driven Detector of Terahertz Radiation", Phys. Status Solidi RRL, 1800464-1800469 (2018).

[7] I. V. Gorbenko, V. Yu. Kachorovskii, and M. S. Shur, "Terahertz plasmonic detector controlled by phase asymmetry", Optics Express, 27, No. 4 (2019).

Terahertz Excitations of a Two-Dimensional Electron Gas in CdTe-Based Quantum Wells

D. Yavorskiy[1], J. Wróbel[2], T. Wojtowicz[3], J. Łusakowski[1]

[1] Faculty of Physics, University of Warsaw, ul. L. Pasteura 5, PL-02-093 Warsaw, Poland
[2] Institute of Physics, PAS,al. Lotników 32/46, PL-02-668 Warsaw, Poland
[3] International Research Centre – MagTop, Institute of Physics, PAS, al. Lotników 32/46, PL-02-668 Warsaw, Poland

E-mail: jerzy.lusakowski@fuw.edu.pl

Abstract – Terahertz spectroscopy experiments on modulation doped CdTe-based single and multiple quantum wells (QW) were carried out at low temperatures and high magnetic fields. Cyclotron resonance and magnetoplasmon excitations were studied on samples with grids lithographically prepared by evaporation of Au or by etching. Dispersion relations of plasmons were obtained and discussed from the point of view of an effective dielectric constant. Tunability of magnetoplasmon resonances with visible light as well as their linear polarization was shown. Results indicate that CdTe-based QW can serve as a good plasmonic-oriented alternative of GaAs-based system. Also, we show that the strength of magnetplasmon resonances allows to use such structures as sensitive magnetic field tunable detectors of THz radiation.

Keywords – THz spectroscopy, magnetoplasmon, CdTe-based quantum wells

I. Introduction

Plasmons in semiconductor systems have been a subject of an intense theoretical and experimental research for already a few decades. Together with a cyclotron resonance transitions, they are one the the basic excitations of an electron plasma in solids. Magnetic field (B) is a useful tool in the plasma spectroscopy because magnetoplasmon (i.e., a plasmon in magnetic field) frequency is B – dependent which allows to use magnetic field as a spectroscopic tuning parameter. A big experimental difficulty in studies of plasmonic excitations of a two-dimensional electron gas (2DEG) is the necessity to ensure fulfillment of the low of conservation of momentum. This comes from the fact that the momentum of a plasmon is much bigger than that of an incident THz photon (at least, at typically used THz frequencies) and a lacking momentum must be supplied by a grid coupler or a mesa.

Thus, in most of cases, plasmon resonances are studied on samples supplied with a grid of a period Λ, which typically falls in a micrometer range, and which defines wave vectors k_n of excited plasmons: $k_n = 2\pi/\Lambda$. A metallic grid serves as a very efficient coupler but it introduces another difficulty which is related to poorly – defined screening of a THz field of plasma waves with the grid. The thing is that the dispersion relation is different for gated and ungated 2D plasmons which results from different effective dielectric constants (ε_{eff}) in these two cases, and a metallic grid offers a partial gating only. It was found in the case of 2D plasmons in GaAs/AlGaAs, GaN/AlGaN and CdTe/CdMgTe systems [1] that a good phenomenological solution to this problem was to take a weighted average of effective dielectric constants for gated and ungated plasmons with the weight defined by the geometrical aspect of the grid.

In the present work, we concentrated mainly on grids defined by etching. This offers an additional tuning parameter, i.e., the depth of etched groves which influences the plasmonic response to THz radiation. What is more, we applied this procedure to structures with single, double and twenty Qws.

The results show that CdTe – based QW are suitable to be used to carry out basic research on plasma in 2D systems. A big amplitude of magnetoplasmon's feature make these structures also suitable for resonant detection of THz radiation.

II. Experiment and Results

Molecular beam epitaxy grown CdTe/CdMgTe quantum wells were modulation doped with Iodine donors. We studied wafers with single, double and 20 QWs. In the case of multi-quantum wells structure, the separation of the wells was large enough to consider them as separate (i.e., an overlap of electron wave functions from neighbour wells can be neglected). Grid patterns (with Λ = 8 μm for all samples) were fabricated with an electron beam lithography. In the case of etched grids, we changed the geometrical aspect of the grid (i.e., the length of etched to non-etched part within the period Λ). A profile of etched surfaces were determined with an atomic force microscope. Samples were put into a variable temperature insert and placed in a helium cryostat with a superconducting coil at the temperature equal to about 2.0 K. A bolometer mounted below the sample allowed to measure intensity of transmitted THz radiation as a function of magnetic field. We used a CO_2 laser – pumped molecular laser (methanol).

The main results obtained can be summarized as follows.

a) AFM scans show that the etching process leads to a non-uniform depth profiles with a surface roughness of about 10 nm. What is more, in the case of the narrowest tranches, deep "spikes" are etched at the border of tranches. This shows that fabrication of etched grids can lead to (unwanted in our case) cutting the 2DEG plane

along tranche borders. Further, if the etching is too deep, one depletes (at least partially) the 2DEG below the etched tranches which influences the amplitude of plasmonic resonances. In fact, at the adopted etching process, a correlation was found between the width and depth of the etched tranches, and – in the next step – with the amplitude of magnetoplasmon resonance.

b) At given frequency of THz excitation and fixed period Λ of the grid, the magnetic field at which a magnetoplasmon resonance occurs (B_p) depends slightly on the geometrical aspect of the grid. Since B_p is determined by a ratio of concentration of 2DEG (n) and the effective dielectric constant, we conclude that this ratio depends on parameters of etched grid. As it was mentioned above, one could expect an influence of etching on the electron concentration (depopulation by surface states) but one should also consider that the electromagnetic environment of 2DEG changes with changing the grid geometry which may influence screening of THz fields, reflected by $\varepsilon_{\mathrm{eff}}$, and thus a magnetoplasmon frequency. To clarify this point, measurements on samples with other grid parameters are neccesary.

c) In the case of some samples with etched grids, we used several laser lines which allowed us to determine a plasmon dispersion relation and a ratio of $n/\varepsilon_{\mathrm{eff}}$ for grids of different parameters. The dispersion was that of ungated – plasmon, consistent with expectations.

d) By using a circular polarizer at the excitation frequency of 2.54 THz, we verified that magnetoplasmon excitation is circularly unpolarized, in opposition to the cyclotron resonance transition.

e) In the case of a metallic grid and for grids with narrow etched tranches, the amplitude of the magnetoplasmon resonance is comparable to that of the cyclotron resonance. When the tranches are wide, the amplitude decreases which is probably related to depopulation of 2DEG.

f) Under an illumination with a white light, the position of magnetoplasmon resonance changes and the resonant line gets almost three times broader. Thus, illumination with visible light transforms a resonant response to a rather broad-band one. In the case of a sample with 20 Qws, the magntoplasmon resonance is much broader than in single of double QW case.

III. Conclusions

We carried out a series of THz magnetospectroscopy experiments on different types of CdTe/CdMgTe quantum wells with a 2DEG plasma. We showed that the magnetoplasmon response is sensitive to parameters of etched grids (even if their period is kept constant). We determined plasmon dispersion relations and showed a polarization properties of a magnetoplasmon resonance. We aslo indicate that magnetoplasmon resonances in CdTe/CdMgTe single or multiple QWs can be used for a resonant or a broadband detection of THz radiation. Additionally, performance of these QW as THz detectors can be tuned with additional illumination with a visible light.

Acknowledgments

This work was financially supported in part by the National Science Centre (Poland) through grants UMO-2014/13/B/ST3/04393, UMO-2017/27/N/ST7/01771 and UMO-2015/17/B/ST7/03630, and by the Foundation for Polish Science through the IRA Programme co-financed by EU within SG OP.

References

[1] J. Łusakowski, *Semicond. Sci. Technol.* **32**, 013004 (2017).

Nonlocal Transport of Photoexcited Carriers in Terahertz Spectral Range in Epitaxial $Hg_{1-x}Cd_xTe$ Films with the Inverted Band Structure

A. S. Kazakov[1], A. V. Galeeva[1], A. I. Artamkin[1], S. A. Dvoretskiy[2], N. N. Mikhailov[2], M. I. Bannikov[3], S. N. Danilov[4], L. I. Ryabova[5], D. R. Khokhlov[1,3]

[1] M.V. Lomonosov Moscow State University, Faculty of Physics, Moscow, 119991, Russia
[2] Rzhanov Institute of Semiconductor Physics, Novosibirsk, 630090, Russia
[3] P.N. Lebedev Physical Institute, Moscow, 119991, Russia
[4] Regensburg University, Regensburg, D-93053, Germany
[5] M.V. Lomonosov Moscow State University, Faculty of Chemistry, 119991, Moscow, Russia

E-mail: askazakov@physics.msu.ru

Abstract – We present our results on terahertz photoconductivity studied in epitaxial $Hg_{1-x}Cd_xTe$ films with the inverted energy spectrum (x<~0.16) in the nonlocal (H-bar type) geometry. We show that the terahertz photoresponse demonstrates nonlocality and chirality in magnetic field. We discuss the results in terms of a qualitative model that takes into account coexistence of the bulk transport and boundary conductive channels.

Keywords – HgCdTe, terahertz photoconductivity, topological insulators

I. Introduction

Electron transport properties of materials exhibiting a topological phase transition are of a great applied and fundamental interest. $Hg_{1-x}Cd_xTe$ solid solutions reveal a composition-driven transition from the trivial semiconductor (x > 0.16), characterized by the direct energy spectrum, to the topological phase (x < 0.16) with the inverted energy band structure. Study of photoelectric effects under terahertz laser excitation may provide an experimental observation of topological conductive states in $Hg_{1-x}Cd_xTe$ solid solutions featured by relatively low bulk carrier concentration. Previously, we discussed bulk- and interface-related non-equilibrium processes, which may contribute to the terahertz photoconductivity in $Hg_{1-x}Cd_xTe$ epitaxial layers [1]. In this work, we study a terahertz photoresponse in $Hg_{1-x}Cd_xTe$ structures with the inverted energy spectrum in a nonlocal configuration to discriminate the edge transport contribution.

II. Experimental

The 4 μm thick $Hg_{1-x}Cd_xTe$ films (0.12 < x < 0.16) were synthesized on a semi-insulating GaAs [013] substrate with ZnTe and CdTe buffer layers by molecular beam epitaxy. Transport properties of the structures were studied in the 4.2–300 K temperature range. All the samples were of the n-type. The typical concentration of electrons in a film bulk was ~ 10^{14} cm^{-3} at T = 4.2 K. Photoconductivity induced by the terahertz laser radiation was studied in the frequency range 0.6–3.9 THz in magnetic fields up to 4 T at T = 4.2 K. The measurements were carried out for both the standard Hall bar sample geometry and the nonlocal H-bar-like geometry (see inset in the fig. 1) with different geometrical parameters, including a variable distance between pairs of current and potential contacts. The typical sample length was ~ 5 mm, the width was varied from 0.5 to 2.5 mm.

III. Results

We show that the magnitude of the photoresponse measured in the nonlocal configuration almost does not depend on the distance between pairs of potential (2-7, 3-6 or 4-5 in the inset in fig. 1) and current (1-8 in the inset) probes within the typical sample length. It should be emphasized, that the voltage, measured in the absence of the laser radiation, decreases dramatically as the distance from the current probes increases.

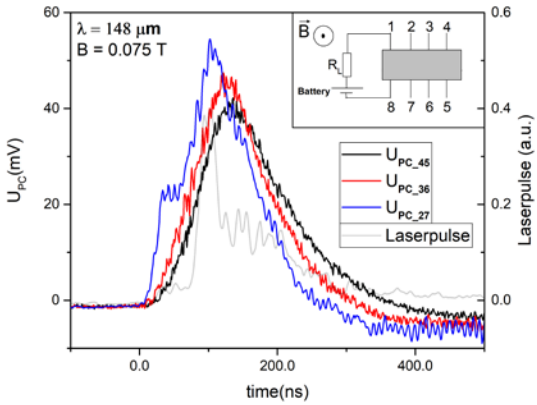

Fig. 1. Kinetics of the photoresponse measured under terahertz photoexcitation with λ = 148 μm at different pairs of potential probes (2-7, 3-6 or 4-5) in magnetic field B = 0.075 T. The sample with the 0.5 mm width. The inset shows schematically the H-bar-like geometry of the sample and the experimental measurement circuit.

The photoresponse kinetics are analyzed taking into account the geometry of the sample and exponential decrease of the bulk current density with a distance from the current probes. The observed strong suppression of the bulk transport allows us to determine the edge channel contribution into the photoconductivity.

The nonlocal response behavior in external magnetic field provides one extra argument for the edge non-equilibrium transport channel formation. In a given weak magnetic field (B < ~1 T) applied, the nonlocal photoresponse sign depends on the potential probe position indicating the chirality of the non-equilibrium transport induced. For a given potential probe position, the photoresponse sign changes to the opposite one when the polarity of the magnetic field is reversed.

IV. Conclusions

The experimental results indicate that in the $Hg_{1-x}Cd_xTe$ epitaxial films with compositions corresponding to the inverted energy spectrum, under the photoexcitation with terahertz radiation, a nonlocal photoconductivity mode can be realized due to the formation of boundary transport channels. There is a reason to assume that the observed nonlocal transport of photoexcited carriers is related to the presence of topological states.

References

[1] A. V. Galeeva, A. I. Artamkin, A. S. Kazakov et al. Beilstein J. Nanotechnol . 9 , 1035 (2018).

Terahertz Photoluminescence from $HgTe/Hg_{1-x}Cd_xTe$ Quantum Well Heterostructures due to Valence Band – Acceptor Transitions

D. V. Kozlov[1, 2]*, V. V. Rumyantsev[1, 2], A. M. Kadykov[1,6], M. A. Fadeev[1,6], N. S. Kulikov[1, 2], V. V. Utochkin[1, 2], N. N. Mikhailov[3,4], S. A. Dvoretskiy[3,5], V. I. Gavrilenko[1, 2], H.-W. Hübers[6], F. Teppe[7] and S. V. Morozov[1,2]

[1] IPM RAS, GSP-105, Nizhny Novgorod, 603950, Russia
[2] Lobachevsky State University of Nizhny Novgorod, Nizhny Novgorod, Russia
[3] Rzhanov Institute of Semiconductor Physics, Siberian Branch, Russian Academy of Sciences, Novosibirsk, Russia
[4] Novosibirsk State University, Novosibirsk, Russia
[5] Tomsk State University, 634050, Tomsk, Russia
[6] Institut für Physik, Humboldt-Universität zu Berlin, Newtonstr. 15, 12489
[7] Laboratoire Charles Coulomb (L2C), Universite Montpellier, Montpellier, France

E-mail: dvkoz@ipmras.ru

Abstract – THz photoluminescence (PL) spectra from QW HgTe/CdHgTe heterostructures are studied in the temperature range of 30–100 K under the excitation power varied from 3 mW to 300 mW. The long-wavelength lines in the PL spectra, whose position does not change with temperature, are associated with the capture of free holes on the states of neutral mercury vacancies. Non-monotonic dependence of the impurity PL signal on the power of the exciting source has been observed.

Keywords – HgTe/CdHgTe heterostructures, photoluminescence, mercury vacancies

I. Introduction

Terahertz (THz) radiation due to transitions involving impurities and defects in bulk semiconductors and semiconductor quantum well (QW) structures has been of interest for a long time [1, 2]. The related effects can be useful for developing terahertz sources employing optical transitions between impurity states. Until recently, studies of impurities and defects were carried out mainly in the most commonly used semiconductor heterostructures based on Ge, GaAs and Si [3]. This work continues a series of work aimed at studying the impurity/defect centers in HgTe/CdHgTe QW heterostructures, in which the most common acceptor is a mercury vacancy. Mercury vacancies manifest themselves in the photoconductivity (PC) [4, 5] and photoluminescence (PL) spectra [6]. In this work we investigate the PL spectra related to the mercury vacancies.

II. Experimental technique

The structures under study were grown by molecular beam epitaxy on semi-insulating GaAs substrates in the (013) direction with ZnTe buffer layers (500 A thick) and CdTe (5 μm thick). On a CdTe buffer a 49 A thick HgTe QW was grown, surrounded by 300g thick $Hg_{0.24}Cd_{0.76}Te$ barrier layers. The bandgap of the structure is about 50 meV at T = 4.2 K, and the residual hole density is $7 \cdot 10^{10}$ cm^{-2}. The PL studies were performed using a Bruker Vertex 80v Fourier spectrometer operating in the step-scan mode. The measurements were carried out in a closed-cycle optical cryostat with temperature range of 20–150 K. A silicon bolometer cooled to 4.2 K was used as a detector. Optical excitation was carried out by a continuous laser with a wavelength of 808 nm. The maximum laser power was 300 mW.

III. Experiment results

Figure 1 shows the PL spectra of under study, measured at 30 K at different pump powers in the range from 3 to 300 mW. The quanta energy for interband transitions in such a structure at a temperature of 30 K is about 450 cm^{-1}. It can be seen that in all spectra there is a PL band from 50 to 400 cm^{-1}, separated by narrow dips in three lines: 50–160 cm^{-1} (line 1), 160–250 cm^{-1} (line 2) and 250–400 cm^{-1} (line 3). Fig. 1 shows that at high excitation intensity (100 and 300 mW), the fourth PL line appears at 450–600 cm^{-1} (line 4).

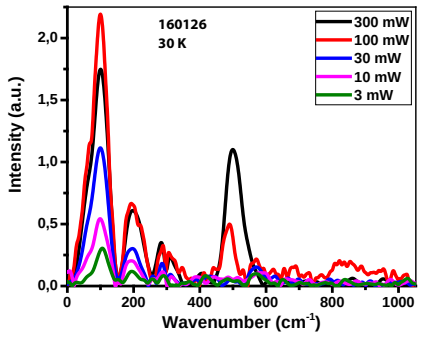

Fig. 1. The PL spectra of sample under study ($HgTe/Hg_{0.24}Cd_{0.76}Te$ 49 A thick QW) measured at 30 K and a source power from 3 to 300 mW.

As the power of the exciting radiation increases, the position of the 1–3 PL bands does not change, and the signal intensity changes non-monotonically. Fig. 1 shows that the amplitude of lines 1–3 grows as the pump power increases from 3 to 100 mW, but when the source intensity increases to 300 mW, the amplitude of the line 1 starts to decrease. The intensity of the short-wavelength band 4 increases with the source power, while the position of the long-wave front of this band remains unchanged.

Figure 2 shows the PL spectra of the studied sample, measured at a fixed source power (300 mW), but at different temperatures. As the temperature rises, the intensity of the PL bands decreases, while the position of the bands 1–3 does not change. Band 4 shifts towards high energy quanta suggesting that band 4 should be associated with interband transitions. Indeed, it is well known [4] that the band gap in the structure under study should increase with temperature. The 1–3 PL bands, however, do not shift with temperature, and, on the contrary, are associated with carrier transitions between states bound to a certain band. Previously, such long wavelength PL bands were associated with transitions involving mercury vacancies [4].

IV. Interpretation of the Measured PL Spectra

The mercury vacancy is a double acceptor and can be found in three charge states: a neutral A^0 center with two holes, an A^{-1} center with one hole and an A^{-2} center without any holes. The PL occurs due to the radiative transitions of holes from the valence band to the acceptor states. One can think of such transitions as the capture of holes to the acceptor centers: either the capture of a hole to a A^{-2} center with the emission of a photon forming an A^{-1} center or the capture of a hole to an A^{-1} center with the emission of a photon forming an A^0 center. A^0 center, cannot capture the holes; therefore, such centers do not participate in PL. The calculation shows that the long-wavelength PL lines 1-3 can be associated with the capture of free holes on the states of neutral mercury vacancies. Band 4, which is associated with interband transitions, appears when the power of the exciting source increases. At the same time, the signal in the long-wavelength bands falls. This may be due to the fact that, under weak excitation, electrons from the conduction band transfer to neutral states of mercury vacancies (A^0 centers) in a nonradiative manner. The resulting A^{-1} centers are contribute to PL. However, at a certain source power, most of the A^0 centers are filled with electrons, i.e. the number of final states for nonradiative transitions from the conduction band decreases. As a result, electrons begin to recombine with holes from the valence band radiatively. With an increase in the pump power, such electron transitions are getting more intense, while the number of holes in the valence band that can be captured to A^{-1} centers decreases, and thus the signal of the impurity PL decreases.

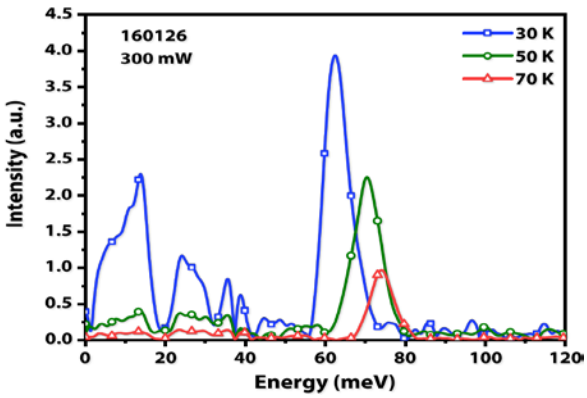

Fig. 2. The PL spectra of sample under study, measured under 300 mW excitation at different temperatures

V. Conclusions

In this work, the THz PL spectra of HgTe / CdHgTe QW heterostructures. The long-wavelength lines in the PL spectra, whose position does not change with temperature, are associated with the capture of free holes on the states of neutral mercury vacancies. Non-monotonic dependence of the impurity PL signal on the power of the exciting source has been observed. It is shown that it is due to the saturation of the number of partially ionized mercury vacancies with increase in pumping intensity.

Acknowledgments

This work was financially supported by RFBR Grants ## 17-02-00898, 18-02-0062, 19-02-00827, 18-32-00628.

References

[1] I.V. Altukhov, E.G. Chirkova, V.P. Sinis, M.S. Kagan, Yu.P. Gousev, S.G. Thomas, K.L. Wang, M.A. Odnoblyudov and I.N. Yassievich. Appl. Phys. Lett., **79**, 3909 (2001).

[2] M.S. Kagan, I.V. Altukhov, V.P. Sinis, S.G. Thomas, K.L. Wang, K.L. Chao, I.N. Yassievich. Thin Solid Films, **380**, 237 (2000).

[3] S. G. Pavlov, H.-W. Hübers, E. E. Orlova, R. Kh. Zhukavin, H. Riemann, H. Nakata, V. N. Shastin, physica status solidi (b), **235**, 126 (2003).

[4] V. V. Rumyantsev, D. V. Kozlov, S. V. Morozov, M. A. Fadeev, A. M. Kadykov, F. Teppe, V. S. Varavin, M. V. Yakushev, N. N. Mikhailov, S. A. Dvoretskii, and V. I. Gavrilenko, Semicond. Sci. Technol. **32**, 095007 (2017).

[5] D. V. Kozlov, V. V. Rumyantsev, S. V. Morozov, M. A. Fadeev, A. M. Kadykov, M.S, Zholudev, V. S. Varavin, M. V. Yakushev, N. N. Mikhailov, S. A. Dvoretskii, V. I. Gavrilenko, F. Teppe, Semiconductors, **50**, 1662 (2016).

[6] D. V. Kozlov, V. V. Rumyantsev, S. V. Morozov, M. A. Fadeev, A. M. Kadykov, V. S. Varavin, N. N. Mikhailov, S. A. Dvoretskii, V. I. Gavrilenko, F. Teppe, JETP, **154**, 1690 (2018) (in Russian).

Time-Domain Terahertz Faraday Spectroscopy of the 3D Topological Insulator HgTe

F. Bayer, W. Beugeling, R. Schlereth, H. Buhmann, L. W. Molenkamp, T. Kiessling

Physikalisches Institut, Universität Würzburg Am Hubland, Würzburg, Germany

E-Mail: florian.bayer@physik.uni-wuerzburg.de

Abstract – We present a high precision TD-THz Faraday spectrometer and first results on optical transitions in strained bulk mercury telluride layers. Our results are well described by eight band $k \cdot p$ perturbation theory and open the way to disentangle surface and bulk contributions to the magneto-optical response.

Keywords – TD-THz spectroscopy, HgTe strained bulk, topological insulator, $k \cdot p$ calculations

I. Introduction

Topological insulators are a special material class that has insulating properties in the bulk but hosts topologically protected conducting surface states [1, 2]. Due to the spin-momentum locking these surface states give rise to novel physics which currently attract huge research interest [3, 4]. Mercury telluride (HgTe) based heterostructures stand out for their exceptionally well controlled properties as representatives of that material class [5].

We employ high precision polarization sensitive time domain THz Faraday-Kerr spectroscopy to investigate the magneto-electric properties of bulk and surface states. The obtained data is compared to $k \cdot p$ perturbation theory [6, 7] results.

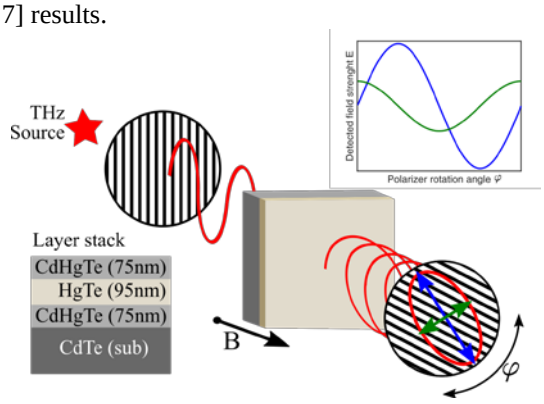

Fig. 1. Detection principle: Incident linear polarization will generally change to an elliptical one. Magnetic field is oriented parallel to the THz propagation (Faraday configuration). (Upper Insert) Projection on the orthogonal polarization basis spanning up the ellipse will generate a modulated signal at the detector when the polarizer is rotated. Phase sensitive demodulation is used to measure intensities and phase difference for both basis. (Lower Insert) Layer stack of the sample.

II. Experimental details

We employ a home built time domain THz spectrometer to measure polarization of THz radiation with very high precision. It employs InGaAs/InAlAs Auston switch type antennas as pulsed emitter and detector units. Both antennas are activated by a sub 100 femtosecond laser pulse. The 1550 nm Er doped fiber laser source has a pulse repetition rate of 100 MHz. Varying the delay time between emitter and detector activation yields the time resolved electric field of the linear polarized THz pulse.

Optical polarization is measured with lock-in techniques based on a fast rotating polarizer. Typical standard deviation is determined to be well below 0.1 degrees in a frequency range from 0.2 to 1.6 THz.

Samples are mounted in an optical bath cryostat with variable temperature insert, providing access to a temperature range from 1.5 to 300 K at magnetic fields up to 10 T. Windows and lenses are made from the THz transparent material TPX.

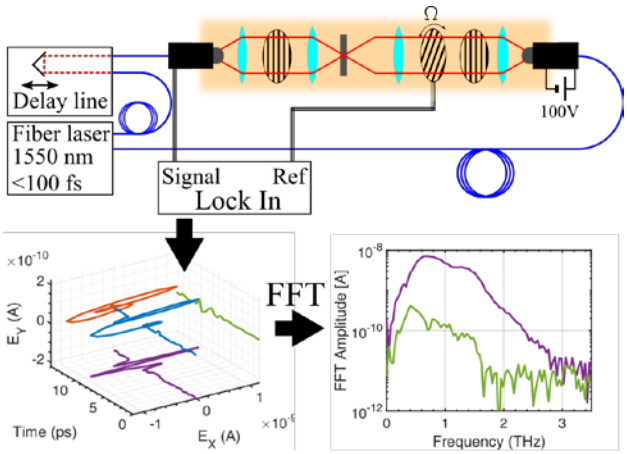

Fig. 2. Schematic of the setup's key components. The THz beam path is purged by dry nitrogen. Insets show an acquired signal in time and frequency domain.

HgTe samples are MBE grown thin films. The layer stack is depicted in Fig. 1 and consists of a 600 µm thick CdTe substrate and a 95 nm HgTe layer sandwiched between two 75 nm CdHgTe buffer layers. DC transport characterization shows the samples are n type with a carrier density on the order of $2 \cdot 10^{11}$ cm^{-2}.

III. Methods

The polarization resolved time domain signal is transformed to the frequency domain by Fast-Fourier-Transformation[8]. The frequency span is determined by the THz pulse itself, whereas the resolution is limited by

the duration between transmitted and reflected pulses (in thin films caused by the sample substrate).

Intensity ratio and phase shift of the two spectrally resolved orthogonal polarization components give the rotation and ellipticity of the THz pulse after it left the sample.

Interaction of THz radiation with states in the sample leads to distinct signatures in rotation and ellipticity spectra. The center frequency of these signatures equals the energetic difference between (bulk) band states at optically allowed transitions.

Eight band $k \cdot p$ perturbation theory is used to calculate the band structure of HgTe depending on an applied magnetic field[7]. It also yields the strength of the transition matrix element for optical excitations between states of two different bands. The strength of the measured rotation signature will be proportional to the transition matrix element and the difference in spin polarization between both bands.

IV. Results and Discussion

Figure 3 shows the position of optical transitions extracted from Faraday rotation experiments in comparison to the transition rate calculated by eight band $k \cdot p$ perturbation theory at the Γ-point. Data and simulation results show qualitative agreement but exhibit some systematic deviations at higher magnetic field values. These differences can be ascribed to the contribution of k states further away from the Γ-point that mix in more with stronger fields.

For the charge carrier densities of our samples we can conclude that bulk carriers dominate the obtained signal. Our method enables us to assign clear origins on the contribution of different Landau Levels to the complex low energy magneto-optical spectra of strained HgTe thin films, providing us with a powerful tool to put clear constraints on the window of parameter space in which the topological surface states dominate the magneto-optical response.

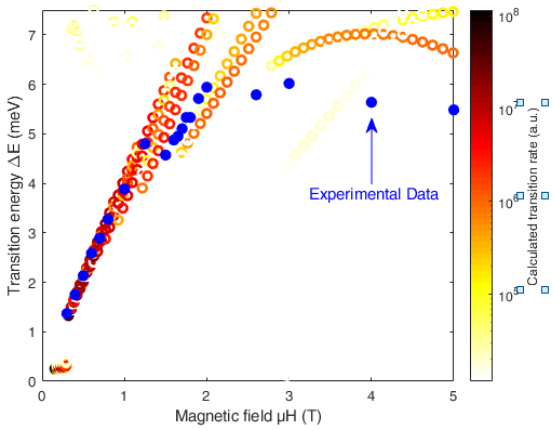

Fig. 3. Calculated vs. measured energetic positions of bulk state optical transitions in a 70 nm thick strained HgTe layer at sample temperature of 2 K.

Acknowledgments

This work was financially supported by the DFG CRC 1170.

References

[1] B. Yan and S. C. Zhang, *Reports on Progress in Physics* **75**, 096501 (2012).
[2] X. L. Qi and S. C. Zhang, *Reviews of Modern Physics* **83**, 1057 (2011).
[3] X. L. Qi *et al.*, *Physical Review B* **78**, 195424 (2008).
[4] W. K. Tse and A. H. MacDonald, *Physical Review B* **82**, 161104 (2010).
[5] C. Brüne et al., *Physical Review Letters* **106**, 126803 (2011).
[6] H. Luo and J. K. Furdyna, *Physical Review B* **41**, 5188 (1990).
[7] E. G. Novik *et al.*, *Physical Review B* **72**, 035321 (2005).
[8] C. M. Morris *et al.*, *Opt. Express* **20**, 12303 (2012).

2D Colloids in Rotating Electric Fields: Tunable Interactions and Particle-Resolved Studies of Generic Phenomena

E. V. Yakovlev[1], N. P. Kryuchkov[1], K. A. Komarov[1], and S. O. Yurchenko[1]

[1] Bauman Moscow State Technical University, Moscow 105005, Russia
E-mail: st.yurchenko@mail.ru

Abstract – We discuss self-assembly and phase transitions in colloidal suspensions of particles with tunable interaction in rotating external electric field. The self-assembly allows to prepare high-quality monolayer photonic crystals as well as to examine phase transitions and interfacial phenomena in condensed matter at the level of individual particles.

Keywords – soft matter, colloids, self-assembly, tunable interactions, particle-resolved studies

I. Introduction

Tunable interactions in colloidal suspensions attract great interest because of their fundamental and practical importance. Self-assembly in suspensions of micro- and nanoparticles is a common phenomenon in nature, and it can be used to create new materials in photonics and catalysis. Apart from practical interest, colloidal systems are of great importance for fundamental studies, since they mimic molecular-like behavior and can be used in particle-resolved studies of generic phenomena in condensed matter.

II. Tunable Self-Assembly

In this work, we present our results of theoretical and experimental studies of two-dimensional colloidal systems wherein attractive interparticle interactions are induced and controlled by external rotating electric fields [1–2]. By placing two-dimensional colloidal systems in external electric field rapidly rotating in the plane of system, we can effectively induce interparticle attraction, which is long-range, tunable, and non-pair. Magnitude of the interaction is controlled by electric field, evolution of the system can be visualized using video-microscopy, that opens a way for particle-resolved studies of such fundamental phenomena as self-assembly, condensation and evaporation, melting and crystallization, spinodal decomposition, dislocation dynamics, nucleation and coalescence, surface phenomena etc. In the framework of presentation, we consider (i) novel experimental technology for particle-resolved studies of colloidal suspensions in rotating electric field and its optimal experimental regimes [1]; (ii) tunable pair and many-body interactions [3]; (iii) ability to create complex crystals and quasi-crystalls [4]; (iv) a novel method for experimental data post-processing [2]; (v) phase diagram of a monodisperse system in external fields [5].

An experiment illustrated in Fig. 1 presents snapshots of colloidal cluster self-assembled in rotating electric fields at different voltages applied to the electrodes. One can see that, by applying in-plane rotating electric field of increasing magnitude, particles can be arranged in large liquid-like cluster, which crystallizes with increase in the voltage. The crystal melts if the field is turned off, and, thus, the whole process of self-assembly is repeatable. Note that the field-controlled reversibility distinguishes this mechanism of self-assembly from other mechanisms, typically driven by chemical reactions.

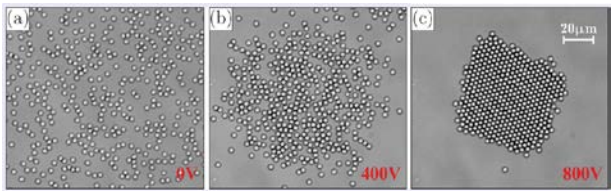

Fig. 1. A demonstration experiment with a self-assembly of colloidal particles in external rotating electric fields: Panels (a)–(c) depict about 450 silica particles of 2.12 μm diameter, undergoing a transition from a (dilute) fluid state to a crystalline state upon a gradual increase of the field (U = 0, 0.4, 0.8 kV, respectively). In this experiment, the field was rotating with the frequency of ν = 30 kHz.

III. Conclusions

Our results open novel prospects in fundamental and applied studies of many-body systems with tunable interactions, and, therefore, will be of interest to wide range of scientists in the fields of soft matter, physical chemistry, chemical physics, photonics, and materials science.

Acknowledgments

Project is supported by RSF Grant #17-19-01691.

References

[1] E.V. Yakovlev, K.A. Komarov, K.I. Zaytsev, N.P. Kryuchkov, K.I. Koshelev, A.K. Zotov, D.A. Shelestov, V.L. Tolstoguzov, V.N. Kurlov, A.V. Ivlev, S.O. Yurchenko, Sci. Rep. **96**, 043201 (2017).
[2] P.V. Ovcharov, N.P. Kryuchkov, K.I. Zaytsev, and S.O. Yurchenko, J. Phys. Chem. C.**121**, pp 26860–26868 (2017).
[3] K.A. Komarov, N.P. Kryuchkov, and S.O. Yurchenko, Soft Mat. **14**, 9657-9674 (2018).
[4] N.P. Kryuchkov, S.O. Yurchenko, Y.D. Fomin, E.N. Tsiok, and V.N. Ryzhov, Soft Mat. **14**, 2152-2162 (2018)
[5] N.P. Kryuchkov, F. Smallenburg, A.V. Ivlev, S.O. Yurchenko, and H. Löwen, J. Chem. Phys. **150**, 104503 (2019).

Prospects for Human Brain Glioma Diagnosis Using Terahertz Spectroscopy and Imaging

K. I. Zaytsev[1,2], I. N. Dolganova[2,3], N. V. Chernomyrdin[1,2], G. M. Katyba[2,3], A. A. Gavdush[1,2], V. E. Karasik[2], V. N. Kurlov[3], G. A. Komandin[1], A. A. Potapov[4], I. V. Reshetov[5], V. V. Tuchin[6]

[1] Prokhorov General Physics Institute of the Russian Academy of Sciences, Moscow 119991, Russia
[2] Bauman Moscow State Technical University, Moscow 105005, Russia
[3] Institute of Solid State Physics of the Russian Academy of Sciences, Moscow 119991, Russia
[4] Burdenko Neurosurgery Institute, Moscow 125047, Russia
[5] Sechenov First Moscow State Medical University, Moscow 119991, Russia
[6] Saratov State University, Saratov 410012, Russia

E-mail: kirzay@gmail.com

Abstract – We studied an ability for the intraoperative diagnosis of human brain tumors using terahertz (THz) technology. For this aim, we applied THz pulsed spectroscopy to measure a dielectric response of gelatin-embedded human brain gliomas *ex vivo*, featuring different grades, according to the World Health Organization (WHO). We demonstrated an ability for differentiation between intact (healthy) tissues and gliomas of all WHO grades relying on the data of THz pulsed spectroscopy. We found that a THz response of edematous tissues in a perifocal region is similar to that of a tumor, which might lead to a false positive errors of diagnosis. The results of our study justify a prospect of THz technology in the intraoperative delineation of tumor margins, in order to ensure its gross-total resection. Finally, we developed novel THz instruments, which would help us to integrate THz diagnosis into a modern neurosurgical workflow.

Keywords – terahertz pulsed spectroscopy, human brain tumors, glioma, glioblastoma, intraoperative neurodiagnosis, terahertz waveguides, terahertz solid immersion microscopy.

I. Introduction

Applications of THz technology in non-invasive, least-invasive, or intraoperative diagnosis of malignancies with different nosology and localization attract considerable interest thanks to the endogenous character of differences observed between healthy and pathological tissues in THz spectra and images; particularly, abnormal vascularity and edema leads to increased water content and, thus, to increased refractive index and absorption coefficient of a tumor [1]. Most recently, an ability to use THz spectroscopy and imaging in the intraoperative diagnosis of brain tumors was studied in several papers involving various models of gliomas from rats and mice *ex vivo* [2–5]. Meanwhile, capabilities of THz technologies in the intraoperative diagnosis of human brain gliomas still remain undiscovered.

II. Results

In our work, we studied an ability for the intraoperative diagnosis of human brain gliomas using THz technology [6, 7]. For this aim, we measured THz dielectric response (optical constants) of gelatin-embedded human brain gliomas *ex vivo* with different WHO grades using THz pulsed spectroscopy. The gelatin embedding of tissues was used in order to preserve them from hydration / dehydration and, thus, to sustain their THz response unaltered for a couple of hours after the surgery, as compared to that of freshly-excised tissues *ex vivo*.

The results of our study demonstrate increased values of THz optical constants of WHO grade I–IV gliomas, as compared to that of intact (healthy) tissues of the human brain. Meanwhile, the THz response of edematous tissues in a perifocal region is close to that of a tumor; thus, edematous tissues might be recognized as a tumor, leading to the false positive results of diagnosis. Our experiments allows for objectively uncover a prospective of THz spectroscopy and imaging for the intraoperative diagnosis of human brain tumors [6].

Considering current developments on THz spectroscopy and imaging, we analyzed an ability to transfer THz technology into a neurosurgical practice. In our opinion, a single-point measurements of tissues using THz spectroscopy or reflectometry could be integrated into modern neurosurgical probes, in order to perform simultaneous intraoperative diagnosis of tissues *in vivo* with further removal of tumorous tissues by their aspiration. For example, sapphire shaped crystals [8] provide a favorable combination of physical and mechanical properties to serve simultaneously as key elements of modern neouroprobes [9, 10] and as highly-efficient THz waveguide [11, 12]. Furthermore, THz technology could aid express-histology of excised tissues *ex vivo*, which is nowadays widely-applied intraoperatively to correct the surgery. For example, THz solid immersion microscopy could be used for rapid detection of the brain tumors margins in freshly-excised tissues with the spatial resolution up to 0.15λ [13, 14].

III. Conclusions

In conclusion, in our research, we studied a dielectric response of gelatin-embedded human brain gliomas of WHO grade I–IV using THz pulsed spectroscopy. We found statistical differences between the response of

intact tissues and tumors; thus, highlighting a prospect of THz technology in the intraoperative neurodiagnosis.

ACKNOWLEDGMENTS

This work was financially supported by the Russian Science Foundation (RSF), Project # 18-12-00328.

REFERENCES

[1] O.A. Smolyanskaya, N.V. Chernomyrdin, A.A. Konovko, K.I. Zaytsev, I.A. Ozheredov, O.P. Cherkasova, M.M. Nazarov, J.-P. Guilleti, S.A. Kozlov, Yu.V. Kistenev, J.-L. Coutaz, P. Mounaix, V.L. Vaks, J.-H. Son, H. Cheon, V.P. Wallace, Yu. Feldman, I. Popov, A.N. Yaroslavsky, A.P. Shkurinover, V.V. Tuchin, *Progress in Quantum Electronics* **62**, 1 (2018).

[2] S.J. Oh, S.-H. Kim, Y.B. Ji, K. Jeong, Y. Park, J. Yang, D.W. Park, S.K. Noh, S.-G. Kang, Y.-M. Huh, J.-H. Son, J.-S. Suh, *Biomedical Optics Express* **5**, 2837 (2014).

[3] K. Meng, T.-N. Chen, T. Chen, L.-G. Zhu, Q. Liu, Z. Li, F. Li, S.-C. Zhong, Z.-R. Li, H. Feng, J.-H. Zhao, *Journal of Biomedical Optics* **19**, 077001 (2014).

[4] S. Yamaguchi, Y. Fukushi, O. Kubota, T. Itsuji, T. Ouchi, S. Yamamoto, *Scientific Reports* **6**, 30124 (2016).

[5] Y.B. Ji, S.J. Oh, S.-G. Kang, J. Heo, S.-H. Kim, Y. Choi, S. Song, H.Y. Son, S.H. Kim, J.H. Lee, S.J. Haam, Y.M. Huh, J.H. Chang, C. Joo, J.-S. Suh, *Scientific Reports* **6**, 36040 (2016).

[6] A.A. Gavdush, N.V. Chernomyrdin, K.M. Malakhov, S.-I. T. Beshplav, I.N. Dolganova, A.V. Kosyrkova, P.V. Nikitin, G.R. Musina, G.M. Katyba, I.V. Reshetov, O.P. Cherkasova, G.A. Komandin, V.E. Karasik, A.A. Potapov, V.V. Tuchin, K.I. Zaytsev, *Journal of Biomedical Optics* **24**, 027001 (2019).

[7] N.V. Chernomyrdin, A.A. Gavdush, S.-I.T. Beshplav, K.M. Malakhov, A.S. Kucheryavenko, G.M. Katyba, I.N. Dolganova, S.A. Goryaynov, V.E. Karasik, I.E. Spektor, V.N. Kurlov, S.O. Yurchenko, G.A. Komandin, A.A. Potapov, V.V. Tuchin, K.I. Zaytsev, *Proceedings of SPIE* **10716**, 107160S (2018).

[8] G.M. Katyba, K.I. Zaytsev, I.N. Dolganova, I.A. Shikunova, N.V. Chernomyrdin, S.O. Yurchenko, G.A. Komandin, I.V. Reshetov, V.V. Nesvizhevsky, V.N. Kurlov, *Progress in Crystal Growth & Characterization of Materials* **64**, 133 (2018).

[9] I.A. Shikunova, D.O. Stryukov, S.N. Rossolenko, A.M. Kiselev, V.N. Kurlov, *Journal of Crystal Growth* **457**, 265 (2017).

[10] I.A. Shikunova, K.I. Zaytsev, D.O. Stryukov, E.N. Dubyanskay, V.N. Kurlov, Proceedings of SPIE **10411**, 104110Q (2017).

[11] K.I. Zaytsev, G.M. Katyba, V.N. Kurlov, I.A. Shikunova, V.E. Karasik, S.O. Yurchenko, *IEEE Transactions on Terahertz Science & Technology* **6**, 576 (2016).

[12] G.M. Katyba, K.I. Zaytsev, N.V. Chernomyrdin, I.A. Shikunova, G.A. Komandin, V.B. Anzin, S.P. Lebedev, I.E. Spektor, V.E. Karasik, S.O. Yurchenko, I.V. Reshetov, V.N. Kurlov, M. Skorobogatiy, *Advanced Optical Materials* **6**, 1800573 (2018).

[13] N.V. Chernomyrdin, A.O. Schadko, S.P. Lebedev, V.L. Tolstoguzov, V.N. Kurlov, I.V. Reshetov, I.E. Spektor, M. Skorobogatiy, S.O. Yurchenko, K.I. Zaytsev, *Applied Physics Letters* **110**, 221109 (2017).

[14] N.V. Chernomyrdin, A.S. Kucheryavenko, G.S. Kolontaeva, G.M. Katyba, I.N. Dolganova, P.A. Karalkin, D.S. Ponomarev, V.N. Kurlov, I.V. Reshetov, M. Skorobogatiy, V.V. Tuchin, K.I. Zaytsev, *Applied Physics Letters* **113**, 111102 (2018).

High Resolution THz Spectrometer Based on Semiconductor Devices for Medical Diagnostics

V. L. Vaks[1], M. B. Chernyaeva[1], E. G. Domracheva[1], S. I. Pripolzin[1], A. A. Yablokov[1], W. Knap[2,3]

[1] Terahertz spectrometry department of IPM RAS, IAP RAS, Nizhny Novgorod, Russia
[2] Laboratoire Charles Coulomb, University of Montpellier, Montpellier, France
[3] Institute of High Pressure Institute Physics, Polish Academy of Sciences, Warsaw, Poland

E-mail: vax@ipmras.ru

Abstract – The capabilities of high resolution THz spectrometry for analysis of exhaled breath and biological liquid vapors as a multicomponent gas mixture are demonstrated. The THz spectrometer based on semiconductor devices is realized. The results of its application for detection of the important biomarkers (acetone, alcohols) in exhaled breath and urine vapors of various patients and healthy people are presented.

Keywords – terahertz spectroscopy, high resolution, exhaled breath

I. Introduction

Now the actual problems in the gas analysis field have been associated with development of novel methods of medical diagnostics. The analysis of composition of human exhaled air allows diagnosing some of pathology processes on the base of measuring concentrations of substance-markers, which are products of physiological and biochemical processes in human organism [1]. The investigations of biological compounds (DNA, proteins, sugars, etc) in solid and gaseous phases as well as liquids are important for medical and biological tasks. During the variety of instrumental methods of analysis of exhaled air and biological compounds the spectroscopic methods including the spectroscopy of THz frequency range are more prospective. The THz technique can also be used for studying of biological tissues based on dielectric function analysis.

II. THz Spectrometer

The essence of a nonstationary spectroscopy is as following: interaction of electromagnetic radiation with ensemble of absorbing molecules results in induction of macroscopic dipole. After a radiation impact is over, absorbed energy is reradiated coherently at the frequency of molecular transition. The operation of nonstationary spectrometers can be realized in a phase switching [2] or fast passage regime [3]. The advantages of the method involve frequency resolution about 10 kHz and high sensitivity [4]. To provide a required resolution, spectroscopic characteristics of a radiation sources are to meet requirements for measurements at Doppler line resolution (~10^{-6}) and frequency measurements with accuracy 10^{-8}÷10^{-10} from the carrier frequency [5].

Spectrometer was elaborated completely with using semiconductor technique and with using the phase switching (PS) approach (Fig. 1). PS spectrometer has the highest sensitivity among the spectrometers detecting the electromagnetic radiation power transmitted through the cell with multicomponent gas mixture.

Fig. 1. High resolution THz spectrometer based on semiconductor devices

The parameters of this spectrometer are presented in the Table 1:

Table 1. Parameters of THz spectrometer

Frequency range	110÷170 GHz
Sensitivity	$3*10^{-9}$ cm^{-1}
Accuracy of frequency tuning	10^{-7}
Accuracy of measuring the amplitudes	10^{-3}

The spectrometer radiation source is elaborated with using the frequency multiplier by 12 ("VDI"). The output power is 3÷5 mW that provides the spectroscopic measurements in quartz evacuated cells with length up to 3 m.

The signal of reference synthesizer ("Luft Research") of 9.17÷14.17 GHz frequency range is fed to multiplier input. This synthesizer is controlled by built-in processor. The phase modulator hopping the phase of reference signal at 15° is placed between synthesizer and multiplier. After multiplying the phase shift is 12 times increased up to 180° that provides the PS mode.

The radiation transmits through the gas cell to detector receiving the signal of 110÷170 GHz. This detector ("VDI") has high sensitivity, low noise and high speed at output.

The signal after detector is amplified by two channel amplifier. At the first channel there is the direct current amplification and signal is fed to slow analog-digital converter (ADC) of receiver. This signal carries the information about incident power. At the second channel of frequency band from hundreds Hz to tens MHz the signal with information about the amplitude of gas absorption line is amplified. After amplification the signal is fed to fast ADC.

The modulation frequency is set with using the digital circuit of signal storage and is synchronized at clock frequency of fast ADC. The modulation frequency is equal to some hundreds kHz that agrees with absorption line width for optimal interaction with gas absorption line.

The storage summarizes the digital signals from the fast ADC output during some thousands cycles. After accumulation this signal is fed to processor where its digital and program processing is carried out for decreasing the parasitic signal and noises of receiving system.

Spectrometer can operate in some modes:

1. The first mode is frequency sweeping mode where the frequency range, frequency step and time of signal storage at every step are set. This mode is used for search of unknown lines.

2. The second mode is the mode of observing the amplitude of absorption line at the central line frequency where the storage time at one measurement is set and dependence of the amplitude on time is shown graphically. The measurement time can be varied from ms to s. This mode is used for observing the dynamics of absorption line during the chemical or thermal reaction.

3. There is the mode of long storage signal at the central frequency of absorption line. It is the mode of the most sensitivity of spectrometer. The sensitivity reaches the value of 10^{-10} cm^{-1}. This mode is used for analytical studies.

4. The last mode is the mode of indication of time process of relaxation the absorption line at central frequency. In this mode the line amplitude and the line width can be determined with using the time of signal relaxation. This mode is used for tuning the spectrometer to maximal signal and for detection and suppression of parasitic signals.

III. Analysis of exhaled breath and urine vapors

The investigations of acetone, methanol and ethanol concentration in the breath samples of 10 conditionally healthy volunteers and 12 diabetes patients (before and after taking the medicines) are carried out. For reference measurements breath samples of 10 healthy volunteers (5 men, 32 ± 3 years old; and 5 women, 40 ± 3 years old) were collected. The group of 12 patients with type-2 diabetes comprised 7 women with a mean age of 55 ± 5 years and 5 men with a mean age of 60 ± 5 years. The precision of concentration determination is 5%. There is found an increased concentration of acetone in the diabetes patients' breath in comparison with healthy volunteers. Furthermore variation of the acetone concentration before and after taking the medicines is revealed. At the same time changing of the methanol and ethanol concentrations is found to be insignificant. The absorption line of hydrogen sulfide (H_2S) at the frequency of 168.762 GHz is detected in the exhaled breath of two diabetes patients [6, 7]. The H_2S concentration in the exhaled breath of diabetes patient is increased about 4 times in comparison with that one in exhaled breath of a healthy volunteer. Moreover, the comparison of acetone content in exhaled breath and urine vapors of 12 patients with type-2 diabetes was carried out. The results of acetone concentration measurements are summarized in Table 2. The analysis of acetone content in exhaled breath and urine vapors has shown the significantly increased concentration of acetone in urine vapors of the patients.

Table 2. The content of acetone in samples of exhaled breath and urine vapors

Patient	$N_{acetone}$ in exhaled breath, ppm	$N_{acetone}$ in urine vapors, ppm
1	13	22
2	18	105
3	17	135
4	30	50
5	7	72
6	24	104
7	26	73
8	21	94
9	6	36
10	10	97
11	9	90
12	8	94

IV. Conclusions

The high resolution THz spectrometer based on semiconductor devices meets all requirements for non-invasive medical diagnostics. Although, its sensitivity is less than that of the best chromatograph-mass spectrometers, the THz spectrometer ensures other advantages. The most important one is unique and reliable identification of a gas marker in contrast to chromatograph-mass spectrometers which can give only identification probability. Furthermore, the THz spectrometer is not expensive, easy-to-use and doesn't require high-priced components and consumables.

The present work demonstrates capabilities of high resolution THz spectrometry for analysis of exhaled breath and biological liquid vapors as a multicomponent gas mixture. The THz spectrometer based on semiconductor devices has been successfully applied for detection of the important biomarkers (acetone, alcohols) in exhaled breath and urine vapors of various patients and healthy people. The lack of optimal "electronic nose",

which can be used both for laboratory research and diagnostics in clinics, is often underlined and discussed in literature and international conferences on breath research. From this point of view, the approach, presented in this paper, could be promising to become the optimal "electronic nose" for non-invasive medical diagnostics of social important diseases analyzing the content of exhaled breath and biological liquids vapors.

ACKNOWLEDGMENTS. This work was carried out in the framework of state targets N 0035-2014-0206 and financially supported by the Russian Foundation for Basic Research (grant N 18-42-520050 r_a_povoljie, N 17-00-00184 KOMFI, N18-52-16017).

REFERENCES

[1] E. V. Stepanov, *Diode Laser Spectroscopy and Analysis of Biomarker Molecules* (Moscow: Fizmatlit, 2009) [in Russian].

[2] V. L. Vaks, A. B. Brailovsky, V. V. Khodos, Millimeter Range Spectrometer with Phase Switching – Novel Method for Reaching of the Top Sensitivity, in *Infrared & Millimeter Waves*, 20 (5), 883–896, 1999.

[3] V. V. Khodos, D. A. Ryndyk, V. L. Vaks, Fast passage microwave molecular spectroscopy with frequency sweeping, in *Eur. Phys. J. Appl. Phys.*, 25, 203-208, 2004.

[4] V. Vaks, High-Precise Spectrometry of the Terahertz Frequency Range: The Methods, Approaches and Applications, Journal of Infrared, Millimeter and Terahertz Waves, 33(1), pp. 43-53, 2012.

[5] V. L. Vaks, E. G. Domracheva, E. A. Sobakinskaya, M. B. Chernyaeva, Exhaled breath analysis: physical methods, instruments, and medical diagnostics, in *Physics – Uspekhi*, 57(7), pp. 684-701, 2014.

[6] H. M. Pickett. E. A. Cohen, B. J. Drouin, J. C. Pearson. Submillimeter, Millimeter, and Microwave Spectral Line Catalog. JPL Molecular Spectroscopy California Institute of Technology. http://spec.jpl.nasa.gov/ftp/pub/catalog/catform.html, (2003).

[7] C. P. Endres, S. Schlemmer, P. Schilke, J. Stutzki, H. S. P. Müller, The Cologne Database for Molecular Spectroscopy, CDMS, in the Virtual Atomic and Molecular Data Centre, VAMDC, in *J. Mol. Spectrosc*. **327,** pp. 95–104, (2016).

Graphene-based van der Waals Heterostructures towards a New Type of Terahertz Quantum-Cascade Lasers

T. Otsuji[1], D. Yadav[1], S. Boubanga-Tombet[1], T. Watanabe[1], A. A. Dubinov[2], and V. Ryzhii[1,3,4]

[1] Research Institute of Electrical Communication, Tohoku University, Sendai, Japan
[2] Institute for Physics of Microstructures, RAS, Nizhny Novgorod, Russia
[3] Institute of Ultra-High Frequency Semiconductor Electronics, Russian Academy of Sciences, Moscow, Russia
[4] Center for Photonics and 2D Materials, Moscow Institute of Physics and Technology, Dolgoprudny, Russia

E-mail: otsuji@riec.tohoku.ac.jp

Abstract – Current-injection pumping in graphene makes carrier population inversion enabling lasing and/or amplification of terahertz (THz) radiation. We've recently demonstrated single-mode THz lasing at 100K in graphene-channel transistor laser structures. Introduction of a gated double-graphene-layered (G-DGL) van der Waals heterostructure is a promising rout to further increase operation temperature and radiation intensity via plasmon- and photon-assisted quantum-mechanical tunneling. We have proposed a cascading of the G-DGL unit element working as a new type of THz quantum-cascade lasers.

Keywords – graphene, terahertz, van der Waals hetero-structure, quantum cascade laser,

I. Introduction

Current-injection or optical pumping makes population inversion of graphene carriers enabling lasing and/or amplification of terahertz (THz) radiation [1–3]. We've recently demonstrated 1-8-THz broadband amplified spontaneous THz emission as well as single-mode THz lasing at 5.2 THz both at 100K [3]. Introduction of a gated double-graphene-layered (G-DGL) van der Waals (vdW) heterostructure in which gate-bias tuned THz radiation emission is obtained via plasmon- and/or photon-assisted quantum-mechanical resonant tunneling is a promising rout to further increase operation temperature as well as output intensity [4–5]. This paper reviews recent advances in the research for graphene-based vdW heterostructures towards a new type of terahertz quantum-cascade lasers (QCLs).

II. Device Structure and Physics

Figure 1 depicts the G-DGL structure. A gated double-graphene-layer (G-DGL) nanocapacitor is the core shell under consideration, in which a thin tunnel barrier layer is sandwiched by outer graphene layers at both sides. A dc bias voltage between the GLs induces charges (electrons (hole) in the negatively (positively) biased GL), resulting in band-offset energy between the GLs. The gate bias voltage can tune the band offset. By applying a pertinent gate bias voltage emission or absorption of photons/plasmons, whose energy coincides with the band offset, can assist the inter-GL resonant tunneling.

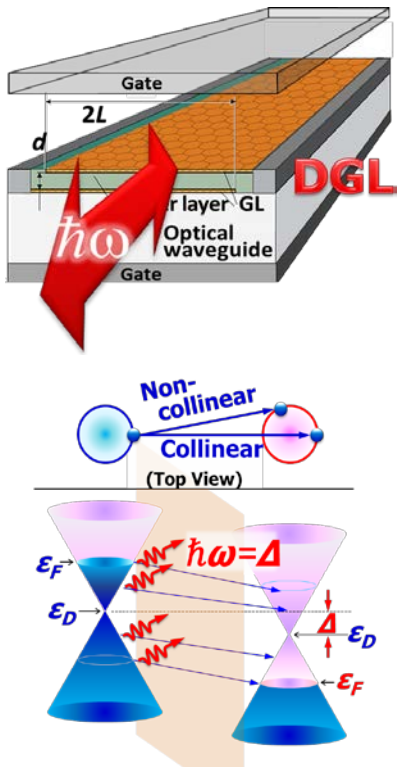

Fig. 1. G-DGL structure (left) and inter-GL tunneling via photon and plasmon emission (right)

We experimentally demonstrated the proof of concept of such an operation mechanism [6]. The DGL can excite symmetric optical and anti-symmetric acoustic coupled plasmon modes in the GLs (Fig. 2). The important physics behind is the acoustic plasmon modes in the DGL, which can modulate the band-offset between the GL, giving rise to modulation of the inter-GL-layer resonant tunneling. This can dramatically enhance the quantum efficiency and resultant THz gain by orders for dc electric power to THz photo radiation power conversion in comparison with that for a simple graphene-channel transistor laser structure [5].

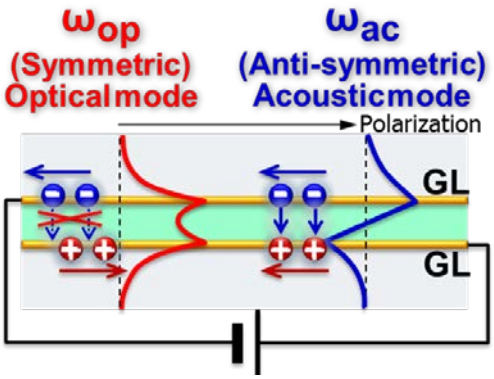

Fig. 2. Plasmon modes in a DGL structure

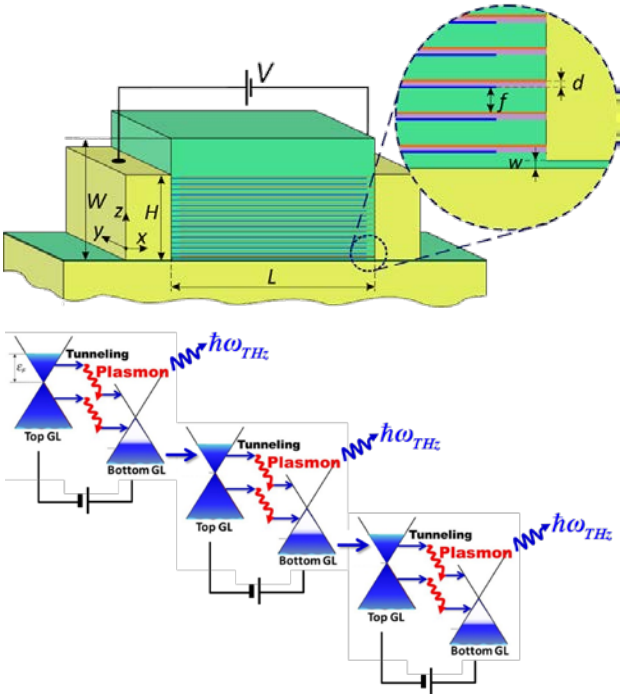

Fig. 3. G-DGL cascade structure (top) and quantum-cascade THz photon emission via plasmon-assisted inter-GL tunneling cascade.

We have proposed a cascading of the G-DGL unit element working as a new type of THz QCLs (Fig. 3) [7]. The laser cavity can be structured along with the in-plane direction of the G-DGL mesa structure. The vertical G-DGL cascade structure can enlarge the mode field of the THz photon radiation to match the free-space impedance. Numerical analyses demonstrate further increase of the quantum efficiency of THz lasing by order of magnitude in comparison with a single G-DGL structure. Experimental verification is now under going.

III. Conclusions

Recent advances in the research for graphene-based vdW heterostructure G-DGLs towards a new type of THz QCLs were reviewed. Theoretical modeling and numerical analyses reveal its impressive performance advancement far beyond the level for a simple graphene-channel laser transistor structure. The graphene-based vdW-QCL device process technology consisting of continuous layer-by-layer stacking or heteroepitaxy of the atomically thin 2D materials followed by standard semiconductor integrated device processes is now being improved. This will make it possible to experimentally demonstrate the device operation in the very near future.

Acknowledgments

We thank Dr. Dmitry Svintsov, Prof. Vladimir Ya Aleshkin, Prof. Vladimir Mitin, Prof. Maxim Ryzhii, and Prof. Michael S. Shur for helpful discussions. This work was supported by JSPS KAKENHI (#16H06361), Japan.

References

[1] V. Ryzhi et al., *J. Appl. Phys.* **101**, 083114 (2007).
[2] M. Ryzhii and V. Ryzhii, *Jpn. J. Appl. Phys.* **46,** L151 (2007).
[3] D. Yadav et al., *Nanophoton.* **7**, 741-752 (2018).
[4] V. Ryzhii et al., *Opt. Exp.* **21**, 31569 (2013).
[5] D. Svintsov et al., *Phys. Rev. B* **94**, 115301 (2016).
[6] D. Yadav et al., *2D Mat.* **3**, 045009 (2016).
[7] A.A. Dubinov et al., *Opt. Exp.* **24**, 279307 (2016).

Long Wavelength Stimulated Emission in HgTe/CdHgTe Quantum Well Heterostructures

S. V. Morozov[1,2], V. I. Gavrilenko[1,2], V. V. Rumyantsev[1,2], M. A. Fadeev[1,3], V. V. Utochkin[1,2], N. S. Kulikov[1,2], A. A. Dubinov[1,2], V. Ya. Aleshkin[1,2], N. N. Mikhailov[4,5], S. A. Dvoretskii[4], F. Teppe[3], C. Sirtori[6]

[1] Institute for Physics of Microstructures of Russian Academy of Sciences, Nizhny Novgorod, 603950, Russia
[2] Lobachevsky State University, Nizhny Novgorod, 603950, Russia
[3] L2C, UMR CNRS 5221, Montpellier University, 34095 Montpellier, France
[4] A.V. Rzhanov Institute of Semiconductor Physics, Siberian Branch of Russian Academy of Sciences, Novosibirsk, 630090, Russia
[5] Novosibirsk State University, Novosibirsk, 630090, Russia
[6] Laboratoire de Physique de l'Ecole Normale Supérieure, Paris, 75005, France

E-mail: more@ipmras.ru

Abstract – We report on stimulated emission at wavelengths up to 31 µm from HgTe/HgCdTe quantum well heterostructures with wide-gap HgCdTe dielectric waveguide, grown by molecular beam epitaxy on GaAs(013) substrates. For SE at 31 µm the mode localization is achieved due to Reststrahlen band in GaAs substrate. The mitigation of Auger processes in structures under study is exemplified and the promising routes towards the 35–50 µm wavelength range, where HgCdTe lasers may be competitive to currently known emitters, are discussed. Summing up, for the first time SE for dielectric waveguide HgTe/HgCdTe quantum well heterostructures in the spectral range "closed" for QCLs based on AIIIBV semiconductors is obtained.

I. Introduction

The problem of developing compact terahertz (THz)/long-wavelength emitters is one of the hottest topics in the applied physics. There is a spectral «gap» λ = 20–60 µm in which no quantum cascade lasers (QCLs) are available (except for several specific wavelengths near 20 µm) since the majority of QCLs are based on AIIIBV materials with strong lattice absorption in this spectral region. Among compact semiconductor lasers, only lead salt lasers cover a part of this gap (up to 48 µm), but their figures of merit are rather low due to formidable problems in growth technology. On the other hand, modern MBE delivers high quality HgTe/CdHgTe quantum well (QW) heterostructures. They allow tailoring the bandgap between hole and electron levels in QW to λ = 20–60 µm and have TO phonon frequencies lying lower than this range. In addition, HgTe/CdHgTe structures offer strongly non-parabolic dispersion law resembling that of graphene but with a finite gap and finite carrier masses which set a considerable energetic threshold for Auger processes.

II. Results and Discussion

We report on stimulated emission (SE) at wavelengths up to 31 µm at 8 K and temperatures up to 245 K at 2.8 µm (Fig. 1) from HgTe/HgCdTe QW heterostructures with wide-gap HgCdTe dielectric waveguide, grown by MBE on GaAs(013) substrates with ZnTe and CdTe buffers.

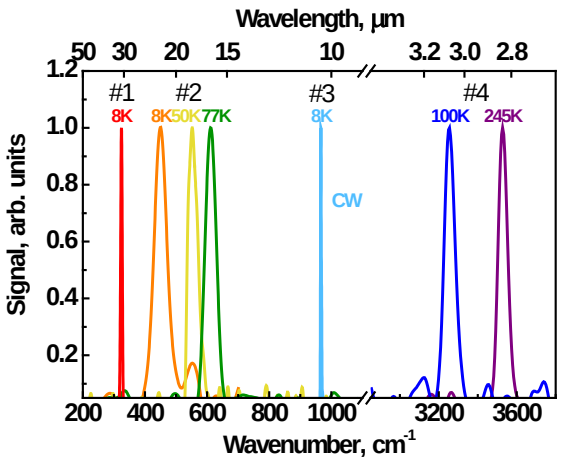

Fig. 1. SE spectra at different temperatures obtained under pulsed (sample #1, #2 – λ_{exc} = 10.6 µm; sample #4 – λ_{exc} = = 1.5 µm) and cw (sample #3, λ_{exc} = 0.9 µm) optical excitation.

As it was shown before, the mitigation of Auger recombination (AR) in structures under study allows achieving long-wavelength/THz operation. Futhermore, Peltier cooled operation is feasible in lasers based on such structures, making them of interest for spectroscopy applications in the atmospheric transparency window from 3 to 5 µm (Str. #4, Fig. 1). We demonstrate SE from multiple HgTe/CdHgTe QW heterostructures under pulsed/continuous-wave optical pumping at wavelengths as long as 11–31 µm, which is more than fourfold increase over previous works[1-3] (Str. #1–3, Fig. 1).

We claim that significant increase in operating temperature (by ~80 K) and wavelength was achieved due to suppression of AR in the studied structures. We show that additional strain in a QW structure modifies the carrier dispersion in the valence band in such a way that it leads to suppression of AR. More precisely, the side maxima arising in the valence band when the QW width is increased proved to be a critical issue for radiative properties of the structure since they enhance AR. At the

same time, implementing narrow HgTe/CdHgTe moves these maxima "aside" and increase the operating wavelength of HgCdTe based lasers to > 20 μm range. Obtained experimental results are in good agreement with theoretical calculations of energetic threshold for AR performed in the framework of Kane 8x8 Hamiltonian model (see Ref. 4, 5).

Recalculated to the equivalent threshold current, the threshold is only 500 A/cm^2 for λ = 20 μm at 8 K – 45 K. In principle, such threshold current density allows the development of continuous wave diode lasers. Eight-band Kane and four-band Bernevig-Hughes-Zhang models were used to calculate radiative and Auger recombination times, respectively. Carrier lifetime measurements agree well with the calculated data. The subnanosecond carrier lifetimes have been explored via the pump-probe measurements of the sample's transmission [3]. For HgCdTe QW with 20 meV, corresponding to 4.8 THz frequency, the carrier lifetime was over 100 ps for a carrier density of 10^{11} cm^{-2} which is sufficient to achieve population inversion. One can estimate the threshold pumping intensity to be 10 kW/cm^2 for an optically pumped laser exploiting such QWs as an active media. It is important to note that in the long-wavelength range the best results were achieved using "cold" excitation with pulsed (100 ns) CO_2 laser (λ = 10.6 μm). At shorter wavelengths λ ~ 10 μm the excitation threshold power (λ_{exc} ~ 2 μm) was shown to be as low as 120 W/cm^2 [2] and the SE was obtained even at CW excitation (λ ~ 0.9 μm, Fig. 1, sample #3).

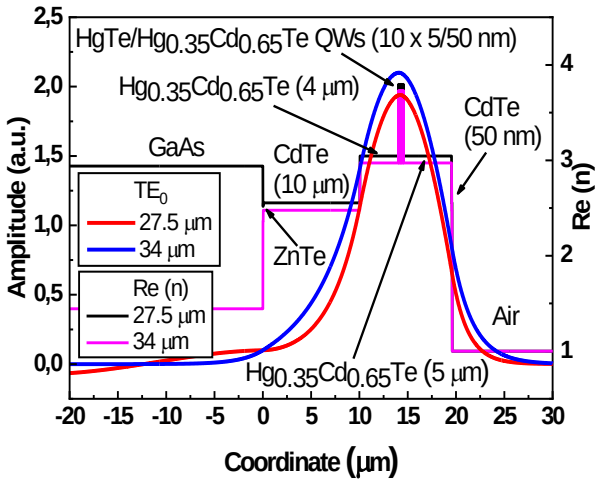

Fig. 2. Real part of refractive index distribution and TE_0 mode localization for 27.5 μm and 34 μm wavelengths for typical structure design.

For the case of SE at 31 μm the mode localization was achieved by utilizing Reststrahlen band in GaAs substrate (Fig. 2). This is a peculiar waveguide design which works in the range of the frequencies of optical phonons in GaAs (from 32 to 36 μm in the wavelength equivalent). Strong reflection of GaAs in this spectral range results into sufficient mode localization from the side of substrate, comparable to that of dielectric waveguide (Fig. 2).

III. Conclusions

For the first time the SE was obtained in HgTe/HgCdTe quantum well heterostructures in the spectral range "closed" for QCLs based on AIIIBV semiconductors: up to 22.3 μm for dielectric waveguide and up to 31 μm for "Reststrahlen band mode localization".

Acknowledgments

This work was supported by the Russian Science Foundation under Grant # 17-12-01360.

References

[1] S.V. Morozov, V.V. Rumyantsev, M.A. Fadeev, M.S. Zholudev, K.E. Kudryavtsev, A.V. Antonov, A.M. Kadykov, A.A. Dubinov, N.N. Mikhailov, S.A. Dvoretsky, and V.I. Gavrilenko, Stimulated emission from HgCdTe quantum well heterostructures at wavelengths up to 19.5 μm. Appl. Phys. Lett., 2017. 111(19): p. 192101.

[2] S.V. Morozov, V.V.Rumyantsev, A.M. Kadykov, A.A. Dubinov, K.E. Kudryavtsev, A.V. Antonov, N.N. Mikhailov, S.A. Dvoretskii, V.I. Gavrilenko. Long wavelength stimulated emission up to 9.5 μm from HgCdTe quantum well heterostructures. Appl. Phys. Lett., 2016, Vol. 108, P. 092104.

[3] S. Ruffenach, A. Kadykov, V. V. Rumyantsev, J. Torres, D. Coquillat, D. But, S. S. Krishtopenko, C. Consejo, W. Knap, S. Winnerl, M. Helm, M. A. Fadeev, N. N. Mikhailov, S. A. Dvoretskii, V. I. Gavrilenko, S. V. Morozov, and F. Teppe. HgCdTe-based heterostructures for terahertz photonics. APL MATERIALS 5, 035503 (2017).

[4] F. Teppe, M. Marcinkiewicz, S. S. Krishtopenko, S. Ruffenach, C. Consejo, A. M. Kadykov, W. Desrat, D. But, W. Knap, J. Ludwig, S. Moon, D. Smirnov, M. Orlita, Z. Jiang, S. V. Morozov, V.I. Gavrilenko, N. N. Mikhailov, S. A. Dvoretskii. Temperature-driven massless Kane fermions in HgCdTe crystals. Nature Communications, 2016, Vol. 7, P. 12576.

[5] A.M. Kadykov, S.S. Krishtopenko, B. Jouault, W. Desrat, W. Knap, S. Ruffenach, C. Consejo, J. Torres, S.V. Morozov, N.N. Mikhailov, S.A. Dvoretskii, and F. Teppe. Temperature-Induced Topological Phase Transition in HgTe Quantum Wells. Physical Review Letters 120, 086401 (2018).

Universal Simple Weak Barrier SL-Based Broad Band Tunable Sources at Any THz?

A. A. Andronov[1], A. V. Ikonnikov[1], K. V. Maremianin[1], V. I. Pozdniakova[1], Y. N. Nozdrin[1], A. A. Marmalyuk[2], A. A. Padalitsa[2], M. A. Ladugin[2], V. A. Belyakov[3], I. V. Ladenkov[3], A. G. Fefelov[3]

[1] Institute for Physics of Microstructures RAS, Nizhny Novgorod, Russia, andron@ipmras.ru
[2] Sigm-Plus, Moscow, Russia
[3] Federal Government Unitary Enterprise "Salut", Nizhny Novgorod, Russia

E-mail: andron@ipmras.ru

Abstract – Discussion of recently demonstrated (2.6–2.8) THz lasing in simple weak barrier GaAs-GaAlAs super lattices and ways of moving such approach to higher THz frequencies are presented. We argue that such lasing scheme represent simple universal way for creation of interband hetero lasers at "any THz frequency".

Keywords – semiconductor superlattices, THz sources

I. Introduction

Recently we have demonstrated THz lasing in GaAs-GaAlAs weak barrier simple superlattices (SLs) on transition between Wannier-Stark levels (WSLs) separated several periods apart[1–4] (Fig. 1). These results are supported also by the non equilibrium Green function simulations[5]. The upper lasing level here is (alike in the second lasing scheme in Kazariniv and Suris work[6]) ground WSL in SL well. This feature provides "universal" population inversion and is a basis for low change of the lasing parameters with rise in temperature[1]: we have demonstrate survival of the SL lasing at least for T > 100 K at about 3 THz. Also due to weak superlattice barriers there is no problem with electric field domain formation under transport: lasing occurs at positive differential conductivity voltage region.

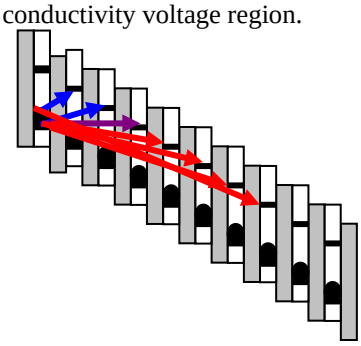

Fig. 1. Scheme of optical absorbing and emissive transition from highly occupied ground levels (balls) to almost empty second levels in wells in weak barrier SL under bias.

All these demonstrations were made on very low doped non optimized SLs. But, on the other hand, with very low number of initial test wafers. And in this contribution we discuss the optimization and possibility to extend this type of lasing to higher frequency (to say about 10–30 THz). We have design of a SL wafer appropriate for such frequencies and hope we will be able to present some observation results at the Symposium. Below we first remind and comment published[1-5] results on THz lasing to establish base for further discussion. Then dimension less SL parameters to move such SL lasers to higher frequency will be presenting

II. THz stimulated emission in SLs

The chips studied in Refs. 3, 4 were made of two SL wafers 1755 and 2239 (grown by MOCVD) and consist of n-type very low doped ($N \approx 4\cdot10^{14}$ cm^{-3}) GaAs-GaAlAs SL of 1000 periods with period d about 170 A and metal (Au) – n$^+$ – SL – n$^+$ – metal (Au) disk resonator 0.2, 0.5 and 1 mm in diameter. The disc resonator was chosen to have whispering gallery modes (WGMs) with low emission losses and dense (quasi continuum) spectrum, keeping in mind possible low amplification as a result of the SL low doping.

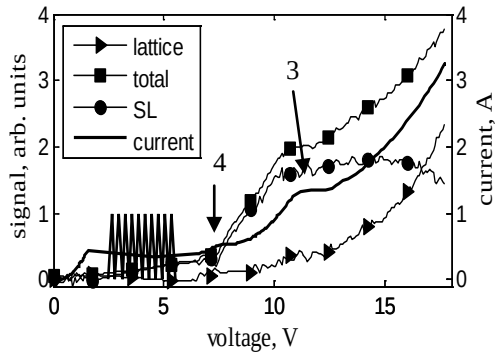

Fig. 2. Ge(Ga) detector signals and current of the 1755 SL chip. Arrows with numbers 3 and 4 indicate voltages for resonant tunneling through 3 and 4 SL period.

The current-voltage (I-V) chip curve consists of ohmic part followed by DC NDC region with current oscillation (at 2–5 V), almost constant current plateau region and rising current portion due to inter miniband tunneling where the THz emissions are observed (Fig. 2). The emission observations are performed by the broad band Ge(Ga) THz detector placed in liquid helium nearby chip subject to pulsed voltage of about 10 μs in duration. The detector registers both the emission from electrons in SL and (at high voltage) also the emission due to heated

chip lattice. The detector signal due to electrons in the SL shows sharp rise at about 7.5 V after the current plateau and gradual rise in current. The emission frequency bands were measured by the absorbing filter employed cyclotron resonance in the mercury-cadmium-telluride quantum well in magnetic field of superconductor solenoid placed between the chip and the Ge(Ga) detector. At voltage 8.6–10 V frequencies are higher (by about 15% – Fig. 4) of the Bloch frequency ω_B while at 12–18 V are lower ω_B. By using the longer voltage pulses (up to 500 μs) chip heating above 78 K was found (by comparing end pulse current with the one at 78 K and higher temperatures measured at short pulses) with eventually no change of detector signal produces by electrons in the SL. This points to prospect for elevated temperature and CW operation.

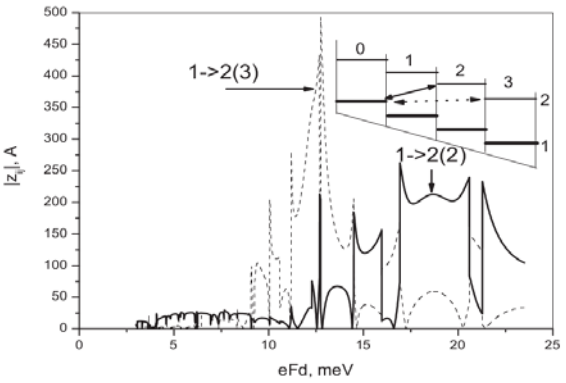

Fig. 3. Matrix element X for transitions shown in the inset. Full and doted lines represent 1 → 2(2) and 1 → 2(3) transitions. Peaks marked 1 → 2(2) and 1 → 2(3) correspond to levels alignment.

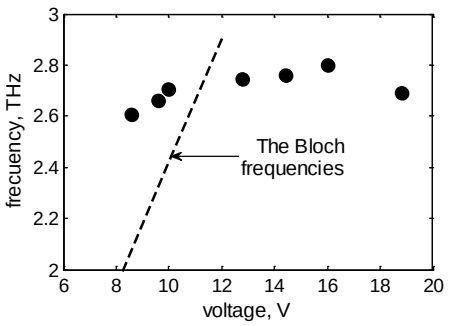

Fig. 4. Emission frequencies versus voltage applied to a SL chip

Arrows in Fig. 2 indicate position of broad tunneling resonance with numbers indicate number of periods involved in the tunneling. Lasing nearby tunneling through 4 periods imply that that well between which transition between first and second level down applied voltage is at about 700 A. Remarkable figure important for moving approach to higher frequency. We think that this is also due to (as indicated in Fig. 3) that transition matrix element has side resonances out off position of tunneling resonance due to broad nature of the resonances providing lasing in broad region of applied voltage (Figs. 2, 4).

The SLs studied are by no means optimal to produce the THz stimulated emission. The optimization must include higher SL doping (up to $N \approx 1–5\cdot10^{15}$ cm^{-3}), lower thicknesses of n+ contact layers (to about 0.1 μm) and decrease of SL barrier strength. Already these changes should permit to decrease two-three times number o SL periods needed for the lasing.

III. PROTECT FOR SL LASING BEYOND 3 THZ

Change of the emission frequency can be achieved by change in SL period with appropriate change in barrier strength: higher frequencies need shorter period, higher barrier strength and higher applied fields. The shorter period SLs should be less sensitive to possible suppression[5] of two-three-four period tunneling by increased doping. This change can be performed on basis of dimension-less parameters of the discussed SLs. The parameters are

$$\Delta = S\cdot V_0\frac{a}{d},\ F = S\cdot eEd,\ \Omega = S\cdot\hbar\omega,$$
$$S = \left(\frac{\hbar^2}{2md^2}\right)^{-1}, \qquad (1)$$

V_0 is the band offset at barrier boundary, a is the barrier thickness, d is the SL period, m is effective mass and ω is the transition frequency. For GaAs-GaAlAs $V_0 = 0.87\,x$, x –Al fraction. Also important parameter is oscillator strength of lasing transitions

$$f = \hbar\omega\left(\frac{\hbar^2}{2mX^2}\right)^{-1} = \frac{2mX^2\omega}{\hbar}, \qquad (2)$$

X is the transition matrix element (Fig. 3). It is proportional period d. But frequency $\omega \sim 1/d^2$. So f does not change for the same dimension less parameters. Another important parameter is Zener tunneling field E_t between first and second miniband in superlattice. Applied field should not be substantially lower than E_t because in such case NDC and electric field domains can emerge. Zener tunneling probability is

$$P = \exp\left(-\frac{mdV_g^2}{\hbar^2 eE}\right) = \exp\left(-\frac{E_t}{E}\right), \qquad (3)$$

where V_g is minigap. In our superlattice $V_g = 2V_0a/d$ and $E_t = m\ d\ V_g^2\ /(\ \hbar^2 e)$; or the dimension-less parameter is $F_t = \Delta^2/2$. The presented above data (Fig. 2) show that lasing transition can take place in the SLs between levels separated about 700 A. For high frequencies such distance may involve transition between levels separated 5–6 and higher periods apart. This permits to decrease voltage needed for lasing at 10–30 THz as it is demonstrate at about 3 THz in Fig. 2, 4: decrease of voltage does not change substantially lasing frequency. Also it must be emphasized that SL wafers (grown by MOCVD) are substantially simple than that of QCLs. Their fabrication had required only a couple of test wafers grown.

Other material system could be promising for the THz SL sources studied. In particular the THz sources based on simple weak barrier SLs made of GaN-AlGaN heterostructures look excitingly promising for the THz sources with high temperature operation (presumably up to room temperature) due to a very high polar optical phonon energy (nearby 1000 K). This heterostructure system was used recently for creation of 5–7 THz QCLs.

ACKNOWLEDGMENTS. This work was done under IPM RAS Goscontract № 0035-2019-0021-C-01.

REFERENCES

[1] A. A. Andronov, E. P. Dodin, D. I. Zinchenko et al., *Quantum Electronics* **40**, 400 (2010).

[2] A. A. Andronov, E. P. Dodin, Yu. N. Nozdrin et al., *JETP Leters* **102,** 207 (2015).

[3] A. A. Andronov, A.V. Ikonnikov, K.V. Maremianin et al., *Semiconductors,* **52**, 431 (2018).

[4] A. A. Andronov, A.V. Ikonnikov, K.V. Maremianin et al., *IOP Conf. Series*, (2019) to be published.

[5] D. O. Winge, D. O. Frianckie, A. Wacker, *AIP Advances* **6,** 045025. (2016).

[6] R. F. Kazarinov and R. A. Suris, *Sov. Phys. Semicond.* **5**, 707 (1971).

Tunneling Conductivity in Superlattices with Electric Domains

I. V. Altukhov[1], M. S. Kagan[1], S. K. Paprotskiy[1], N. A. Khvalkovskiy[1], I. A. Kohn[1], I. S. Vasil'evskii[2], A. N. Vinichenko[2], N. D. Il'inskaya[3], A. A. Usikova[3], A. N. Baranov[4], R. Teissier[4]

[1] Kotel'nikov Institute of Radio Engineering and Electronics, Russian Ac. Sci., Moscow, Russia
[2] National Research Nuclear University MEPhI, Moscow, Russia
[3] Ioffe Physico-Technical Institute, Russian Ac. Sci., St. Petersburg, Russia
[4] IES, Université Montpellier 2, CNRS, Montpellier, France

E-mail: kagan@cplire.ru

Abstract – Tunneling current in GaAs/AlAs and InAs/AlSb short-period superlattices (SLs) at the domain formation was studied. The current hysteresis observed at sweep-up and sweep-down of the bias was explained by a transition from moving to static domain regime. The series of maxima in the current-voltage characteristics in the range of moving domains is supposed to be due to optical phonon assisted tunneling through barriers inside the triangular domain. The large photoresponse to interband illumination at the domain formation was found.

Keywords – superlattices, electrical domains, tunneling

I. Introduction

The electron transport in semiconductor SLs has been studied in detail in recent decades[1, 2], mainly in connection with the predicted amplification of Bloch waves, which can make it possible to create tunable sources of THz radiation. The main hindrance to the Bloch wave amplification is the formation of electrical domains owing to the static negative differential conductivity (NDC) arising in superlattices at resonant tunneling between confined states in neighboring quantum wells[1-3]. The domain formation in superlattices eliminates the Bloch gain. In this work the studies of tunneling electronic transport in short-period GaAs/AlAs and InAs/AlSb superlattices (SLs) with electric domains are presented.

II. Experimental

Two kinds of MBE grown SLs have been used: GaAs-based and InAs-based. GaAs/AlAs SLs consisted of 100 periods of 4 nm GaAs quantum wells (QWs) divided with 2 nm AlAs barriers. InAs/AlSb SLs consisted of 60 periods of 4.5 nm InAs QWs and 3.5 nm AlSb barriers. SLs were positioned between heavily doped ($\sim 10^{19}$ cm^{-3}) n^+ cap layer and n^+ substrate ($2*10^{18}$ cm^{-3}). GaAs quantum wells (QWs) were Si doped with concentration of $2*10^{17}$ cm^{-3}. The ring-shaped mesa structures with the diameters from 10 to 15 μm and 0.8 to 1.5 μm widths formed the distributed THz cavity with resonant frequencies corresponding to the free-space wavelengths from ~110 to ~170 μm. The most efficiently excited electromagnetic modes in such ring cavities should be polarized across the layers and propagated along the ring perimeter. It was succeed to observe the self-excitation of some of our cavity SLs[4] (probably with good quality factors).

In this work, the tunneling conductance of the SLs with electrical domains arisen because of the negative differential resistance of the SLs in some voltage range. Triangular voltage pulses with a sweep-up times of 0.5 to 10 μs and sweep-down times up to 100 μs applied to the sample were used to record I-V curves.

III. Results and discussion

Fig. 1 shows the current-voltage characteristics of GaAs/AlAs SL. The step-like decrease in current (up to 50%) at some threshold voltage is caused by moving domain formation. The current rise at the voltage above the threshold (after the domain formation) indicate the triangular form of the domain[5] (inset in Fig. 1). Indeed, the charge of domain boundaries (domain "walls"') needed to ensure the electric field difference between the regions of high and low fields can be estimated from experimental I-V curves. It is of the order of $5*10^{18}$ cm^{-3} being one order more than the donor concentration. The negatively charged domain wall is formed by free electrons accumulated mostly in one QW. The positive charge of another domain wall is due to ionized donors with the concentration being one order less ($2*10^{17}$ cm^{-3}).

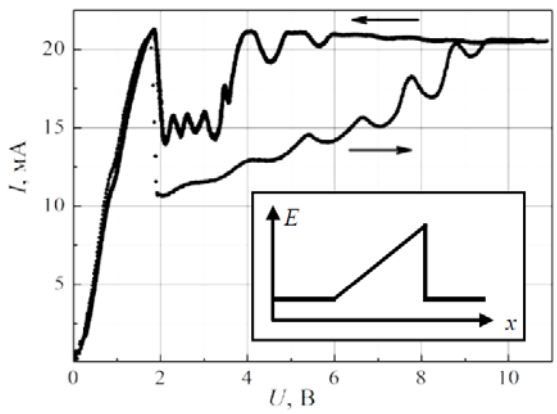

Fig. 1. Current–voltage characteristics of the GaAs/AlAs SLs at sweep-up and sweep-down of voltage. Inset: field distribution inside the moving domain (schematically).

So, the positive charge is formed by uniformly distributed completely ionized donors resulting in a linear growth of the field and the triangular form of the domain. (Here and in what follows, to analyze domain characteristics, we use the analogy with the Gunn effect.)

The hysteresis in current at sweep-up and sweep-down of voltage can be explained by a transition from moving to static field domain and back. The evidence of static domain formation is the current saturation which appears at voltage sweep-up when the current reaches the value at the maximum of the I-V curve. The current saturation region at sweeping voltage down widens to lower voltages. The reason is the transition from moving to static domain occurs at higher voltage than the back transition at sweep-down of voltage.

As the saturated current corresponds to the maximum of I-V curve, the high field domain (in n-type material) should be attached to the anode (see, e.g., Ref. 6). The different case was observed in InAs/AlSb SLs (Fig. 2). The current rise begins *after* current saturation caused by static domain formation. In this case the saturated current should correspond to the minimum of I-V characteristic of initially uniform sample and the static domain should be near the cathode. The high-field domain position – at the anode or cathode – depends on contact conditions[6].

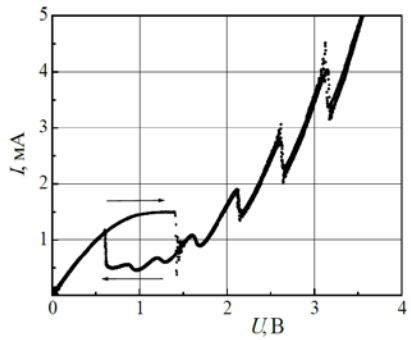

Fig. 2. Current–voltage characteristics of the InAs/AlSb SL

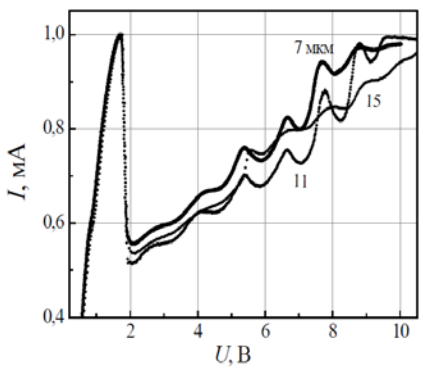

Fig. 3. Current–voltage characteristics of the GaAs/AlAs SL for resonant cavities of different diameters

Let's discuss now the origin of the maximums in I-V characteristic observed both for GaAs/AlAs and InAs/AlSb SLs. These maxima don't be connected with the resonant cavities; their periods coincide practically for the samples with 7, 11 and 15 μm diameters of ring contacts (Fig. 3). Note that the maximums were absent in cavity structures where self-excitation has been observed[4]. However, the period of maximums changed appreciably with temperature. The I-V curves of a GaAs/AlAs SL at the temperatures from 74 to 412 K are presented in Fig. 4.

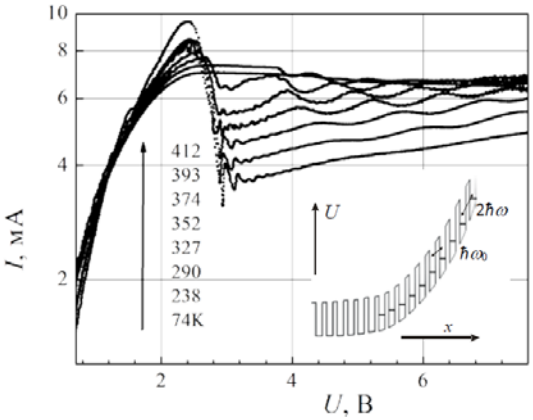

Fig. 4. Current–voltage characteristics of the GaAs/AlAs SL at different temperatures. Inset: scheme of optical phonon assisted tunneling inside the domain.

We attribute the origin of the maximums to the optical phonon assisted tunneling between quantum wells inside the triangular domain. The maximal field in the domain can be estimated by means of Poisson equation considering the field distribution inside the domain to be continuous. Then, it is possible to estimate the potential and so the potential energy difference between QWs on the apex of the triangular domain. The energy difference turns out to be of the order of 200 meV at the applied voltage of 10 V. So, the tunneling assisted by optical phonon emission is possible when the energy difference between neighboring QWs is multiple of optical phonon energy $\hbar\omega_0$. Outside of this resonance, the tunneling current should be considerably decreased. The scheme of these tunneling transitions is shown in the inset in Fig. 4.

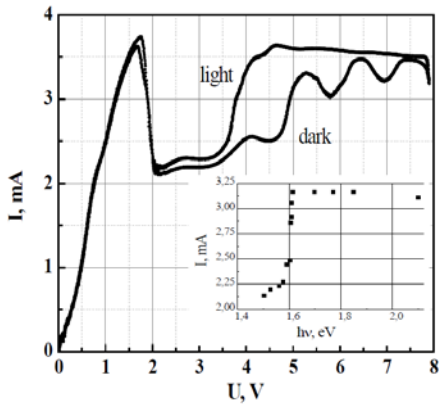

Fig. 5. Current–voltage characteristics of the GaAs/AlAs SL in the dark (lower curve) and under band-to-band illumination (upper curve). Inset: spectrum of photocurrent.

One more effect we refer to the triangular form of the domain is the influence of illumination. At the conditions of electric domains formation, the rather weak illumination (with a LED or a filament bulb) considerably increases the tunneling current in GaAs/AlAs SLs. Figure 5 shows

the current-voltage characteristics with and without illumination. The photocurrent at the domain regime could reach 50% of the dark current. While it was several orders of magnitude less at voltages below the threshold one (before the domain formation) as the free carrier concentration excited with light was considerably less than Si donor concentration.

The measured photocurrent spectrum (the inset in Fig. 5) points to the band-to-band excitation. The spectral long-wavelength cutoff allows us to determine the GaAs QW gap and the energy of first size quantization level. These energies coincide with known values for GaAs QW.

The strong effect of weak illumination is supposed to be due to very small electron concentration inside the triangular domain where donors are completely ionized. The additional concentration of electron-hole pairs created by interband illumination exceeds significantly the stationary concentration inside the domain, which results in a change of space charge at domain boundaries. This leads to a change of domain movement regime. The sufficiently intense illumination could initiate the traveling-to-static domain transition, which becomes apparent in current saturation regions in I-V curves (Fig. 4).

IV. Conclusions

Current-voltage characteristics of GaAs/AlAs and InAs/AlSb short-period superlattices (SLs) was studied at the conditions of domain formation. At forward and backward bias sweep, the current hysteresis and the series of almost voltage-periodic maximums were observed. The current hysteresis can be explained by a transition from moving to static field domain at sweeping the bias up and the return at its sweeping down. The origin of the maximums is attributed to the optical phonon assisted tunneling between quantum wells inside the triangular domain. The maximums are on a background of current rise in the mean which gives evidence of triangular form of the domain with the extended region of completely ionized donors. The large photocurrent under interband illumination is attributed also to triangular domains.

Acknowledgments

This work was carried out in the framework of the state task and supported in part by RFBR projects 16-29-09626, 16-29-03135 and RAS program "Nanostructures: Physics, Chemistry, Biology, Basics of Technology."

References

[1] A. Wacker, *Physics Reports*, **357**, 1 (2002).
[2] L. L. Bonilla, H.T. Grahn, *Rep. Prog. Phys.*, **68**. 577 (2005).
[3] F. Klappenberger, K. N. Alekseev, K. F. Renk, et al., *Eur. Phys. J. B*, **39**, 483 (2004).
[4] I. V. Altukhov, S. E. Dizhur, M. S. Kagan, et al., *JETP Letters*, **103**, 122 (2016).
[5] R. A. Suris, *Sov. Phys. Semicond*., **7**, 1035 (1973).
[6] V. L. Bonch-Bruevich, I. P. Zvyagin, A. G. Mironov, *Domain Electrical Instability in Semiconductors* (Nauka, Moscow, 1972; Consultant Bureau, New York, 1975).

Room Temperature Terahertz HgCdTe-Based Quantum Cascade Laser

A. A. Dubinov[1], A. A. Afonenko[2], D. V. Ushakov[2], V. Ya. Aleshkin[1], R. A. Khabibullin[3]

[1] Institute for physics of microstructures of RAS, Nizhny Novgorod, Russia
[2] Belarusian State University, Minsk, Belarus
[3] Institute of Ultra High Frequency Semiconductor Electronics of RAS, Moscow, Russia

E-mail: sanya@ipmras.ru

Abstract – The simulation and optimization of a terahertz quantum-cascade laser based on narrow-gap HgCdTe quantum wells was carried out. It is shown that for a quantum cascade structure with two $Hg_{0.7}Cd_{0.3}Te$ quantum wells with a thickness of 12.9 and 4.9 nm and with $Hg_{0.4}Cd_{0.6}Te$ barriers with a thickness of 1.9 nm, a gain of 50 cm^{-1} at a frequency of 8.3 THz is achieved at room temperature.

Keywords – terahertz, quantum cascade laser

I. Introduction

Currently, compact sources of terahertz frequency range are in high demand. Quantum cascade lasers (QCLs) based on GaAs/AlGaAs and InGaAs/InAlAs/InP semiconductor heterosystems have achieved the greatest progress in this field [1]. However, the generation of radiation in the frequency range 6–10 THz in QCL based on them is impossible because of the resonant absorption by optical phonons in this frequency range. In HgCdTe heterostructures, the frequency of optical phonons is almost two times less (3.6–5 THz). Therefore, the creation of HgCdTe-based QCL opens up prospects for mastering the range of 6–10 THz. In addition, in the narrow-gap HgCdTe material, the effective electron mass is 2–3 times less than that in the GaAs/AlGaAs based heterosystem, which should favorably affect the increase in the dipole matrix element for laser levels [2].

In the present work, we simulated terahertz QCL on the basis of narrow-gap HgCdTe quantum wells (QWs), calculated its characteristics and determined the optimal design of such QCL.

II. Model

In this work, numerical optimization of HgCdTe-based QCL with a cascade of two QWs was performed. Due to the small band gap of HgCdTe material, the effect of nonparabolicity of the conductivity band is significant. Therefore, calculations of wave functions, matrix elements of dipole transitions, and state energies were carried out using the 3 band *kp* method [3]. The degree of filling of energy levels was found by numerically solving the system of balance equations [4]. The frequency depended gain for intrasubband transitions was calculated in a multilevel approximation according to [5, 6]. Calculations of the current – voltage characteristics and current – power characteristics were performed on the basis of a distributed model for localized states and continuum states [7].

The main task of designing a QCL is to obtain a structure gain in an increasing portion of the current-voltage characteristic. To this end, a scheme with a phonon resonance, when the operating voltage on a single stage is close to the sum of the radiation quant of energy and the energy of a longitudinal optical phonon, was investigated in the work. In this case, a phonon resonance is realized in the structure for a pair of levels. Reducing the voltage below the working level leads to convergence of levels, distance from the resonance, and decrease in the rate of transitions. This should provide a rising branch of the current – voltage characteristic.

III. Results of modeling

To select the structure with the maximum gain, the thickness of the $Hg_{0.4}Cd_{0.6}Te$ barrier layers in the range 1.3–3.9 nm and the $Hg_{0.7}Cd_{0.3}Te$ QWs in the range 5.2–14.9 nm were enumerated. Figure 1 shows the calculations of the levels and wave functions for one of the optimal structures, the layers of which are 1.9/<u>12.9</u>/1.9/<u>4.9</u> nm at a temperature of 300 K. Underlined fonts indicate the thickness of the QWs. The upper laser level is the fundamental level of the structure. The lower laser level is the second level of the structure in two lattice periods. Figure 2 shows the corresponding gain spectrum in an electric field of 24.5 kV/cm.

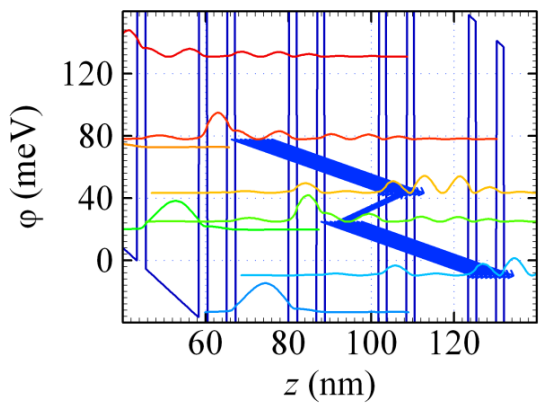

Fig. 1. The zone diagram and squares of the module of wave functions (the number of arrows is proportional to the speed of stimulated transitions between levels, which determine the gain (absorption) at the frequency of 8.3 THz) at a voltage on the cascade 53 mV.

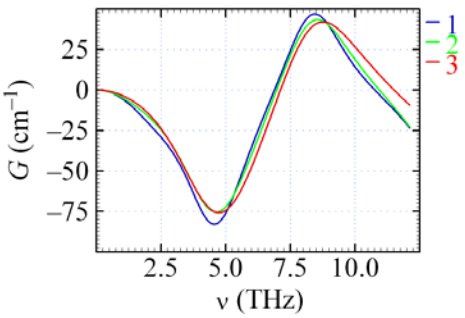

Fig. 2. The gain spectra for different temperatures T = 250 (1), 300 (2), 350 (3) K at a voltage on the cascade 53 mV.

IV. Conclusions

The performed simulations showed that the gain of the optimized structure of terahertz QCL based on narrow-gap HgCdTe QWs reaches 50 cm^{-1} at a frequency of 8.3 THz at room temperature. Note that the calculated gain is sufficient to overcome the losses in the double metal waveguide, usually used for terahertz QCLs [8].

Acknowledgments

This work was financially supported by the Russian Science Foundation (grant № 18–19–00493).

References

[1] M. S. Vitiello et al., *Opt. Exp.* **23**, 5167 (2015).
[2] E. Benveniste et al., *Appl. Phys. Lett.* **93**, 131108 (2008).
[3] C. Sirtori et al. *Phys. Rev. B* **50**, 8663 (1994).
[4] D. V. Ushakov, I. S. Manak. *J. Appl. Specrtoscopy* **74**, 892 (2007).
[5] V. B. Gorfinkel et al. *IEEE J. Quantum Electron.* **32**, 1995 (1996).
[6] D. V. Ushakov, V. K. Kononenko, I. S. Manak. *Quant. Electon.* **40**, 195 (2010).
[7] R. A. Khabibullin et al. *Semiconductors* **52**, 1380 (2018).
[8] D. V. Ushakov et al., *Quant. Electon.* **48**, 1005 (2018).

Polarons in Semiconductor Heterostructures and Their Possible Application in Terahertz Sources

V. G. Popov[1,2], V. G. Krishtop[2], S. G. Chigarev[3], T. I. Ahmedov[3], M. Henini[4]

[1] Infotecs, CSPD, Stariy Petrovsko-Razumovskii proezd, 1/23 b-ing 1, Moscow 127287
[2] Institute of Microelectronics Technology of RAS, Academician Osipyan st, 6,Chernogolovka, Moscow region, 142432
[3] Institute of Radio-Engineering and Electronics of RAS, Vvedenskiy sq. 1, Fryazino, Moscow region 141190
[4] School of Physics and Astronomy of Nottingham University, Nottingham NG7 2RD, UK

E-mail: sokhatiy@gmail.com

Abstract – Polarons forming in polar semiconductors are considered both theoretically and experimentally in resonant tunneling diodes. The polarons are forming by electron coupled to real and virtual LO-phonons. In the case of real LO-phonon the polaron has an singularity in the spectrum at energy of the LO-phonon. In the case of the heterostructure one can have several types of the LO-phonons and singularities that can significant role in the terahertz emission.

Keywords – polarons, semiconductor heterostructures, terahertz sources.

I. Introduction

Polarons are frequently considered in resonant-tunneling diodes (RTD) to explain some exotic behavior of spectral features in strong magnetic and electric fields [1]. In particular a model of the polaron resonant-tunneling was proposed to describe phonon replicas in a current-voltage characteristic of the RTD made of a heterostructure of polar semiconductors [2]. Recently this model was applied to consider transformation of the phonon replica as a transition of polarons in to magnetopolarons in a quantizing magnetic fields [3].

II. Discussion

We discuss polarons formed in a quantum well with subband energy E_{02} between tunnel barriers of the RTD. In this case there are two branches of bulk LO-phonons in the heterostructure. For the investigated heterostructure those are GaAs and AlAs LO-phonons with energy $\hbar\omega_{GaAs}$ = 36 meV and $\hbar\omega_{AlGaAs}$ = 53 meV accordingly. Considering electron-LO-phonon interaction it is more appropriate to speak about a low mass or light polaron formed by electrons and virtual LO-phonons and heavy that formed by virtual electrons and LO-phonons. Following this approach the LO-phonons should be considered as intersubband polaron excitation. Moreover the polaron model admits the intersubband trasitions between polaron states formed on different LO-phonons. The energy of the transition is close to the phonon-energy difference $\varepsilon_{12} = \hbar\omega_{AlGaAs} - \hbar\omega_{GaAs}$ = 15 meV. Similar excitations have been observed in tunnel spectra of the RTD at low density of electrons and liquid helium temperatures when the electron-LO-phonon interaction is weakly screened [4]. In this case electrons or polarons with light mass can tunnel from other quantum well with level E_{01} and excite the intersubband transitions of the heavy polarons (see Fig. 1). Another way to decrease the electron screening is temperature increase [5]. This gives a chance for polarons to survive even at room temperature. Thus one can expect the polaron intersubband transitions at room temperatures and even higher those.

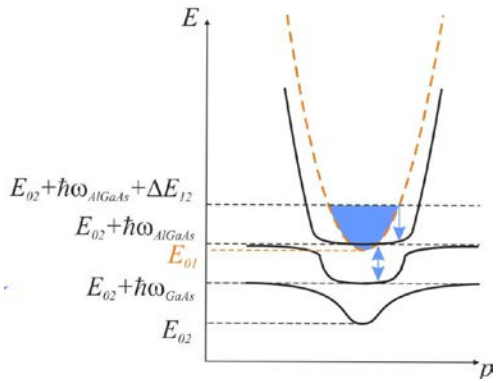

Fig. 1. The polaron spectra of the quantum wells in the RTD

III. Conclusion

In this report we will review our old and new experimental results confirmed the polaron picture in different RTDs made of GaAs/$Al_XGa_{1-X}As$ heterostructures. We shell discuss also theoretical aspects of the temperature dependence of the electron-phonon interaction, polaron density of states and probability of intersubband transitions and their coupling with electromagnetic waves.

References

[1] G.S. Boebinger, A.F.J. Levi, S. Schmitt-Rink, A. Passner, L. N. Pfeiffer, and K.W. West, Phys. Rev. Lett. **65**, 235 (1990).
[2] V.G. Popov, V.G. Krishtop, O. Makarovskii, M. Henini. JETP **111**, 220 (2010).
[3] V.G. Popov, V.G. Krishtop, L. Eaves, M. Henini, J-C. Portal. Proceedings of XXIIth International Simposium "Nanophysics and nanoelectronics". Nizhniy Novgorod, March 12-15, 2018, p. 735-736 (2018) (http://nanosymp.ru/ru/proceedings in Russian).
[4] V.G. Popov, O.N. Makarovskiy, L. Eaves, M. Henini, J.-C. Portal. Proceedings of XXth International Simposium "Nanophysics and nanoelectronics". Nizhniy Novgorod, March 14-18, 2016, p. 695-697 (2016) (http://nanosymp.ru/ru/archive in Russian).
[5] T. Ando, A. Fowler, F. Stern. Electronic Properties of Two Dimensional Electron Systems. Rev. Mod. Phys. **54**, p. 155 (1982).

Terahertz Photoluminescence from Free Excitons in Silicon

A. V. Andrianov and A. O. Zakhar'in

Ioffe Institute, St. Petersburg, Russia

E-mail: alex.andrianov@mail.ioffe.ru

Abstract – We report experimental observation of terahertz photoluminescence due to intra-exciton radiative transitions. These transitions are excited during the binding of nonequilibrium electrons and holes into free excitons. Experiments are carried out on high-purity Si crystals with a resistivity of 12 kOhm cm at helium temperatures and under interband photoexcitation with densities from 0.1 to 140 W/cm^2.

Keywords – terahertz photoluminescence, intra-exciton transitions, silicon

I. Introduction

Processes of energy relaxation under the binding of non-equilibrium electrons and holes into free excitons and under the capture of charge carriers to attracting impurity centers have much in common. Therefore, one can expect that under the binding of non-equilibrium carriers into excitons, THz radiative transitions between energy levels of free excitons also take place in a similar manner to the intra-center radiative transitions in shallow impurity centers, which were observed in number of doped semiconductors [1–3]. However, the THz emission caused by intra-exciton optical transitions was not explored experimentally until now.

In the present paper, the THz photoluminescence (PL) from semiconductors caused by optical transitions between energy levels of free excitons has been observed and studied for the first time. The experiments were carried out on silicon crystals but observed regularities have a general character and concern a broad range of semiconductor materials.

II. Experimental procedure

High-purity silicon crystals grown by floating-zone melting were used in experiments. A continuous wave (CW) semiconducting laser operating at λ=660 nm or a CW diode-pumped solid state laser with wavelength of 530 nm were used as the interband photoexcitation sources. Samples under study were mounted in a He optical cryostat with the temperature control optimized for the THz spectral domain. Spectral measurements were performed with the spectral resolution of 4 cm^{-1} (0.5 meV) using a step-scan Fourier spectrometer for the 5–350 cm^{-1} spectral range, as described elsewhere [2]. The THz emission signal was measured by a liquid helium cooled Si bolometer using a lock-in detection technique.

III. Results

It has been established that the intra-exciton optical transitions dominate the THz emission spectrum under conditions of both low excitation densities and at excitation densities well above the electron-hole liquid (EHL) formation threshold. The photoluminescence spectrum, which occupies a spectral range from 2 to 7 THz, clearly shows narrow lines of optical transitions between the sublevels of the 2P excited and 1S ground states of free excitons. Optical transitions from highly excited exciton states and transitions from continuum states to the exciton ground state also contribute to the THz PL.

It has been found that at a high level of photoexcitation and temperatures above 20–25 K, a superlinear dependence of the intensity of the intra-exciton THz radiation on the photoexcitation density appears. The transition from linear to superlinear dependence occurs at a photoexcitation density of about 10 W/cm^2. We attribute the observed superlinear increase in the intensity of the intra-exciton THz emission with increasing pump intensity to the appearance of stimulated radiative transitions between energy levels of free excitons under intense interband pumping. It is necessary to add that the possibility of achieving population inversion between the energy levels of free excitons at a high level of photoexcitation of a crystal was predicted theoretically in a number of works [4, 5]. The elevated temperatures create conditions favorable for the manifestation of stimulated optical transitions between the exciton energy levels due to the mechanisms proposed in [5], since under these conditions EHL drops are not formed (the temperature of the order of 24 K is the critical temperature for the formation of EHL in Si), and all nonequilibrium electrons and holes are bound to excitons. We will present additional data supporting the appearance of population inversion between the energy levels of free excitons under intense interband photoexcitation.

References

[1] T.V. Adam et al, *Appl. Phys. Lett.*, **83**, 1713, 2003.
[2] A.V. Andrianov et al, *JETP Lett.*, **96**, 365, 2004.
[3] S.G. Pavlov et al, *Phys. Rev. Lett.* , **84**, 5220, 2000..
[4] M. Kira et al, *Phys. Rev. Lett.*, **93**, 076402, 2004.
[5] G.K. Vlasov et al, *Int. J. Infrared and Millimeter Waves*, **4**, 955, 1983.

Silicon Based THz Lasing

V. N. Shastin

Institute for Physics of Microstructures, Russian Academy of Sciences, Nizhny Novgorod, Russia

E-mail: shastin@ipmras.ru

Abstract – The very first discussion on THz lasing from silicon crystal attributed to the effect of stimulated emission of hot holes in crossed electric and magnetic fields. Using numerical calculation it was shown that THz gain can be obtained on the light-heavy hole valence band transitions [1]. Unfortunately experimental study of this effect has not got any progress. The next burst of activity around silicon is happened in connection with quantum-cascade lasers. Following theory the use of Si/SiGe design of a QCL can meet extended frequency range larger gain and higher temperature of operation [2]. Nevertheless until now Si-based QCL has not been demonstrated. At present the only Si-based THz lasers operate on the intra center transitions of optically excited group-V donors [3]. The operating principles and recent experimental investigations of Si-based donor lasers are reviewed and discussed.

Keywords – silicon, lasing, donors, intra center transition

REFERENCES

[1] A.A. Andronov, L.S. Mazov, I.M. Nefedov *Submillimeter Wave Lasers in Semiconductors Using Hot Holes*, paper collection *A.A. Andronov (ed), Gorky, IAP Acad. Sci. USSR*, 157 (1986).

[2] D.J. Paul, *Laser Photonics Rev*. **4**, 610 (2010).

[3] S.G. Pavlov, R.Kh. Zhukavin, V.N. Shastin, and H.-W. Hubers, *Phys. Status Solidi B* 250, No.1 (2013).

Dynamics of Terahertz Excitations in Group-IV Semiconductors Doped by Hydrogen-Like Impurity Centers

S. G. Pavlov[1], N. Deßmann[2,3], A. Pohl[2], R. Kh. Zhukavin[4], K. A. Kovalevsky[4], S. A. Tarelkin[5,6,7], V. S. Bormashov[5,8], Yu. Yu. Choporova[9,10], S. A. Lynch[11], K. L. Litvinenko[12], B. Redlich[3], N. Stavrias[3], A. F. G. van der Meer[3], V. V. Tsyplenkov[4], N. A. Bekin[4], V. N. Shastin[4], B. A. Knyazev[9], S. A. Terentiev[5], V. D. Blank[5,6,7], B. Murdin[12], S. Winnerl[13], J. M. Klopf[13], N. V. Abrosimov[14], H. Riemann[14], and H.-W. Hübers[1,2]

[1] Institute of Optical Sensor Systems, German Aerospace Center, Berlin, Germany
[2] Institut für Physik, Humboldt-Universität zu Berlin, Berlin, Germany
[3] FELIX Laboratory, Radboud University, Nijmegen, The Netherlands
[4] Institute for Physics of Microstructures, Russian Academy of Sciences, Nizhny Novgorod, Russia
[5] Technological Institute for Superhard and Novel Carbon Materials, Troitsk, Moscow, Russia
[6] National University of Science and Technology MISiS, Moscow, Russia
[7] Moscow Institute of Physics and Technology, Dolgoprudny, Moscow Region, Russia
[8] The All-Russian Research Institute for Optical and Physical Measurements, Moscow, Russia
[9] Budker Institute of Nuclear Physics, Siberian Branch, Russian Academy of Sciences, Novosibirsk, Russia
[10] National Research Novosibirsk State University, Novosibirsk, Russia
[11] Cardiff University, Cardiff, UK
[12] University of Surrey, Guildford, UK
[13] Helmholtz Zentrum Dresden-Rossendorf, Dresden, Germany
[14] Leibniz-Institut für Kristallzüchtung, Berlin, Germany

E-mail: sergeij.pavlov@dlr.de

Abstract – The hydrogen-like impurity centers are the major contributors to electrical and infrared properties of the group-IV semiconductors. Dynamics of nonequilibrium charge carriers bound to excited impurity states has been intensively studied over last decade by time-resolved THz spectroscopies. Typical characteristic times observed for excited impurity states, mechanisms of electron-phonon coupling will be reviewed for lightly, moderately and heavily doped diamond, silicon, germanium and silicon-germanium crystals.

Keywords – time-resolved spectroscopy, group-IV semiconductors, hydrogen-like impurity centers

Atomic-like energy spectrum of hydrogen-like substitutional impurities in bandgaps of semiconductors attracts specific interest due to its potential for infrared / THz photonics[1] and quantum technologies[2]. Among key characteristics of electronic states of such impurity centers for optical and optoelectronic applications are those related to dynamics of non-equlibrium electron distributions. Due to strong interaction of impurity states with characteristic lattice phonons typical nonradiative relaxation times of excited states often fall down to picosecond (ps) time scale.

Time-resolved spectroscopies utilizing ps-pulsed infrared free electron lasers are the most direct approach to assess ultrafast dynamics of excited states of such impurity centers.

In crystals with low/residual concentration of dopants induced populations in excited impurity states have, as a rule, the longest lifetimes, up to a few nanoseconds (ns) (Table 1) determined mainly by nonradiative decay due to interaction with single or multiple optical and acoustic phonons. Targeted (co-)doping and compensation of semiconductors allows to control intracenter electron dynamics, usually reducing intracenter relaxation times down to a few tens ps, and by this to enable design of fast / broad-band infrared photoconductive detectors[3] as well as to predict feasibility and performance of impurity-based THz emitting devices.

Table 1. The ranges of lifetimes of optically excited charge carriers measured by time-resolved spectroscopy in different group-IV semiconductors doped by hydrogen-like impurity centers

Semi-conductor	Range [THz]	Lifetimes in excited states	References
p-C [a]	73÷89	2.5 ps ÷ 330 ps	[4]
n-Si [b]	7.3÷20.0	25 ps ÷ 236 ps	[5], [6], [7], [8]
p-Si	7.3÷10.3	6 ps ÷ 130 ps	[9], [10]
n-Ge [c]	1.6÷2.9	70 ps ÷ 3.2 ns	[3], [11], [14]
p-Ge [c]	2.3÷15.8	30 ps ÷ 10.9 ns	[3], [12]
n-SiGe [c]	8.1÷10.8	90 ps ÷ 160 ps	[13]

[a] including isotopically enriched dopant.

[b] including isotopically enriched host lattice and co-doped crystals.

[c] including heavily doped highly compensated crystals, uniaxial stress.

REFERENCES

[1] H.-W. Hübers, S. G. Pavlov and V. N. Shastin, *in the Special Issue "Photonic Terahertz Technology" of Semicond. Sci. Technol.* **20** (7), S211-S221 (2005).

[2] K. J. Morse, R. J. S. Abraham, A. DeAbreu, C. Bowness, T. S. Richards, H. Riemann, N .V. Abrosimov, P. Becker, H.-J. Pohl, M. L. W. Thewalt and S. Simmons, *Science Advances* **3** (7), e1700930 (2017);
L. R. Schreiber, H. Bluhm, Science **359** (6374), 393 (2018).

[3] N. Deßmann, S. G. Pavlov, A. Pohl, N. V. Abrosimov, S. Winnerl, M. Mittendorff, R. Kh. Zhukavin, V. V. Tsyplen-kov, D. V. Shengurov, V. N. Shastin, and H.-W. Hübers, *Appl. Phys. Lett.* **106**, 171109 (2015).

[4] S. G. Pavlov, S. A. Tarelkin, V. S. Bormashov, N. Stavrias, K. Saeedi, A. F. G. van der Meer, N. A. Bekin, R. Kh. Zhukavin, V. N. Shastin, M. S. Kuznetsov, S. A. Terentiev, S. A. Nosukhin, D. D. Prikhodko, V. D. Blank, M. Wienold, H.-W. Hübers, *Diam. Relat. Mater.* **92**, 259-265 (2019).

[5] N. Q. Vinh, P. T. Greenland, K. Litvinenko, B. Redlich, A. F. G. van der Meer, S. A. Lynch, M. Warner, A. M. Stoneham, G. Aeppli, D. J. Paul, C. R. Pidgeon, and B. N. Murdin, *Proc. Natl. Acad. Sci. USA* **105**, 10649 (2008).

[6] H.-W. Hübers, S. G. Pavlov, S. A. Lynch, P. T. Greenland, K. L. Litvinenko, B. Murdin, B. Redlich, A. F. G. van der Meer, H. Riemann, N. V. Abrosimov, P. Becker, H.-J. Pohl, R. Kh. Zhukavin, V. N. Shastin, *Phys. Rev. B* **88**, 035201 (2013).

[7] K. L. Litvinenko, S. G. Pavlov, H.-W. Hübers, N. V. Abrosimov, C. R. Pidgeon, and B. N. Murdin, *Phys. Rev. B* **89**, 235204 (2014).

[8] N. Stavrias, K. Saeedi, B. Redlich, P. T. Greenland, H. Riemann, N. V. Abrosimov, M. L. W. Thewalt, C. R. Pidgeon, and B. N. Murdin, *Phys. Rev. B* **96**, 155204 (2017).

[9] N. Q. Vinh, B. Redlich, A. F. G. van der Meer, C. R. Pidgeon, P. T. Greenland, S. A. Lynch, G. Aeppli, and B. N. Murdin, *Phys. Rev. X* **3**, 011019 (2013).

[10] K. Saeedi, N. Stavrias, B. Redlich, H. Riemann, N. V. Abrosimov, P. Becker, H.-J. Pohl, M. L. W. Thewalt, and B. N. Murdin, *Phys. Rev. B* **97**, 125205 (2018).

[11] N. Deßmann, S. G. Pavlov, V. N. Shastin, R. Kh. Zhuka-vin, V. V. Tsyplenkov, S. Winnerl, M. Mittendorff, N. V. Abrosimov, H. Riemann, and H.-W. Hübers, *Phys. Rev. B* **89**, 035205 (2014).

[12] N. Deßmann, S. G. Pavlov, V. V. Tsyplenkov, E.E. Orlova, A. Pohl, V. N. Shastin, R. Kh. Zhukavin, S. Winnerl, M. Mittendorff, J. M. Klopf, N. V. Abrosimov, H. Schneider, and H.-W. Hübers, *phys. stat. sol. b* **254**, 1600803 (2017).

[13] S. A. Lynch, G. Matmon, S. G. Pavlov, K. L. Litvinenko, B. Redlich, A. F. G. van der Meer, N. V. Abrosimov, H.-W. Hübers, *Phys. Rev. B* **82**, 245206 (2010).

[14] R. Kh. Zhukavin, K. A. Kovalevskii, S. M. Sergeev, Yu. Yu. Choporova, V. V. Gerasimov, V. V. Tsyplenkov, B. A. Knyazev, N. V. Abrosimov, S. G. Pavlov, V. N. Shastin, H. Schneider, N. Deßmann, O. A. Shevchenko, N. A. Vinokurov, G. N. Kulipanov, H.-W. Hübers, *JETP Lett.* **106**, 571 (2017).

High-Resolution Spectroscopy with Terahertz Quantum-Cascade Lasers

H.-W. Hübers[1,2], T. Alam[1], T. Hagelschuer[1], H. Richter[1], M. Wienold[1,2]

[1] Institute of Optical Sensor Systems, German Aerospace Center (DLR), Rutherfordstraße 2, 12489 Berlin, Germany
[2] Department of Physics, Humboldt-Universität zu Berlin, Newtonstraße 5, 12489 Berlin, Germany

E-mail: heinz-wilhelm.huebers@dlr.de

Abstract – Terahertz (THz) quantum-cascade lasers (QCLs) are narrow-band, high-power, and frequency-agile sources. This makes them attractive for applications in high-resolution molecular and atomic spectroscopy. In the past years, various techniques and methods regarding high-resolution spectroscopy with THz QCLs have been developed, namely direct absorption spectroscopy and heterodyne spectroscopy. We will present recent developments in molecular spectroscopy using THz QCLs in a heterodyne spectrometer and in a laser absorption spectrometer.

Keywords – terahertz, quantum-cascade laser, molecular spectroscopy, heterodyne spectroscopy, laser absorption spectroscopy

INTRODUCTION

Terahertz (THz) molecular spectroscopy is fundamental for unveiling the structure and energy levels of molecules and atoms. Information on Doppler and pressure broadening can be obtained from their THz spectra [1]. These data are a prerequisite for the interpretation of molecular spectra obtained in atmospheric science and astronomy [2]. Molecular absorption lines are produced by transitions between rotational states of the molecule. Typically, light-weight molecules such as CO or OH have most of their rotational transitions at THz frequencies. In the case of atoms, transitions occur within a multiplet of orbital angular momentum, whose states are split by the spin-orbit interaction. These are called fine structure lines. A prominent example is the fine structure line of neutral atomic oxygen, OI, at 4.7448 THz, which is important in astronomy and atmospheric science.

THz quantum-cascade lasers (QCLs) are important for high-resolution molecular spectroscopy, because they are powerful, narrow-band sources and their spectral brightness is very high, typically in the order of mW per MHz [3]. THz QCLs have been implemented in absorption spectrometers as well as heterodyne spectrometers. In absorption spectroscopy, the goal is to detect a small fractional change of a relatively large amount of power. Heterodyne spectrometers are mostly used for remote sensing in astronomy and in atmospheric science. In this case, a very weak signal on a low background has to be detected. In a heterodyne spectrometer, the QCL serves as a local oscillator (LO) for the mixer, which downconverts the signal from the THz range to a few GHz [4]. Although both applications are different, the requirements regarding the QCL are similar. With respect to its frequency characteristics, the QCL should provide large frequency coverage while having a narrow linewidth. Its power should be large enough to pump the mixer while the power stability should be sufficient in order not to introduce additional noise in the spectrometer. The beam emitted by the QCL should be a fundamental Gaussian, because this relaxes the requirements regarding the optics of the spectrometer, independently whether it is an absorption spectrometer or a heterodyne spectrometer.

This presentation will give an overview of several techniques for high-resolution spectroscopy of molecules at THz frequencies using QCLs. The employed QCLs emit around 3.5 and 4.7 THz. They are based on active-region designs, which have been optimized for continuous-wave operation, high output powers, and low electrical pump powers [5, 6]. Efficient carrier injection is achieved by resonant longitudinal-optical-phonon scattering.

Two spectroscopic methods will be discussed. The first is heterodyne spectroscopy with a 4.7-THz QCL as a local oscillator on board of SOFIA, the Stratospheric Observatory for Infrared Astronomy [7]. This enables high-resolution spectroscopy of atomic oxygen in the interstellar medium and in planetary atmospheres. The second method is absorption spectroscopy with QCLs as frequency-tunable sources. Frequency tuning is achieved by either changing the driving current or the operating temperature of the QCL. Alternatively, the back-facet of the QCL is illuminated with radiation from a near-infrared laser [8]. The radiation from the QCL is transmitted through an absorption cell and is detected either with conventional power detectors or by exploiting the self-mixing effect [9]. The latter is a particularly attractive approach, because no external detector is required. Both detection methods allow for sub-Doppler spectroscopy by observing the Lamb dip [10]. Finally, the prospects of high-resolution THz spectroscopy with QCLs will be discussed.

REFERENCES

[1] F. C. De Lucia, “The submillimeter: A spectroscopist's view,” J. Mol. Spectrsoc., vol. 261, pp. 1-17 (2010).

[2] S. Schlemmer, “High-Resolution Laboratory Terahertz Spectroscopy and Applications to Astrophysics,” in: Frontiers and Advances in Molecular Spectroscopy, 471 (Elsevier Science, Amsterdam, 2018).

[3] H.-W. Hübers, “Terahertz heterodyne receivers,”IEEE J. Sel. Top. Quantum Electron., vol. 14, pp. 378-291 (2008).
[4] H.-W. Hübers, H. Richter, and M. Wienold, “High-resolution terahertz spectroscopy with quantum-cascade lasers,” J. Appl. Phys., vol. 125, 151401 (2019).
[5] L. Schrottke, M. Wienold, R. Sharma, X. Lü, K. Biermann, R. Hey, A. Tahraoui, H. Richter, H.-W. Hübers, and H. T. Grahn, “Quantum-cascade lasers as local oscillators for heterodyne spectrometers in the spectral range around 4.745 THz,” Semicond. Sci. Technol., vol. 28, 03511 (2013).
[6] H. Richter, M. Greiner-Bär, S. G. Pavlov, A. D. Semenov, M. Wienold, L. Schrottke, M. Giehler, R. Hey, H. T. Grahn, and H.-W. Hübers, “A compact, continuous-wave terahertz source for imaging and spectroscopy based on a quantum-cascade laser and a miniature cryocooler,” Opt. Express, vol. 18, pp. 10177−10187 (2010).
[7] H. Richter, M. Wienold, L. Schrottke, K. Biermann, H. T. Grahn, and H.-W. Hübers, “4.7-THz local oscillator for the GREAT heterodyne spectrometer on SOFIA,” IEEE Trans. Terahertz Sci. Technol., vol. 5, pp. 539–545 (2015).
[8] T. Alam, M. Wienold, X. Lü, K. Biermann, L. Schrottky, H. T. Grahn, and H.-W. Hübers, “Wideband, high-resolution terahertz spectroscopy by light-induced frequency tuning of quantum-cascade lasers,” Opt. Express, vol. 27, pp. 5420-5432 (2019).
[9] T. Hagelschuer, M. Wienold, H. Richter, L. Schrottke, H. T. Grahn, and H.-W. Hübers, “Real-time gas sensing based on optical feedback in a terahertz quantum-cascade laser,” Opt. Express, vol. 25, pp. 30203−30213 (2017).
[10] M. Wienold, T. Alam, L. Schrottke, H. T. Grahn, and H.-W. Hübers, “Doppler-free spectroscopy with a terahertz quantum-cascade laser,” Opt. Express, vol. 25, pp. 6692–6697 (2018).

Terahertz-Infrared Spectroscopy of Single Crystalline M-Type Hexaferrite $BaTi_xFe_{12-x}O_{19}$

S. R. Yegiyan[1], L. N. Alyabyeva[1], V. I. Torgashev[2], D. A. Vinnik[3], S. A. Gudkova[3,4], A. S. Prokhorov[1,5], M. Dressel[1,6], B. P. Gorshunov[1]

[1] Laboratory of Terahertz Spectroscopy, Moscow Institute of Physics and Technology, Moscow, Russia
[2] Faculty of Physics, Southern Federal University (SFedU), Rostov-on-Don, Russia
[3] Laboratory of crystal growth, South Ural State University, Chelyabinsk, Russia
[4] SEC Nanotechnology, Moscow Institute of Physics and Technology, Moscow, Russia
[5] Prokhorov General Physics Institute of Russian Academy of Sciences, Moscow, Russia
[6] 1.Physikalisches Institut, Universität Stuttgart, Stuttgart, Germany

E-mail: Samvel_y@mail.ru

We have studied polarization-dependent broad-band dielectric response of single-crystalline Ti-substituted barium hexaferrites $BaTi_xFe_{12-x}O_{19}$, x = 0.6, 0.7, 1.1, in the frequency range from 10 to 8000 cm^{-1} and at temperatures from 5 to 300 K. In addition to a rich set of phonon resonances located at frequencies from 100 to 800 cm^{-1} we observed an unusual low-energy response (in the terahertz region, 10–100 cm^{-1}) stemming from two different effects: relaxational process and second order spin-orbit coupling in Fe^{2+} ground state, that may set up new prospects for doped hexaferrites in terahertz technologies.

Keywords – terahertz spectroscopy, M-type hexaferrite, multiferroics

I. Introduction

The M-type hexaferrites $AFe_{12}O_{19}$ (A – Ba, Pb, Sr, etc.) attract interest of scientific research groups due to their exciting physical properties, such as significant absorption at microwave frequencies and multiferroism. Being structurally identical to natural magnetoplumbite $PbFe_{12}O_{19}$, M-type hexaferrites possess centrosymmetric structure with $P6_3/mmc$ space group: the hexagonal lattice with characteristic cell parameters 5.89 Å in *ab*-plane and 23.17 Å along the *c*-axis[1], that alludes the strong single-axis anisotropy. Substituted compounds play crucial role for practical utilization of hexaferrites since specific doping can provide the most beneficial material in each particular application as is discussed in Refs. 2–4. Nowadays, hexaferrites are successfully used in radio/microwave devices, still being unexplored in terahertz frequency region. In this work, we have investigated the dielectric response of $BaTi_xFe_{12-x}O_{19}$ by means of terahertz/infrared spectroscopy. The significant point of our study was the use of single crystalline[5] form of substituted hexaferrites.

II. Experiment

In our research we have measured transmission and reflection spectra of plane-parallel samples of $BaTi_xFe_{12-x}O_{19}$ compounds with x = 0.6, 0.7, 1.1 in a wide frequency range from 10 to 8000 cm^{-1} and at temperatures from 5 to 300 K. Plane-parallel slabs with the c-axis in the plane of the slabs were carefully cut from single crystals using wire saw. This orientation allows one to provide measurements in two principal polarizations of the probing radiation relative to the main crystallographic axis (E||*c*, E⊥*c*). The samples were polished down to a thickness of about 100 micrometers with an accuracy of 2 micrometers. The measurements of transmission spectra at frequencies from 10 to 100 cm^{-1} where performed with the help of time-domain spectrometer Tera-View TPS Spectra 3000 with resolution 1.2 cm^{-1}. Measurements of reflection coefficient in the infrared region (100–8000 cm^{-1}) with the resolution 2 cm^{-1} were performed by means of commercial Fourier-transform spectrometer Bruker Vertex 80v with a microscope setup Hyperion 2000. The measured spectra were modeled using a least-square fitting procedure with regular Lorentzian lineshapes and Debye relaxation models.

III. Results

The analysis revealed deplete sequence of phonon resonances in the range from 100 to 800 cm^{-1}, in agreement with the previous results[6] obtained for pure $BaFe_{12}O_{19}$. The spectral behavior in the terahertz range (10–100 cm^{-1}) in the orientation E⊥*c* can be described by the Debye relaxation model. The set of overdamped resonances observed in the orientation E||c were assigned to electronic transitions within the fine structure of ground state of Fe^{2+} ions, which play the role of charge compensator towards aliovalent substitution. Freezing out of dynamical oscillations of Fe^{3+} ions within the split bi-pyramidal site-position 2b manifests itself in the temperature-dependent parameters of the resonance modes at the critical temperatures 70 K < T < 90 K (Fig. 1).

Acknowledgments

This work was financially supported by Russian Ministry of Education and Science (Project 5-100).

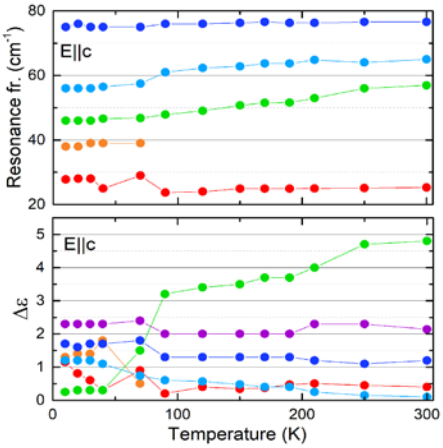

Fig. 1. Temperature dynamics of resonance frequency and dielectric contribution of the terahertz absorption lines (10–100 cm^{-1}) region in $BaTi_{1.1}Fe_{10.9}O_{19}$.

References

[1] X. Obradors, et., Crystal structure of strontium hexaferrite $SrFe_{12}O_{19,}$ Journal of Solid State Chemistry, Volume 72, Issue 2, February (1988), Pages 218-224.

[2] Gutfleisch O., Willard M. A., Brück E., Chen C. H., Sankar S. G., Liu J. P. "Magnetic Materials and Devices for the 21st Century: Stronger, Lighter, and More Energy Efficient". Adv. Mater., 23 (2011) 821-842.

[3] Adamtcov A. U. Properties of hexagonal ferrites $BaFe_{12}O_{19}$ and $BaFe_{12-x}Me_xO_{19}$ for magnets and microwave devices, dissertation thesis, Moscow, 177 p, (2016) [in Russian].

[4] Pereira, F.M.M., Santos, M.R.P., Sohn, R.S.T.M. et al. J Mater Sci: Mater Electron (2009) 20: 408.

[5] Denis A. Vinnik, Dmitry A. Zherebtsov, et al., Ti-Substituted BaFe12O19 Single Crystal Growth and Characterization, *Cryst. Growth Des.*, 2014, 14 (11), pp. 5834–5839.

[6] Mikheykin A.S. et al.. Lattice anharmonicity and polar soft mode in ferromagnetic M-type hexaferrite $BaFe_{12}O_{19}$ single crystal. The European Physical Journal. (2014).

Terahertz Dynamics of a Network of Nanoconfined Electric Dipoles

M. Belyanchikov[1], M. Savinov[2], P. Bednyakov[2], Z. Bedran[1], V. Thomas[3], V. Torgashev[4], V. B. Anzin[1,5], A. Loidl[6], P. Lunkenheimer[6], E. Zhukova[1], E. Uykur[7], M. Dressel[1,7], B. Gorshunov[1]

[1] Moscow Institute of Physics and Technology, Dolgoprudny, Moscow Region, 141700 Russia
[2] Institute of Physics AS CR, 18221 Praha 8, Czech Republic
[3] Institute of Geology and Mineralogy, RAS, 630090 Novosibirsk, Russia
[4] Faculty of Physics, Southern Federal University, 344090 Rostov-on-Don, Russia
[5] Prokhorov General Physics Institute, RAS, Moscow, 119991 Russia
[6] Experimental Physics V, University of Augsburg, 86135 Augsburg, Germany
[7] 1.Physikalisches Institut, Universität Stuttgart, 70569 Stuttgart, Germany

E-mail: belyanchikov@phystech.edu

Abstract – We apply terahertz and radio-frequency spectroscopic techniques to study excitations of interacting electric dipoles spatially arranged in a network with an interdipole distance of 5–10 Å. The dipoles with a magnitude of 1.85 Debye are represented by single H_2O molecules located in voids 0.5 nm in size formed by ions of the crystal lattice of dielectric crystals - beryl and cordierite. We observe and characterize rich sets of highly anisotropic and temperature-dependent single-particle and collective excitations whose origin is analyzed basing on the density functional and molecular dynamics approaches.

Keywords – electrical dipole, nanoconfinement, terahertz spectroscopy

I. Introduction

Recently, considerable attention has been given to the properties of systems that contain interacting point electric dipoles. Such systems are expected to manifest rich variety of ordered phases resulting from competition between the dipole-dipole coupling and disordering effects, both dependent of many factors, like spatial symmetry, dimensionality, defects, frustration, etc. An additional issue is to study dipoles as quantum rotors that experience, in general, a multi-well potential in presence of hindering effects and quantum rotational tunneling. It is important, that the electro-static coupling among the dipoles makes such systems qualitatively different from their magnetic counterparts. Since interacting spins have been studied during last decades, significant progress has been achieved in understanding the underlying magnetic physics. In electric dipolar systems, the interplay of quantum tunneling, fluctuations and frustration provides with the possibility to realize new exotic phases, like quantum electric dipolar liquids and glasses, lead to quantum critical phenomena and quantum phase transitions. Understanding the nature of the corresponding phases, their formation and possible relations with magnetic counterparts is of great fundamental and technological interest, but is presently still at its infancy.

An ideal playground for corresponding studies is provided by dielectrics whose crystal lattice contains voids filled with electric-polar molecules that only weakly interact with surrounding ions and are thus nearly free, but "feel" each other via long-range dipole-dipole interaction. Corresponding broad-band spectroscopic studies of the gemstone beryl with 0.5 nm sized pores hosting polar H_2O molecules (each carrying a dipole moment of 1.85 Debye) allowed to discover incipient ferroelectricity within the H_2O dipoles along with a rich set of single-particle excitations at terahertz-infrared frequencies [1–4]. It was suggested that the ferroelectric phase transition into the macroscopically ordered state is suppressed by quantum tunneling of H_2O molecules between 1 meV deep wells of localizing hexagonal potential. Here, we present comparative detailed studies of single-particle and collective vibrational states of the hexagonally arranged H_2O molecular network in beryl and of orthorhombic matrix of H_2O molecules in cordierite whose localizing potential is represented by two 10 meV deep minima felt by the molecule when it rotates 360° around c-axis (Fig. 1).

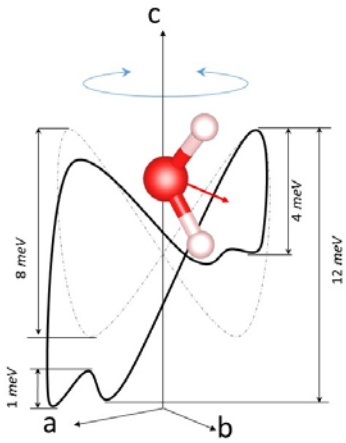

Fig. 1. Electric dipole of water molecule (p = 1.85 Debye) in asymmetric localizing potential within ≈5 Å size cage formed by ions of crystal lattice of orthorhombic cordierite.

II. Results and discussions

Using terahertz (THz), radio-frequency (RF) and microwave (μW) spectroscopies, we measure polarization-dependent (E-field component of the probing

radiation parallel to a, b and c axes) spectra of the complex dielectric permittivity $\varepsilon^*(\nu) = \varepsilon'(\nu) + i\varepsilon''(\nu)$ and conductivity $\sigma^*(\nu) = \sigma_1(\nu) + i\sigma_2(\nu)$ of hydrous beryl and cordierite in the range ν = 1 Hz – 3 THz at temperatures 0.3 K – 300 K. Measurements on water-free crystals allowed us to extract the spectra determined exclusively by electric dipoles of the water molecules. In the THz range, 0.3 THz – 3 THz, rich sets of highly anisotropic excitations are discovered in cordierite (see Fig. 2).

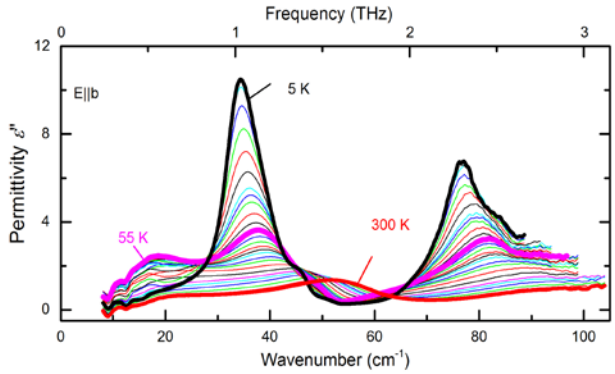

Fig. 2. Temperature evolution of terahertz spectra of imaginary permittivity of a network of electric dipoles (polar H_2O molecules) confined to sub-nanometer-sized pores within crystal lattice of cordierite.

Applying molecular dynamics analysis allowed us to associate their origin with complex librational-rotational vibrations of the nanoconfined electric dipoles of water molecules. In the RF- μW ranges, 1 Hz – 1 GHz, for the E||a polarization we discover a strongly temperature-dependent overdamped excitation and assign its origin to relaxational dynamics of separate molecular dipoles. Below 3 K, weak signatures are observed of a phase transition into a glassy state formed by frozen water dipoles. We will perform comparative analysis of the results obtained on dipoles arranged in hexagonal (beryl matrix) and in orthorhombic (cordierite matrix) arrays.

III. Conclusions

We have performed broad-band (1 Hz up to several terahertz) spectroscopic investigations of vibrational states of interacting separate electric dipoles spatially arranged in an openwork structure within crystalline dielectrics, where the dipoles (polar water molecules) are confined within pores several Angstroms in size and are only weakly coupled to surrounding ions of the lattice. We firstly observe emergence of (incipient) ferroelectricity among the water molecules in beryl. Rich sets of strongly anisotropic and temperature dependent single-particle excitations are observed within dipolar networks in beryl and cordierite hosting matrices and their origin analyzed.

Acknowledgments

Authors acknowledge support from RFBR 18-32-00286, 18-32-20186, DFG via DR228/61-1 and Center of Integrated Quantum Science and Technology IQST Stuttgart/Ulm.

References

[1] B.P. Gorshunov, E.S. Zhukova, V.I. Torgashev et al., *J. Physical Chemistry Letters*, **4**, 2015 (2013).
[2] B.P. Gorshunov, V.I. Torgashev, E.S. Zhukova et al., *Nature Communications*, **7**, 12842 (2016).
[3] M. Dressel, E.S. Zhukova, V.G. Thomas, B.P. Gorshunov. *J. Infrared, Millimeter, and Terahertz Waves*, **39**, 799 (2018).
[4] E.S. Zhukova, M.A. Belyanchikov, M. Savinov, et al. *EPJ Web of Conferences*, **195**, 06018 (2018).

Graphene/Black As_xP_{1-x} Heterostructures for Terahertz and Infrared Devices

V. Ryzhii[1,2,3], T. Otsuji[1], M. Ryzhii[4], V. Leiman[3], V. E. Karasik[5], D. Ponomarev[2], P. P. Matsev[2], V. Mitin[6], and M. S. Shur[7,8]

[1] Research Institute of Electrical Communication, Tohoku University, Sendai, Japan
[2] Institute of Ultra-High Frequency Semiconductor Electronics, Russian Academy of Sciences, Moscow, Russia
[3] Center for Photonics and 2D Materials, Moscow Institute of Physics and Technology, Dolgoprudny, Russia
[4] Department of Computer Science and Engineering, University of Aizu, Aizu-Wakamatsu, Japan
[5] Center of Photonics and IR Technology, Bauman Moscow State Technical University, Moscow, Russia
[6] Department of Electrical Engineering, University at Buffalo, SUNY, Buffalo, USA
[7] Department of Electrical, Computer, and System Engineering, Rensselaer Polytechnic Institute, Troy, NY, USA
[8] Electronics of the Future, Inc., Vienna, VA, USA

E-mail: v-ryzhii@riec.tohoku.ac.jp

Abstract – We present and discuss the concepts of novel terahertz and infrared devices based on the Graphene/Black As_xP_{1-x} heterostructures

Keywords – Graphene, black arsenic-phosphorus, terahertz and infrared devices

I. INTRODUCTION

The gapless energy spectrum of the graphene layers (GLs) [1] enables the possibility to use the interband transitions in GLs for the detection of electromagnetic radiation in a wide spectral range (including the terahertz (THz), far-infrared (FIR) and mid-infrared (MIR) ranges). The emergence of the black-phosphorus (b-P), black-Arsenic (b-As), and the compounds of these materials (b-As_xP_{1-x}), in which the energy gap Δ_G varies from 0.15 to 1.2 eV, depending on the number of the atomic sheets and the component relative content, opens new prospects for the creation of the FIR and MIR photodetectors [2–10]. Both the b-P and b-As and their compounds exhibit a strong in-plane anisotropy. The ratios of the electron effective masses (as well as the hole effective masses) in different in-plain directions is about 30. The carrier mobility in the small mass direction and the mobility in the transverse direction are sutable for many electronic and optoelectronic applications.

The combination of the GLs with the b-As_xP_{1-x} few-atomic layers and relatively thick layers can be useful for the enhancement of the GL-based photodetectors (GLIPs), electro-optical modulators and sources of THz/FIR/MIR radiation performance. One of the crucial properties of the GL heterostructures with the b-A_xP_{1-x} barrier layers are associated with the fact that the GL Dirac point corresponds to the energy gap in the barriers. In this paper, we revie the concepts of THz and IR devices based on the heterostructures in question focusing on our recent results (see Refs. 11–18).

II. DEVICES UNDER CONSIDERATION

In our communication, we briefly discuss the main electron properties of b-P, b-As, and b-As_xP_{1-x} as well as the state-of –the art of the related technology. The main part of this paper is focused on the new device concepts devices on the heterostructures, in which the GLs are integrated with the layers of the abovementioned materials.

The device structures, band diagrams, and calculated characteristics of the following devices are considered:

- THz and IR photodetectors based on the vertical G/b-As_xP_{1-x} heterostructures and using the intersubband transitions in the GL followed by the carrier propagation across the b-As_xP_{1-x} layers and the injection of the extra carriers from the emitter contact. The latter provides the photoconductive gain, which can enable fairly high values of the detector responsivity [11–14];
- Sources of the THz radiation using the vertical injection from the b-A_xP_{1-x} emitter layer. A relatively small energy gap in such layers and an appropriate band alignment lead to moderate energies of the carriers injected from the emitter to the GL. This helps the realization of the interband population inversion [15, 16];
- Devices based on lateral GL/b-A_xP_{1-x} heterostructures using the real space transfer of the light carriers from the GL to the neighboring b-A_xP_{1-x} layers with relatively heavy carriers. These devices can be used as logical switches, electro-optical modulators of the THz radiation by controlling of the carrier effective temperature by the electric field, and bolometric THz detectors utilizing heating of the carriers by the incident THz radiation combined with their real-space transfer [17, 1].

III. CONCLUSION

The conducted analysis demonstrates that the G/b-As_xP_{1-x} vertical and lateral heterostructures could enable prospective THz and IR devices with the superiorperformance.

REFERENCES

[1] A. H. Castro Neto, F. Guinea, N. M. R. Peres, K. S. Novoselov, and A. K. Geim, Rev. Mod. Phys. **81**, 109 (2009).
[2] R. W. Keyes, Phys. Rev. **92**, 580 (1953).
[3] A. Morita, Appl. Phys. A **39**, 227 (1986).

[4] H. Asahina and A. MoritaJ. Phys. C: Solid State Phys. **17**, 1839 (1984).
[5] Xi Ling, H. Wang, S. Huang, F. Xia, and M. S. Dresselhaus, PNAS **112**, 4523 (2015).
[6] F. Xia, H. Wang, Y. Jia, Nat. Comm. **5**, 4458 (2014).
[7] Z. Guo, H. Zhang, S. Lu, Z. Wang, S. Tang, J. Shao, Z. Sun, H. Xie, H. Wang, X,-F. Yu, and P. K. Chu, Adv. Funct. Mat. **25**, 6996 (2015).
[8] B. Liu, M. Kopf, A. N. Abbas, X. Wang, Q. Guo, Y. Jia, F. Xia, R. Weihrich, F. Bachhuber, F. Pielnhofer, H. Wang, R. Dhall, S. B. Cronin, M. Ge, X. Fang, T. Nilges, and C. Zhou, Adv. Mater. **27**, 4423 (2015).
[9] M. Long, A. Gao, P. Wang, et al. Sci. Adv. **3**, No.6, e1700589 (2017).
[10] S. Yuan, C. Shen, B. Deng, et al, Nano Lett. **18**, 31723179 (2018).
[11] V. Ryzhii, M. Ryzhii, D. Svintsov. V. Leiman, V. Mitin, M. S. S Shur, and T. Otsuji, Infrared Phys. Technol. **84**, 72 (2017).
[12] V. Ryzhii, M. Ryzhii, V. Leiman, V. Mitin, M. S. Shur, and T. Otsuji, J. Appl. Phys. **122**, 054505 (2017).
[13] V. Ryzhii, M. Ryzhii, D. Svintsov. V. Leiman, V. Mitin, M. S. S Shur, and T. Otsuji, Opt. Exp. **25**, 5536 (2017).
[14] V. Ryzhii, T. Otsuji, V. E. Karasik, M. Ryzhii, V. G. Leiman, V. Mitin, and M. S. Shu,r, IEEE J. Quantum Electron. **54**, No. 2 (2018).
[15] V. Ryzhii, T. Otsuji, M. Ryzhii, A.A.Dubinov, V. Ya. Aleshkin, V. E. Karasik, and M.S.Shur, arXiv:1901.00580 (2019).
[16] M. Ryzhii, V. Ryzhii, T. Otsuji, and V. Mitin, arXiv:1901.10755 (2019).
[17] V. Ryzhii, T. Otsuji, M. Ryzhii, D.S. Ponomarev, et al. Semicond. Sci. Technol. **33**, No.12 (2018).
[18] V. Ryzhii, M. Ryzhii, D.S. Ponomarev, V. Leiman, V. Mitin, M.S. Shur, and T. Otsuji, J. Appl. Phys. **125**, 151608 (2019).

Graphene Based Plasmonic Interferometer for Terahertz Radiation Detection

G. E. Fedorov[1*], D. Svintsov[1], D. Bandurin[1,2], I. Gayduchenko[3], G. Goltsman[3]

[1] Moscow Institute of Physics and Technology (State University), Russia
[2] School of Physics, University of Manchester, United Kingdom
[3] Physics Department, Moscow State University of Education (MSPU), Russian Federation

E-mail: fedorov.ge@mail.ru

Plasmons, collective oscillations of electron systems, can efficiently couple light and electric current, and thus can be used to create sub-wavelength photodetectors, radiation mixers, and on-chip spectrometers. Despite considerable effort, it has proven challenging to implement plasmonic devices operating at terahertz frequencies. The material capable to meet this challenge is graphene as it supports long-lived electrically tunable plasmons. Here we demonstrate plasmon-assisted resonant detection of terahertz radiation by antenna-coupled graphene transistors that act as both plasmonic Fabry-Perot cavities and rectifying elements. By varying the plasmon velocity using gate voltage, we tune our detectors between multiple resonant modes and exploit this functionality to measure plasmon wavelength and lifetime in bilayer graphene as well as to probe collective modes in its moiré minibands. Our devices offer a convenient tool for further plasmonic research that is often exceedingly difficult under non-ambient conditions (e.g. cryogenic temperatures) and promise a viable route for various photonic applications.

Keywords – graphene, plasmons, terahertz radiation

I. Introduction

Graphene has recently demonstrated great promise for midand far-infrared plasmonics[1] and attracted a great deal of attention as a platform for plasmonic radiation detectors[2,3]. With lowering the operation frequency down to the THz domain, the resonant excitation of plasmons becomes exceedingly difficult and can only be achieved if the momentum relaxation rate is below the plasmon frequency, which, in turn, requires ultra-high electron mobility. For this reason, in all graphene-based far-field THz detectors reported so far, the plasma waves—if any—were overdamped, and the devices exhibited only a broadband (nonresonant) photoresponse[4,5]. As a result, numerous applications relying on resonant plasmon excitation (see e.g. refs. 3, 6–9) remain experimentally yet unrealized.

II. Experimental Results

There are three crucial steps to consider in the design of resonant photodetectors. First, the incoming radiation needs to be efficiently compressed into plasmons propagating in the FET channel. Second, the channel should act as a high-quality plasmonic cavity, where constructive interference of propagating plasma waves leads to the enhancement of the field strength. Third, the high-frequency plasmon field needs to be rectified into a dc photovoltage. To meet these hard-to-satisfy 5–8 requirements, we fabricated proof-of-concept detectors using high-mobility bilayer graphene (BLG) FETs.

Figure 1 shows the gate voltage dependence of device responsivity recorded in response to 2 THz radiation. The device response exhibits prominent oscillations, despite the fact that the FET-factor, $F = dG/dV_G \cdot G^{-1}$, as a function of Vg is featureless (black curve in Fig. 1). The oscillations are clearly visible for both electron and hole doping and display better contrast on the hole side, likely because of the aforementioned p–n junction rectification. Resonances are well discerned at 10 K, although they persist up to liquidnitrogen T, especially for Vg < 0 (see the inset of the Fig. 1).

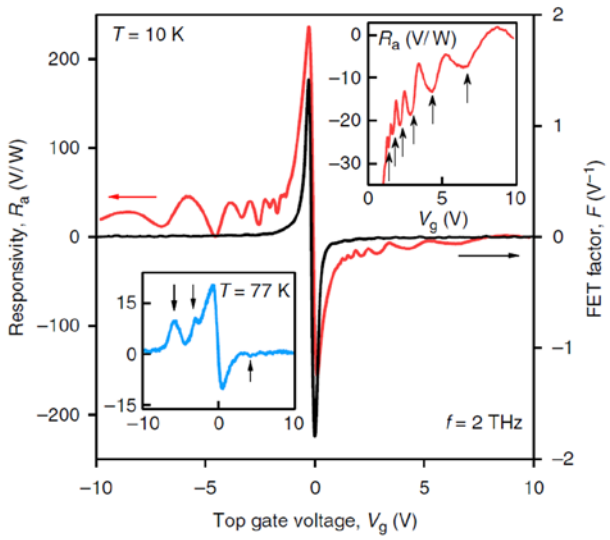

Fig. 1. Gate dependence of responsivity recorded under 2 THz radiation. The upper inset shows a zoomed-in region of the photovoltage for electron doping. Resonances are indicated by black arrows. Lower inset: resonant responsivity at liquid-nitrogen temperature.

III. Discussion

We argue that the observed peaks in the photoresponse emerge as a result of plasmon resonance in the FET channel. To this end, we model our FET as a plasmonic Fabry-Perot cavity endowed with a rectifying element. In gated 2D electron systems, the relation between the frequency ω and the real part of the wave

vector q' is linear, $\omega = sq'$, where the plasmon phase velocity is a function of the carrier concentration and is tuned by the gate voltage[10]. For bilayer graphene square of plasmon phase velocity is proportional to the gate voltage. Our data allows for further analysis of the plasmon spectrum in bilayer graphene, estimation of the resonance q-factor and characteristic decay time, τ_p.

IV. Conclusions

In conclusion, we have shown that high-mobility graphene FETs exploiting far-field coupling to incoming radiation can operate as resonant THz photodetectors. In addition to their potential applications in high-responsivity detection and on-chip spectroscopy of the THz radiation, our devices also represent a convenient tool to study plasmons under conditions where other approaches may be technically challenging.

Acknowledgments

This work was financially supported by the Rissian Foundation for Basic Research (Project N° 18-29-20116-mk).

References

[1] Dhillon, S. S. *et al*. *J. Phys. D Appl. Phys.* **50**, 043001 (2017).
[2] Grigorenko, A., Polini, M. and Novoselov, K. *Nat. Photonics* **6**, 749–758 (2012).
[3] Koppens, F. H. L. et al. *Nat. Nanotechnol*. **9**, 780–793 (2014).
[4] Cai, X. et al. *Nat. Nanotechnol*. **9**, 814–819 (2014).
[5] Auton, G. et al. *Nano Lett*. **17**, 7015–7020 (2017).
[6] Otsuji, T., Hanabe, M., Nishimura, T. & Sano, E. *Opt. Express* **14**, 4815–4825 (2006).
[7] Tomadin, A., Tredicucci, A., Pellegrini, V., Vitiello, M. S. and Polini, M. *Appl. Phys. Lett*. **103**, 211120 (2013).
[8] Ryzhii, V., Otsuji, T., Ryzhii, M. & Shur, M. S. *J. Phys. D Appl. Phys*. **45**, 302001 (2012).
[9] Fateev, D. V., Mashinsky, K. V. and Popov, V. V. *Appl. Phys. Lett.* **110**, 061106 (2017).
[10] D. Bandurin, et al., *Nature Communications*, **9**, 5392 (2018).

Excitation of the Propagating "Nonradiative" Plasmon Modes in Periodic Graphene Structures

D. V. Fateev[1,2], K. V. Mashinsky[1], I. M. Moiseenko[1], O. V. Polischuk[1], V. V. Popov[1]

[1] Kotelnikov Institute of Radio Engineering and Electronics, Russian Academy of Sciences, Saratov, Russia
[2] Saratov State University, Saratov, Russia

E-mail: FateevDV@yandex.ru

Abstract – We theoretically investigate the excitation of nonradiative plasmon modes in an asymmetric graphene structures. The combining excitation of radiative and "nonradiative" plasmon modes lead to the unidirectional energy flux along the graphene plane.

Keywords – plasmon, graphene, terahertz

I. Introduction

Graphene is a perspective media for excitation and investigation of the plasmons in terahertz (THz) frequency range[1] mostly to the high charge carriers mobility around 100000 cm2/(Vs)[2] and momentum relaxation time of charge carriers $\tau = 2$ ps at room temperature.[3] It has been suggested to use the plasmon properties of a periodical graphene structure to amplify,[4] detect,[5] and transform THz waves.[6] Coupling of plasma waves in graphene[7] to incident electromagnetic wave demands special couplers which balance different momenta of the incident electromagnetic wave and the plasmon. Typical wide-area couplers to be used for exciting standing THz plasmon in graphene are periodical one-dimensional[8] and two-dimensional[9] gratings. Plasmon excitation in such wide-area graphene structures can be identified via absorption of the energy of incident electromagnetic wave.

Incident THz wave couples with a radiative eigen plasmon modes in a spatially symmetric plasmon systems. While the "nonradiative" plasmon modes with almost zero net dipole momenta can be excited only spatially asymmetric systems.[10]

In this work, we demonstrate that the excitation of "nonradiative" plasmon modes in a periodic graphene structure with dual-grating gate (DGG) and asymmetric unit cell induced the lateral plasmon energy flux in structure.

II. Theoretical model

The DGG structure under consideration is shown in Fig. 1. The homogeneous graphene layer is separated from the DGG by a thin dielectric slab with thickness *d*. The graphene layer is screened by spatially homogeneous metallic back gate. The thickness of dielectric slab between graphene and the back gate is *h*. The THz electromagnetic wave with the electric field polarized across the DGG fingers is normally incident from the top onto the metal DGG. The DGG consists of two periodical interdigitated sub gratings. Two subgratings of the DGG are laterally shifted in respect to each other in order to introduce an asymmetry into the unit cell of the periodic DGG-graphene structure.

We solve the problem of the excitation of plasmon modes in DGG-graphene structure within a self consistent electromagnetic approach using the full system of the Maxwell equations. The solving of the electromagnetic problem consists of transforming the Maxwell equations and boundary conditions into the spatial Fourier representation, then formulating the integral equations with respect to the surface currents in DGG strips, and numerically solving the integral equations by the Galerkin procedure with the expansion of surface currents into series on the Legendre polynomials The THz response of graphene is described by the dynamic conductivity. [11]

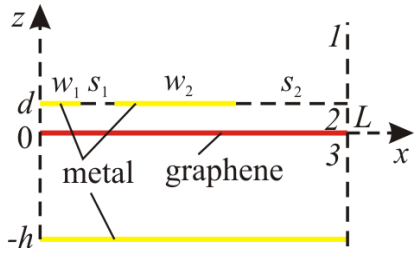

Fig. 1. Schematic view of the one unit cell of the DGG graphene structure.

The electromagnetic energy flux in the graphene structure is described by the time-averaged Poynting vector $S = 0.5\,\mathrm{Re}[\mathbf{E}\mathbf{H}^*]$, where **E** is the total electric field and **H** is the total magnetic field. We investigate the excitation of the plasmons in DGG graphene structure by the TM electromagnetic wave of the DGG and, therefore, the energy flux has two components: incident flux of THz wave $S_z = 0.5\,\mathrm{Re}\left(E_x H_y\right)$ and lateral plasmon flux $S_x = -0.5\,\mathrm{Re}\left(E_z H_y\right)$. The lateral energy flux of the plasmon in the x-direction given by averaged over the spatial period of the structure and integrated over z-coordinate the x-component of the Poynting vector

$$S_x^{\mathrm{P}} = \frac{1}{L}\int_{-\infty}^{+\infty}\int_{0}^{L} S_x\,dx\,dz\,,$$

where *L* is the spatial period of the structure.

We introduce the coefficient of transformation of the incident wave into propagating plasmon as

$$T_P = \frac{S_x^{\mathrm{P}}}{\left|S_{L,z}^{\mathrm{inc}}\right|},$$

where $S_{L,z}^{\mathrm{inc}} = LS_z^{\mathrm{inc}}$ and S_z^{inc} is the Poynting flux of THz wave incident onto one unit cell of the periodic DGG structure.

III. Results and discussions

In DGG graphene structure with long distances between graphene and DGG *d*, it is possible to excite the plasmon modes with wavenumbers quantized as $k_x = 2\pi n / L$ (where n is an integer) (Fig. 2). Such plasmon modes can be excited when the distance between the DGG and graphene is comparable with (or greater than) DGG finger widths. Additionally to radiative plasmon modes, in spatially asymmetric DGG structures the "nonradiative" plasmon modes can be excited. We examine the interaction of the radiative and "nonradiative" plasmon modes optimizing every geometrical parameters of the DGG graphene structure. Due to tuning of resonant frequencies of the radiative and "nonradiative" modes with changing filling factor $(s_1 + s_2)/(w_1 + w_2)$ it can be possible to excite radiative and "nonradiative" plasmon modes at the same frequency (5.025 THz at Fig. 3). The maximum transformation coefficient reaches its maximum of 71.5% (Fig. 3) for 1 ps carrier momentum relaxation time in case of excitation of the plasmon mode with wavenumber $k_x = 4\pi / L$. The transformation coefficient for this plasmon mode reaches its maximum value for the asymmetry coefficient of K = 0.7. The distribution of in-graphene-plane component of the electric field at the maximum transformation point corresponds to the excitation of spatially asymmetric plasmon mode with $k_x = 4\pi / L$ (Fig. 3). In such case, the calculated velocity of the propagating plasmon is 3.77×10^6 m/s.

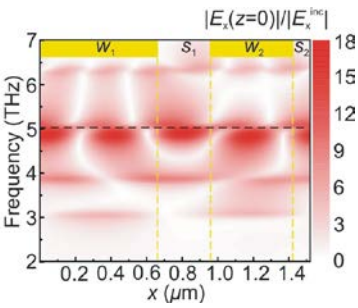

Fig. 2. Spectra of transformation coefficient T_p depending on the width of the gate finger w_1. The point of maximum transformation is shown by the cross of the dashed straight lines.

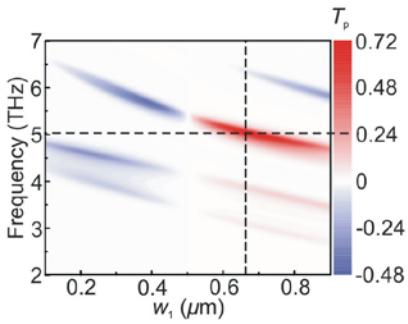

Fig. 3. Spatial distribution of the *x*-component of the electric field over the unit cell of DGG graphene structure at the point of maximum transformation frequency for w_1 = 0:672 μm and frequency 5.025 THz.

IV. Conclusions

The combining excitation of radiative and "nonradiative" plasmon modes lead to the unidirectional energy flux along the graphene plane. The excitation of interaction of Periodical structures with asymmetric unit cell can be utilized as transformers of the incident electromagnetic wave into propagating plasmons.

Acknowledgments

This work was financially supported by Russian Science Foundation through the Grant No. 18-79-10041.

References

[1] F. J. Garcia de Abajo, *ACS Photonics* **1**, 135 (2014).
[2] A. S. Mayorov, R. V. Gorbachev, S. V. Morozov, L. Britnell, R. Jalil, L. A. Ponomarenko, P. Blake, K. S. Novoselov, K. Watanabe, T. Taniguchi, and A. K. Geim, *Nano Lett.* **11**, 2396 (2011).
[3] D. Svintsov, V. Vyurkov, S. Yurchenko, T. Otsuji, and V. Ryzhii, *J. Appl. Phys.* **111**, 083715 (2012).
[4] O. V. Polischuk, D. V. Fateev, T. Otsuji, and V. V. Popov, *Appl. Phys. Lett.* **111**, 081110 (2017).
[5] D. V. Fateev, K. V. Mashinsky, and V. V. Popov, *Appl. Phys. Lett.* **110**, 061106 (2017).
[6] O. V. Polischuk, V. S. Melnikova, and V. V. Popov, *Appl. Phys. Lett.* **109**, 131101 (2016).
[7] V. Ryzhii, *Japan. J. Appl. Phys.* **45**, L923 (2006).
[8] L. Ju, B. Geng, J. Horng, C. Girit, M. Martin, Z. Hao, H. A. Bechtel, X. Liang, A. Zettl, Y. R. Shen, and F. Wang, *Nature Nanotech.* **6**, 630634 (2011).
[9] H. Yan, X. Li, B. Chandra, G. Tulevski, Y. Wu, M. Freitag, W. Zhu, P. Avouris, and F. Xia, *Nature Nanotech.***7**, 330334 (2012).
[10] V. V. Popov, D. V. Fateev, E. L. Ivchenko, and S. D. Ganichev, *Phys. Rev. B* **91**, 235436 (2015).
[11] M. S. Jang, V. W. Brar, M. C. Sherrott, J. J. Lopez, L. Kim, S. Kim, M. Choi, and H. A. Atwater, *Phys.Rev. B* **90**, 165409 (2014).

Influence of the Length of the CNT and Plasma Treatment on the Terahertz Conductivity Spectra of CNT Films

S. S. Zhukov[1], D. S. Kopylova[2], A. P. Tsapenko[2], A. V. Mogorychnaia[1], E. S. Zhukova[1], A. G. Nasibulin[2], B. P. Gorshunov[1]

[1] Moscow Institute of Physics and Technology, Dolgoprudny, Moscow Region, Russia
[2] Skolkovo Institute of Science and Technology, Moscow, Russia

E-mail: zs1978@mail.ru

Abstract – The time-domain spectroscopy is used to study the conductivity mechanisms of free-standing macroscale films of disordered single-walled carbon nanotubes of two types — of various tube's lengths and films treated with oxygen plasma. Change in the temperature dependence of the terahertz conductivity from metallic type in long tubes to non-metallic in short tubes and similar behavior of the conductivity with increase in the plasma exposure time is found and analyzed.

Keywords – conductivity, carbon nanotubes, terahertz spectroscopy

I. Introduction

Large-scale films of disordered carbon nanotubes (CNTs) are the materials with physical properties determined by the intrinsic parameters of individual CNTs, the fabrication method of films and the post-processing [3–4]. Presently, it is possible to obtain free-standing thin films composed of nanotubes of fixed length [1–3]. Such material is potentially attractive for the application in photonics and electronics [4]. In this view, understanding of the fundamental mechanisms of interaction of the electromagnetic radiation with CNT films seems to be of high relevance. Therefore, thin films composed of randomly oriented single-walled carbon nanotubes (SWCNT), pristine and treated by oxygen plasma, are ideal materials for studying such mechanisms.

Using terahertz time-domain and standard Fourier-transform spectrometers a systematic study of the electrodynamic properties of free-standing macroscale films composed of high-quality pristine SWCNTs [5] of various lengths and treated by oxygen plasma is performed. Spectra of the complex dielectric permittivity $\varepsilon^*(\nu)=\varepsilon'(\nu)+i\varepsilon''(\nu)$ and conductivity $\sigma^*(\nu)=\sigma_1(\nu)+i\sigma_2(\nu)$ in the range of 5–100 cm^{-1} and transmission coefficient in the range of 100–15000 cm^{-1} are measured at temperatures 4–300 K. Obtained broadband conductivity spectra are modeled with a standard Drude-Lorenz expression. Due to the friability of the films, their thickness *d* cannot be accurately determined. Therefore, all the results are analyzed in terms of the complex conductance of the films $\sigma^*(\nu)*d$.

II. Results

Figure 1 demonstrates conductance spectra for macroscale films with average lengths of CNTs of 0.3, 1, 6, 13 and 40 μm (Fig. 1a), and films treated by oxygen plasma with exposure time of 1, 10, 30, 90,105,180, 210 and 420 seconds (Fig. 1b).

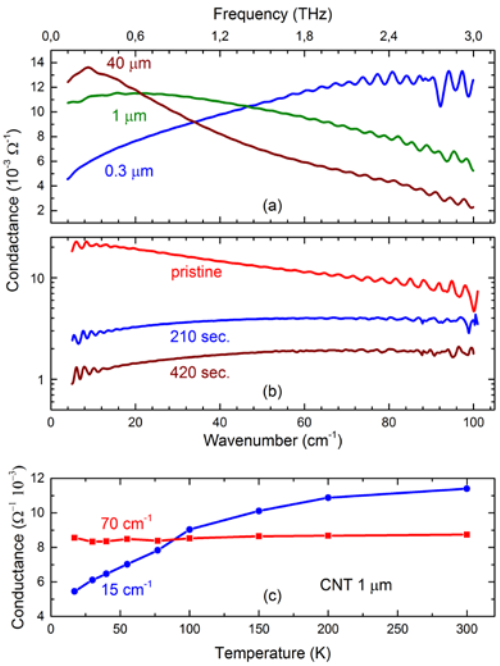

Fig. 1. Real part of conductance, $\sigma_1(\nu)*d$, of films composed of CNT with average lengths of 0.3, 1, and 13 μm (a) and films treated with oxygen plasma with an exposure of 210 and 420 seconds (b), temperature dependence of conductance of films composed of CNT with average lengths of 1 μm for 15 cm^{-1} and 70 cm^{-1} (c) .

For plasma treated samples conductivity transforms from typically metallic for pristine films to more semiconductor-like with increasing of exposure time simultaneously becoming more transparent over the

entire measured frequency range. With decreasing temperature spectra of the real part of conductance $\sigma_1(\nu)*d$ also decreases.

For the films compiled of CNTs with different lengths change in the temperature dependence of conductivity from metallic type to semiconductor occurs below a certain frequency determined by the length of CNTs (Fig. 1c). These specific frequency shifts to the longwave region with decrease of the length of the CNTs.

Temperature dependence of the conductance spectra in the terahertz frequency range is similar for both films treated with oxygen plasma and for films with CNTs of different lengths. All samples demonstrate a peak in the spectra of the real part of the terahertz conductance $\sigma_1(\nu)*d$ which is more pronounced in the films with CNTs of different length. Frequency position of these peak decreases with increasing temperature. In addition, the peak shifts towards lower frequencies with increasing the length of the CNTs or with decreasing plasma exposure time. We consider such frequency-temperature behavior of CNT films as a result of interplay between intrinsic properties of carriers inside individual CNT and their ability of hopping through potential barriers at the contact points of the tubes – phonon-assisted hopping.

ACKNOWLEDGMENTS

This work was financially supported by RFBR 18-32-00246.

REFERENCES

[1] E.S. Zhukova, A.K. Grebenko, A.V. Bubis et al., *Nanotechnology* **28,** 44 (2017).
[2] B.P. Gorshunov, E.S. Zhukova, Ju.S. Starovatykh et al., *Carbon* **126** (2018).
[3] E.S. Zhukova, B.P. Gorshunov, A.P. Tsapenko et al., *Journal of Physics: Conference Series* **1092**, art. no. 012178 (2018).
[4] D.S. Kopylova, F.S. Fedorov, A.A. Alekseeva et al., *Nanoscale* **10** (2018).
[5] A. Kaskela, A.G. Nasibulin, M.Y. Timmermans et al., *Nano Lett.* **10** (2010).

Giant Amplification of Terahertz Plasma Waves in Tapered Heterostructure with Active Graphene

M. Yu. Morozov, V. V. Popov

Kotelnikov Institute of Radio Engineering and Electronics (Saratov Branch), RAS, Saratov, Russia

E-mail: mikhail.yu.morozov@gmail.com

Abstract – Amplification of terahertz plasmons in tapered metal-insulator-graphene heterostructure is studied. It is shown that the plasmon energy flux in the tapered structure can become nearly four orders of magnitude greater as compared to the same value in active pristine graphene due to nanofocusing of the plasmon electromagnetic field.

Keywords – terahertz plasmons, graphene, tapered structures, amplification

I. Introduction

Nanofocusing of the surface plasmon propagating toward the tip in a tapered plasmonic waveguides was predicted and demonstrated theoretically [1] and experimentally [2]. Graphene, being a two-dimensional material with a zero band-gap [3], is a prospective material for terahertz (THz) lasers [4] and plasmonic amplifiers [5, 6]. Strong field localization of plasmons allows for high efficiency of the interaction between electromagnetic radiation and free charge carriers in graphene. Shielding the graphene by the metal plane leads to further increase of plasmon field localization in vicinity of graphene layer [7]. We study the nanofocusing and amplification of THz plasmons in tapered metal-insulator-graphene heterostructure schematically shown in Fig. 1. We consider the propagation of plasmons in active graphene (with inversion of population of free charge carriers in it). Graphene is placed on a dielectric cladding and shielded by a metallic plane, separated from graphene by the tapered dielectric barrier layer with varying width $d(x)$. We study the plasmon propagation toward the taper apex. The taper angle is assumed to be small (equal to or less than $\alpha = 5^\circ$).

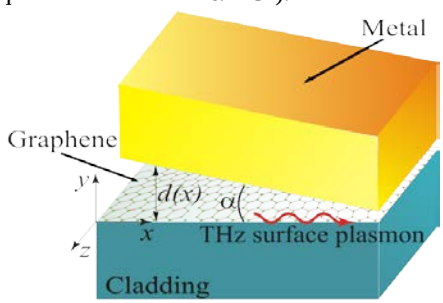

Fig. 1. Schematic view of the structure under consideration

II. Theoretical model

To study nanofocusing of THz plasmons in the mentioned tapered structure one needs to obtain the plasmon energy flux and energy density values in an arbitrary point of the tapered structure. To evaluate the energy flux in the tapered structure, the structure is considered as a sequence of thin layers in the direction of the wave propagation. In each layer a graphene and a metal are supposed to be parallel to each other. When going from the previous layer to the next one, the distance between a graphene and a metal changes instantly by a finite value at the layers boundary.

We focus on transverse magnetic (TM) plasmon modes and suggest the following algorithm of determination of the energy flux value along the tapered structure. First, we solve the Maxwell equations and find the relations between the electric and magnetic field components in the layers of the structure as well as derive the dispersion relation for plasmons in the tapered structure

$$\frac{\varepsilon_b}{k_x(x_n)}\coth\left(k_x(x_n)\cdot d(x_n)\right)+\frac{\varepsilon_c}{k_x(x_n)}=-i\frac{\sigma(\omega)}{\varepsilon_0\omega}, \quad (1)$$

where k_x and ω are the wavevector and the frequency of the plasmon, ε_b and ε_c are the dielectric constants of the barrier layer and the cladding, respectively, ε_0 is the electric constant, x_n (where n is a natural number) means the discrete coordinate along the x axis with a step equals to the thickness of the thin layer, in other words $x_{n+1}-x_n=\Delta_x$, where Δ_x is a thickness of the layer from the sequence of thin layers into which the tapered structure is divided, and $\sigma(\omega)$ is the dynamic conductivity of active graphene [5].

The plasmon energy flux in the x-direction can be related to the plasmon field components as

$$S(x_n)=1/2\int_{-\infty}^{d(x_n)}\mathrm{Re}\left(E_y(x_n,y)\cdot H_z^*(x_n,y)\right)dy. \quad (2)$$

Substituting the relations between the electric and magnetic field components of plasmon field in formula (2) one can find the plasmon electric and magnetic field components in a given layer of the structure corresponding to the specific value of the plasmon energy flux in this layer. Once knowing the electric field component value in a given layer of the structure, one can define the power density, released in graphene layer due to interaction of the plasmon electric field with graphene in a certain layer of the structure

$$P(x_n) = -1/2 \cdot \mathrm{Re}\,\sigma(\omega) \cdot \left|E_x(x_n, y=0)\right|^2, \qquad (3)$$

where $E_x(x, y=0)$ is the tangential to graphene component of the plasmon electric field in the graphene plane.

The spatial variation of the energy flux is defined by the value of power density released in the graphene layer [8], and is given by the recurrent formula:

$$S(x_{n+1}) = S(x_n) + P(x_n) \cdot \Delta_x, \qquad (4)$$

So, knowing the plasmon energy flux and power density, released in graphene, in a given layer of the structure, one can find the plasmon energy flux in the neighboring layer, using formula (4).

To evaluate the energy flux value along the active pristine (unshielded) graphene one can use the algorithm presented above deriving the relations between the electric and magnetic field components in the layers of the structure with the pristine graphene from the Maxwell equations and applying the dispersion relation for plasmons in the active unshielded graphene instead the Eq. (1), that could be written as

$$k_x(x_n) = i\frac{\varepsilon_0(\varepsilon_\mathrm{b} + \varepsilon_\mathrm{c})\omega}{\sigma(\omega)}.$$

Note, that in the structure with pristine graphene the plasmon wave vector remains constant along the structure for fixed frequency and parameters of the structure while in the tapered structure the plasmon wave vector changes along the structure due to changing of dielectric barrier layer width $d(x_n)$.

III. Discussion

In Fig. 2 we plot the plasmon energy fluxes in the tapered structure (curve *1*) versus the distance from the taper apex and in active pristine graphene (curve *2*) versus the distance along the graphene layer.

One can see that, for both the tapered structure and an active pristine graphene, the energy flux of the plasmon monotonically increases while the wave moves along the graphene layer due to amplification of plasmon by the power released from graphene.

At the same time, the plasmon energy flux in the tapered structure becomes nearly four orders of magnitude greater as compared to the same value in active pristine graphene approaching the taper apex. This is because of the plasmon electromagnetic field nanofocusing due to increasing of plasmon mode localization when moving toward the taper apex in tapered structure.

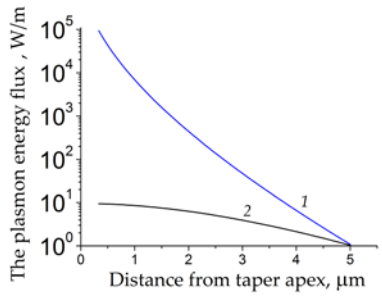

Fig. 2. The plasmon energy fluxes in the tapered structure (curve *1*) versus the distance from the taper apex and in active pristine (unshielded) graphene (curve *2*) versus the distance along the graphene layer.

IV. Conclusions

We have studied the amplification of THz plasma waves in the tapered metal-insulator-graphene heterostructure. It is shown that the plasmon energy flux in the tapered structure can become nearly four orders of magnitude greater as compared to the same value in active pristine graphene due to nanofocusing of the plasmon electromagnetic field. Amplified plasmons can be used in the active elements of the THz plasmonic graphene nanocircuits.

Acknowledgments

This work was financially supported by Russian Science Foundation through Grant No. 18-72-00009.

References

[1] M. I. Stockman, *Phys. Rev. Lett.* **93**, 137404 (2004).
[2] V. S. Volkov, et al., *Nano Lett.* **9**, 1278, 2009.
[3] K. S. Novoselov, A. K. Geim, et al., *Science* **306**, 666 (2004).
[4] V. Ya. Aleshkin, A. A. Dubinov, V. Ryzhii, *Pisma v JETF* **89**, 70 (2009).
[5] A. A. Dubinov, et al., *J. Phys.: Condens. Matter* **23**, 145302 (2011).
[6] V. V. Popov, et al., *Phys. Rev. B* **86,** 195437 (2012).
[7] M. Yu. Morozov, et al., *Technical Physics Letters* **42**, 40 (2016).
[8] M. Yu. Morozov, I. M. Moiseenko, V. V. Popov, *J. Phys.: Condens. Matter* **30**, 08LT02 (2018).

Broadband Dielectric Spectroscopy of Eumelanin

Z. V. Gagkaeva[1], K. A. Motovilov[1], V. Grinenko[2,3], M. Savinov[4], L. S. Kadyrov[1], A. A. Pronin[5], Z. V. Bedran[1], E. S. Zhukova[1], A. B. Mostert[6], B. P. Gorshunov[1]

[1] Moscow Institute of Physics and Technology, Moscow, Russia
[2] Institute for Solid State and Materials Physics, Dresden, Germany
[3] Institute for Metallic Materials, IFW Dresden, Dresden, Germany
[4] Institute of Physics AS CR, Praha, Czech Republic
[5] Prokhorov General Physics Institute of the Russian Academy of Sciences, Moscow, Russia
[6] Department of Chemistry, Swansea University, Wales, UK

E-mail: gagkaeva@phystech.edu

Abstract – The recent development of bioelectronics provoked a growth in demand for conductive biomaterials. Natural pigment eumelanin is a promising material for this field of science and technology. In the current study, we investigate the impact of water content on charge transfer in eumelanin by means of broadband dielectric spectroscopy and specific heat measurements.

Keywords – eumelanin, spectroscopy, conductivity

I. Introduction

Bioelectronics is a rapidly evolving area of science at the junction of physics, biology and medicine. One of its major goals is investigation of materials for already existing and many potential applications in such important research areas as health monitoring, drug delivery, implanting, biosensing, etc. (1) Among the problems, which rise during searching for the appropriate materials for bioelectronic devices, one of the most important is the impact that water has on the electrical conductivity. This follows from the fact that in biological systems, electric currents are mostly due to protons and other ions, whose mobility depends on the presence of water molecules. (2) Therefore, a thorough investigation of water influence on charge transport becomes extremely important for development of bioelectronic devices. (3)

Herein we demonstrate the results of wide temperature range (5–300 K) measurements of heat capacity and complex dielectric parameters (frequency range from 1 Hz to 3 THz) of two eumelanin samples with different humidity levels and show how spectroscopic analysis can deepen the understanding of water-controlled internal processes in the material.

II. Results

The measured spectra of real part of complex AC conductivity for two samples at several temperatures are shown in Figure 1. One of the samples (dry) was preliminary dried in vacuum for 10 hours; another one (wet) was hydrated at 48% RH at 22°C. In the low-frequency part of spectra one can see (dashed blue line) typical for disordered materials nearly constant losses regime (4)

$$\varepsilon''(\nu) \sim \sigma_1/\nu \approx \text{const},$$

$$\sigma(\nu) \sim \nu^s,\ s \approx 1 \qquad (1)$$

This regime describes well the low-frequency behavior of dry eumelanin at all temperatures.

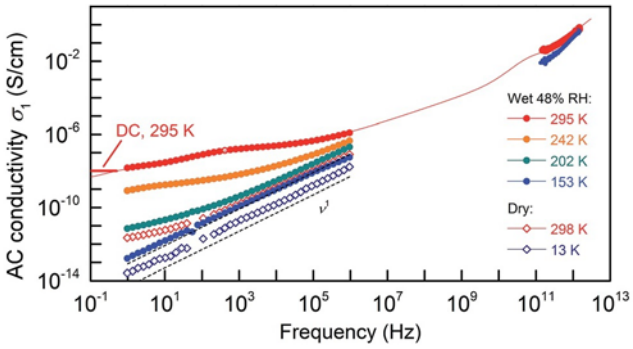

Fig. 1. Broadband spectra of real part of AC conductivity (σ_1) of dry and wet eumelanin samples at different temperatures. Solid circles correspond to melanin incubated at 48% RH, empty rhombuses – to melanin dried in vacuum, red solid line – to fitting of the room-temperature wet sample spectrum, and dashed blue line – to the $\sigma_1 \sim \nu^s$, $s \approx 1$, dispersion in the nearly-constant loss regime.

The situation changes when water content within the sample increases: in the wet sample spectra, two relaxation processes with characteristic frequencies of 0.2 Hz and 60 Hz are observed, that are accompanied by hopping-type contribution to the conductivity that is getting more pronounced with heating up to the room temperature. The relaxations are described using Havriliak-Negami model (5):

$$\varepsilon^*(\nu) = \varepsilon_\infty + \Delta\varepsilon\,[1 + (i\omega)/f_R]^{-\beta}, \qquad (2)$$

where $\Delta\varepsilon$ is dielectric contribution, ω is circular frequency, f_R is relaxation frequency, α and β characterize broadness and asymmetry of the peak, respectively, and the term that describes the hopping conductivity (6)

$$\sigma_1(\nu) = A\nu^s. \qquad (3)$$

The lower frequency relaxation process in wet sample can be identified with slow relaxation of large colloidal particles formed by melanin monomers with semiquinone anion moieties. These monomers appear as a result of the comproportionation reaction, which is driven by change in the water content (3). The 60 Hz feature, which is also weakly manifested in the spectra of dry sample, can be connected with carboxylic acid groups

present in melanin. The changes that correlate with increase of water content also correlate with the changes in terahertz spectra, where the Debye-like relaxation that is typical for bulk water is observed for wet melanin and is vanishing while cooling down or drying the samples.

The specific heat data for both dry and wet samples reveal a boson peak excitation – a feature that is characteristic for disordered systems. Analysis of the boson peak parameters allows to conclude that there exist structural changes in wet sample compared to dry sample.

III. Conclusions

We have conducted broadband dielectric spectroscopic and heat capacity measurements in a wide temperature range of eumelanin samples with different water contents. The obtained results show strong correlation between humidity levels and conductivity values and mechanisms in eumelanin.

Acknowledgments

This work was financially supported by the project N3.9896.2017/BY.

References

[1] P. Meredith, C.J. Bettinger, M. Irimia-Vladu, A. B. Mostert and P.E. Schwenn, *Reports on Progress in Physics*, **76**, 034501 (2013).
[2] M. Sheliakina, A.B. Mostert and P. Meredith, *Advanced Functional Materials* **28**, 1805514 (2018).
[3] K.A. Motovilov, V. Grinenko, M. Savinov, Z.V.Gagkaeva, L.S. Kadyrov, A.A. Pronin, Z.V. Bedran, E.S. Zhukova, A.B. Mostert and B.P. Gorshunov, *RSC Advances* **9**, 3857–3867 (2019).
[4] K.A. Motovilov, M. Savinov, E.S. Zhukova, A.A. Pronin, Z.V. Gagkaeva, V. Grinenko, K.V. Sidoruk, T.A. Voeikova, P.Y. Barzilovich, A. K. Grebenko, S.V. Lisovskii, V.I. Torgashev, P. Bednyakov, J. Pokorn´y, M. Dressel and B.P. Gorshunov, *Sci. Rep*. **7**, 15731 (2017).
[5] S. Havriliak and S. Negami, *Polymer* **8**, 161–210 (1967).
[6] A. K. Jonscher, *Dielectric Relaxation in Solids*, (Chelsea Dielectrics Press Ltd, London, 1983).

Plasmonics with Graphene Nanoribbons

V. Perebeinos

Department of Electrical Engineering, University at Buffalo, the State University of New York, Buffalo, NY, 14260, USA

E-mail: vasilipe@buffalo.edu

Abstract – In recent years, 2D materials, such as graphene, have attracted much attention due to their excellent transport and optical properties. I will discuss our recent results on plasmon scaling in graphene nanoribbon arrays as a function of nanoribbon width, spacing between ribbons, and doping level [1].

Keywords – graphene, plasmon, infrared photonics, spectroscopy

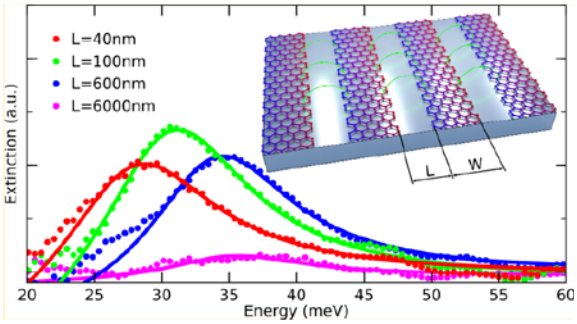

Fig. 1. Extinction coefficient measured (dots) and calculated (solid curves) in graphene nanoribbon arrays of fixed width W = 600 nm and varied spacing between them L.

References

[1] V. Semenenko, S. Schuler, T. Mueller, and V. Perebeinos, ACS Photonics 5, 3459-3465 (2018).

Gyrotrons for High-Power Terahertz Science and Technologies

M. Yu. Glyavin

Institute of Applied Physics RAS, Nizhny Novgorod, Russia

E-mail: glyavin@appl.sci-nnov.ru

Abstract – This review aims to bring together information about the development and the most striking examples of high frequency gyrotrons applications. The paper describes the main features of terahertz gyrotrons. Some data about pulsed and CW tubes, working in the specified frequency range, are given. These gyrotrons demonstrate (in some specific combinations) extremely low voltage and beam current, narrow frequency spectrum, wide frequency tuning. Novel schemes of high frequency gyrotrons are analyzed. Examples of new technologies, opened by high-power THz radiation, are presented.

Keywords – gyrotron, THz, high power THz radiation, spectrum, spectroscopy and diagnostic

I. INTRODUCTION

The last decade has contributed to the rapid progress in the development of THz sources, in particular gyrotrons. Although in comparison with the classical microwave tubes the gyrotrons are characterized by greater volume and weight due to the presence of bulky parts (such as superconducting magnets and massive collectors where the energy of the spent electron beam is dissipated) they are much more compact and can easily be embedded in a sophisticated laboratory equipment (e.g. spectrometers, technological systems, etc.) than other devices with a comparable value of Pf^2 such as free-electron lasers (FEL) and radiation sources based on electron accelerators (Fig. 1). All these advantageous features have opened the road to many novel and prospective applications of gyrotrons as radiation sources in a great number of high power THz technologies, advanced spectroscopic techniques, plasma science and materials processing, fusion research as well as in many other scientific and technological fields.

II. RESAULTS

The gyrotron developed at IAP RAS provides CW radiation with a power from 1 W up to 1 kW in the frequency range 0.26–0.52 THz [1, 2] (see experimental facility in Fig. 2) and up to 1 MW at frequencies 0.14–0.17 THz. It is important, that low power (about 10 W) needed, for example, for spectroscopy applications can be obtained at low voltage about 1.5 kV or low beam current – tens mA.

The frequency stability of the gyrotron for spectroscopy application $df/f \sim 10^{-12}$ is demonstrated [3] by anode voltage feedback control. It is interesting, that the same scheme can be used for quick power modulation and data transmitting.

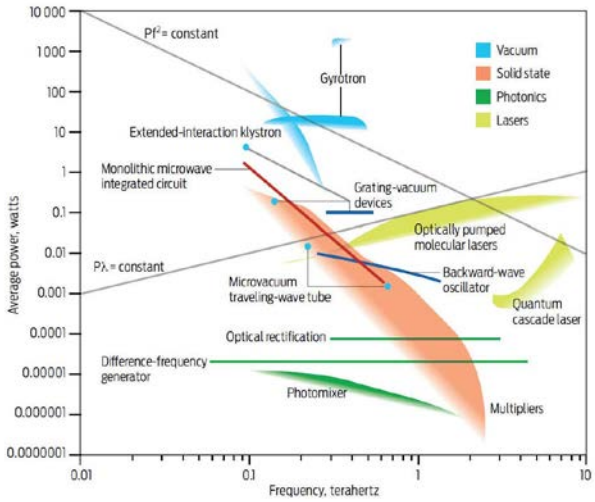

Fig. 1. The status of THz sources presented by C.M. Armstrong. "The truth about terahertz". IEEE Spectrum , 49(9):36–41, Sept. 2012.

The gyrotrons with pulsed magnetic fields operates with 100 kW power level at 0.7 THz and 1 kW at 1 THz frequency. The second harmonic CW gyrotron with improved mode selection based on double electron beam has been tested [4]. The wide step tuning of frequency by excitation of various modes was demonstrated in the range 0.4–0.75 THz. The stable operation at the frequency 0.76 THz on the second harmonic with power level about few Watts has been obtained, which useful for modern NMR/DNP spectroscopy application. The projects of "cold" (field emission) cathode [5] and low voltage (at the level 1.5–2 kV) gyrotrons are under development [6]. Preliminary calculation demonstrates possibility of wide (about 10%) fine frequency tuning. The complex cavities are under discussion for high harmonic excitation.

The pulsed gyrotron has been used successfully for initiation of localized gas discharges (Fig. 3). Such plasma is promising for development of both a point source of multi-charged ions and a source of high-energy ultraviolet (extreme ultraviolet EUV or XUV). The gas discharge has been successfully obtained also with 0.26 THz/CW IAP RAS gyrotron mentioned above [7]. The same gyrotron has been used also for the high-resolution molecular spectroscopy in a gas mixture. A significant improvement of spectrum quality due to

power growth in contrast with traditional BWO, has allowed observing the theoretically predicted earlier transitions in SO_2 molecule [8]. The sensitivity of the radio-acoustic detector was increased about three orders due to high power. The last interesting feature is high speed production of pure nanopowders by material evaporation and condensation. In the case of evaporation by 1 kW/CW/0.26THz radiation, the evaporation rate was increased approximately by an order in comparison with traditional heating methods [9].

Fig. 2. The CW experimental setup with liquid helium free cryomagnet

The prototype of CW 250 GHz /200 kW gyrotron has been successfully developed. The power up to 300 kW in 40 microsecond pulses has been obtained, and at the moment, the gas discharge experiments, initiated by mentioned microwaves, demonstrate unique plasma parameters.

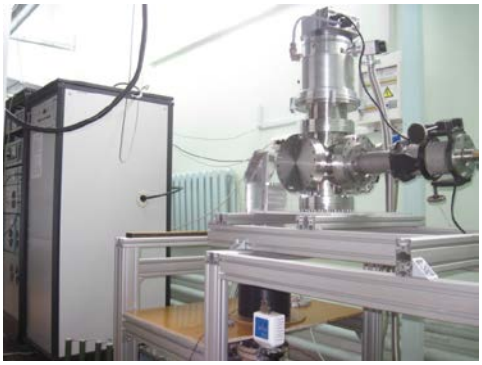

Fig. 3. The experimental setup for initiation of localized gas discharge based on the gyrotron with pulsed magnetic field

III. Conclusions

Despite the requirement for strong operating magnetic fields, sub-terahertz and terahertz frequency ranges have been already achieved both by the pulse and CW gyrodevices operating not only on fundamental, but also higher cyclotron harmonics. Today, relatively small-size gyrodevices with an output power significantly high than in solid-state or classical vacuum electronic devices are available soon for many applications (Fig. 4).

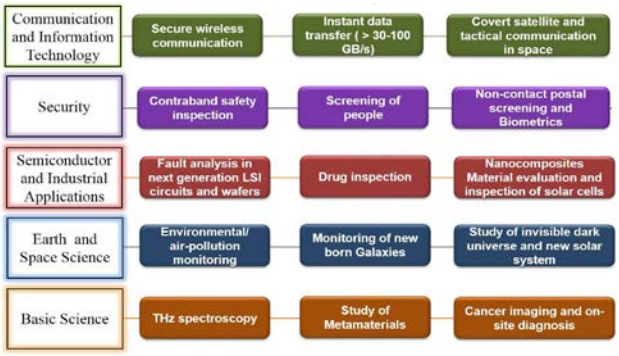

Fig. 4. The possible application of high-power THz from A. Srivastava "Microfabricated Terahertz Vacuum Electron Devices: Technology, Capabilities and Performance Overview" European Journal of Advances in Engineering and Technology, 2015, 2(8): 54-64.

Acknowledgments

The work supported in part by the Russian Scientific Foundation under the project 19-12-00141.

References

[1] M. Glyavin, G. Denisov, V. Zapevalov et al. High-power terahertz sources for spectroscopy and material diagnostics *PHYSICS-USPEKHI*, 59, 6, 595-604 (2016).

[2] M.Yu. Glyavin, A.V. Chirkov, G.G. Denisov et al. Experimental tests of 263 GHz gyrotron for spectroscopy applications and diagnostic of various media, *Rev. Sci. Instr.*, 86(5), 054705 (2015).

[3] A. Fokin, M. Glyavin, G. Golubiatnikov, L. Lubyako, M. Morozkin, B. Movschevich, A. Tsvetkov, G. Denisov. High power sub-terahertz microwave source with record frequency stability up to 1 Hz. *Scientific Reports* 8, 4317 (2018).

[4] T. Idehara, M. Glyavin, A. Kuleshov, et al. A Novel THz-Band Double-Beam Gyrotron for High-Field DNP-NMR Spectroscopy, *Rev. Sci. Instr.*, 88, 094708 (2017).

[5] M.Yu. Glyavin, V.N. Manuilov, G.G. Sominski et al. The concept of an electron-optical system with field emitter for a spectroscopic gyrotron. *Infrared Physics & Technology*, 78, 185-189 (2016).

[6] V. Bratman, A. Fedotov, A. Fokin et al. Operation of a sub-terahertz CW gyrotron with an extremely low voltage. *Physics of Plasmas*, 24, 11, 113105 (2017).

[7] M.Yu. Glyavin, S.V. Golubev, I.V. Izotov et al. A point-like source of extreme ultraviolet radiation based on a discharge in a non-uniform gas flow, sustained by powerful gyrotron radiation of terahertz frequency band, *Applied Physics Letters* 105, 174101 (2014).

[8] M.A. Koshelev, A.I. Tsvetkov, M.V. Morozkin et al. Molecular gas spectroscopy using radioacoustic detection and high-power coherent subterahertz radiation sources. *Journal of Molecular Spectroscopy*, 331, 9-16 (2017).

[9] A.V. Vodopyanov, A.V. Samokhin, N.V. Alexeev et al. Application of the 263GHz/1kW gyrotron setup to produce a metal oxide nanopowder by the evaporation-condensation technique. *Vacuum*, 145, 340-346, (2017).

Development of CW 527 GHz Gyrotron for DNP/NMR Spectroscopy

G. G. Denisov[1,2], A. V. Chirkov[1], A. P. Fokin[1], A. N. Kuftin[1], M. V. Morozkin[1], M. D. Proyavin[1], A. S. Sedov[1], E. M. Tai[2], A. I. Tsvetkov[1], and M. Yu. Glyavin[1,2]

[1] Institute of Applied Physics RAS, Nizhny Novgorod, Russia
[2] GYCOM Ltd., Nizhny Novgorod, Russia

E-mail: ap.fokin@mail.ru

Abstract – The paper presents the design features and results of experimental investigation of continuous wave gyrotron with operating frequency 527 GHz and output power of several W. The report includes the calculated parameters of the gyrotron, operating at the second cyclotron harmonic and experimental data of power, spectrum and wave beam profile.

Keywords – gyrotron, 527 GHz, spectroscopy

I. Introduction

In recent years, the interest in medium-power sources of sub-THz and THz radiation has steadily increased. Modern applications and scientific tasks require microwave sources with a frequency of more than 0.3 THz and power from several watts to tens of kilowatts. One of the most promising powerful sources in the terahertz frequency range are gyrotrons – devices based on the interaction of electrons rotating in an external magnetic field with an electromagnetic waves under cyclotron resonance conditions[1]. However, advancing into the terahertz range raises additional difficulties in the design and manufacturing of gyrotrons. The absence of commercially available cryomagnets with magnetic fields higher than 15 T and a sufficiently large hot bore diameter determines the operation at harmonics of the cyclotron frequency.

Radiation sources with a frequency of 0.4–0.5 THz and a power level of several tens of watts are necessary for modern DNP / NMR spectroscopy, therefore the development of gyrotrons in this frequency band is very important [2]. In this report, we present the design features and results of experimental investigation of a new continuous wave gyrotron with a frequency of 527 GHz operating at the second cyclotron harmonic.

II. Design and fabrication

After a scrupulous analysis of the spectrum of cylindrical cavity, the $TE_{-6,5}$ mode at the second cyclotron harmonic was chosen as the operating one. Selection of rather large cavity length ($L/\lambda \sim 35$) allowed to achieve reasonable starting current for operating mode (about 70 mA – see Fig. 1) at the cost of high ohmic losses – about 85% of the microwave energy dissipates in the cavity walls. The optimal injection radius of the electron beam is close to R_b = 0.875 mm. For selected cavity length L = 20 mm and beam pitch-factor g = 1.4 the total efficiency value, calculated based on self-consistent model [3], is about 3%.

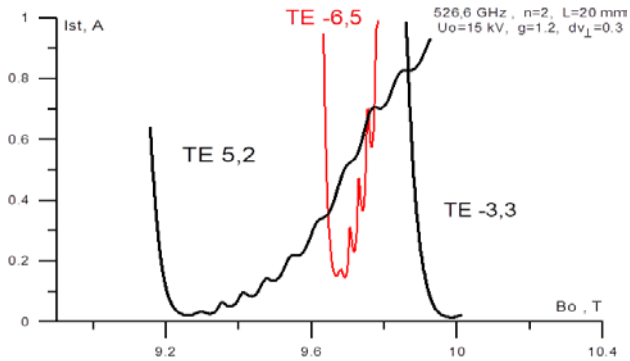

Fig. 1. Starting currents for the operating mode $TE_{-6.5}$ and two main competitors $TE_{-3.3}$ and $TE_{5.2}$

Since the cavity diameter of 3.976 mm is rather small and the optimal length of the uniform part is 20 mm, the manufacturing of the cavity with μm accuracy is a rather challenging task. For this gyrotron the cavity, together with the subcritical narrowing and the output waveguide, was made by sputtering copper onto a precisely made aluminum bar. Subsequently, the insert was etched.

The gyrotron has a built-in quasi-optical converter consisting of a regular waveguide cut, a parabolic mirror, two profiled corrective mirrors and two flat mirrors. Converter is optimized for working mode $TE_{-6,5}$, so other modes may scatter inside the converter and do not exit completely through the output window.

III. Experimental tests

For tests of the new tube the experimental facility[4] with 10 Tesla field intensity and 100 mm hot bore liquid helium free magnet JMTD-10T100 (JASTEC Inc., Japan) and 18 kV / 0.6 A high-voltage power supplies, equipped by control system, was used. Taking into account the low radiation power of the second harmonic sub-THz gyrotron, we updated the calorimetric dummy load for more accurate measurements. New dummy load is smaller with silicone oil used as a coolant instead of water. Lower flow rates as well as smaller heat capacity of oil allowed to achieve the sensitivity of this new power measurement device less than 0.5 Watts.

Fig. 2. The 527 GHz gyrotron in a liquid-helium free cryomagnet. The calorimetric dummy load (on the left) is attached to the output window.

We measured dependence of output power on magnetic field in the cavity while scanning magnetic field from 10 to 8.8 T and determined the zones of generation of the desired operating mode and the nearest parasitic modes (see Fig. 3). The accelerating voltage was 15 kV and the beam current was 0.4 A. Separately, more thorough investigation of dependences of the power on the magnetic field for the operating mode at currents of 400 and 500 mA was carried out. The maximum output power achieved in the experiment was 3 and 5 Watts respectively.

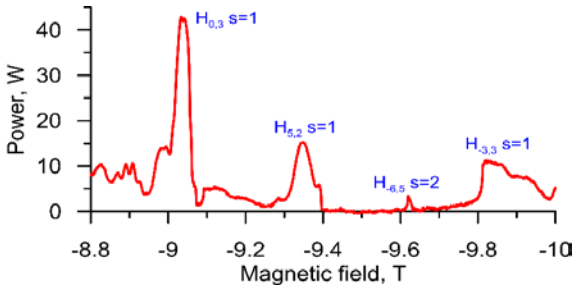

Fig. 3. Experimental dependence of gyrotron output power on magnetic field. Operating mode and nearest parasitic modes are noted.

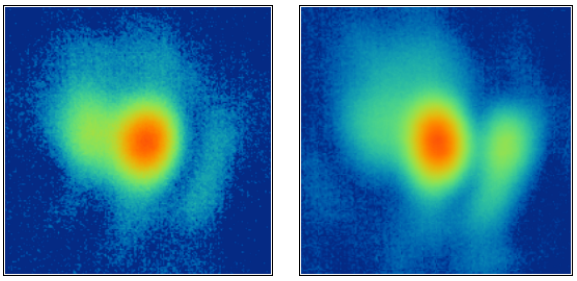

Fig. 4. Experimental wave beam profile at 1176 mm from the window for modes $H_{6,5}$ with positive magnetic field (left) and $H_{-6,5}$ with negative magnetic field (right). Aperture 135x135 mm.

In order to check whether low output power can be explained by an error in the cavity manufacturing or in design or manufacture of a quasi-optical converter, we measured the power loss in the resonator walls and the distribution of power in the wave beam emerging from the output window (see Fig. 4).

Similar wave beam profiles with both positive (directed from cathode to collector) and negative magnetic field direction (and corresponding inversion of wave rotation direction) indicate that high frequency field in the cavity does not rotate, i.e. two modes with opposite rotations are simultaneously excited. Since the radiation wavelength at the second harmonic is two times smaller, the operating mode is more sensitive to resonator misalignment – distortion of the geometry or surface defects. All this suggests that the cause of low power and efficiency is the mismatch of the parameters of the resonator to the design ones.

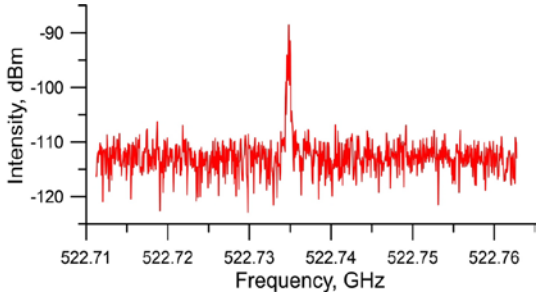

Fig. 5. Frequency spectrum of the output radiation

Frequency measurements were carried out using a Keysight N9010A spectrum analyzer with external mixer. Fig. 5 shows acquired frequency spectrum of the output radiation at the second cyclotron harmonic. Relative width of the frequency spectrum $\Delta f/f \sim 2\text{x}10^{-6}$. The central frequency is lower than the design one because of larger cavity radius, which is also points to possible errors in the manufacturing process.

IV. Conclusion

A 527 GHz continuous-wave second harmonic gyrotron was tested at IAP RAS. The output power of about 5 W was obtained with 15 kV / 500 mA beam. The reason for the low output power and efficiency is probably the lack of precision manufacturing of the cavity.

Acknowledgments

This work was financially supported by Russian Science Foundation grant № 19-12-00141

References

[1] V. A. Flyagin, A. V. Gaponov, I. Petelin, and V. K. Yulpatov, “The Gyrotron,” *IEEE Trans. Microw. Theory Tech.*, vol. 25, no. 6, pp. 514–521, Jun. 1977.

[2] “DNP-NMR Bruker-Biospin,” 2018. [Online]. Available: https://www.bruker.com/products/mr/nmr/dnp-nmr/technical-details.html.

[3] M. A. Moiseev, L. L. Nemirovskaya, V. E. Zapevalov, and N. A. Zavolsky, “Numerical simulation of mode interaction in 170 GHz/1 MW gyrotrons for iter,” *Int. J. Infrared Millimeter Waves*, vol. 18, no. 11, pp. 2117–2128, Nov. 1997.

[4] M. Y. Glyavin *et al.*, “Experimental tests of a 263 GHz gyrotron for spectroscopic applications and diagnostics of various media,” *Rev. Sci. Instrum.*, vol. 86, no. 5, p. 054705, May 2015.

Improving of a Terahertz Radiation Efficiency due to Optical Light Confinement in Nanoantennas

D. V. Lavrukhin[1,2], I. A. Glinskiy[1,2], R. A. Khabibullin[1,2,3], A. V. Arsenin[3], V. S. Volkov[3,4], I. V. Minin[5,6], O. V. Minin[5,6], K. I. Zaytsev[2,7], D. S. Ponomarev[1,2,3]

[1] Institute of ultra high frequency semiconductor electronics of RAS, Moscow, Russia
[2] Prokhorov General Physics Institute of the Russian Academy of Sciences, Moscow, Russia
[3] Moscow Institute of Physics and Technology, Dolgoprudny, Russia
[4] University of Southern Denmark, Odense, Denmark
[5] Tomsk Polytechnic University, Tomsk, Russia
[6] National Research Tomsk State University, Tomsk, Russia
[7] Bauman Moscow State Technical University, Moscow, Russia

E-mail: ponomarev_dmitr@mail.ru

Abstract – We propose and consider different approaches aimed at increasing the performance of a photoconductive antenna (PCA)-emitter due to enhanced optical light confinement using a high-aspect ratio plasmonic grating (plasmonic nanoantenna) maintaining plasmonic guided modes as well as an asymmetric dielectric particle with a prism (dielectric nanoantenna) for providing a sub-wavelength focusing of a laser excitation spot in a PCA's gap and sustaining Mie resonances.

Keywords – photoconductive antenna, plasmonic gratings, sub-wavelength focusing, terajet, polarization-independent antenna, LT-GaAs

I. Introduction

Photoconductive antenna (PCA)-emitters are widely used as key elements in various spectroscopic and imaging systems [1–4]. Therefore the increase in their efficiency is crucial for enhancement of a resolution of these systems. The two main factors: a short photocarriers free path and low photocarriers lifetime severely limit the performance of a PCA-emitter. In present article we propose and consider two different approaches aimed at overcoming these problems which rely on the optical light confinement enhancement in a PCA's gap.

II. Results and Discussion

As it can be seen in Fig. 1a, an integral dipole moment is formed only near the edges of the laser beam spot (i.e. in the perifocal region), the thickness of which is defined by the carrier free path of about $l_e \sim 100$ nm (for LT-GaAs). On contrary, from Fig. 2b one can notice that the use of periodical metallic and/or dielectric nanoparticles (with a period of $d < \lambda$, where λ is a laser wavelength) formed in the PCA's gap leads to the case when all edges of the multiple sub-wavelength beam spots are formed behind metal or/and dielectric nanoparticles. Let us consider the both cases separately.

The first approach is based on incorporation of the plasmonic gratings into the PCA's gap [5]. Recently we fabricated a high-aspect ratio dielectric-embedded metal gratings (Au-nanoridges) with record height (thickness) of the plasmonic electrode 100 nm. With thus fabricated plasmon-assisted PCA-emitter we demonstrated 3000-times enhancement of the THz power compared to the conventional PCA (i.e. without plasmonic gratings) which can be explained by the standing wave resonances in the finite-size parallel plate metallic waveguide formed by the Au-nanoridges [6]. We note that further enhancement might be achieved using strain-induced photoconductive substrates [7].

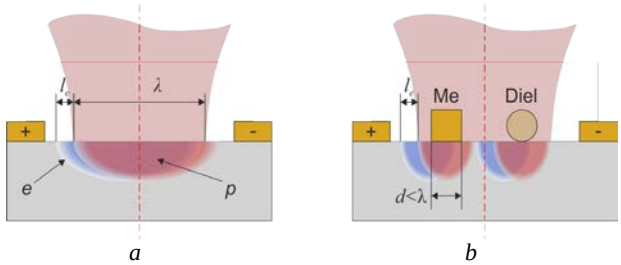

Fig. 1. Schematics of integral dipole moment formation: a conventional PCA (a) and a PCA with periodical metallic and/or dielectric nanoparticles with a period $d < \lambda$ (plasmonic and dielectric nanoantennas, respectively) (b). As seen in (b) a laser beam spot is divided into several beam caustics leading to formation of either plasmonic guided modes thanks to metal nanoparticle or Mie resonances due to dielectric nanoparticle. We also note that a dielectric nanoparticle under certain conditions can efficiently focus a lightwave into a sub-wavelength volume (see, for instance in [8, 9]).

The second approach is related to incorporation of dielectric nanoparticles in the PCA's gap. It is known that a nanoparticle can act as a refractive THz micro-lens to focus the light wave within a sub-wavelength volume, due to formation of photonic terajets [8–10]. Also recently we predicted theoretically a new curved plasmon surface wave, the photonic hook plasmon, which can be realized using the in-plane focusing of the surface plasmon-polariton wave [11] through an asymmetric dielectric particle with a prism formed on a metal surface [12]. We

will expand our approach on a PCA introducing single or multiple asymmetric dielectric particles into the PCA's gap. With thus optimized dielectric PCA (Mie resonances and sub-wavelength fs-laser focusing) we expect the further enhancement of optical light confinement and as consequence, increase of the PCA performance.

CONCLUSIONS

We propose and consider two different approaches aimed at enhancing of optical light confinement in the PCA's gap and thus increasing the efficiency of antenna-emitter.

ACKNOWLEDGMENTS

The work was supported by the Russian Scientific Foundation, project # 18-79-10195. The authors are grateful to their collaborators: Profs. M. Skorobogatiy, M. Shur, T. Otsuji and M. Ryzhii for fruitful discussions on the topic.

REFERENCES

[1] S. Lepeshov, A. Gorodetsky, A. Krasnok, N. Toropov, T.A. Vartanyan, P. Belov, A. Alú, E.U. Rafailov, Scientific Reports, **8**, 6624 (2018).

[2] N. Yardimci and M. Jarrahi, Scientific Reports, **7**, 42667 (2017).

[3] E. Castro-Camus and M. Alfaro, Photonics Research, **4**, A36 (2016).

[4] D.V. Lavrukhin, A.E. Yachmenev, A.Y. Pavlov, R.A. Khabibullin, Y.G. Goncharov, I.E. Spektor, G.A. Komandin, S.O. Yurchenko, N.V. Chernomyrdin, K.I. Zaytsev, D.S. Ponomarev, Semicond. Sci. Technol. **34**, 034005 (2019).

[5] C. Berry, N. Wang, M. Hashemi, M. Unlu, and M. Jarrahi, Nature Communications, **4**, 1622 (2013).

[6] D.V. Lavrukhin, A.E. Yachmenev, I.A. Glinskiy, R.A. Khabibullin, Y.G. Goncharov, M. Ryzhii, T. Otsuji, I.E. Spector, M. Shur, M. Skorobogatiy, K.I. Zaytsev, D.S. Ponomarev, AIP Adv. **9**, 015112 (2019).

[7] D.S. Ponomarev, A. Gorodetsky, A. E. Yachmenev, S.S. Pushkarev, R.A. Khabibullin, M.M. Grekhov, K.I. Zaytsev, D.I. Khusyainov, A.M. Buryakov, E.D. Mishina, J. Appl. Phys. **125**, 151605 (2019).

[8] I.V. Minin and O.V. Minin. *Diffractive Optics and Nanophotonics: Resolution Below the Diffraction Limit* (Springer, 2016).

[9] L. Yue, B. Yan, J.N. Monks, Z. Wang, N.T. Tung, V.D. Lam, O.V. Minin and I.V. Minin. J. Phys. D: Appl. Phys., **50**(17), (2017)

[10] L. Yue, B. Yan, J.N. Monks, R. Dhama, Z. Wang, O.V. Minin, I.V. Minin. J. of Infrared, Millimeter, and THz Waves, **39**(6), 546 (2018)

[11] V. Pacheco Peña, I.V Minin, O.V Minin, M. Beruete. Annalen der Physik, 1-9, 00098 (2016)

[12] I.V. Minin, O.V. Minin, D.S. Ponomarev, I.A. Glinskiy, Annalen der Physik, **530** (12), 1800359 (2018).

Optically Generated Terahertz Pulses with High-Field DC Precursors

M. I. Bakunov[1], M. V. Tsarev[2], A. V. Maslov[1], E. S. Efimenko[3], S. A. Sychugin[1]

[1] University of Nizhny Novgorod, Nizhny Novgorod, Russia
[2] Ludwig-Maximilians-Universität München, Garching, Germany
[3] Institute of Applied Physics, Russian Academy of Sciences, Nizhny Novgorod, Russia

E-mail: bakunov@rf.unn.ru

Abstract – An ultrashort laser pulse undergoing optical rectification and multiphoton absorption in an electro-optic crystal can generate terahertz wave with a high-field dc precursor. The electric and magnetic fields in the precursor can exceed the fields in the terahertz wave. We explore this phenomenon and propose ways to enhance the precursor's magnitude. In particular, we show that using the tilted-pulse-front excitation technique and higher orders of multiphoton absorption allows one to increase the precursor's fields by orders of magnitude. For example, the electric and magnetic fields as high as 0.4 MV/cm and 0.13 T can be generated in a 5-mm-thick $LiNbO_3$ crystal by a pulse (500 fs, 70 GW/cm^2) from Yb-doped laser amplifier.

Keywords – optical rectification, multiphoton absorption, strong terahertz fields

I. Introduction

Strong electric and magnetic fields in the terahertz frequency range are in great demand nowadays for a diversity of applications, including compact particle acceleration, molecular orientation and alignment, ultrafast control of magnetization, nonlinear terahertz spectroscopy, and terahertz streaking techniques. The most efficient table-top sources of strong terahertz fields are currently based on optical rectification of ultrashort laser pulses in electro-optic crystals. To generate strong terahertz fields, high optical pump intensities are required.

Multiphoton absorption is considered as one of the main detrimental factors that limits the optical pump intensity. It causes the depletion of the pump laser pulse and generation of free carriers that absorb terahertz waves. Recently, however, a useful effect of free carrier generation (FCG) was found.[1] It was shown that FCG can give rise to the generation of quasistatic electromagnetic fields (dc precursor) propagating ahead of the pump laser pulse. The precursor is emitted by a surge of an electric current, which is produced by optically generated carriers. The electric and magnetic fields in a precursor can exceed the fields in the terahertz wave copropagating the laser pulse.

Here, we discuss the factors that affect the precursor generation, such as the pump laser beam width, pump depletion, and Kerr nonlinearity, and propose ways to enhance substantially the precursor's fields.

II. Collinear Excitation

In the conventional collinear geometry of terahertz generation, dc precursor can be generated in electro-optic crystals with $n_g > n_{THz}$ (n_g is the optical group refractive index and n_{THz} is the terahertz phase refractive index), such as ZnTe or GaP pumped by Ti:sapphire laser.[1] Let an ultrashort laser pulse propagate in such a crystal in the $+z$ direction with a group velocity c/n_g (c is the speed of light) and generates a copropagating pulse of nonlinear polarization $\mathbf{P}^{NL}(z,t)$ via optical rectification. The optical intensity $I(z,t)$ is high enough to produce n-photon ionization with the density of free carriers

$$N(z,t) = \frac{\beta_n}{n\hbar\omega}\int_{-\infty}^{t} dt I^n(z,t), \qquad (1)$$

where β_n is the n-photon absorption coefficient and $\hbar\omega$ is the quantum energy of the laser radiation.

Figure 1(a) shows the snapshots of the electric field E_y generated by a Ti:sapphire laser pulse (780 nm central wavelength) in a 3-mm thick GaP crystal with $n_g = 3.66$, $n_{THz} = 3.31$, and $\beta_2 = 1$ cm/GW. The field is normalized to the amplitude of the nonlinear polarization P_0.

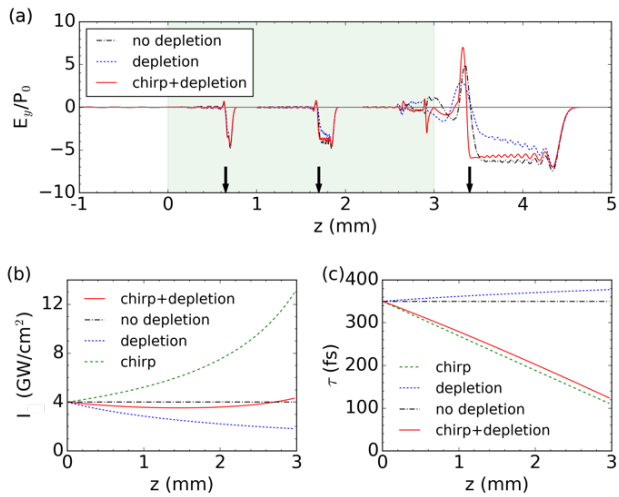

Fig. 1. (a) Snapshots of E_y at three instants of time for the pump depletion neglected, included, and compensated by chirping the laser pulse. The crystal (shaded region) is 3 mm thick. The arrows depict the position of the laser pulse. (b) Peak intensity and (c) 1/e-duration of the laser pulse as functions of z.

When pump depletion is neglected, the precursor looks like a plateau propagating ahead of the laser pulse [Fig. 1(a)]. The plateau's length increases with propagation, its magnitude becomes larger in free space. For the peak optical intensity $I_0 = 4$ GW/cm^2, a unity of

E_y/P_0 in Fig. 1(a) corresponds to $E_y = 0.2$ kV/cm so that the precursor's magnitude exceeds 1 kV/cm.

With pump depletion included, the rear part of the precursor is attenuated [Fig. 1(a)]. To restore the plateau-like shape of the precursor, we propose to use a chirped laser pulse with negative chirp parameter, $\gamma < 0$. Such a pulse undergoes dispersive compression in the crystal. This can compensate two-photon absorption thus sustaining high optical intensity and efficient precursor generation. To confirm the predicted effect, we solved nonlinear Schrodinger equation for the optical field envelope. For $I_0 = 4$ GW/cm^2, $\tau_F = 30$ fs (Fourier limited pulse duration), and $\gamma = -12$, the peak optical intensity indeed remains almost constant in the crystal [Fig. 1(b)]. The pulse duration τ evolves in the crystal from $\tau_0 = 350$ fs at $z = 0$ to about 130 fs [Fig. 1(c)]. The precursor's shape is completely restored [Fig. 1(a)].

For high optical intensities and thick crystals, the optical Kerr effect can become significant. Its influence can be compensated by a proper choice of γ.[2].

III. Tilted-Pulse-Front Excitation

To generate dc precursors in the crystals with $n_g < n_{THz}$, such as $LiNbO_3$, we propose to use the tilted-pulse-front excitation technique.[3] The excitation by tilted-pulse-front laser pulses can be treated as an excitation by non-tilted pulses but in a virtual material with an effective optical group refractive index $n_{eff} = n_g/\cos\theta$, where θ is the tilt angle.[4] For $\theta > \cos^{-1}(n_g/n_0)$, the necessary requirement for the precursor generation, i.e., $n_{eff} > n_{THz}$, can be met.

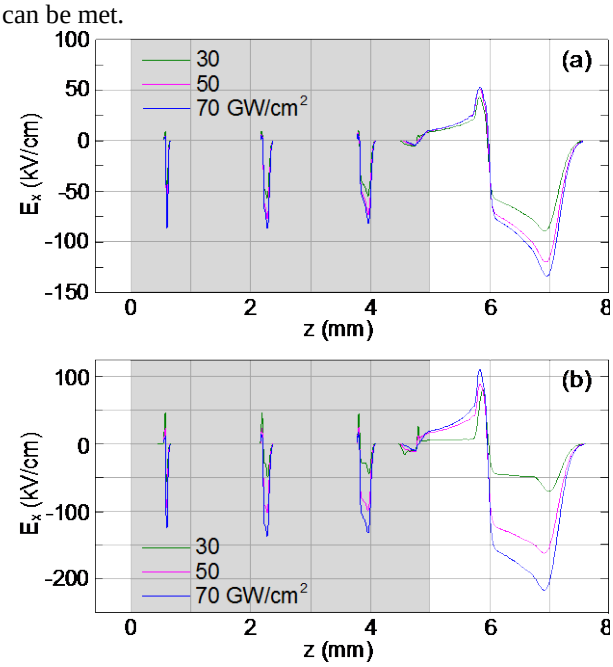

Fig. 2. Snapshots of the electric field at four instants of time for (a) 0.8-μm pump and (b) 1.05-μm pump. The $LiNbO_3$ crystal (shaded region) is 5 mm thick, $n_{eff} = 5.18$, and $\tau_0 = 300$ fs.

Figure 2(a) shows the precursor generation in $LiNbO_3$ ($n_{THz} = 4.94$, $n_g = 2.20$) by a tilted-pulse-front laser pulse of a 0.8-μm wavelength (Ti:sapphire laser) that undergoes three-photon absorption, $\beta_3 = 10^{-3}$ cm^3/GW^2 in Eq. (1). The magnitude of the precursor is as high as ~100 kV/cm, and its length exceeds 1 mm. Increasing I_0 above 50 GW/cm^2 adds little to the precursor's magnitude. This can be explained by fast depletion of a high intensity pump.

Using a 1.05-μm pump (Yb-doped laser) with a higher (4th) order multiphoton absorption, $\beta_4 = 3\times10^{-6}$ cm^5/GW^4 in Eq. (1), allows one to reduce the pump depletion rate and, as a result, to increase the precursor's magnitude [Fig. 2(b)].

Figure 3 shows that approaching n_{eff} to n_{THz} allows one to enhance the precursor's magnitude (up to ~400 kV/cm) but at the expense of its shorter length (about 0.5 mm).

Our calculations also show that the precursor's magnitude at low pump intensities can be substantially enhanced by increasing the pump pulse duration, for example, from 50 kV/cm in Fig. 2(b) for 30 GW/cm^2 to 100 kV/cm by increasing τ from 300 to 600 fs.

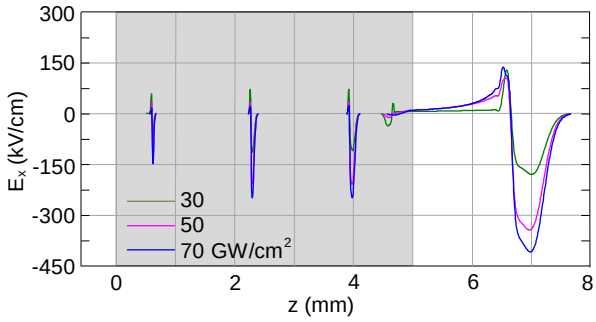

Fig. 3. The same as in Fig. 2(b) but for $n_{eff} = 5.05$

IV. Conclusions

Excitation by chirped laser pulses allows one to circumvent the limitations imposed on the precursor generation by pump depletion and Kerr nonlinearity. Tilted-pulse-front excitation scheme is promising for the generation of high-magnitude dc precursors in $LiNbO_3$.

Acknowledgments

This work was supported by the Russian Science Foundation (RSF), Project 18-19-00486.

References

[1] M. I. Bakunov, A. V. Maslov, and M. V. Tsarev, *Phys. Rev. A* **95**, 063817 (2017).
[2] E. S. Efimenko, S. A. Sychugin, M. V. Tsarev, and M. I. Bakunov, *Phys. Rev. A* **98**, 013842 (2018).
[3] M. V. Tsarev and M. I. Bakunov, *Opt. Express* **27**, 5154 (2019).
[4] M. I. Bakunov, S. B. Bodrov, and M. V. Tsarev, *J. Appl. Phys.* **104**, 073105 (2008).

Surface vs Bulk Second Optical Harmonic Generation from Fused Quartz in Strong Terahertz Field

S. B. Bodrov[1,2], M. Y. Emelin[1], Y. A. Sergeev[1], A. I. Korytin[1], M. Y. Ryabikin[1], A. A. Murzanev[1] and A. N. Stepanov[1]

[1] Institute of Applied Physics of the Russian Academy of Sciences, Nizhny Novgorod 603950, Russia
[2] University of Nizhny Novgorod, Nizhny Novgorod 603950, Russia

E-mail: bosbor@ufp.appl.sci-nnov.ru

Abstract – Generation of second harmonic (SH) of femtosecond laser radiation from fused quartz in strong (~200 kV/cm) terahertz field was investigated. It was shown that the THz induced SH is generated only near the entrance and exit surface of the quartz and not from the bulk. The magnitude of SH signal for different polarization relation of interacting fields was obtained in reflection and transmission geometries. The contribution to the SH signal of bulk (located near the surface) and pure surface sources was discussed. In was conclude that in reflection geometry of surface source significantly exceeded the bulk source. In transmission geometry the bulk source dominated. To explain high magnitude of the surface source a model based on interaction of electromagnetic radiation with an electron in coulomb potential biased by embedded surface electric field was proposed and analyzed.

Keywords – second harmonic generation, THz pulse, surface

I. Introduction

Optical second harmonic (SH) generation from interfaces is widely used for surface studies of centrosymmetric materials where SH generation is forbidden in the bulk. Application of external DC electric field breaks the symmetry and allows bulk SH generation that changes the magnitude of the generated SH signal[1]. On the over hand the electric field should also act on the surface and change the surface SH signal[2].

In this paper we investigated terahertz induced SH generated by femtosecond optical radiation from a surface of fused quartz and compared bulk and surface contributions to the SH signal. To explain the experimental results a model based on interaction of electromagnetic radiation with an electron placed in coulomb potential biased by embedded surface electric field was proposed and analyzed.

II. Experimental setup

A Ti:Sapphire laser system (0.5 mJ, 700 Hz, 70 fs) was used in our experiment. The optical radiation was divided into two parts. The first part generated THz radiation in a LiNbO3 crystal by the tilted-front technique [3]. The THz radiation was focused in 3 mm thick fused quartz sample collinear with the second part of laser pulse with variable time delay (see Fig. 1). The magnitude of the THz field near the focus was ~ 200 kV/cm. SH signal was detected by PMT in reflection and transmission setups.

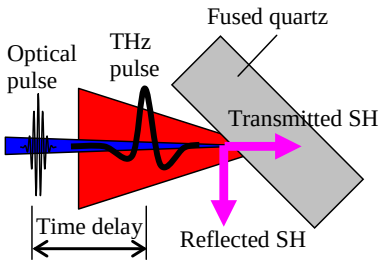

Fig. 1. A scheme for THz induced SH generation

III. Experimental results

Figure 2 shows generated SH signals in transmission and reflection geometries as a function of time delay between optical and THz pulses (all interacting fields have s polarization). The signal profiles are different that indicates different generation regimes or/and different types of SH sources. The peak amplitude of the reflected signal is about 5% of the transmitted signal. This value significantly exceeds the value of back radiated SH during generation in the bulk of the quartz due to small differences of refractive indexes of the first and the second optical harmonics. These facts allowed us to conclude that the reflected SH signal originated from the quartz surface and the main part of the transmitted signal is generated from the bulk located near the surface.

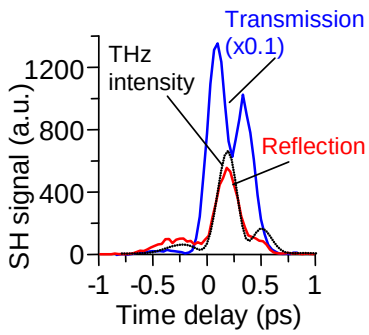

Fig. 2. SH signals in reflection and transmission setups as a function of time delay. THz intensity profile is shown by dotted line.

IV. Theoretical calculation

To qualitatively explain the above-discussed experimental result we considered a nonlinear response of hydrogen-like atom in the field of optical and THz radiation (see Fig. 3(a)). The presence of the interface was modeled by applying DC field perpendicular to the surface. The simulation was based on 2D and 3D numerical solution of Schrödinger equation.

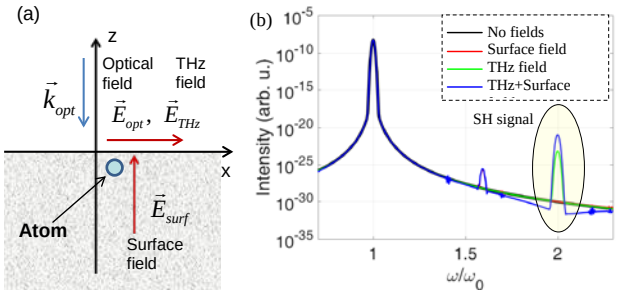

Fig. 3. (a) Geometry of the problem for theoretical calculation. (b) Intensity spectrum of nonlinear atom dipole response for different conditions (with/without THz and surface fields).

It was shown that including surface DC field in consideration leaded to several order of magnitude increase in SH signal (see Fig. 3(b)). This means that several atomic layers near the surface (where the surface field exists) are the main source of SH in reflection in agreement with experimental data.

Acknowledgments

This work was supported in part by the RFBR, research project No. 18-02-00968.

References

[1] O. A. Aktsipetrov, A. A. Fedyanin, A. V. Melnikov, E. D. Mishina, A. N. Rubtsov, M. H. Anderson, P. T. Wilson, M. ter Beek, X. F. Hu, J. I. Dadap, and M. C. Downer, *Phys. Rev. B.* **60**, 8924 (1999).

[2] O.A. Aktsipetrov, A.A. Fedyanin, A.V. Melnikov, J.I. Dadap, X.F.Hu, M.H. Anderson, M.C. Downer, J.K. Lowell, *Thin Solid Films* **294**, 231 (1997).

[3] S.B. Bodrov, A.A. Murzanev, Y.A. Sergeev, Y.A. Malkov, and A.N. Stepanov, *Appl. Phys. Lett.* **103**, 251103 (2013).

Terahertz Time-Domain Spectroscopy of Interstellar and Circumstellar Ice Analogs: Experimental Setup and Pilot Results

A. A. Gavdush[1,2], B. M. Giuliano[3], B. Müller[3], G. A. Komandin[2], M. E. Palumbo[4], G. A. Baratta[4], C. Sciré[4], S. O. Yurchenko[2], K. I. Zaytsev[1,2], A. V. Ivlev[3], P. Caselli[3]

[1] Prokhorov General Physics Institute of RAS, Moscow 119991, Russia
[2] Bauman Moscow State Technical University, Moscow 105005, Russia
[3] Max-Planck-Institute für extraterrestrische Physik, Garching bei München 85748, Germany
[4] Osservatorio Astrofisico di Catania, Catania 95123, Italy

E-mail: arsenii.a.gavdush@gmail.com

Abstract – A knowledge of the complex dielectric permittivity of interstellar and circumstellar ice analogs in the terahertz (THz) band is of particular importance for the interpretation of the future astrophysical observations. In our work, we assembled an experimental setup, which allows growing the astrophysical ice analogs in a laboratory, as well as measuring their dielectric response using the THz TDS. In the pilot study, we detected and analyzed the THz dielectric properties of CO ice.

Keywords – astrochemistry, spectroscopy, ice analogs, CO, terahertz pulsed spectroscopy

I. INTRODUCTION

Ices are one of the most common kinds of dense matter in the Universe. There are more than 180 various molecular astrophysical ices, including H_2O, CO, CO_2, CH_3OH, etc.[1]. Surface chemical processes on icy mantles of dust particles play an important role in formation of new molecules, including biologically relevant organic species[2,3]. Therefore, thorough studies of the ice properties may shed light to such astrophysical problem, as understanding the origin of the volatiles and organics – the building blocks of life – in space and then on the early Earth.

Analysis of astronomical observations in different ranges of electromagnetic spectrum is the main tool for experimental studies of ices in the Universe. These observations employ mostly a mid-infrared (IR) range of wavelengths[1,4], but also cover far-IR and terahertz (THz) ranges, provided by such space telescopes, as Hershel[5] and SOFIA[6]. A corner stone of proper interpretation of these observations is their comparison to IR and THz spectra of astrophysical ice analogs obtained in laboratory conditions. Recent works were mainly dedicated to the analysis in mid-IR frequency region[1], with only a few works concerned on THz spectroscopy[7,8]. However, in spite of its importance, the presently available data related to spectroscopy in IR and THz range are still incomplete or even have not been performed for a lot of ice compounds, to our knowledge.

II. METHODS

In the present work, we apply previously developed method[9-13] for reconstruction of both real and imaginary parts of dielectric permittivity, using the THz time-domain spectroscopy (TDS). This technique allows us to measure optical properties of astrophysical ice analogs in a broad range of wavelengths, that is required for detailed study of radiative transfer in ice mantles of astrophysical dust particles. We developed an experimental setup allowing simultaneous growth and THz TDS of thin ice films of different molecular compositions.

The experimental setup for the spectroscopic measurements is composed closed-cycle He cryostat and THz time-domain pulsed spectrometer (TPS). The cryostat is mounted on a motor controlled translational stage to tune its position with respect to the THz beam. The cryocooler vacuum chamber is equipped with four ports for optical access and for the gas inlet. Optical windows and a substrate for the ice growing are made of high-resistivity float-zone silicon (HRFZ-Si) with different thickness, the smallest one for the substrate, in order to suppress multiple resonances in the THz spectra. The pumping station that operates with gas mixture for ice sample deposition is composed of a turbomolecular pump combined with a backing rotary pump. The THz TPS used for the present work has been basically purchased from the Batop GmbH, and it is coupled with two photoconductive antennas made of low-temperature grown gallium arsenide and a femtosecond laser with a pulse repetition rate of 100 MHz and an average input power of 65 mW. Further technical details on an experimental setup one can find in the upcoming work at Astronomy & Astrophysics journal[14].

Growth of the ices on the substrate is organized using standard technique using vapor deposition on the cold substrate in the vacuum chamber. To attain ice thickness of a mm order, fast deposition regime is employed. The first experiments were performed with ice of CO, deposited at 14 K in a several deposition regimes, with 4, 5 and 6 min deposition steps, and up to the total 30 min deposition time.

III. Results and conclusions

The reconstruction procedure of the optical properties of ice layers is organized in the same manner as in previous works[9-13]. The signal propagated through the empty vacuum chamber at 14 K was used as the reference one for analysis of the sample signal propagated through the chamber with grown ice layers on the substrate. Then, the time-domain signals (reference ballistic and sample satellite pulses) were analyzed to have initial estimations of ice layers' thicknesses and a real part of the sample refractive index, to enhance the accuracy of data post processing. Reliability of the employed approach is confirmed by independent measurements of the sample thickness[15], and observed linear increase of the total initial thickness of ices in different deposition regimes. In result[14], the optical properties of CO ice were measured in the range of 0.3–2.0 THz, with a clearly expressed Lorentz-like peak centered near 1.5 THz, which stands in a good agreement with previous studies[16-17].

The present study is the first to provide the method to direct study of THz dielectric properties of interstellar ice analogs, to the best of our knowledge. The obtained results on CO ice are in a good agreement with available data. The dielectric properties of interstellar and circumstellar ice analogs provide further investigations on the radiative transfer phenomenon in the ices on the cold dust grains in space.

Acknowledgments

This work was partly supported by the Russian Foundation for Basic Research (RFBR), Project #18-32-00816.

References

[1] A. C. A. Boogert, P. A. Gerakines, D. C. B. Whittet, *Ann. Rev. of Astronomy and Astrophysics* **53**, 541-581 (2015).
[2] K. I. Öberg, *Chem. Rev.* **116** (17), 9631-9663 (2016).
[3] B. A. McGuire et al., *Science* **352** (6292), 1449-1452 (2016).
[4] E. F. van Dishoeck, *Faraday Discuss.* **168**, 9-47 (2014).
[5] D. Doyle, G. Pilbratt, and J. Tauber, J., *Proc. of the IEEE* **97** (8), 1403-1411 (2009).
[6] R. D. Gehrz et al., *Advances in Space Research* **44** (4), 413-432 (2009).
[7] M. A. Allodi et al., *Phys. Chem. Chem. Phys.* **16** (8), 3442-3455 (2014).
[8] B. A. McGuire et al., *Phys. Chem. Chem. Phys.* **18** (30), 20199-20207 (2016).
[9] K. I. Zaytsev et al., *Optics and Spectroscopy* **118** (4), 552-562 (2015).
[10] K.I. Zaytsev et al., *IEEE Trans. on Terahertz Science and Technology* **5** (5), 817-827 (2015).
[11] E. V. Yakovlev et al., *IEEE Trans. on Terahertz Science and Technology* **5** (5), 810-816 (2015).
[12] K. I. Zaytsev et al., *Applied Phys. Let.* **106** (5), 053702 (2015).
[13] K. I. Zaytsev et al., *J. of Applied Phys.* **115**, 193105 (2014).
[14] B. M. Giuliano, A. A. Gavdush, B. Müller, K. I. Zaytsev, T. Grassii. A. V. Ivlev, M. E. Palumbo, G. A. Baratta, C. Sciré, G. A. Komandin, S. O. Yurchenko, and P. Caselli,. Broadband spectroscopy of astrophysical ice analogs. I. Direct measurement of complex refractive index of CO ice using terahertz pulsed spectroscopy, *Astronomy & Astrophysics (under review)*.
[15] G. A. Baratta, M. E. Palumbo, *J. Opt. Soc. Am. A* **15** (12) 3076-3085 (1998).
[16] A. Anderson, G. E. Leroi, *J. of Chem. Phys.* **45**, 4359 (1966).
[17] A. Ron, O. Schnepp, *J. of Chem. Phys.* **46** (10), 3991-3998 (1967).

Terahertz Induced Optical Second Harmonic Generation from Zinc Blende Crystals

S. B. Bodrov, A. I. Korytin, Y. A. Sergeev, A. N. Stepanov

Institute of Applied Physics of the Russian Academy of Sciences, Nizhny Novgorod, Russia

E-mail: yas@ufp.appl.sci-nnov.ru

We studied optical second harmonic generation in zinc blende type crystals with simultaneous action of THz pulse. Energy and time dependences for different combinations of polarizations are obtained.

Keywords – terahertz pulses, second harmonic, zinc blende

I. Introduction

The combined action of femtosecond optical radiation and strong short-pulse terahertz fields on materials allows to get additional information in the study of the second harmonic (SH) signal of optical radiation. It becomes possible to investigate the SH generation for a greater number of polarization combinations (taking into account the additionally applied THz field). The combined action of optical and THz radiations make it possible to study the temporal dynamics of nonlinear processes. The proposed method is experimentally demonstrated on crystals of the zinc blende type such as GaAs, InAs, GaP. Because crystals of this type don't have the inversion center, generation of SH isn't prohibited in dipole approximation. However, the presence of THz field can lead for some combinations of polarizations to the increasing of SH generation.

II. Experimental setup

A titanium-sapphire laser system (pulse energy 0.5 mJ, central wavelength 795 nm, pulse duration 70 fs, repetition frequency 600 Hz) was used to study the generation of optical SH in the presence of pulsed THz field.

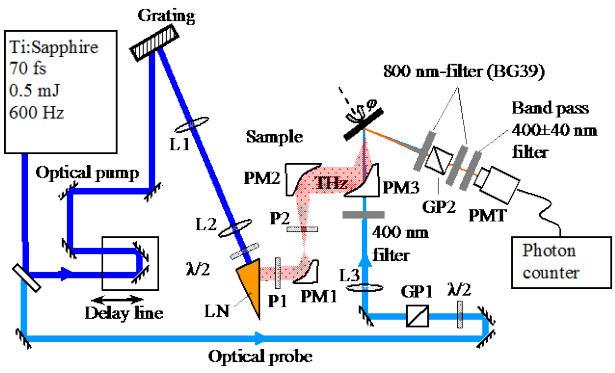

Fig. 1. Experimental setup (L1, L2, L3 – lenses; PM1, PM2, PM3 – parabolic mirrors; LN – LiNbO3; GP1, GP2 – Glan prism; P1,P2 – THz polarizer).

Optical radiation was divided into two beams (see Fig. 1). The pump beam was used to generate THz radiation by the tilted intensity front method in a LiNbO3 crystal[1,2]. Terahertz radiation was focused on the sample using a system of off-axis parabolas. The maximum THz field in focus reached a value of 200 kV/cm. For the attenuation of THz fields were used two THz polarizers. The probe laser pulse passed through the delay line and was focused on the sample in ~ 100 microns spot (smaller than the size of The THz spot). The second harmonic radiation generated from the surface was detected by the PMT connected to the pulse counting system. For studying the polarization properties of the SH a polarizer in front of the photomultiplier was mounted. A special set of filters was used to block laser radiation.

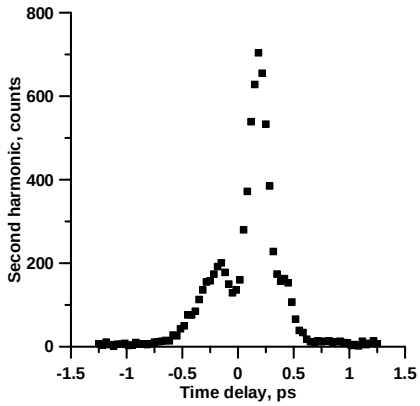

Fig. 2. The dependence of the SH signal from the time delay between the THz and optical pulses.

III. Results

In the experiments the generation of SH was investigated for various polarization combinations of optical and THz radiation. The dependences of the SH intensity on the delay between optical and THz pulses, on the energies of the optical and THz fields were also studied. Fig. 2 is an example of the time dependence of SH intensity. Phenomenological theory is developed to describe the experimental results.

References

[1] J. A. Fulop et al., Opt. Express **18**, 12311 (2010).
[2] S. B. Bodrov et al., Appl. Phys. Lett. **103**, 251103 (2013).

Electro-Optic Sampling of Terahertz Waves in $LiNbO_3$ with Avoided Intrinsic Birefringence

A. I. Shugurov[1], E. A. Mashkovich[2], S. B. Bodrov[1,3], M. I. Bakunov[1]

[1] University of Nizhny Novgorod, Nizhny Novgorod, Russia
[2] Institute for Molecules and Materials, Radboud University, 6525 AJ Nijmegen, the Netherlands
[3] Institute of Applied Physics, Russian Academy of Sciences, Nizhny Novgorod, Russia

E-mail: mbakunov@gmail.com

Abstract – We propose a new scheme for electro-optic sampling of terahertz waveforms with femtosecond laser pulses in a $LiNbO_3$ crystal. To avoid intrinsic birefringence of $LiNbO_3$, the optical axis of the crystal is set along the propagation direction of the probe laser beam. To synchronize the terahertz wave and the probe beam, the terahertz wave is introduced into the crystal at the Cherenkov angle, through a Si prism. The scheme is verified experimentally with a 1.55 μm fiber laser as a light source.

Keywords – Terahertz detection, electro-optic sampling, Cherenkov synchronism

I. Introduction

Electro-optic (EO) sampling is a widely used technique for characterization of terahertz waveforms. In this technique, a femtosecond laser pulse co-propagates with terahertz wave in an EO crystal and undergoes a change of polarization due to the Pockels effect. By measuring the polarization change, the terahertz waveform can be mapped. For efficient EO sampling, the optical group velocity should equal the terahertz phase velocity. However, no crystal can provide velocity matching at the wavelength 1.55 μm of fiber lasers, which are preferable for compact terahertz spectrometers.

To achieve velocity matching for an arbitrary optical wavelength, a Cherenkov-type scheme of EO sampling was proposed and experimentally demonstrated.[1] In this scheme, terahertz wave enters $LiNbO_3$ crystal through a Si prism and propagates at the Cherenkov angle to the probe optical beam thus providing optical-terahertz velocity synchronism. A drawback of the scheme is intrinsic birefringence of $LiNbO_3$, which requires an additional optics for its compensation.[1]

Here, we propose a modified Cherenkov-type scheme of EO sampling in $LiNbO_3$ that avoids intrinsic birefringence of the crystal. The scheme is based on using the degenerate configuration with the probe beam propagating along the optical axis of the crystal.

II. Detection Scheme

In our scheme [Fig. 1 (a)], the probe beam propagates in a $LiNbO_3$ crystal along the *c*-axis as an ordinary wave. Terahertz beam enters the crystal through a Si prism cut at 41°. The terahertz beam polarization is orthogonal to the *c*-axis. The polarization of the probe beam can be either orthogonal or parallel to the polarization of the terahertz beam. By analyzing the second-order nonlinear susceptibility tensor of $LiNbO_3$,[2] the interaction of the terahertz and optical beams of such polarizations gives rise to an orthogonally polarized component in the probe beam. This component propagates as an ordinary wave and can be detected by standard ellipsometric method.

The experimental setup [Fig. 1(b)] is similar to Ref. 3, except for the $LiNbO_3$-Si-prism structure used as a detector crystal. The $LiNbO_3$ crystal is 1 mm-thick and has 10×10 mm^2 lateral dimensions. A fiber laser (1.55 µm, 70 fs, 100 MHz) is used as a light source. Proof-of-principle experiment confirmed the scheme's workability.

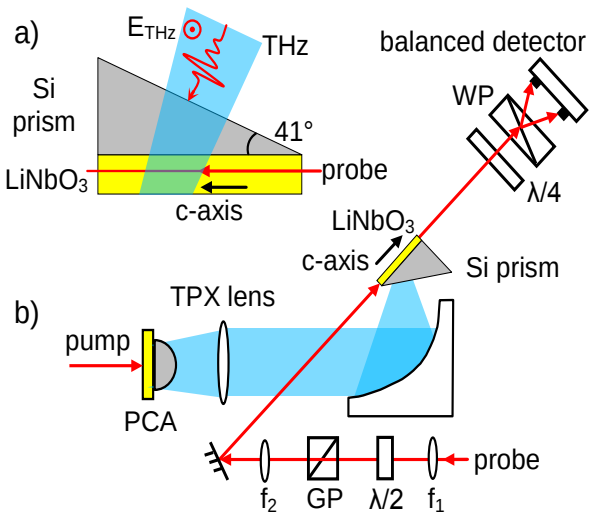

Fig. 1. (a) Detection scheme.
(b) Schematic of the experimental setup

Acknowledgments

This work was supported by the Ministry of Science and Higher Education of the Russian Federation, Projects 3.3854.2017/4.6 and 3.6252.2017/9.10.

References

[1] M. Tani, K. Horita, T. Kinoshita, C. T. Que, E. Estacio, K. Yamamoto, and M. I. Bakunov, *Opt. Express* **19**, 19901 (2011).
[2] R. W. Boyd, *Nonlinear Optics* (Academic Press, 2003).
[3] E. A. Mashkovich, A. I. Shugurov, S. Ozawa, E. Estacio, M. Tani, and M. I. Bakunov, *IEEE Trans. Terahertz Sci. Techn.* **5**, 732 (2015).

Mechanisms of Laser-Induced THz Response of Metallic Structures

I. V. Oladyshkin, D. A. Fadeev, V. A. Mironov

Institute of Applied Physics of the Russian Academy of Sciences, Nizhny Novgorod, Russia

E-mail: oladyshkin@gmail.com

Abstract – The talk is devoted to the nonlinear electromagnetic phenomena in metallic gratings and nanoparticles irradiated by femtosecond laser pulses. Possible mechanisms of low-frequency (terahertz) response are considered and specific non-quadratic nonlinear regimes of conversion are analyzed. In contrast to some previous models, we consider only low-frequency currents inside the metal not involving electron emission and acceleration above the surface. Special attention is paid to the role of surface plasmon resonances at optical frequency in the enhancement of terahertz response.

Keywords – terahertz radiation, metal, femtosecond laser pulses, thermal effects, surface plasmons

I. Introduction

Plasmonics is a rapidly developing field covering optics and condensed matter physics. The key concept connecting both of these areas is "plasmon polariton" – collective movement of free electron gas coupled with the oscillation of electromagnetic field. One of the most significant and well-known achievements of plasmonics is the possibility to localize electromagnetic waves in subwavelength area, for example, near the metal surface or around the nanoparticle. When the coupling between the plasmonic mode and the propagating optical wave in free space is efficient enough, the local electrical field grows by orders of magnitude. This opens up new possibilities for studying nonlinear optical properties of materials using non-damaging incident radiation of moderate intensities.

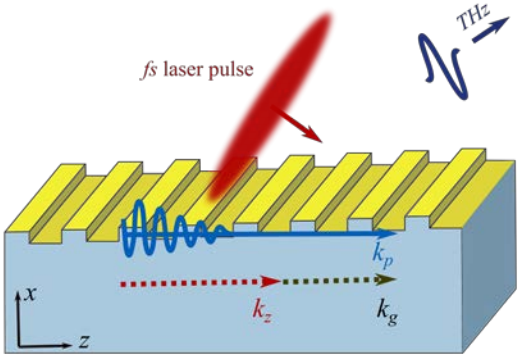

Fig. 1. Typical experimental scheme of surface-plasmon-enhanced THz radiation generation: a metal (e.g., gold) foil deposited on a dielectric substrate is irradiated by a femtosecond laser pulse. Resonant conditions for the forward surface plasmon excitation is $k_z + k_g = k_p$ (the sum of the grating wavenumber and the "z" component of optical wavevector equals to the surface plasmon wavenumber).

Here we discuss a microscopic theory of THz radiation generation on metal gratings and arrays of nanoparticles under the action of intense femtosecond laser pulses[1,2]. The proposed model is based on plasmon-enhanced ultrafast thermal effects[3] and explains the resonant character of the delayed low-frequency response giving an adequate absolute value of the full THz signal energy.

II. Methods and Results

We have performed detailed numerical study of subpicosecond thermal effects in metals and their role in THz currents generation using the hydrodynamical description of free electron gas. The strongest source of low-frequency currents here is a gradient of the electronic temperature appearing due to the laser pulse absorption in the skin-layer. The computational scheme was similar to the scheme used in our previous studies of optical-to-terahertz conversion on flat metal surfaces[3].

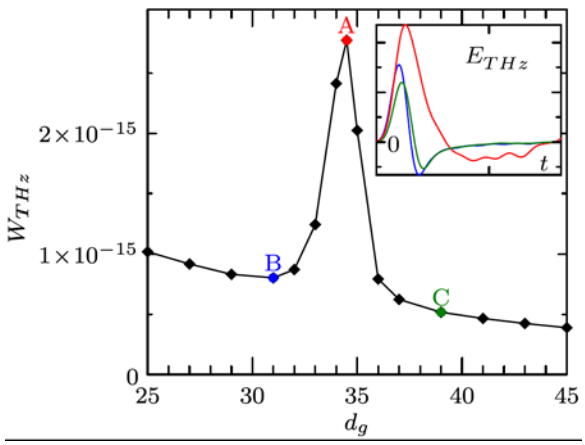

Fig. 2. Resonant dependence of the terahertz signal energy on the grating period obtained in the numerical modeling. Inset: THz waveforms corresponding to marks A, B and C respectively.

Modeling results reproduces a resonant character of the terahertz response when the laser pulse incidence angle or the grating period is varied (see Fig. 2). The angular dependence is significantly smoother when the grating shape is modified from the sinusoidal to the rectangular one. Performed analytical study and numerical modeling allow to explain specific experimental features like low conversion efficiency on the deep gratings or the existence of optimal metal foil

thickness. We should note that non-quadratic conversion regimes $W_{\mathrm{THz}} \sim (W_{\mathrm{opt}})^n$ can be interpreted as a consequence of temperature-dependent collision frequency of electrons which leads to the nonlinear laser pulse absorption and, correspondingly, nonlinear rise of electronic temperature.

III. Conclusions

We analyzed laser-induced subpicosecond thermal effects inside the metal gratings and inside the arrays of metallic nanoparticles focusing on their manifestation in the delayed electromagnetic response of the terahertz range. In the case of metal gratings, excitation, absorption and diffraction of surface plasmons at optical frequency found to be the main factors influencing the resonance character of the THz response and determining its dependence on the grating depth.

Acknowledgments

The work was financially supported by Russian Foundation for Basic Research (RFBR), grants #18-42-520023 and #17-02-00387.

References

[1] G.H. Welsh, N.T. Hunt, K. Wynne, "Terahertz-pulse emission through laser excitation of surface plasmons in a metal grating," *Physical Review Letters*, vol. **98**, p. 026803, 2007.

[2] D.K. Polyushkin, E. Hendry, E.K. Stone, and W.L. Barnes, "THz Generation from Plasmonic Nanoparticle Arrays", *Nano Letters*, vol. **11**, pp. 4718–4724, 2011.

[3] I.V. Oladyshkin, D.A. Fadeev, and V.A. Mironov, "Thermal mechanism of laser induced THz generation from a metal surface", *Journal of Optics*, vol. **17**, p. 075502, 2015.

Superconducting Hot-Electron and Normal Metal Bolometer

S. V. Antipov, N. A. Tovpeko, A. V. Trifonov, N. S. Kaurova, N. A. Titova, A. V. Semenov and G. N. Goltsman

Moscow Pedagogical State University, 1/1 M. Pirogovskaya Str., Moscow, 119991, Russia

E-mail: goltsman10@mail.ru

Abstract – In this paper, we report on the concept of fast normal metal bolometer targeted to the whole THz frequency range and capable to operate in a wide temperature range up to 300 K.

Keywords – Normal metal, bolometer, room temperature.

I. Introduction

The semiconductor technology presented by Schottky diodes enables the development of heterodyne receiver instruments for a wide variety of frequencies up to THz, operating in a wide range of temperatures, from room down to liquid nitrogen. However, T_{noise} of modern Schottky mixers varies from hundreds of Kelvins (~ 500 – 600 K) at GHz frequencies and rapidly increases to tens of thousands (~ 80000 – 100000 K) of Kelvins at THz frequencies (~ 5 THz). Further extension of Schottky technology to THz and IR frequency ranges becomes more and more challenging in terms of fabrication technology together with degradation of mixers performance.

The superconductor based mixing technology mainly employs SIS and HEB mixers. On the one hand, modern SIS mixers have supreme performance almost at the quantum noise level, which is only limited by the superconducting gap frequency at the level ~ 1 THz for the state of art SIS mixers. On the other hand, HEB mixers can operate from hundreds of GHz up to far THz frequency range. The cryogenic operation temperature of low noise mixers is usually associated with specific demands to a carrier platform in terms of power consumption and setup design. The complexity of such platforms pushes the development of mixers, operating at ~ 15–20 K, based on MgB_2 technology.

II. Gain bandwidth

There are two crucial parameters for any terahertz mixer, which enable its practical applicability in a certain field: bandwidth and noise performance. Thorough analysis of literature on thermal conductance of epitaxial interfaces between ultrathin metal films and dielectric substrates indicates that ultrathin TiN films on top of MgO or Al_2O_3 substrates have advanced properties of transport of thermal energy [1] to the substrate. Present of an efficient thermal transport in TiN films on top of MgO or Al_2O_3 makes this material to be very interesting for fabrication of metal THz bolometer. The interest is related to the bottle neck, which limits the bandwidth performance, namely the heat transport from a metal film to a substrate.

Our preliminary experiments under heterodyne mixing conditions at room temperature indicate that TiN bolometer on the sapphire substrate has pretty wide bandwidth. The measurements were taken at 145 GHz. 5 nm thin TiN bolometer can provide gain bandwidth of ~ 5–6 GHz in a wide bath temperature range 77–300 K.

III. Noise performance

Speaking about the second main parameter - noise performance of metal THz bolometer we should point out a relatively steep slope of TiN temperature coefficient of resistance, which allows to make simplified theoretical estimations of the noise performance of such bolometer. The lowest estimated T_{noise} is expected to be in the range of several thousands (~ 1000 K) of Kelvins, which makes this type of bolometer very attractive for practical applications in the THz frequency range.

IV. Conclusions

We have presented the concept of the normal metal bolometer, which is capable to operate in a wide range of temperature from 77 K up to 300 K and provides the gain bandwidth up to 6 GHz for 5 nm thin TiN films. The theoretical expectations of the noise performance give T_n ~ 1000 K at bath temperature of 300 K.

Acknowledgments

This work was financially supported by the Russian Scientific Foundation (contract # 17-72-30036).

References

[1] R. M. Costescu, M.A. Wall and D.G. Cahill “Thermal conductance of epitaxial interfaces”, *Phys. Rev. B*, vol. 67, pp. 054302, 2003.

Low-Temperature Scanning Laser Microscopy of Niobium Josephson Junction Arrays

A. M. Klushin[1], M. A. Galin[1], V. V. Kurin[1,2], V. M. Krasnov[3], F. Rudau[4], D. Koelle[4], R. Kleiner[4]

[1] Institute for Physics of Microstructure RAS, Nizhny Novgorod, Russia
[2] Lobachevsky State University of Nizhny Novgorod, Nizhny Novgorod, Russia
[3] Department of Physics, Stockholm University, AlbaNova University Center, Stockholm, Sweden
[4] Physikalisches Institut and Center for Quantum Science (CQ) in LISA+, Universität Tübingen, Tübingen, Germany

E-mail: a_klushin@ipmras.ru

Abstract – Low-temperature scanning laser microscopy (LTSLM) of two large niobium Josephson junction (JJ) arrays with different design has been performed at different bias current *I*. The images of both JJ arrays show wavy contrast at some range of *I*, which is explained by resonator modes excited in the superconducting circuit. The data may indicate the influence of the biased part of JJ array to the unbiased part via electromagnetic interaction. The images may also reveal a traveling-wave synchronization regime in the JJ array at higher *I*.

Keywords – Josephson junction array, scanning laser microscopy, strip resonator modes, traveling waves

I. Introduction

The Josephson effect can be used for the generation of electromagnetic radiation[1,2], with the maximum frequency limited by the superconducting energy gap. For low-temperature superconductors the gap frequency is in the sub-THz range[2]. For high-temperature superconductors it can be up to approximately 20 THz[3,4]. A single Josephson junction (JJ) emits very small power, at the picowatt level[1]. The power can be enhanced using JJ arrays containing many synchronized junctions[5–10]. At present, stacks of intrinsic JJ's show promising figures of merit[3,4,6,9,10], however they suffer strongly from Joule heating and there is a complex interplay of thermal physics and electromagnetism. Discrete planar JJ arrays offer a much higher flexibility in design and may be less prone to thermal and nonequilibrium effects[5,7,8,11].

Synchronization of large planar JJ arrays can be mediated by resonant electromagnetic modes, such as a cavity mode, located either in an external cavity[5], in the resonator parts of the superconducting circuit[8] or in the dielectric substrate[7]. Recently a nonresonant mechanism of synchronization, driven by a traveling wave, was revealed in two niobium JJ arrays[11]. It became obvious that in general the synchronization in planar JJ arrays may be established by both the resonator mechanisms and by the excitation of the traveling wave modes.

In the work, we use low-temperature scanning laser microscopy (LTSLM)[12] to study the mechanism of synchronization in two large niobium JJ arrays with different designs. In LTSLM a laser locally warms up the sample while the beam-induced changes in the global voltage across the sample are detected. The method is indirect but allows to, e.g., identify the formation of standing electromagnetic waves.

II. Measurement setup and design of samples

In the LTSLM setup[12] the sample is mounted inside an optical helium-flow cryostat which is cooled down to 4.2 K. The beam of a diode laser is directed by a scanning unit to the surface of the JJ array and is focused to a spot size of 1–2 μm in diameter. If the array is in the resistive state with constant bias current *I*, the power brought in by the laser causes a local temperature rise of a part of superconducting circuit. As a consequence, the voltage across the circuit changes by an amount ΔU. While scanning the surface by the laser beam, ΔU serves as a contrast for the LTSLM image. In order to improve the signal-to-noise ratio the beam is modulated at 10–80 kHz and ΔU is detected by a lock-in amplifier.

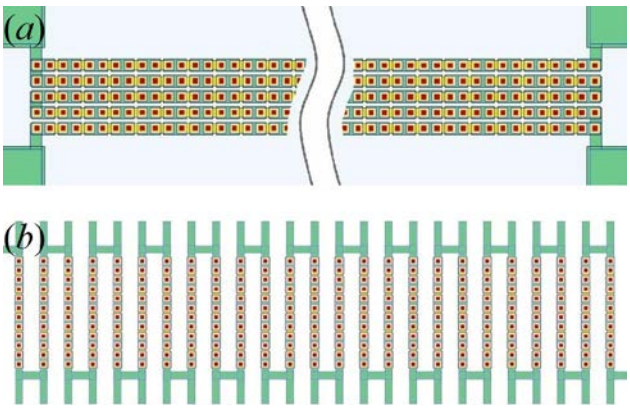

Fig. 1. JJ arrays investigated by LTSLM. (*a*) The linear sample. Rectangles at the corners are the parts of contact pads. The wavy lines indicate a break in the scheme. (*b*) A part of a subarray of the meander array. The JJs in both schemes are indicated by red squares.

The investigated samples are a 1-D arrays of Nb/NbSi/Nb JJs fabricated at PTB Braunschweig[13]. The dimension of junctions is 8 × 8 μm and the spatial period of their repetition in the structure is 15 μm. The arrays are fabricated on 10 × 10 mm silicon substrates with the thickness 0.38 mm. The first, "linear", array has the form of 5 long parallel strips (Fig. 1*a*). A single line includes 332 JJs, so the total number of junctions in the array is

$N_l = 1660$. Contact pads are connected to the corners of the array. This allows the bias current be also applied to either of two outside stripes. The second, "meander", array consists of six subarrays but we study only one (Fig. 1*b*). The subarray contains 125 short lines with 12 JJs per line so the total number of the junctions in the subarray is $N_m = 1500$.

The critical current I_c of both samples, compared to measurements in well-shielded cryostats, was slightly suppressed by residual magnetic fields and thermal radiation in the setup and was in the range I_c=1.5–2 mA.

III. LTSLM OF THE LINEAR ARRAY

Fig. 2 shows ΔU images of a part of the linear array recorded at two different values of bias current on adjacent steps of the IVC. The voltage is $U = 371$ mV for Fig. 2*a* and $U = 409$ mV for Fig. 2*b*. The image displays five horizontal lines which correspond to the five strips. Each strip consists of many pieces with rectangular form which represent the top electrodes covering two JJs each. There is a wavy contrast along the strips. The most distinct waves are seen on the three inner strips. The spatial period of the waves in both images is $w \approx 0.5$ mm.

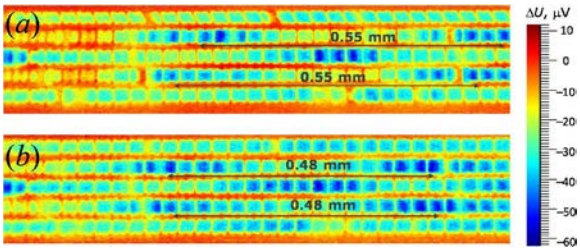

Fig. 2. LTSLM images of the linear JJ array obtained at $I = 2.17$ mA (*a*) and at $I = 2.37$ mA (*b*). For better view the scans are stretched by 2 times along vertical direction. The spatial period of wavy contrast in the inner strips is indicated in both scans.

We consider that the wavy contrast in the scans displays the standing electromagnetic waves excited in the strip-line resonators by the Josephson radiation. Standing waves have in fact been imaged before in LTSLM[12]. In essence, in the presence of a standing wave the voltage across the JJs is different from the voltage in the absence of such a wave. When the laser is positioned at an antinode, the wave is strongly perturbed leading to a large change ΔU. By contrast, the perturbation and the response ΔU are small when the laser is positioned at a node of the wave. Consequently the wavelength seen in LTSLM is half of the electromagnetic wavelength.

The conclusion that the strip-line resonator of a similar JJ array synchronizes the junctions was already made in Ref. 8 from an analysis of the IVC, but now we have the visualization of these resonator modes. Here w must be multiplied by 2 in order to obtain the length of a traveling wave i.e. $\lambda = 2w \approx 1$ mm. Let us calculate the wavelength λ_t of the Josephson radiation traveling along the surface of the substrate with the use of the Josephson relation. Taking into account the dielectric permittivity of silicon substrate $\varepsilon = 11.9$ we obtain for the case in Fig. 2*b*:

$$\lambda_t = \hbar c N_l \Big/ \left(2eU\sqrt{(\varepsilon+1)/2}\right) = 0.99 \text{ mm}$$

where $\hbar$, c, e are Planck's constant, the velocity of light and the elementary charge, respectively. We obtain $\lambda_t \approx \lambda$ in very good agreement with our suggestion that the wavy contrast in the scans is due to resonator modes in the strip-line resonator. More precise estimations of w show, that the standing waves in Fig. 2*a* and Fig. 2*b* are provided by 9th and 10th resonator modes correspondingly.

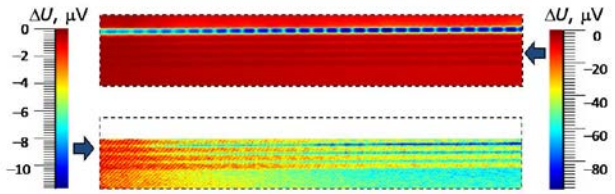

Fig. 3. LTSLM image, using two different color scales, of the linear JJ array at $I = 2.38$ mA with biasing the outside (upper) strip only. In the lower graph the response of unbiased strips is clearly visible.

We also performed LTSLM of the linear array with only a single strip-line biased. The image obtained at $I = 2.38$ mA supplied to the outside strip is shown in Fig. 3. Here the voltage is $U = 128$ mV. A nonzero response is also seen, when the laser beam is focused to the unbiased strips. Moreover, this response is positive although a scan of the biased strip causes a negative voltage response. Presently we cannot explain the inversion of the response but we suppose that this effect may be due to the interaction between biased and unbiased strips via electromagnetic waves generated by the JJs and propagating in the silicon wafer, as it was previously discussed[7].

IV. LTSLM OF MEANDER ARRAY

Fig. 4*a* shows a ΔU image of a part of the meander array, recorded at a bias which is slightly higher than I_c, so the voltage is only $U = 174$ mV. As in the case of the linear array the image allows to identify the design of the array with the top electrodes as the most contrast-giving objects. The value ΔU strongly differs for different straight strips, while it modulates less within single straight sections. Moreover, the sign of ΔU also changes. Very close to I_c a superposition of the response due the laser-induced reduction of the junction critical currents and the laser-induced perturbation of the standing electromagnetic wave is possible and may cause the sign change of ΔU. Besides this effect, if one traces along the superconducting circuit the contrast changes quite smoothly and with almost constant period $w \approx 1.2$ mm. Similar to the linear array, we argue that this is caused by the excitation of a standing electromagnetic wave along the whole length of superconducting circuit forming the meander section of JJ array.

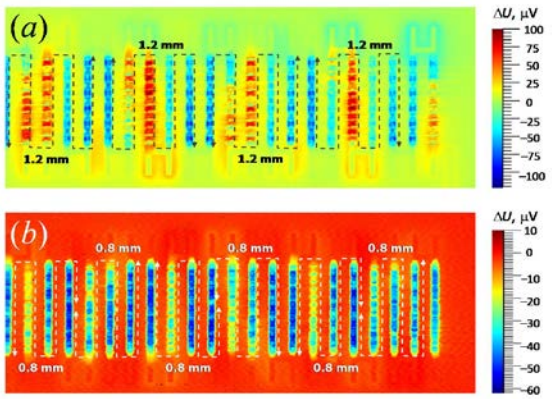

Fig. 4. LTSLM images of the meander JJ array at I = 1.9 mA (a) and at I = 2.18 mA (b). Arrows in the figures indicate the spatial period of standing waves meandering along the superconducting circuit.

The length of the traveling wave estimated from the scan in Fig. 4a is $\lambda = 2w \approx 2.4$ mm. The theoretical value of the wavelength λ_t obtained from the Josephson relation is

$$\lambda_t = \hbar c N_m \Big/ \left(2eU\sqrt{(\varepsilon+1)/2}\right) = 2.1 \text{ mm},$$

which is close to λ.

With the increase of bias current the period of the wavy contrast decreases, as we also saw for the linear array. Fig. 4b shows an image obtained at I = 2.18 mA. The voltage here is U = 262 mV, that is 1.5 times larger than U for the scan in Fig. 4a. As it follows from the Josephson relation the wavelength is also 1.5 times smaller than before, i.e. λ_t = 1.4 mm. The analysis of w from the image shown in Fig. 4b gives $\lambda \approx 1.6$ mm, which is again very close to λ_t.

If I is increased further, the wavy contrast decays and finally disappears. Fig. 5 demonstrates this for an image obtained at I = 2.9 mA and U = 369 mV. We see that all strips exhibit almost the same contrast. A possible explanation is that the mechanism of synchronization by resonator modes becomes minor in comparison with the traveling wave mechanism, as experimentally revealed for the meander array in Ref. 11.

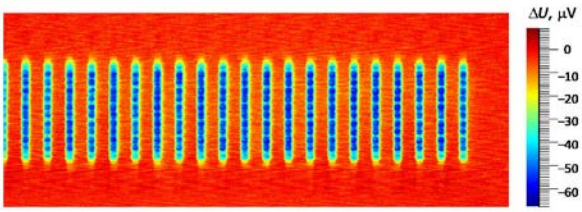

Fig. 5. LTSLM image of the meander JJ array at I = 2.9 mA

V. Conclusions

Low-temperature scanning laser microscopy (LTSLM) has been performed for two large 1-D arrays of Nb/NbSi/Nb JJs. The images obtained for the linear array exhibit wavy contrast associated with the excitation of resonator modes in straight strips of the array. In the case of the meander array we have also observed a wavy contrast of ΔU at I slightly higher the critical current. This contrast is likely to be due to standing electromagnetic waves excited along the meandering superconducting circuit. The experimentally observed wavelengths of such geometrical resonator modes at different I agree very well with the ones estimated from Josephson relation. LTSLM of a single strip of the linear array showed a nonzero response from other unbiased strips which may indicate an electromagnetic interaction between biased and unbiased strips in the linear array. The images of the meander array at comparatively high I have a homogeneous contrast along the circuit, indicating the dominance of the traveling wave mechanism in the synchronization of JJs in the meander array.

Overall, LTSLM of discrete planar JJ arrays provides an opportunity to visually observe the different mechanisms of synchronization of JJs, and also the interaction between different parts of the arrays.

Acknowledgments

The work was financially supported by the Russian Foundation for Basic Research, grant No. 18-02-0092, the Russian Science Foundation, grant No. 19-19-00594, the program of presidium RAS No. I.1 “Nonlinear dynamics: fundamental problems and applications” (the project “Nonlinear dynamics of superconducting and semiconducting superlattices”), the program of presidium RAS No. 12 “Fundamental problems of high-temperature superconductivity”, by the EU-FP6-COST Action CA16218 and by the Deutsche Forschungsgemeinschaft via project KL93013/2.

References

[1] I. K. Yanson, V. M. Svistunov, and I. M. Dmitrenko, *Zh. Eksp. Teor. Fiz.* **48**, 976 (1965) [*Sov. Phys. JETP* **21**, 650 (1965)].
[2] V. P. Koshelets and S. V. Shitov, *Supercond. Sci. Technol.* **13**, R53 (2000).
[3] E. A. Borodianskyi and V. M. Krasnov, *Nat. Commun.* **8**, 1742 (2017).
[4] S. O. Katterwe, H. Motzkau, A. Rydh, and V. M. Krasnov, *Phys. Rev. B* **83**, 100510(R) (2011).
[5] P. Barbara, A. B. Cawthorne, S. V. Shitov, and C. J. Lobb, *Phys. Rev. Lett.* **82**, 1963 (1999).
[6] U. Welp, K. Kadowaki, and R. Kleiner, *Nat. Photonics* **7**, 702 (2013).
[7] F. Song, F. Müller, R. Behr, A. M. Klushin, *Appl. Phys. Lett.* **95**, 172501 (2009).
[8] M. A. Galin, A. M. Klushin, V. V. Kurin, et al, *Supercond. Sci. Technol.* **28**, 055002 (2015).
[9] L. Ozyuzer, A. E. Koshelev, C. Kurter, N. Gopalsami, et al. *Science* **318**, 1291 (2007).
[10] T. Kashiwagi, T. Yamamoto, T. Kitamura, K. Asanuma, et al. *Appl. Phys. Lett.* **106**, 092601 (2015).
[11] M. A. Galin, E. A. Borodianskyi, V. V. Kurin, I. A. Shereshevskiy, et al., *Phys. Rev. Appl.* **9**, 054032 (2018).
[12] H. B. Wang, S. Guénon, J. Yuan, A. Iishi, S. Arisawa, T. Hatano, T. Yamashita, D. Koelle, and R. Kleiner *Phys. Rev. Lett.* **102**, 017006 (2009).
[13] F. Müller, R. Behr, T. Weimann, L. Palafox, et al., *IEEE Trans. Appl. Supercond.* **19**, 981 (2009).

Mutual Synchronization of Two Stacked Josephson Junction Arrays

M. A. Galin[1], V. M. Krasnov[2,3], A. M. Klushin[1]

[1] Institute for Physics of Microstructure RAS, Nizhny Novgorod, Russia
[2] Department of Physics, Stockholm University, AlbaNova University Center, Stockholm SE-10691 Sweden
[3] Moscow Institute of Physics and Technology (State University), Dolgoprudny, Moscow region, 141700 Russia

E-mail: galin@ipmras.ru

Abstract – We report on measurement of electromagnetic wave emission from two Nb/NbSi/Nb Josephson junction arrays stacked on top of each other. Each of the two arrays individually emits slightly different radiation spectra with maxima at certain resonant modes in the array. However, we observe that when both arrays are biased simultaneously at the same voltage, the total emission power is approximately doubled with respect to the sum of emission powers of individually biased arrays. This provides a clear evidence for synchronization of the two stacked arrays, leading to superradiant enhancement of emission.

Keywords – Josephson junction array, synchronization, InSb detector

I. Introduction

Mutual synchronization of Josephson junction (JJ) arrays is a crucial requirement for various applications [1]. The radiation power emitted from the JJ array can be enhanced proportionally to the square of the number of phase-locked JJs. The synchronization is usually facilitated by some resonant modes in the sample[2–6]. Those can be modes in an external cavity[2], parts of the superconducting circuit[3], dielectric substrate[4], or geometrical resonances in the junctions[5,6]. The geometry of JJs and the array do influence the process of phase locking via electromagnetic interactions between the neighboring JJs and subarrays.

In this work we study experimentally electromagnetic wave emission from two chain-like JJ arrays. Here we demonstrate that the two arrays can be mutually synchronized by stacking them on top of each other. We argue that vertical stacking is an effective way of coupling the arrays and can significantly increase the junction density and the emission power per area of the chip.

II. Scheme of measurements

Fig. 1 represents a scheme of measurements. Two arrays are stacked on top of each other and the emission power is measured by an InSb bolometer. Both arrays have a similar geometry with 332 Nb/NbSi/Nb JJs[7] in a linear chain. The JJs sizes are 8 × 8 μm and the spatial period of JJs in the chain is 15 μm. Characterization of similar types of Nb/NbSi/Nb arrays can be found in Refs. [3, 8]. The arrays are placed on silicon substrates with the sizes 1.5 × 10 mm and 10 × 10 mm for the upper and lower arrays, respectively. The thicknesses of both substrates are 0.38 mm. The orientation of contact pads for the two arrays, sketched in Fig. 1, allowed us to independently bias each array and to measure the generated electromagnetic power from the two arrays separately and together.

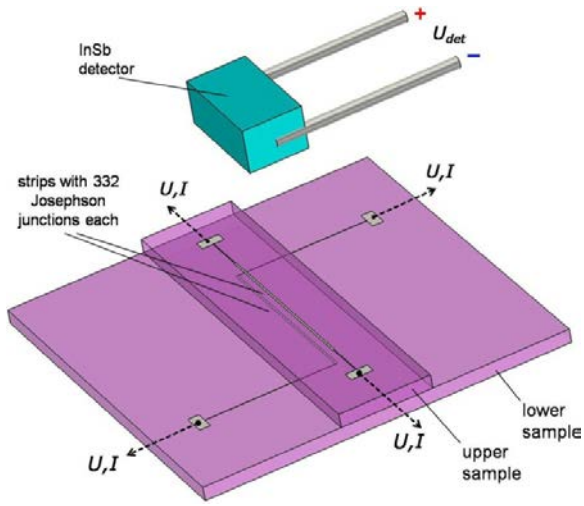

Fig. 1. The scheme of radiation measurements

The measurements were performed in ^{4}He cryostat at $T \sim 4.2$–4.4 K. For detecting the electromagnetic power emitted by arrays we used crystalline, high purity *n*-type InSb detector with longest size of 2.5 mm. It was positioned at a distance of ~ 5 mm above the surface of the upper array. We measured a dc-voltage response U_{det} at a fixed dc-bias current through the detector[3,8].

III. Results

First we analyze characteristics of individual arrays, when only one array is biased and the other is unbiased. Fig. 2a shows the current-voltage characteristics (red symbols, left axis) of the upper array, IVC_{up}, biased individually. The corresponding trace of the output voltage of the *n*-InSb detector U_{det}^{up}, which is proportional to the detected electromagnetic power, solely for the upper array (the lower array unbiased) is depicted in the same figure by olive symbols (right axis). The minimal critical current of a single junction of the upper array is about $I_c^{up} = 2.1$ mA and the average normal resistance is $R_n^{up} = 0.12\ \Omega$. Therefore, the average

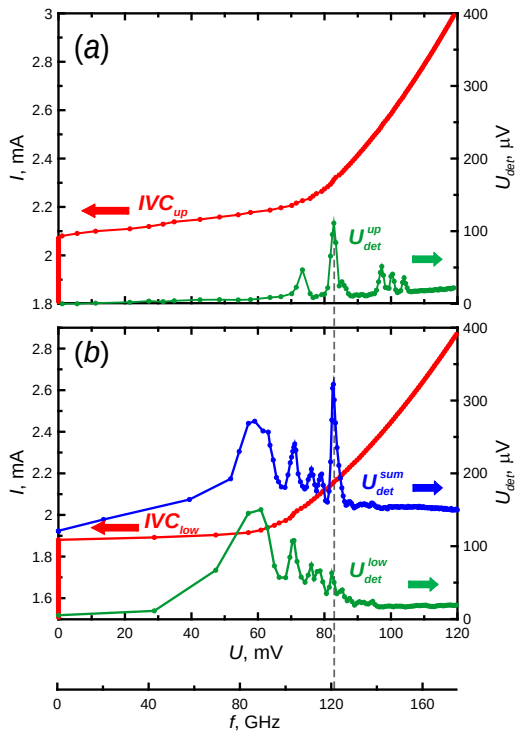

Fig. 2. (*a*) Current-voltage characteristic IVC_{up} of the upper JJ array and corresponding trace of the output voltage of the *n*-InSb detector U_{det}^{up}. (*b*) Current-voltage characteristic IVC_{low} of the lower JJ array and corresponding trace of the output voltage of the *n*-InSb detector U_{det}^{low}. The output voltage of the *n*-InSb detector shows the emission of the lower array if the upper array is biased to the maximum of U_{det}^{up} at frequency equal to f_s = 121 GHz. The dashed line indicates the output voltages of the detector at frequency f_s.

characteristic voltage for JJs in the upper array is $U_c^{up} = 253$ μV and the characteristic frequency $f_c^{up} = 122$ GHz. This frequency was derived from the equation $f = \Phi_c U_c$ where Φ_0 is the flux quantum.

Fig. 2b represents similar data for individually biased lower array. Red symbols represent the current-voltage characteristics of the lower array, IVC_{low}, and olive symbols show the corresponding emission signal U_{det}^{low} solely from the lower array with the top array unbiased. The minimal critical current of a single junction I_c^{low} of the lower array is about 1.94 mA and the average normal resistance $R_n^{low} = 0.13\ \Omega$. Therefore, JJs in the lower array have slightly different average characteristic voltage $U_c^{low} = 238$ μV and the characteristic frequency $f_c^{low} = 115$ GHz.

The scale with the Josephson frequency for both arrays is shown by the bottom axis in Fig. 2b. We can see that arrays emit in the range f = 80–140 GHz. The emitted power of each sample oscillates and rapidly decreases with the increasing of I and correspondently f as it is seen for the traces U_{det}^{up} and U_{det}^{low} (Fig. 2). According to the resistive shunted junction model of Josephson junctions their emission power should decrease with f for $f > f_c$.

The observed non-monotonous variation of the emitted power with increasing bias voltage $U_{det}^{up}(U)$, $U_{det}^{low}(U)$ is a clear indication[3,5,6,8] that the detected signal is caused by emission of electromagnetic waves with maxima at some specific resonant modes in a single-strip line (SSL) resonator containing a straight chain of 332 JJs. This is in contrast to the trivial heating effect, which increases monotonously with the total dissipated power in the array. The SSL resonances in similar but much larger arrays we studied in Refs. [3, 8]. In those larger arrays, correspondingly larger emission power leads to formation of pronounced self-induced resonant steps in current-voltage characteristics at maxima of the emitted power. Arrays studied here contain ~20 times less JJ and, therefore, self-induced resonant steps are much less pronounced. They are barely visible in the current-voltage characteristics in Figs. 2 a, b.

Finally, we explore interaction of two, simultaneously biased, arrays. Since biases in the two arrays can be varied independently, this leads to a complex two-dimensional variable space for the problem. To simplify the presentation, we have chosen to bias the upper array at a fixed bias, corresponding to the maximum emission power at f_s = 121 GHz, which is marked by a dash line in Fig. 2. Then the total emission power from both biased arrays is measured upon sweeping the bias in the lower array. The detected sum-emission signal from both arrays is shown by blue symbols in Fig. 2b and marked as U_{det}^{sum}. The sum-signal is lifted by ~150 μV, which is approximately equal to the individual signal from the upper array at the bias point, indicated by the dashed vertical line in Fig. 2a.

Upon increasing the bias voltage in the lower array, the detected sum-signal initially changes in a similar way as an individual signal from the lower array, compare olive and blue symbols in Fig. 2b. In this bias range the voltage and the Josephson frequency in the lower array are smaller than in the upper array. Consequently the two arrays cannot be synchronized and the total emission power is just a sum of two uncorrelated emissions from the two arrays.

However, a pronounced strong maximum of the sum-power appears when the voltage of the lower array becomes equal to that in the upper array (dashed line). This maximum was absent in the individual emission spectrum of the lower array, see the olive symbols in Fig. 2b at the dashed line. Therefore, the sum-signal at this point is non-additive In fact, it is approximately two times larger than the sum of the individual signals from the two arrays. The value of the synchronized signal is almost $U_{det}^{sum} \cong 350$ μV while the signal U_{det}^{low} without biasing of the upper array was approximately 60 μV. Taking into account the emitted power of the upper array equal to $U_{det}^{up} \cong 120$ μV we conclude that the gain of the radiation due to mutual synchronization is about factor 2.

The factor two increment of the emitted power from the two phase-locked arrays with respect to the sum of the powers of individual arrays is expected for the case of coherent superradiant emission. Indeed, in the non-coherent, unsynchronized state the emission power from the two sources is just the sum of the corresponding individual powers, as observed in experiment for $U_{det}^{low} < U_{det}^{up}$, c.f. blue and olive symbols in Fig. 2b to the left from the dashed line. For similar sources the

uncoherent emission power would just be two times the power from the individual source. However, at the phase-locking point the emitted waves from the two sources become coherent, which leads to quadrupling of the total emission power with respect to the individual source. Therefore, the observed factor two increment of the total emitted power with respect to the sum of individual powers provides a clear evidence for synchronization of the two arrays at the equal bias point, resulting in a coherent superradiant emission from the stack.

IV. Conclusions

We have measured power of Josephson radiation emitted by two linear JJ arrays stacked on top of each other. We observed a supperradiant enhancement of the total emission power with respect to the sum of individual powers of the two arrays. This provides a clear evidence for mutual synchronization of the arrays, which occurs when their oscillating frequencies coincide. Thus, we demonstrate that stacking of arrays provide an effective way of coupling of oscillator arrays. We anticipate that such stacking can lead to significant increase of the junction density and the emitted power per area of the chip. The latter should be proportional to the square of the number of stacked layers. Therefore, stacking provides a new dimension for creation of high-power coherent radiation sources.

Acknowledgments

Represented research was financially supported by the Russian Foundation for Basic Research, grant No. 18-02-0092, the Russian Science Foundation, grant No. 19-19-00594, the program of presidium RAS No. I.1 “Nonlinear dynamics: fundamental problems and applications” (the project “Nonlinear dynamics of superconducting and semiconducting superlattices”), the program of presidium RAS No. 12 “Fundamental problems of high-temperature superconductivity” (the project “Interaction of high temperature superconductor Josephson junctions with microwave and THz radiation”).

References

[1] M. Darula, T. Doderer, and S. Beuven, *Supercond. Sci. Technol.* 1**2**, R1 (1999).
[2] P. Barbara, A. B. Cawthorne, S. V. Shitov, C. J. Lobb, *Phys. Rev. Lett.* **82**, 1963 (1999).
[3] M. A. Galin, A. M. Klushin, V. V. Kurin, et al, *Supercond. Sci. Technol.* **28**, 055002 (2015).
[4] F. Song, F. Müller, R. Behr, A. M. Klushin, *Appl. Phys. Lett.* **95**, 172501 (2009).
[5] V. M. Krasnov, *Phys. Rev. B* **82**, 134524 (2010).
[6] E. A. Borodianskyi, and V. M. Krasnov, *Nature Commun.* **8**, 1742 (2017).
[7] F. Müller, R. Behr, T. Weimann, L. Palafox, et al., *IEEE Trans. Appl. Supercond.* **19**, 981 (2009).
[8] M. A. Galin, E. A. Borodianskyi, V. V. Kurin et al., *Phys. Rev. Appl.* **9**, 054032 (2018).

THz Dirac Gated Plasmons in Graphene: Landau Damping, Electron "Streaming" and Problem of THz Amplification

A. A. Andronov, V. I. Pozdniakova

Institute for Physics of Microstructures RAS, Nizhny Novgorod, Russia

E-mail: andron@ipmras.ru

Abstract – Phase velocities of gated plasmon in graphene with Dirac electron dispersion is found on bases of classical kinetic equation for equilibrium electron distribution. It is shown that decrease of electron sheet density towards charge neutral point the plasmon velocity V_P saturated above the Fermi velocity V_F before switching on Landau damping. It is pointed out that similar situation should take place also for non equilibrium distribution showing impossibility to explain THz amplification observed in Ref. 1 by drifted electron scheme. Some preliminary consideration pointed to possibility to explain results in Ref. 1 basing on momentum space negative transit time conductivity under non equilibrium "streaming" electron distribution in graphene.

Keywords – graphene, THz plasmons

I. Introduction

Recent observations of THz electromagnetic wave loss/gain in the transmission at 300 K through multiple gated grapheme – hBN sandwich (Ref. 1, Boubanga-Tombet et al.) under current flow along graphene layer and resonant THz detection by gated graphene plasmons at T = 10–300 K (Ref. 2, Bandurin et. al.) are considered by the authors as the beginning of THz Graphene Electronics. In particular THz amplification observed in Ref. 1 considered by the present authors as quite convincing and mechanism of THz amplification must be found. These results become possible due to development of grapthene – hBN sandwich fabrication technology which permits to have the sandwiches with graphene mobility above 50 000 cm^2/(V·sec) and drift velocities above 7·10^7 cm/sec at T = 300 K [3,4]. And for further development of this field and in particular for understanding mechanism of amplification observed in Ref. 1 discussion of the plasmon properties with full account of graphene Dirac type electronic band should be done. Below we first consider Dirac gated plasmon with Maxwell electron distribution that showing termination of plasmon phase velocity at the Fermi electron velocity. Then remarks on plasmon dispersion under electron drift will be given. We argue that similar plasmon velocity termination should occur also for drifted electron in graphene pointing to impossibility of explanation of the THz amplification basing on plasmon drifting model. And we propose "streaming" electron distribution and resonance effects its determine as a way to explain mechanism of the observed THz amplification.

II. THz Dirac gated plasmons in Graphene

The plasmons in gated 2-d gas and their excitation by current flow to provide electromagnetic emission out of the excited plasmons are discussed for at least for two decades starting from works by Dyakonov and Shur[5,6] (see also works cited in Refs. 1, 2). The plasmons in 2-d gas are depicted in the scheme in Fig. 1 where both simple and gated plasmons are shown together with scheme of THz amplification observation in Ref. 1. Here we consider only gated plasmons (below just plasmons).

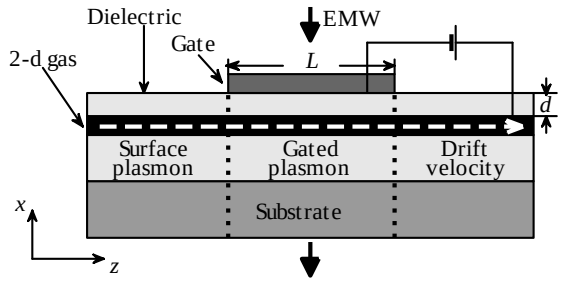

Fig. 1. Plasmons in sandwiched 2-d gas and scheme of observation of electro-magnetic wave (EMW) transmission through drifted 2-d gas.

Plasmons in 2-d gas are described by electrical potential $\varphi = \varphi(x,z,t)$: for our case without any dependence along y-axis. Electric field $\boldsymbol{E}$ is found from φ by standard for electrostatic way: $\boldsymbol{E} = \nabla\varphi$ with potential φ found from Laplace equation: $\Delta\varphi = 0$ and boundary conditions. A) At the 2-d gas layer $E_x(x-0) - E_x(x+0) = 4\pi eN/\varepsilon$; here e is an electron charge, N is electron sheet density in 2-d layer and ε is dielectric constant between 2-d gas and gate. In gated plasmon at $kd \ll 1$, k is the plasmon wavenumber, it is possible to neglect $-E_x(x-0)$. B) At surface of the gate for $x = d$ $E_z = 0$. Electron sheet density N is determined by electron dynamics and continuity equation in 2-d gas. For usually used simple approach with just Newton equation for electron in 2-d gas used and gets plasmon velocity

$$V_P = V_{G0} = \sqrt{\frac{4\pi e^2 dN_0}{m\varepsilon}}, \qquad (1)$$

e and m are an electron charge and mass, d – distance between gate and 2-d gas, N_0 – sheet electron density in

2-d layer. But in graphene electrons has relativistic (Dirac) like electron band with constant Fermi velocity V_F:

$$\varepsilon = V_F\, p. \tag{2}$$

In this case just Newton law is not appropriate. And we use linear scattering free Boltzman equation for perturbation of distribution function $\tilde{f}$ under influence of plasmon electric field wave $E_z = E_{z0}\mathrm{e}^{i(\omega t - kz)}$ with $\tilde{f} = \tilde{f}_0 \mathrm{e}^{i(\omega t - kz)}$ and equation for $\tilde{f}_0(p_y, p_z)$, p_y, p_z are in-plain electron momentums:

$$\tilde{f}_0 = -\frac{eE_{z0}}{i(\omega - kv_z)} \cdot \frac{\partial f_0}{\partial p_z}. \tag{3}$$

Here $f_0(p_y, p_z)$ is unperturbed electron distribution function. Now expression for perturbed sheet electron density $\tilde{N} = \tilde{N}_0 \mathrm{e}^{i(\omega t - kz)}$ is:

$$\tilde{N}_0 = \int \tilde{f}_0\, dp_y dp_z = -eE_{z0} \int \frac{\partial f_0}{\partial p_z} \cdot \frac{dp_y dp_z}{i(\omega - kv_z)}. \tag{4}$$

With gated plasmon potential $\varphi = \tilde{\varphi}_0 \mathrm{e}^{i(\omega t - kz)}(d - x)/d$ and $E_{z0} = ik\tilde{\varphi}_0$, $E_{x0} = \tilde{\varphi}_0 / d$ we get the gated plasmon dispersion relation

$$\frac{4\pi e^2 kd}{\varepsilon} \int \frac{\partial f_0}{\partial p_z} \cdot \frac{dp_y dp_z}{i(\omega - kv_z)} = -1. \tag{5}$$

This expression show specific for Dirac plasmon features of the Landau loss/gain (originated from zeros of denominator and derivative df_0 / dp_z) with constant Fermi velocity V_F. It exists for fixed $V_P < V_F$ not for fixed p_z but for a line in $p_y - p_z$ plane crossing both loss ($df_0 / dp_z > 0$) and gain ($df_0 / dp_z < 0$) and providing singularity in electron response to electric field.

We consider here first maxwellian equilibrium unperturbed electron distribution functions:

$$f_0 = A\mathrm{e}^{-\varepsilon/(kT)}, \quad A = \frac{N_0}{2\pi p_T^2}, \tag{6}$$

$p_T = \kappa T / V_F$, κ is the Boltzmann constant. Taking cylindrical coordinate system from Eq. (5) we have

$$\frac{2e^2 kdN_0}{p_T^3 \varepsilon} \int \mathrm{e}^{-p/p_T} \frac{p\cos\varphi\, d\varphi dp}{\omega - kV_F \cos\varphi} \tag{7}$$

Or

$$1 = \frac{V_G^2}{V_F^2}\left(\frac{1}{\sqrt{1-\left(kV_F/\omega\right)^2}} - 1\right), V_G^2 = \frac{4\pi e^2 V_F N_0 d}{p_T \varepsilon} \tag{8}$$

The presented here square root singularity is a common thing for any electron distribution providing termination of plasmon phase velocity at V_F. As it was mentioned above this is due to singularity of Landau damping for the Dirac electrons. From Eq. (8) we get V_P to V_G connection (Fig. 2)

$$\frac{V_P}{V_F} = \frac{1 + \left(V_G / V_F\right)^2}{\sqrt{1 + 2\left(V_G / V_F\right)^2}}. \tag{9}$$

We see that at any electron sheet density plasmon phase velocity is higher than Fermi velocity V_F and Landau damping is absent. On the other hand the maximum drift velocity V_D observed in grapheme sandwiches is only about $0.7V_F$. And this consideration seems demonstrate that it is impossible to have "supersonic" electron drift with $V_D > V_P$. But this consideration is related only to equilibrium distribution. Situation in Ref. 1 with high drift velocity is highly non equilibrium and the above conclusion could be not appropriate for discussion of results in that work because with highly non equilibrium distribution electron situation could be quite different.

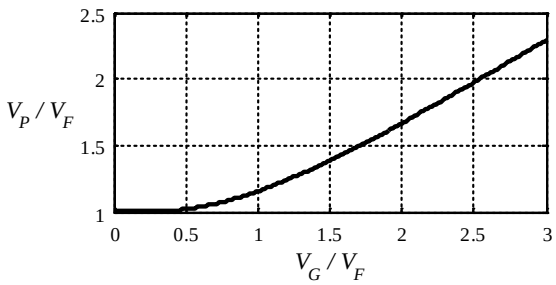

Fig. 2. Ratio of plasmon phase velocity to Fermi velocity versus ratio velocity V_G to Fermi velocity for maxwellian distribution.

But consideration has shown that singularity at $V_P = V_F$ in dispersion relation (5) survives also in non equilibrium electron distribution case. We discuss this point in more details at the Symposium. But contribution of the singularity is different for plasmons propagating along and contrary to electron drift. And Doppler shifted by the drift plasmon occurs. But such Doppler shifting by drift with even with $V_D \approx 0.7V_F$ cannot provide observed shifting mode frequency almost to zero as observed in Ref. 1. This drift velocity can shift mode frequency at maximum at 50 %. It is clear that Doppler shifting is not the mechanism of observation results in Ref. 1 and other mechanism must be looking for. There is seems only one effects which could be involved: electron dynamic response under electron "streaming" in graphene in high electric field with momentum space transit time resonance and negative conductivity under the streaming.

III. Electron Streaming and momentum spase transit time effects in Gpaphene

Streaming is cigar-like electron distribution (Fig. 3) on $p_y p_z$-plane with large distribution portion with constant f. Streaming is well known for holes in Ge in strong field[7]. It occurs under condition when an electron

reaches optical phonon energy almost without elastic scattering and quickly return back to $p \approx 0$ due to strong optical phonon emission.

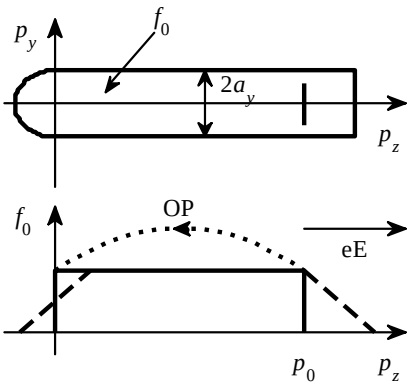

Fig. 3. Schemes of electron distributions under streaming: OP – optical phonon; full lines – ideal streaming

Recently simulation of electron distribution in graphene on SiO2 in high electric field was performed in Ref. 8. Though mobility in grapheme on SiO2 is at least ten times below that in hNB-grathene sandwiches weak streaming is seen in the plot. It is important that width of the cigar in graphene due to Dirac momentum energy dependence (2) is different from the situation in semiconductors (see e.g. Ref. 7, 9). In graphene the width is equal to momentum penetration in electric field beyond $p_0 = \varepsilon_0 / V_F$, ε_0 is the optical phonon energy. This is advantages for low cigar width. The width in the sandwiches in high electric field may be estimating basing on measured in the sandwiches drift velocity $V_D \approx 0.7 V_F$ that gives cigar width $\langle a_y \rangle$ about $0.3 p_0$. And we do think that momentum space transit time phenomena including negative conductivity (proposed[9] and demonstrated[10] in semiconductors in microwaves) could work here and explain observation in Ref. 1. To clarify these phenomena we present here only simple one dimensional model.

We consider momentum p_z region $(0, p_0)$ and spatially independent perturbation of distribution function $\tilde{f} = \tilde{f}_0 \mathrm{e}^{i\omega t}$ in electric field $E = E_0 + \tilde{E}_0 \mathrm{e}^{i\omega t}$, E_0 is the applied DC field . We take kinetic equation (without elastic scattering at $p_z < p_0$) for $\tilde{f}_0$:

$$i\omega \tilde{f}_0 + eE_0 \frac{d\tilde{f}_0}{dp_z} = -e\tilde{E}_0 \frac{df_0}{dp_z}, \qquad (10)$$

$f_0 = N_0 / p_0$ at $(0, p_0)$ is unperturbed time independent distribution function with $df_0 / dp_0 = N_0 \delta(p) / p_0$, $\delta(p)$ is delta function. We must add condition for perturbation of electron density $\tilde{N}_0 = \int \tilde{f}_0 \, dp_z = 0$. For $\tilde{E}_0 = 0$ we have solution $\tilde{f}_0 = C \mathrm{e}^{i\omega p_0 / (eE_0)}$ and from condition $\tilde{N}_0 = C\left(\mathrm{e}^{-i\omega p_0 / (eE_0)} - 1\right) = 0$ we get for $C \neq 0$ frequencies $\omega_n = 2\pi n e E_0 / p_0 = 2\pi n / \tau$, τ is the transit time in DC field from $p_z = 0$ to $p_z = p_0$. They are frequencies of transit time oscillations. We see that at such conditions electron system has resonance frequency which should influence electron system reaction on plasmon field and change plasmon behavior. Surely such approach is too simplified and elastic electron scattering and spread of the τ due to non ideal streaming provide attenuation of transit time oscillations. On the other hand these frequencies changed with DC field alike plasmon frequency changed due to Doppler effect. And at the Symposium we will give a little bit more developed calculation of transit time effects under streaming and discussion of its effects on plasmons.

IV. Conclusion

We have discussed gated plasmon in grapheme with full account of Dirac electron energy band and found that plasmon velocity terminates at Fermi velocity that shows impossibility to explain by drifted electron model observation[1] of tunable by drift THz loss/gain in gated plasmon system. Resonance effect in streaming electron system proposed as way for the explanation.

Acknowledgments

This work was done under IPM RAS Goscontract № 0035-2019-0021-C-01.

References

[1] S. Boubanga-Tombet et al., http://www.arXiv.org/abs/1801.04518.
[2] D. A. Bandurin et al., *Nature Communications* **9**, 5392 (2018).
[3] M. A. Yamoah, W. Yang, E. Pop and D. Goldhaber-Gordon, *ACS Nano* **11**, 9914 (2017).
[4] V. Perebeinos and P. Avouris, *Phys. Rev B* **81**, 195442 (2010).
[5] M. Dyakonov and M. Shur, *Phys. Rev. Letters* **71**, 2465 (1993)
[6] M. Dyakonov and M. Shur, *IEEE Trans. EL. Dev.* **43**, 380 (1996).
[7] T. Kurosawa, *J. Phys. Soc. Japan* **31**, 668 (1971).
[8] J. Chauhan and J. Guo, *Appl. Phys. Letters* **95**, 023120 (2009).
[9] A. A. Andronov and V. A. Kozlov, *Pizma v ZETF* **17**, 124 (1973).
[10] L.E. Vorobyev et al., *Pizma v ZETF* **73**, 253 (2001).

Terahertz Spectra of Drug-Laden Magnetic Nanoparticles

A. A. Baranova[1], V. N. Trukhin[1,2], P. G. Gavrilova[1], A. V. Semenova[3], K. G. Gareev[4], D. V. Korolev[5], O. A. Smolyanskaya[1]

[1] ITMO University, Saint Petersburg, Russia
[2] Ioffe Physicotechnical Institute, Russian Academy of Sciences, Saint-Petersburg, Russia
[3] IPM RAS, IAP RAS, Nizhny Novgorod, Russia;
[4] Micro and Nanoelectronics Department, Saint Petersburg Electrotechnical University, Saint Petersburg, Russia
[5] IEM, Federal Almazov North-West Medical Research Center, Saint Petersburg, Russia

E-mail: smolyanskaya@corp.ifmo.ru

Abstract – In this work it has been simulated the contribution of nanoparticles and the shell of organic molecules (glycose) to the dielectric properties of the pressed pellets, consisting of the polyethylene and nanoparticles. We studied experimentally the possibility of using terahertz radiation for spectral diagnosis of NPs based on iron oxide in a biologically inert shell of silicon dioxide drug-laden with a glycose.

Keywords – terahertz time-domain spectroscopy, iron oxide, magnetite, silica, nanoparticles, polyethylene, glycose, pellets

I. Introduction

An important problem of clinical medicine is currently the possibility of delivering drugs to a zone of ischemic damage for various purposes (delivery of a medicine, visualization of the injury itself, etc.) [1]. This can be done by using nanoparticles (NPs) based on iron oxide and controlling their movement along a blood vessel in the region of the lesion by means of an external magnetic field [2]. THz spectroscopy of nanoparticles with adsorbed organic and biological molecules could enable estimation of drug delivery efficiency of the nanoparticles sample and curative effect of delivering chemical substance [3].

II. Theoretical model of interaction the terahertz radiation with nanoparticles

The quasistatic approximation was used for estimation the electromagnetic field spatial distribution and corresponding dipole moment of nanoparticles. Each nanoparticle without adsorbed molecules was treated as a homogeneous isotropic dielectric sphere with radius r_0 and complex dielectric permittivity ε_2, surrounded by spatially uniform isotropic dielectric (polyethylene) with permittivity ε_0. A nanoparticle with adsorbed molecules was treated as the same sphere surrounded by a spherical layer with the external radius R and permittivity ε_1.

III. Materials and methods

Magnetic nanoparticles (MNPs) of two types were used: magnetite nanoparticles (MNP1) and iron oxide–silica colloidal particles (MNP2). The shape and size of the MNPs were examined by transmission electron microscopy (TEM) using a JEM-1400 STEM instrument with a field emission cathode (JEOL, Japan). The specific surface area of the MNP1 was determined by the simplified BET method on the Klyachko-Gurvich installation. In both cases (MNP1, MNP2), it was possible to identify the shell in which the nanoparticles are enclosed. The thickness of this shell is 5–7 nm. Glucose-treated MNP1 are individual coated nanoparticles. Modified MNP2, by contrast, are globules ranging in size from 20 to 100 nm, where several individual particles are included in the shell.

The pellets were prepared as follows: the nanoparticles were thoroughly mixed with 0.1 g of polyethylene in an agate mortar, so as each pellet contained 1.0 mass% NP powder. The dry mixture has been pressing into a pellet die for 1 min using a force of 100 bars. The diameter was 10 mm while measured thickness of the pellets was about 1.20–1.32 mm.

The measurements were carried out using the THz–TDS set-up. The femtosecond laser based on the titanium -sapphire laser was used as the radiation, which was used to generate THz radiation and to detect it. The optical pulse length of the femtosecond laser was 15 fs, the average wavelength was 800 nm, and the pulse repetition rate was 80 MHz with an average power of 0.65 W. The laser output beam was divided into two beams: a pump pulse and a probe pulse. Coherent THz radiation was obtained by excitation of InAs film grown on a GaAs substrate.

IV. Results and discussion

The calculations were based on the use of formulas for transmission of electromagnetic radiation through the absorbing medium. It has been demonstrate that the refractive index n has weak dispersion and its value is about 1.4–1.5 in the given spectral range. It should be noted that the refractive index n and absorption coefficient for samples 1-3 have in the spectral region 1.7 THz a feature similar to that for polyethylene in this region.

V. Results and discussion

Drag-laden magnetic nanoparticles can deliver drugs to a zone of ischemic damage for various purposes of clinical medicine. THz spectroscopy of nanoparticles with adsorbed organic and biological molecules could enable estimation of drug delivery efficiency of the nanoparticles sample and curative effect of delivering chemical substance. The first task of this work was to simulate the contribution of nanoparticles and the shell of organic molecules (glycose) to the dielectric properties of the pressed pellets, consisting of the polyethylene and nanoparticles. The second task of this paper was to study experimentally the possibility of using terahertz radiation for spectral diagnosis of NPs based on iron oxide in a biologically inert shell of silicon dioxide drug-laden with a glycose.

Acknowledgments

The reported study was funded by RFBR / RFBR-CNRS according to the research project #17-00-00275 (17-00-00272, 17-00-00184), by the Government of the Russian Federation (Grant 08-08), and in the framework of state targets N0035-2014-0206.

References

[1] Korolev, D. V., Galagudza, M. M., Uskov, I. S., Ostashev, V. B., Aleksandrov, I. V., Afonin, M. V., and Umenushkina, E. A., “Basis for using magnetic nanoparticles for directed delivery of medicines to an ischemic skeletal muscle,” *Biotekhnosfera* **19**(1), 2–6 (2012).

[2] Kharitonskii, P. V., Gareev, K. G., Ionin, S. A., Ryzhov, V. A., Bogachev, Yu. V., Klimenkov, B. D., Kononova, I. E., and Moshnikov, V. A., “Microstructure and magnetic state of Fe3O4-SiO2 colloidal particles,” *J. Magn*. **20**(3), 221–228 (2015).

[3] Smolyanskaya, O. A., Chernomyrdin, N. V., Konovko, A. A., Zaytsev, K. I., Ozheredov, I. A., Cherkasova, O. P., Nazarov, M. M., Guillet, J.-P., Kozlov, S. A., Kistenev, Y. V., Coutaz, J.-L., Mounaix, P., Vaks, V. L., Son, J.-H., Cheon, H., Wallace, V. P., Feldman, Y., Popov, I., Yaroslavsky, A. N., et al., “Terahertz biophotonics as a tool for studies of dielectric and spectral properties of biological tissues and liquids,” *Prog. Quantum Electron*. **62**, 1–77 (2018).

Magnetic Field Induced Interband THz Absorption in HgTe Quantum Wells

L. Bovkun[1], A. Ikonnikov[2], M. Potemski[3], M. Orlita[3], N. Mikhailov[4], S. Dvoretskii[4], V. Aleshkin[5], V. Gavrilenko[5]

[1] Physikalisches Institut, Universität Würzburg Am Hubland, Würzburg, Germany
[2] Faculty of Physics, M.V. Lomonosov Moscow State University, 119991 Moscow, Russia
[3] LNCMI-CNRS-UGA-UPS-INSA-EMFL, Grenoble, France
[4] Institute of Semiconductor Physics, Siberian Branch RAS, 630090 Novosibirsk, Russia
[5] Institute for Physics of Microstructures RAS, Nizhny Novgorod, Russia

E-mail: leonid.bovkun@physik.uni-wuerzburg.de

Abstract – The Landau level spectroscopy technique has been used to explore the electronic structure of the 20 nm HgTe quantum wells known for their semimetallic behaviour. THz absorption observed not only as classical cyclotron resonance but also in quantized magnetic fields due to inter-Landau levels transitions originated from the valence band. The obtained results were interpreted within the 8×8 k·p model, particular magneto-optical transitions are followed up to the magnetic field of 34 T.

Keywords – cyclotron resonance, HgTe/CdTe heterostrucutres, HgTe quantum wells, Landau level spectroscopy

I. Introduction

Nowadays CdHgTe-based heterostructures attract the attention of both fundamental and applied researcher due to their interesting properties and potential applications. While the quantum wells (QWs) with the so-called critical thickness of around $d_c \approx 6.4$ nm are interesting for their topological properties,[1,2] for wider QWs of $d \approx 20$ nm a semimetallic band structure was observed where electrons and holes of high mobility coexist in the same active layer.[3]

An absolute majority of experimental results were obtained with transport measurement, yet forming significant characterization of the case. In this work, we continue magneto-optical investigation emerged in Ref. 4. We carried out detailed measurements of a similar sample in magnetic fields up to 34 Tesla at different Fermi energies. The interpretation of the experimental results was based on the calculated intensities of the magneto-optical transitions.

II. Experimental details

The samples under study were grown by molecular beam epitaxy on semi-insulating GaAs (013) substrates.[5] Active part of HgTe 20 nm QW surrounded by 40-nm widegap CdHgTe barrier. Native defects (dominantly mercury vacancies) imply the *p*-type conductivity of as-grown samples, with the hole concentration below 10^{11} cm^{-2}.

The magneto-optical experiments were performed in the Faraday configuration using Fourier transform spectrometer. We used Globar as a radiation source and composite silicon bolometer as a detector. The radiation from spectrometer was guided via light-pipe optics to the sample and detector placed below the sample. Two types of magnets were employed: (i) superconducting solenoid for fields up to 11 T at T = 4.2 K and (ii) resistive solenoid for fields up to 35 T at T = 1.6 K. In former case, we were able to change the carrier concentration by blue LED illumination. The measured transmission spectra were normalized to the zero-field spectrum of the sample and empty optical tract. The transport data were collected using the standard Van der Pauw method simultaneously with the magneto-optical measurements.

The Landau level spectrum was calculated by the diagonalization of the 8×8 k·p Hamiltonian for (013)-oriented heterostructures, thus considering states with the symmetries Γ_6, Γ_8 and Γ_7 bands. A tensile strain in individual layers arising due to the mismatch of lattice constants in the CdTe buffer, HgTe QW, and CdHgTe barriers was also included, with material parameters taken from.[6] In order to facilitate the identification of individual absorption lines, we calculated the corresponding matrix elements for electric-dipole transitions between different pairs of LLs proportional to the relative strength of excitations.

III. Results and discussion

Figure 1 represents transmittance spectra collected with the step of 0.25 T. Darker regions corresponds to T_B/T_0 of more than 6%. Low B-field response is dominated with strong cyclotron resonance of electrons evolving into well-known β transition in quantizing fields. There are additional absorptions lines higher in energy then β and with a different slope. Such a behaviour could be explained if we assume that final Landau levels of this transitions lying higher in conduction band but originated below Fermi level in valence band with a high density of states.

Of particular interest another absorption feature of the data shown on Fig. 1. There are two low energy transitions of 5 meV around 8 T with pronounced splitting for B > 9 T, another clear evidence of quantized energy levels. One may conclude that latter transitions have negative bandgap at B = 0, but in fact, the influence

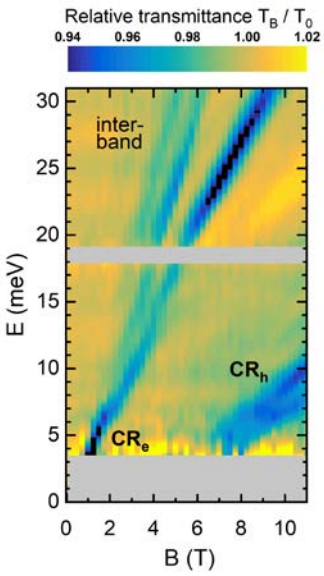

Fig. 1. Magneto-transmission of semimetallic sample plotted as a false color-map. The intraband absorption lines are labeled as CR_e and CR_h. The grey stripe corresponds to the spectral region fully opaque due to the reststrahlen band of HgCdTe. At low energies, both the low intensity of the radiation source and the low efficiency of the used beamsplitter, did not allow us to collect the data with a sufficiently high signal-to-noise ratio.

of side maxima $\boldsymbol{k} \neq 0$ of the valence band "bumps" Landau levels in the higher magnetic field as seen from calculations. Thus, 20-nm QW of HgTe with particular Fermi energy can demonstrate THz absorption not only due to intraband CR linear-dependent on B but additionally in quantized magnetic fields due to inter-Landau levels transitions of the valence band.

ACKNOWLEDGMENTS

This work was supported by the Russian Foundation for Basic Research and Program of Presidium RAS No 4, by CNRS through the LIA TeraMIR project and by ANR through Dirac3D project. L.B. also acknowledges Vernadski scholarship of the French government. The authors acknowledge the support of LNCMI-CNRS, a member of the European Magnetic Field Laboratory (EMFL).

REFERENCES

[1] B. A. Bernevig, T. L. Hughes, and S. C. Zhang, *Science* **314**, 1757 (2006).
[2] M. Konig, S. Wiedmann, C. Brune, A. Roth, H. Buhmann, L. W. Molenkamp, X. L. Qi, and S. C. Zhang, *Science* **318**, 766 (2007).
[3] Z. D. Kvon, E. B. Olshanetsky, D. A. Kozlov, N. N. Mikhailov, and S. A. Dvoretskii, JETP Lett. 87, 502 (2008).
[4] M. S. Zholudev et al., Nanoscale research letters 7, 534 (2012).
[5] N. N. Mikhailov, R. N. Smirnov, S. A. Dvoretsky, Y. G. Sidorov, V. A. Shvets, E. V. Spesivtsev, and S. V. Rykhlitski, International Journal of Nanotechnology 3, 120 (2006).
[6] E. G. Novik, A. Pfeuffer-Jeschke, T. Jungwirth, V. Latussek, C. R. Becker, G. Landwehr, H. Buhmann, and L. W. Molenkamp, Phys. Rev. B 72, 035321 (2005).

The Operation of THz Quantum Cascade Laser in the Region of Negative Differential Resistance

R. A. Khabibullin[1,2], N. V. Shchavruk[1], D. S. Ponomarev[1,2], D. V. Ushakov[3], A. A. Afonenko[3], K. V. Maremyanin[4], A. A. Dubinov[4], O. Yu. Volkov[5], V. V. Pavlovskiy[5]

[1] V.G. Mokerov Institute of Ultra High Frequency Semiconductor Electronics of RAS, Moscow, Russia
[2] Center for Photonics and 2D Materials, Moscow Institute of Physics and Technology, Dolgoprudny, Russia
[3] Belarusian State University, Minsk, Belarus
[4] Institute for Physics of Microstructures of RAS, Nizhny Novgorod, Russia
[5] Institute of radio-engineering and electronics of RAS, Moscow, Russia

E-mail: khabibullin@isvch.ru

Abstract – We investigate the light-current-voltage characteristics and emission spectra of 2.3 THz quantum cascade laser operating in the NDR region.

Keywords – quantum-cascade laser, THz region, resonant-phonon design, negative differential resistivity

I. Introduction

The electron transport in quantum cascade lasers (QCLs) is based on a combination of resonant tunneling and intersubband scattering in multiple quantum wells (MQWs), which may be called as sequential resonant-tunneling. The first experimental observation of the sequential resonant-tunneling is demonstrated for MQWs superlattice with an operating bias point outside the region of negative differential resistance (NDR) [1]. Using this approach and adding to the structure doped digitally graded alloy ("injector"), the first QCL is demonstrated [2]. Thus, avoiding NDR in operating dynamic range is a common design concept for QCL active regions in order to prevent instabilities. At the same time, the resonant coupling between injector level and upper laser level is expected to result in NDR, which is confirmed experimentally in many works [3–5].

In this work, we investigate the light-current-voltage (L-I-V) characteristics and emission spectra of THz quantum cascade laser operating in the NDR region.

II. Experimental results and discussions

We have designed THz QCL with active module based on 4 QWs GaAs/$Al_{0.15}Ga_{0.85}As$ with resonant-phonon (RP) depopulation scheme. The maximum gain of the proposed design is realized under RP conditions at 130 mkm wavelength which corresponds to the frequency of 2.3 THz.

The laser structure was grown by MBE with 10 µm active region thickness. For fabrication of THz QCL with Au-Au double metal waveguide we used the conventional processing described in [6]. The fabricated ridge structures with 1 mm cavity length and 100 µm cavity width were mounted onto copper C-mounts.

Fig. 1 shows the current-voltage (I-V) characteristic and the dependence of the total optical power on current (L–I). The lasing threshold occurs at J_{th} = 458 mA (voltage – 9.82 V). The nonmonotonic behavior of L–I characteristic is observed as what we associate with mode hopping. The peak power of THz QCL is achieved at a current 542 mA (voltage – 10.55 V) which corresponds to the alignment of the injector level and upper laser level.

A pronounced NDR region appears at voltages higher than 10.55 V. In this region, the I-V characteristic has a large number of discontinuities (see the inset of Fig. 1). This is due to the fact that in the initial part of the voltage pulse, a small step appears with an amplitude significantly higher than the rest of the pulse amplitude. The duration of this step (with constant amplitude) increases with increasing current, until it is equal to the duration of the voltage pulse. Since the voltage on the I-V characteristic is defined as the average value over the selected interval of time, then the increase in the duration of this step appears as an sharp increase of the voltage on I-V curve.

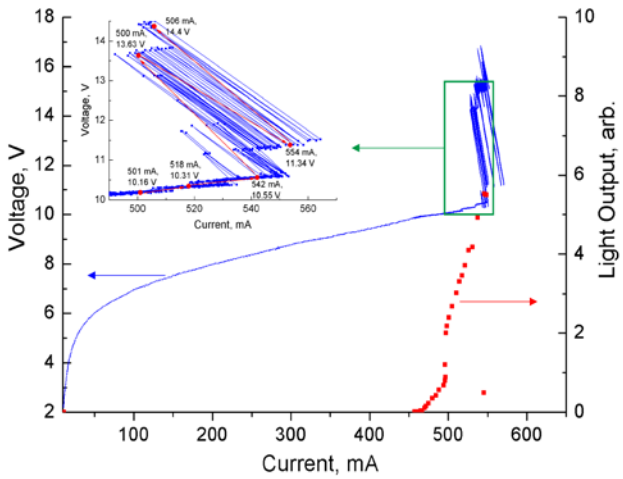

Fig. 1. L–I–V characteristic of fabricated THz QCL measured at 21 K in pulse mode with pulse width of 4 µs and repetition rate of 1 kHz. The inset shows the I–V characteristic in the NDR region (green rectangle on an enlarged scale). The red circles in the inset indicate the operation points for spectra measurements (see on Fig. 3).

We propose that such electric instabilities associated with the field inhomogeneity across the active region. Our calculations show that on the ascending branch of the

I–V characteristic, the electric field is almost uniform over the entire structure. On the descending branch of the I–V characteristic, the dynamic domains of the electric field arise in the structure. For the described structure the formation of sections across the active region with distinctly different electric field under the bias higher than 8.6 V (see Fig. 2). The field strength in the domain grows until it reaches the next positive portion of the I–V characteristic. In this case, the gain is realized only in a part of the structure outside the region of a strong field, and the radiation power decreases. Due to the instability of the domains, jumps on the I–V characteristics of the laser occur (see Fig. 1). Similar voltage profile in QCLs was observed experimentally in Ref. [7].

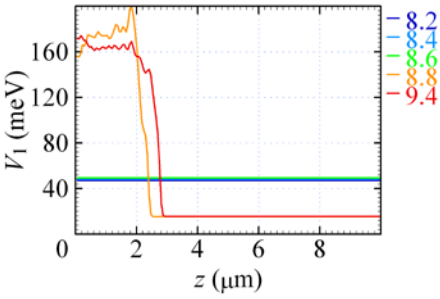

Fig. 2. Voltage profile across the active region of a THz QCL under different bias. The numbers indicate the voltage (in V) on the structure without the account of the contacts and external resistances.

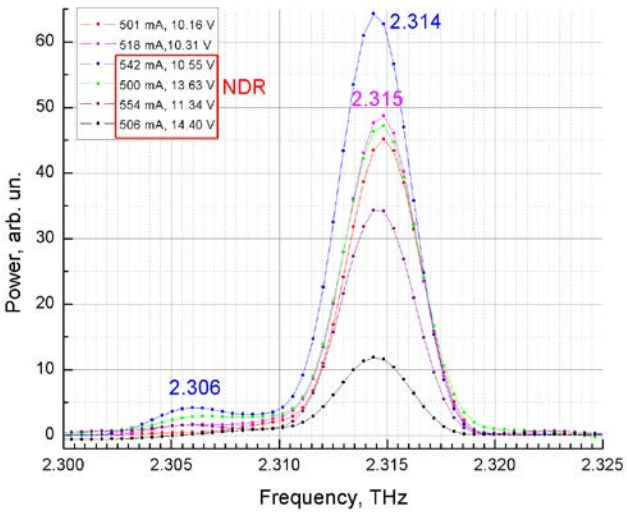

Fig. 3. Emission spectra of THz QCL at different current in the NDR region at 21 K

Fig. 3 shows the emission spectra of THz QCL operating at different current (prior the NDR region and in the NDR region). It is important to note that fabricated THz QCL demonstrates single mode generation with 2.314–1.315 THz spectral line at voltages higher than 10.0 V. In the NDR region the intensity of spectral line starts to decrease sharply which is due to two reasons: 1) misalignment of the electron levels (in particular between lower laser level and extractor level) at high bias; 2) formation of the electric field domain in active region.

III. Conclusions

We investigate the light-current-voltage characteristics and emission spectra of 2.3 THz quantum cascade laser with RP design operating in the NDR region. The I–V characteristic has a large number of discontinuities due to the formation of multiple sections across the active region with distinctly different electric field (electric field domains) in this NDR region.

Acknowledgments

This work was supported by the Russian Science Foundation (RSF), Project #18-19-00493, Russian Foundation for Basic Research (RFBR), Project #18-52-00011 Bel_a and the Belarussian Republican Foundation for Basic Research, Project # F18R-107.

References

[1] F. Capasso, K.Mohammed, A. Y. Cho, *Appl. Phys. Lett.* **48** (7), 478 (1986).
[2] J. Faist, F. Capasso, D. L. Sivco, C. Sirtori, A. L. Hutchinson, A. Y. Cho, *Science*, **264**, 553 (1994).
[3] S. L. Lu, L. Schrottke, R. Hey, H. Kostial, H. T. Grahn, *J. Appl. Phys.* **97**, 024511 (2005).
[4] A. Albo, Q. Hu, J. Reno, *Appl. Phys. Lett.* **109**, 081102 (2016).
[5] M. Wienold, L. Schrottke, M. Giehler, R. Hey, H.T. Grahn, *J. Appl. Phys.* **109**, 073112 (2011).
[6] R.A. Khabibullin, N.V. Shchavruk, A.Y. Pavlov, D.S. Ponomarev, K.N. Tomosh, R.R. Galiev, P.P. Maltsev, A.E. Zhukov, G.E. Cirlin, F.I. Zubov, Z.I. Alferov, *Semicond.* 50(10), 1377 (2016).
[7] R.S. Dhar, S.G. Razavipour, E. Dupont, C. Xu, S. Laframboise, Z. Wasilewski, Q. Hu, D. Ban, *Sci. Rep.* 4, 7183 (2014).

Auger Recombination Thresholds in Narrow Gap HgTe/CdHgTe QW Heterostructures

N. S. Kulikov[1], A. A. Dubinov[1], V. Ya. Aleshkin[1], V. V. Utochkin[1,2], S. V. Morozov[1,2], M. A. Fadeev[1,4], V. V. Rumyantsev[1,2], N. N. Mikhailov[5,6], S. A. Dvoretsky[5]

[1] Institute for Physics of Microstructures of RAS, Nizhny Novgorod, Russia
[2] Lobachevsky State University, Nizhny Novgorod, Russia
[3] Tohoku University, Sendai, Japan
[4] Laboratoire Charles Coulomb (L2C), Universite de Montpellier, Montpellier, France
[5] A.V.Rzhanov Institute of Semiconductor Physics, SBRAS, Novosibirsk, Russia
[6] Novosibirsk State University, Novosibirsk, Russia

Abstract – We performed numerical analysis of the Auger recombination energy threshold in $Hg_yCd_{1-y}Te/Cd_xHg_{1-x}Te$ heterostructures. The dependence of the threshold energy for such case has a non-monotonic dependence on the cadmium content in the barriers and reaches a maximum at x ~ 0.6-0.7. Comparison of numerical calculations with experimental results allows us to count on more than twofold increase in the temperature of quenching of stimulated radiation in optimal structures.

Keywords – QW, HgCdTe, heterostructures, Auger

I. Introduction

Nowadays there are semiconductor lasers operating in the wavelength range from far infrared up to x-rays. However, the range $\lambda \in 20 - 60\ \mu m$ remains void of effective semiconductor sources. Quantum cascade lasers (QCLs) provide high efficiency and narrow spectral band of radiation in the infrared range (IR) but it can be hard to create a QCL structure with precisely known ε_g. Moreover lattice absorption in GaAs/InAs/InP [1,2] (the most common materials for QCLs fabrication) for wavelength band $\lambda \in 20 - 60\ \mu m$ is too high to be overcome by optical gain.

The interband diode laser (IDL) is a straightforward alternative to unipolar QCL. It generates light in a process of radiative recombination between electron-hole pair. These lasers are widely used in near IR and visible range but their progression towards far IR range is limited by the slow-down of radiative recombination at lower energies and the amplification of non-radiative Auger recombination (AR).

AR is a process when an electron-hole pair recombines transferring released energy to the third particle. It strongly depends on temperature and carrier concentration and most importantly features energy threshold. This means that AR is not allowed until the energy of the particles involved in recombination exceeds certain value due to the requirement of compliance with energy-momentum conservation laws [3]. The threshold energy of AR is generally determined by dispersion relation of electrons and holes in the structure. For a "Dirac-like" dispersion of a free-space relativistic particle, threshold tends to infinity and Auger process is not allowed by conservation laws. There is evidence that similar carrier dispersion can be achieved in HgCdTe QWs greatly increasing the threshold of AR [4, 5]. At the same time, dispersion in HgCdTe QWs is "Dirac-like" only at low energies and depends on multiple parameters: QW and barrier composition, thickness and profile of QW and the strain of the structure. In order to achieve the best performance of HgCdTe-based emitters, one needs to design structures with such parameters to get the highest threshold of AR at a given bandgap. This "optimization" has been done for QW composition and thickness which allowed to obtain SE in the range up to 20 μm [5]. However, the influence of the other parameters of the structure on AR is still unclear.

In this research we study the dependence of dispersion relation in HgCdTe heterostructures on Cd content in barriers and QWs. We develop the model for numerical estimation of the AR threshold for arbitrary dispersion relation and apply it to calculated dispersion in $HgTe/Cd_xHg_{1-x}Te$ QWs with different *x*. We find the barrier composition which leads to the highest threshold of AR and is the most suitable for lasers on the base of HgTe/HgCdTe.

II. Materials and Methods

The energy-momentum relation $\varepsilon(\vec{k})$ in $Hg_{1-x}Cd_xTe/Cd_yHg_{1-y}Te$ QW heterostructures was calculated on the basis of axially symmetrical 4-band Kane Hamiltonian. The threshold energy was found as a minimal energy of a hole/electron which can participate in CCHC/HHCH Auger-processes respectively.

In order to find threshold values we optimize the final state energy as function of initial momentums with condition of energy and momentum conservation:

$$\begin{cases} \varepsilon_{th} = \varepsilon_f\left(\vec{k}_1 + \vec{k}_2 + \vec{k}_3\right) - \varepsilon_g \\ \varepsilon_f\left(\vec{k}_1 + \vec{k}_2 + \vec{k}_3\right) = \varepsilon_1\left(\vec{k}_1\right) + \varepsilon_2\left(\vec{k}_2\right) + \varepsilon_3\left(\vec{k}_3\right) \end{cases}$$

Where ε_{th} is threshold energy; ε_i and $\vec{k}_i$ are initial energies and momentums of three particles.

In order to verify the results of calculations we compared threshold value to the critical temperature of stimulated emission in the model $Hg_{1-x}Cd_xTe/Cd_yHg_{1-y}Te$ waveguide heterostructure. The structure was grown by molecular beam epitaxy on semi-insulating GaAs(013) substrate. It contains 10 $Cd_{0.1}Hg_{0.9}Te/Cd_{0.65}Hg_{0.35}Te$ QWs

with ~70 meV bandgap at 40-70 K range. It was put in a closed-cycle cryostat with variable temperature 8–300 K, connected to infrared Fourier spectrometer. CO_2 laser with 10.6 μm wavelength and pulse energy of up to 40 mJ was used for optical pumping.

III. Results

Fig. 1 shows dispersion of the first electron and hole subbands in three $Hg_{1-x}Cd_xTe/Cd_yHg_{1-y}Te$ QWs with different parameters. Structures (a) and (b) have the same barrier composition but different QW composition, while structures (a) and (c) have the same QW composition but different barriers. The thicknesses of QW were selected to obtain same bandgap in all structures.

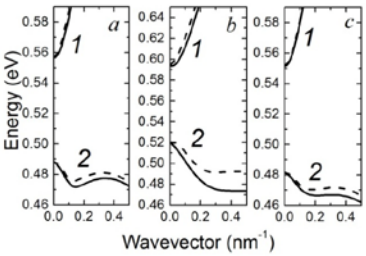

Fig. 1. Energy band spectra at 20 K calculated for (a) 8.7 nm $Cd_{0.1}Hg_{0.9}Te/Cd_{0.65}Hg_{0.35}Te$ QW (b) 4.2 nm HgTe/ $Cd_{0.65}Hg_{0.35}Te$ QW (c) 5.7 nm $Cd_{0.1}Hg_{0.9}Te/Cd_{0.3}Hg_{0.7}Te$ QW. 1 denotes electron subband, 2 denotes hole subband in each structure. Solid and dashed lines correspond to different spin-split subbands.

As one can see, the side maxima in valence band are most pronounced in structure (a) which has low Cd concentration in the barriers and high Cd concentration in the QW. These side maxima enhance AR. At low temperature of non-equilibrium carriers only the hole near the top of the valence band can participate in Auger processes. As the temperature grows the valence band fills up and when the holes reach the region of side maxima with high effective mass ($m = \frac{\varepsilon(k)}{k^2}$). As a result, Auger recombination surges up. In other two structures side maxima are lower and shifted to higher momentums, thus both the threshold and the critical temperature are higher.

Experimental results agree with our analysis and confirm that AR threshold decreases when decreasing Cd content in a QW and pure HgTe QWs allow achieving the highest temperature of SE quenching [5].

Contrary to the case of the QW, the threshold dependence on Cd content in barriers is not monotonous and reaches its maximum at $x_{Cd} \approx 0.6$ (Fig. 2). It can be explained in terms of dispersion relation. In a QW with high Cd fraction in barriers the effect of side maxima of valence band is negligible because AR starts before they are filled. Thus the onset of AR is determined by carrier dispersion at lower momentums. The increase of Cd content in barriers leads to lower ratio $\mu = \frac{\varepsilon_e(k)}{\varepsilon_h(k)}$ which enhances AR similar to the parabolic dispersion case with heavy-hole subband [3]. As a result, at high Cd fraction we observe a decrease in threshold energy. The position of threshold energy maximum varies depending on the bandgap and temperature but for the whole range 20–60 μm it is approximately 0.6–0.7.

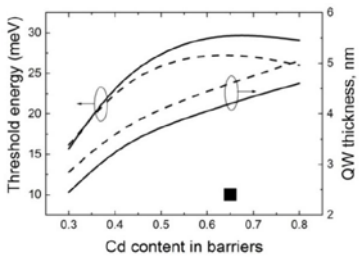

Fig. 2. HgTe QW thickness and Auger recombination threshold versus Cd content in barriers for 20 K (solid curves) and 70 K (dashed curves). QW thickness is calculated to have constant bandgap of 70 meV. Square symbol shows the highest temperature of stimulated emission observation in energy equivalent for model structure with 8.7 nm $Cd_{0.1}Hg_{0.9}Te/Cd_{0.65}Hg_{0.35}Te$ QW.

We compared the calculated threshold with experimental results of stimulated emission in a heterostructure with $Cd_{0.1}Hg_{0.9}Te/Cd_{0.65}Hg_{0.35}Te$ QW. Temperature quenching of stimulated radiation happens in the model structure at 110 K, which is equivalent to 10 meV and is twice as big as calculated threshold for this structure (Fig. 2). Comparing this result to threshold energy in optimised structures with HgTe QWs and $Hg_{0.4}Cd_{0.6}Te$ barriers allows us to count on more than twofold increase in the temperature of quenching of stimulated radiation.

IV. Conclusion

By modifying parameters of $Hg_{1-x}Cd_xTe/Cd_yHg_{1-y}Te$ QWs it is possible to manipulate dispersion relation of carriers in a QW and suppress Auger recombination. By implementing binary HgTe QWs and optimal Cd content in barriers (≈60%) it can be possible to achieve more than twofold increase in the temperature of SE quenching compared to the model $Cd_{0.1}Hg_{0.9}Te/Cd_{0.65}Hg_{0.35}Te$ structure.

Acknowledgments

This work was financially supported by grants of Russian Foundation of Basic Research ## 18-32-00628 and 18-02-00362.

References

[1] M.F. Anwar, T.W. Crowe, T. Manzur, W. Terashima, H. Hirayama. Proc. SPIE, 9483, 948304 (2015).
[2] R. Colombelli, F. Capasso, G. Gmachl, A.L. Hutchinson, D.L. Sivco, A. Tredicucci, M.C. Wanke, A.M. Sergent, A.Y. Cho. Appl. Phys. Lett., 105 (20), 201 102 (2014).
[3] Абакумов В.Н., Перель В.И., Яссиевич И.Н. Безызлучательная рекомбинация в полупроводниках. С.-Петербург: ПИЯФ РАН, 1997, 378 с.
[4] M. Marcinkiewicz, S. Ruffenach, S.S. Krishtopenko, A.M. Kadykov, C. Consejo, D.B. But, W. Desrat, W. Knap, J. Torres, A. V. Ikonnikov, K.E. Spirin, S. V. Morozov, V.I. Gavrilenko, N.N. Mikhailov, S.A. Dvoretskii, and F. Teppe, Phys. Rev. B, 96, 35405 (2017).
[5] Morozov S.V., Rumyantsev V.V., Fadeev M.A., Zholudev M.S., Kudryavtsev K.E., Antonov A.V., Kadykov A.M., Dubinov A.A., Mikhailov N.N., Dvoretsky S.A. and Gavrilenko V.I. Appl. Phys. Lett., 111, 192101 (2017).

Integration of UTC-PD Structure with InGaAs-HEMT for Optical-to-Wireless Carrier Frequency Down-Conversion

K. Nishimura[1,3], Y. Omori[1,3], T. Hosotani[1,3], T. Suemitsu[2,3], K. Iwatsuki[3], and T. Otsuji[1,3], and A. Satou[1,3]

[1] Research Institute of Electrical Communication, Tohoku University, Sendai, Japan
[2] Center for Innovative Integrated Electronic Systems, Tohoku University, Sendai, Japan
[3] Research Organization of Electrical Communication, Tohoku University, Sendai, Japan

E-mail: nkazuki@riec.tohoku.ac.jp

Abstract – We newly developed an InGaAs-channel high-electron-mobility transistor (HEMT) integrated with a uni-traveling-carrier photodiode (UTC-PD) structure as a carrier frequency down-converter from optical data signals to wireless data signals, which utilizes the photonic double-mixing functionality. It was demonstrated that the output intensity of the down-converted millimeter-wave signal is enhanced by 34 dB compared with a standard HEMT, owning to the integration of the UTC-PD structure. We also examined the hybrid integration of the UTC-PD-integrated HEMT with a preamplifier for further enhancement of the output intensity.

Keywords – fiber-wireless convergence network, double-mixing, InGaAs-HEMT, UTC-PD

I. INTRODUCTION

To realize future ultra-broadband ubiquitous, resilient communication networks, the seamless convergence of optical networks and wireless networks (the full coherent networks) is required[1,2]. For this purpose, a carrier frequency down-converter from optical data signals to wireless data signals with the preservation of their data modulation format (e.g., QPSK or QAM) is needed. We have studied the so-called photonic double-mixing functionality of graphene-channel FETs and InGaA high-electron-mobility transistors (InGaAs-HEMTs) to perform the conversion of the 1.5-μm bands to the millimeter-wave (MMW) bands[3]. The photonic double-mixing comprises two mixing functionalities: the usual photomixing of an optical carrier signal and an optical subcarrier signal, which generates the difference-frequency beat-note signal, and the RF mixing of the beat-note signal and an RF signal, which generates an IF data signal (i.e., a double-mixed signal) with a desired frequency. The photomixing can be realized using a transistor structure with high-speed photodetection functionality, if the photomixed current is generated either by the direct photoabsorption in the channel or by the injection from a certain absorption layer into the channel, while the RF mixing can be realized by impinging the RF signal to the gate and utilizing the nonlinear I-V characteristics. We have demonstrated the frequency down-conversion of a 10-Gbps-class ASK or BPSK modulated optical data signal into an MMW IF signal at 22.5 GHz by using an InGaAs-HEMT[4]. However, the double-mixing efficiency of the InGaAs-HEMT is very low due to its very thin absorption layer (i.e., the channel layer) and also due to generation of photoholes in the channel, which limits the high-speed operation due to their very low mobility.

In this work, we examine the integration of the uni-traveling-carrier photodiode (UTC-PD) structure in an InGaAs-HEMT for improvement of photoabsorption efficiency and for fast extraction of photogenerated holes. We fabricated a UTC-PD-integrated HEMT, measured its double-mixing performance, and demonstrated that the output intensity is enhanced significantly by the integration of the UTC-PD structure. We also examine the hybrid integration of the device with a preamplifier and observed the enhancement of the IF intensity over 10 dB.

II. UTC-PD-INTEGRATED INGAAS-HEMT

Figure 1 shows a cross-sectional schematic view of an InGaAs-HEMT integrated with the UTC-PD structure on its source side, which was originally proposed for the plasmonic enhancement of the THz photomixed signal generated from a UTC-PD[5]. In this structure, the input optical signals are mainly absorbed in the *p*-$In_{0.53}Ga_{0.47}As$ absorption layer and only photogenerated electrons are injected into the *i*-InP carrier-collection layer and photogenerated holes are extracted very fast to the contact, as in standard UTC-PDs[6]. Then, those electrons are injected into the source side of the $In_{0.53}Ga_{0.47}As$ channel layer of the HEMT. The hetero-epitaxial layers shown in Fig. 1 were grown by the molecular-beam epitaxy, while the electron-beam lithography and the standard lift-off process were used for the device fabrication. The fabricated device had the gate length 100 nm, the channel width 50 μm, and the UTC-PD area 18×50 μm^2. DC characteristics of a HEMT without the UTC-PD integration with the same gate length showed the maximum transconductance over 0.3 S/mm at the drain voltage 0.8 V. Measured cutoff frequency of a HEMT without the UTC-PD integration was 113 GHz.

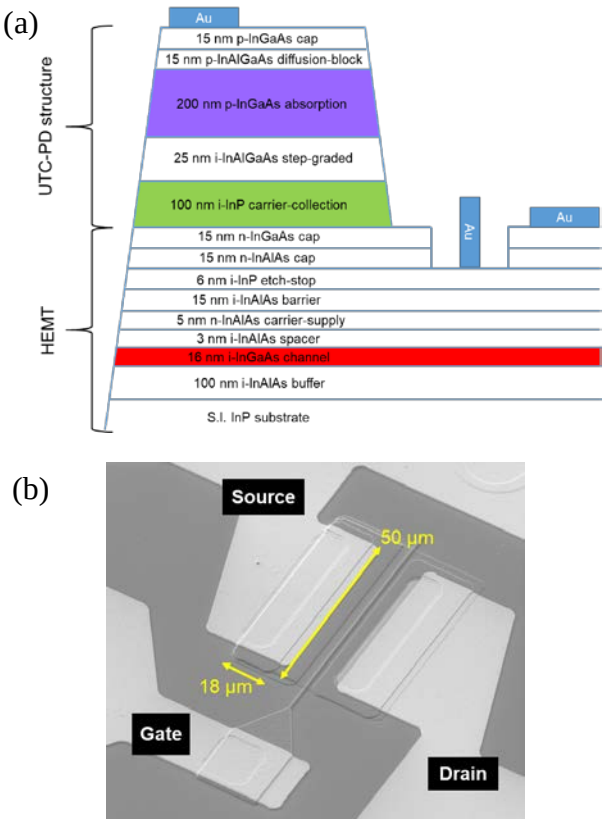

Fig. 1. (a) A cross-sectional schematic view of a UTC-PD-integrated InGaAs-HEMT and (b) an SEM image of the fabricated device.

The double-mixing measurement was conducted as follows. A pair of two optical signals with the difference frequency 112.5 GHz were generated from a set of a 1.58-μm tunable CW fiber laser source, a frequency comb generator, and an arrayed waveguide grating filter (details are found in [3]). Then, those optical signals were irradiated onto the absorption layer in the UTC-PD structure from the backside via a focusing lens. Their total power was 5.3 dBm. We focused the optical beam and aligned its position so that the maximum DC photocurrent is obtained. An RF signal with the frequency 90 GHz and the power 7.7 dBm was impinged to the gate. The HEMT was biased in a common-source configuration with a DC gate bias V_{GS} varied from –1.0 to 0.6 V and a DC drain bias V_{DS} varied from 0 to 0.8 V. The drain output IF intensity at 22.5 GHz was measured by an RF spectrum analyzer.

Figure 2 shows IF intensities of the photonic double-mixing measurement by (a) a standard HEMT and (b) a UTC-PD-integrated HEMT, both of which were fabricated on the same wafer. Bias voltages applied to each device were chosen such that they give the maximum IF intensity. As seen in Fig. 2, a significant enhancement of the intensity, over 34 dB, was achieved by the integration of the UTC-PD structure. The 10-dB enhancement is due to the increase in the absorption layer thickness by factor of about 10, while the remaining 24 dB should be attributed to the fast extraction of photoholes. Also, the photomixing output intensity by

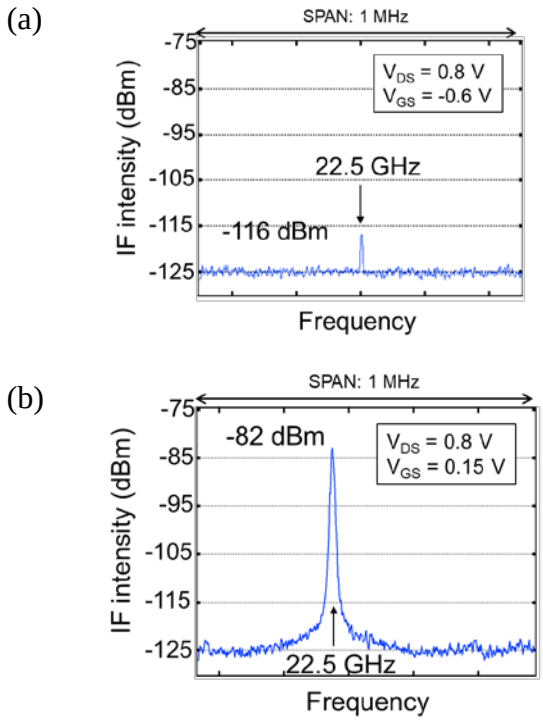

Fig. 2. Measured IF intensities of the photonic double-mixing by (a) a standard HEMT and (b) a UTC-PC-integrated HEMT.

the UTC-PD-integrated HEMT measured at the same biasing conditions as the double-mixing measurement in Fig. 2(b), with the optical difference frequency 25 GHz, was -62 dBm. Although this value is much lower than the photomixing output intensity that can be achieved by a commercially available MMW UTC-PD[8], estimated to be more than -20 dBm, with the same optical input intensity, further improvement of the UTC-PD structure (such as independent biasing of the UTC-PD and the HEMT and reduction of large mesa size of the UTC-PD compared with the focused spot size of the optical input) would allow us to enhance the performance. In addition, the loss caused by the RF mixing in the HEMT part, the difference between the double-mixing and photomixing output intensities, is 20 dB. The RF mixing loss can be reduced by the enhancement of the HEMT transconductance, i.e., by employing a thinner barrier layer and by employing an InAs channel layer.

III. Hybrid Integration with Preamplifier

Next, to further enhance the IF intensity, we implemented hybrid integration of a UTC-PD-integrated HEMT with a preamplifier. Figure 3 shows a photograph of a module of the hybrid integration. The preamplifier chip was fabricated with the GaAs-PHEMT MMIC technology and has a gain 12.5 dB and the cutoff frequency 48 GHz. The HEMT chip and the preamplifier chip are connected by a coplanar waveguide through bonding wires. The optical signals were irradiated to the UTC-PD part of the HEMT chip through a hole on the backside of the module.

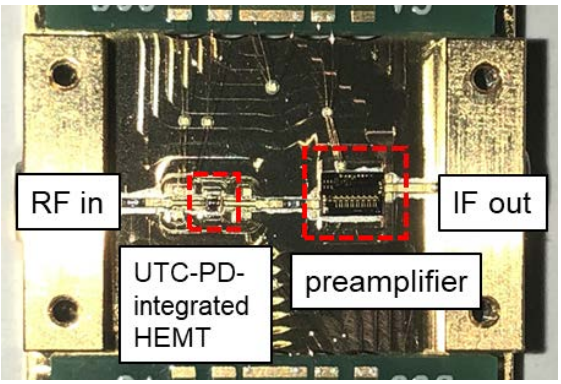

Fig. 3. A module of a UTC-PD-integrated HEMT with hybrid integration of a preamplifier

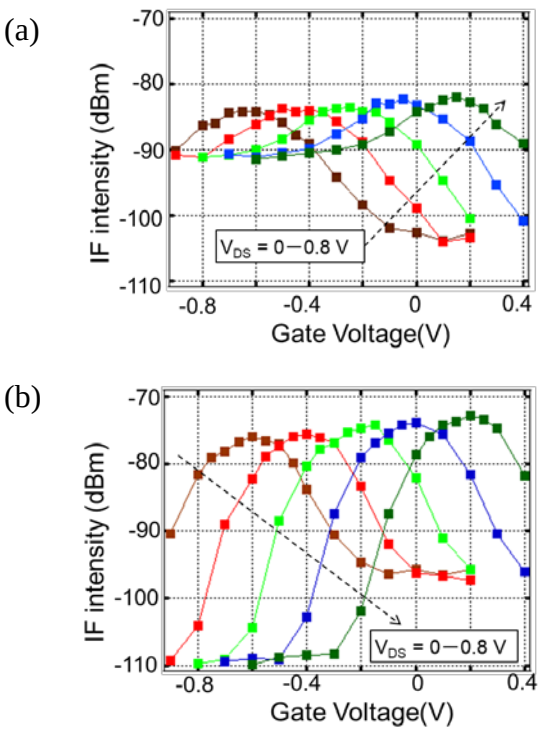

Fig. 4. Gate- and drain-bias dependences of measured IF intensities by (a) a bare chip of a UTC-PD-integrated HEMT and (b) a module of a UTC-PD-integrated HEMT with a preamplifier.

Figure 4 shows the gate- and drain-bias dependences of measured IF intensities by (a) a bare chip of a UTC-PD-integrated HEMT and (b) a module of a UTC-PD-integrated HEMT with a preamplifier. The conditions of the double-mixing measurement are the same as described in Sec. II. As can be seen in Fig. 4, the IF intensities are enhanced by a factor of 10 dB in the entire range of bias voltages, except below the peaks, as expected from the gain 12.5 dB of the preamplifier with a loss caused by an RF cable that transmits the RF signal at 90 GHz to the module input port. The exception at the gate voltages below the peaks can be attributed to the difference between the transconductances of the bare chip and the chip inside the module. Together with the further enhancement of the double-mixing performance of the device itself, cascade connection of amplifier(s) after the preamplifier or even monolithic integration of the device with a HEMT amplifier circuit on the same wafer should be examined for the practical use in the full-coherent networks.

IV. Conclusions

We examined the integration of the UTC-PD structure into an InGaAs-HEMT for the photonic double-mixing, that can be utilized for the carrier frequency down-conversion from optical to MMW data signals. The photonic double-mixing measurement was conducted, and the output IF intensity of the UTC-PD-integrated HEMT was significantly enhanced, over 34 dB, compared with a standard InGaAs-HEMT. We also showed a further enhancement of the IF intensity, 10 dB, by hybrid integration of the device with a preamplifier.

Acknowledgments

This work was financially supported by “R&D project on carrier-conversion technology with high environmental tolerance Research and System demonstration on high capacity O/E and E/O carrier-conversion technology for next generation wireless and wired networks,” NICT, Japan. The fabrication of the UTC-PD-integrated HEMTs was carried out at the Laboratory for Nanoelectronics and Spintronics of Tohoku University, Japan. We thank Drs. J. Terada and J. Kani, NTT Access Network Service System Labs., Japan, for the use of their equipment and valuable discussions about the measurement system. We thank Takada RF Labs., Inc., Japan, for implementation of the UTC-PD-integrated HEMT module and for fruitful discussions about the results.

References

[1] K. Iwatsuki, K. Tsukamoto, T. Nagatsuma, and N. Yoshimoto, presented at the 6th Global Symp. Millimeter Wave, Sendai, Japan, 2013, Paper M4.1.
[2] K. Iwatsuki and K. Tsukamoto, Proc. SPIE **9387**, 9387-1-9387-8 (2015).
[3] K. Sugawara *et al.*, J. Lightwave Technol. **34**, 2011-2019 (2016).
[4] A. Satou and T. Otsuji, Proc. SPIE **10403**, 104030S-1-104030S-12 (2017).
[5] V. Ryzhii and A. Satou, IEICE Technical Report **105**, 29-37 (2006).
[6] T. Ishibashi, N. Shimizu, S. Kodama, H. Ito, T. Nagatsuma, and T. Furuta, OSA Trends in Optics and Photonic Series, Ultrafast Electronics and Optoelectronics **13**, 83-87 (1997).

Compression of Unipolar Terahertz Pulses at Ionization Fronts in GaP

A. L. Novokovskaya, M. I. Bakunov

University of Nizhny Novgorod, Nizhny Novgorod, Russia

E-mail: bakunov@rf.unn.ru

Abstract – The transformation of a unipolar terahertz pulse at a counter-propagating ionization front in a GaP crystal has been considered theoretically. The pulse and the front are created by fractions of the same femtosecond laser beam via optical rectification and two-photon free-carrier generation, respectively. It is shown that, depending on the regime of the transformation, the reflected terahertz pulse with a highly uniform spectrum or with a time duration much shorter than the incident pulse can be generated.

Keywords – optical rectification, ionization front, frequency upshifting

I. INTRODUCTION

The transformation of terahertz pulses by reflection from optically induced ionization fronts in semiconductors has attracted attention recently as a method of terahertz frequency upconversion[1,2] and terahertz spectroscopy.[3] The experiments[2,3] were performed with ionization fronts created by linear interband excitation of a Si wafer by a Ti:sapphire laser. In this case, the propagation distance of the ionization front is limited by only ~10 μm, thus restricting the interaction time between the front and the terahertz pulse by ~140 fs.[1] Meanwhile, much longer propagation distances can be achieved if ionization fronts are created by nonlinear multiphoton absorption of laser pulses.[4]

An analytical theory of wave transformation at ionization fronts has been developed only for monochromatic waves in the approximation of stationary-propagating fronts.[5,6] FDTD modeling has been performed only for terahertz pulses of alternating polarity and exponentially decaying fronts in Si.[1-3] In this paper, we develop a theory of the transformation of broadband terahertz pulses at ionization fronts in electro-optic crystals. As a practical example, we consider the transformation of optically generated unipolar free- and forced-wave terahertz pulses[7] at an ionization front in a GaP crystal.

II. MODEL AND APPROACH

We assume that an ionization front $x = -V_f t$ moves with velocity $V_f = c/n_g$ (n_g is the optical group refractive index) in an electro-optic crystal and creates free carriers with plasma frequency ω_p. Terahertz field $E_z = E_0 f(t - x/V_{\mathrm{THz}})$ propagates with velocity V_{THz} in the counter direction and impinges the front. We consider two situations. First, the terahertz field is a freely propagating wave generated by the optically rectified pump laser pulse at the entrance boundary of the crystal.[7,8] In this case, $V_{\mathrm{THz}} = c/n_{\mathrm{THz}}$ with n_{THz} the terahertz phase refractive index. Second, the terahertz field is a forced wave that copropagates the pump optical pulse with the optical group velocity, i.e., V_f.[7,8]

To find the scattered fields, we use a Galiliean transformation to a coordinate system moving with the front, with $\xi = x + V_f t$, $t' = t$. Since the plasma density profile is immobile in this system, we apply a Fourier transformation with respect to t' to the Maxwell equations and match the Fourier transforms of the fields at the front by boundary conditions.[9] Then, we apply the inverse Fourier transformation and return to the x,t coordinates. Finally, we obtain for the reflected terahertz field:

$$E_z^r = E_0 \gamma^{-1} \int_{-\infty}^{\infty} d\omega\, \tilde{f}(\omega/\gamma) R(\omega) e^{i\omega t + ix\omega/V_{\mathrm{THz}}}, \qquad (1)$$

where $\tilde{f}$ is the Fourier transform of $f(t)$, R is the reflection coefficient, and γ is the kinematic factor. If the incident terahertz field is a freely propagating wave, R is given by

$$R = \left(1 - \sqrt{1 - \gamma\omega_p^2/\omega^2}\right) \Big/ \left(1 + \sqrt{1 - \gamma\omega_p^2/\omega^2}\right) \qquad (2)$$

and $\gamma = (1 + n_{\mathrm{THz}}/n_g)/(1 - n_{\mathrm{THz}}/n_g)$. If the incident field is a forced wave, then $\gamma = 2/(1 - n_{\mathrm{THz}}/n_g)$ and R is given by a more complex formula than (2). For the parameters of GaP, however, $R(\omega)$ numerically almost coincides with Eq. (2).

In further calculations we assume a Gaussian optical intensity envelope, i.e., $f(t) = \exp(-t^2/\tau^2)$. For GaP we use following parameters: $n_g = 3.66$ (for 800-nm wavelength of a Ti:sapphire laser) and $n_{\mathrm{THz}} = 3.31$.

III. RESULTS

Figure 1 shows the spectra and temporal waveforms of the reflected terahertz pulse in comparison with the incident pulse. Since the graphs for free- and forced-wave incident pulses practically coincide, we do not distinguish these cases. One can see two interesting effects in Fig. 1. The first effect is the generation of a perfectly uniform terahertz spectrum in a wide frequency range 0–5 THz (Fig. 1(a)). The second effect is the generation of a strongly compressed terahertz pulse with an amplitude comparable to the amplitude to the amplitude of the incident pulse (Fig. 1(d)).

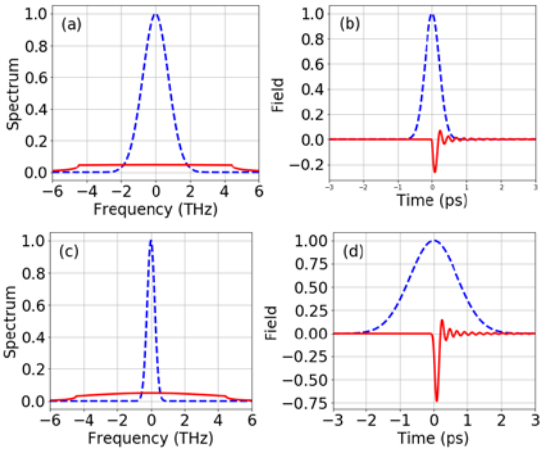

Fig. 1. Spectra (a, c) and waveforms (b, d) of the reflected (solid) and incident (dashed) terahertz pulses for τ = 300 fs (a, b) and 1 ps (c, d). The plasma frequency is $\omega_p/2\pi$ = 1 THz.

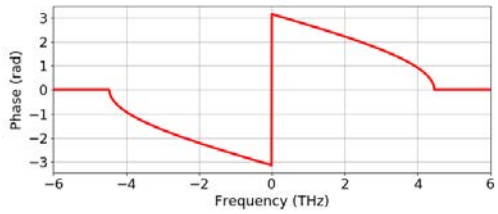

Fig. 2. Phase spectrum of the reflected terahertz pulses for $\omega_p/2\pi$ = 1 THz

Figure 2 shows the phase spectrum of the reflected pulse.

IV. Conclusions

Reflection of unipolar terahertz pulses from optically induced ionization fronts in electro-optic crystals can be used for the generation of uniform broadband terahertz spectra, very short high-amplitude terahertz pulses, and phase modulated pulses.

Acknowledgments

This work was supported by the Ministry of Science and Higher Education of the Russian Federation (3.3854.2017/4.6).

References

[1] M. D. Thomson, S. M. Tzanova, and H. G. Roskos, *Phys. Rev. B* **87**, 085203 (2013).

[2] F. Meng, M. D. Thomson, and H. G. Roskos, *Phys. Rev. B* **90**, 155207 (2014).

[3] N. Kohno, R. Itakura, and M. Tsubouchi, *Phys. Rev. B* **94**, 155205 (2016).

[4] E. S. Efimenko, S. A. Sychugin, M. V. Tsarev, and M. I. Bakunov, *Phys. Rev. A* **98**, 013842 (2018).

[5] V. I. Semenova, *Sov. Radiophys*. **10**, 1077 (1967).

[6] M. Lampe, E. Ott, and J. Walker, *Phys. Fluids* **21**, 42 (1978).

[7] M. I. Bakunov, M. V. Tsarev, S. B. Bodrov, and M. Tani, *J. Appl. Phys.* **105**, 083111 (2009).

[8] M. I. Bakunov, A. V. Maslov, and S. B. Bodrov, *Phys. Rev. Lett.* **99**, 203904 (2007).

[9] M. I. Bakunov and A. V. Maslov, *IEEE Trans. Plasma Sci.* **27**, 655 (1999).

Terahertz Pulse Time-Domain Holography Method for Phase Imaging of Breast Tissue

E. L. Odlyanitskiy[1], M. S. Kulya[1], N. S. Balbekin[1], Q. Cassar[2], O. V. Kravtsenyuk[1], J.-P. Guillet[2], P. Mounaix[2], K. I. Zaytsev[3,4], N. V. Petrov[1], O. A. Smolyanskaya[1]

[1] ITMO University, Saint-Petersburg, Russia
[2] Bordeaux University, IMS Laboratory, Bordeaux, France
[3] Bauman Moscow State Technical University, Moscow, Russia
[4] Prokhorov General Physics Institute of the Russian Academy of Science, Moscow, Russia

E-mail: smolyanskaya@corp.ifmo.ru

Abstract – In this work we have created the experimental scheme that involves measurement of diffraction pattern of the collimated THz pulse field spatial distribution at some distance behind the object in the time-domain mode, thus allowing reconstruction of amplitude and phase distribution at the object plane by numerical backpropagation of the wavefront in the spectral domain. In our experiment, we used a breast biopsy sample containing cancer tissues, we also performed numerical simulations accounting for experimental conditions to confirm the conceptual applicability of the reconstruction method.

Keywords – terahertz spectroscopy, pulsed time-domain holography method, optical properties, breast cancer, tumor, tissue, reconstructed images

I. Introduction

The angular spectrum representation is a numerical technique describing optical fields in a homogeneous media [1–2]. Optical fields are described as a superposition of plane waves and evanescent waves. A useful approach to describe optical field diffraction is to conduct the Fourier analysis at a given plane so that the different Fourier components of the field distribution are identified as plane waves propagating away from that plane in different directions. Thus taking less computation time for numerical reconstruction. This technique is preferable for the analysis of light diffraction by histological slides [3]. Pulse holographic imaging along with timedomain spectroscopy scan and tomographic techniques are of great interest. Since the advantages of holography are the lack of focusing optics and high spatial resolution, and, comparing with tomography, less computation cost for numerical reconstruction, this technique is preferable for the analysis of thin histological samples.

II. Theoretical model of interactionthe terahertz radiation with nanoparticles

Angular spectrum representation consists of the following stages. Firstly we form initial temporal form of THz pulse. The THz pulse is an ideal one-period structure with the envelope of the modulus square of E(t) about 1 ps. It is decomposed through the Fourier spectrum into frequencies. Then we form two-dimentional beam, multiplying the amplitude and phase by corresponding masks (gaussian amplitude mask and plane phase mask). Angular spectrum representation consists of following stages: 1) the representation of the field through the angular spectrum of 2D wave vectors; 2) then multiplication by the transfer function; 3) then the transition back from plane waves to the wave field in the calculated z-plane. The propagation dynamics of the pulsed THz radiation through a tissue sample was numerically simulated in the temporal and spectral domains. Moreover, optical parameters such as the index of refraction, $nre(\lambda)$, absorption coefficient, λ, and its dispersion behavior was taken from the experiment.

III. Materials and methods

A commercially available TeraPulse4000 (Teraview Ltd, Cambridge, UK) configured in reflection geometry by the means of external added optics was used to probe freshly excised breast tissues. THz-pulses were generated on a photoconductive antenna using a titanium:sapphire laser emitting 800 nm ultrafast pulses. Generated THz-pulses bandwidth is lying between 100 GHz and 4 THz. Pulses were focused by a 50 mm focal length tsuripica lens (Microtech Instruments, USA) on a 2 mm thick C-cut sapphire window.

IV. Results and discussion

We made a simulation of the image reconstruction of breast tissue with cancer. We used the refractive index and the absorption coefficient of healthy tissue and diseased tissue, which were obtained experimentally, to take into account the optical properties of the sample. In the numerical simulation we used following parameters: distance z between object and detector was 5 mm, object size and screen size are 50 mm (128x128 pixels); pixel size was determined by screen size divided by 128, Δx = 390 um. taking into account the optical properties

of the object under study is important for correct data analysis. In particular, in the case of working with biological objects, the accuracy of the localization of tumors or foreign bodies in the tissue is important. We believe that these studies will find application in medicine (THz tomography) and pharmacology.

ACKNOWLEDGMENTS

The reported study was funded by RFBR-CNRS according to the research project 18-51-16002 and by the Government of the Russian Federation (Grant 08-08).

REFERENCES

[1] Ziegler, R., Kaufmann, P., and Gross, M., A framework for holographic scene representation and image synthesis, *IEEE transactions on visualization and computer graphics* **13**(2), 403{415 (2007).

[2] Petrov, N. V., Kulya, M. S., Tsypkin, A. N., Bespalov, V. G., and Gorodetsky, A., Application of terahertz pulse time-domain holography for phase imaging, *IEEE Transactions on Terahertz Science and Technology* **6**(3), 464{472 (2016).

[3] Smolyanskaya, O., Schelkanova, I., Kulya, M., Odlyanitskiy, E., Goryachev, I., Tcypkin, A., Grachev, Y. V., Toropova, Y. G., and Tuchin, V., Glycerol dehydration of native and diabetic animal tissues studied by thz-tds and nmr methods, *Biomedical optics express* **9**(3), 1198{1215 (2018).

Terahertz Photoconductivity Studies of Waveguide HgCdTe Structures with Quantum Wells for Long-Wavelength Lasers

A. A. Razova[1,2], V. V. Rumyantsev[1], M. A. Fadeev[1], M. S. Zholudev[1], A. A. Dubinov[1], V. Ya. Aleshkin[1], N. N. Mikhailov[3], S. A. Dvoretsky[3], V. I. Gavrilenko[1] and S. V. Morozov[1]

[1] IPM RAS, Nizhny Novgorod, Russia
[2] Lobachevsky State University, Nizhny Novgorod, Russia
[3] Rzhanov Institute of Semiconductor Physics, Siberian Branch, Russian Academy of Sciences, Novosibirsk, Russia

E-mail: rumyantsev@ipmras.ru

Abstract – Photoconductivity and emission spectra of narrow gap $Hg_{1-x}Cd_xTe/Cd_yHg_{1-y}Te$ quantum well structures with dielectric waveguide are studied. It is shown that the position of the side maxima of the first valence subband limits the maximum temperature at which stimulated emission can be obtained.

Keywords – HgCdTe, photoconductivity, long-wavelength radiation, stimulated emission

I. Introduction

In the recent years, coherent radiation with a wavelength of up to 20 μm has been obtained in HgCdTe heterostructures with quantum wells (QWs) [1] paving the way to development of new type of lasers in the wavelength range of 20–60 μm. As yet, in this range quantum cascade lasers (QCLs) are scarce due to strong lattice absorption in InP and GaAs, which are used for the majority of the QCLs [2, 3]. Lead salt lasers are the only semiconductor sources that cover 20–50 μm range [4]. At the same time, their figures of merit suffer from growth technology disadvantages. In HgCdTe, the phonon frequencies are low enough to enter 20–60 μm spectral region[5], while $Hg_{1-x}Cd_xTe/Cd_yHg_{1-y}Te$ quantum wells (QWs) allow bandgap tuning in a wide range from several hundred of meV down to less than 10 meV [6]. It is important to note that in such structure the same bandgap can be obtained for different x, y and QW thickness d, with different carrier energy spectrum for each case. This can affect the efficiency of radiation.

Light confinement in far infrared spectral range requires thick dielectric waveguides and, accordingly, a high growth rate of the structures, which can affect the shape and the composition of the QW [7]. Despite modern molecular beam epitaxy allowing in situ monitoring of the QW parameters [8] detailed ex situ characterization of the grown structures can be of interest.

In this work we report on the studies of photoconductivity (PC) spectra of narrow gap HgCdTe QW structures. We identify the interband and "impurity-related" transitions and extract the QW parameters. Finally, we estimate the efficiency of Auger recombination in structures under study based on the analysis of carrier dispersion laws calculated with parameters extracted from PC spectra.

II. Experimental

All structures under study were grown by molecular beam epitaxy on semi-insulating GaAs substrates with ZnTe and CdTe buffers. The PC spectra were studied via Fourier transform infrared spectroscopy at liquid helium (4.2 K) and liquid nitrogen (77 K) temperature. The sample was mounted at the end of the waveguide insert immersed into the dewar. The spectra were obtain with Bruker Vertex 80v FTIR spectrometer with globar as a radiation source. More information on the experimental setup can be found in Ref. [9]. The photoluminescence (PL) and stimulated emission (SE) spectra were obtained using the same FTIR operating in step-scan mode. Details of this experiment can be found in Ref. [1]

III. Results and discussion

An example of PC spectrum of structure No. 170331, is shown in the fundamental interband transition v1 – c1 as well the transition from the second valence subband v2 to the second conduction subband c2 (Fig. 1). The cut-off wavelength decreases with temperature, since in such structures the bandgap increases with temperature [10]. The spectral feature at 600 cm^{-1} does not shift with temperature and does not correspond to any of the interband transitions; therefore, we attribute it to impurity/defect related transition. This line is also observed in the PL spectrum of the structure (Fig. 2). It demonstrates faster quenching than interband line, which is related to impurity depopulation. For the other two structures this line was not observed.

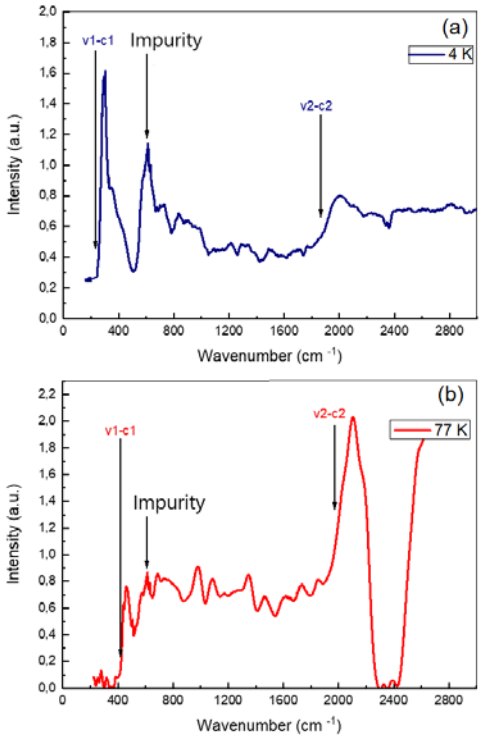

Fig. 1. PC spectra of structure #170331 at 4.2 K (a) and 77 K (b). Low energy cut-off corresponds to the frequency filter. The feature around 2400 cm^{-1} at 77 K is due to absorption in nitrogen.

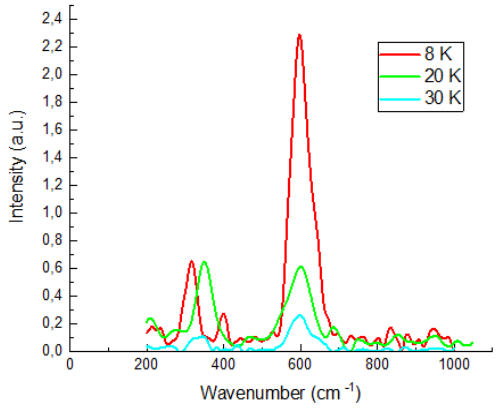

Fig. 2. PL spectra of the structure #170331 at different temperatures

QW thickness and Cd content in both QW and barrier for derived from the PC spectra are given in (Table 1). In order to obtain these values we used 8x8 Kane model with temperature-dependent parameters to fit the energies of both observed transitions at two temperatures.

Table 1. QW thickness (d), Cd content in barriers (y), Cd content in QWs (x) critical temperature above which no SE was observed (T_{cr}) and energy difference between the maxima of the first valence subband (ΔE) for three studied structures.

Sample #	d, nm	y	x	T_{cr}, K	ΔE, meV
170331	11	0.56	0.1	--	7.2
170130	7.8	0.66	0.08	50	15.8
190225	6.9	0.65	0.078	80	19.6

Although in structures #170130 and #190225, SE was obtained at close wavelengths (~ 20–22 μm at 8 K) the maximum temperature above which SE is not observed (T_{cr}) was different (Table 1). To understand this phenomenon, we consider the band spectrum of these structures calculated using the QW parameters extracted from the PC spectra (Fig. 3). One can roughly estimate the threshold energies of non-radiative Auger recombination as the difference between the energies of the main maximum at Γ-point and side maximum in the first valence subband (ΔE). For structure #190225 ΔE is larger than that for #170130 by 3.8 meV, which corresponds to equivalent temperature difference of 40 K. The latter value agrees well with a difference in T_{cr} for the structures under consideration observed in experiment -30 K. Thus, it is plausible that the position of the side maxima of the first valence subband is a key factor determining the maximum temperature at which the SE can be observed. This fact is also indirectly confirmed by the absence of SE observed from structure #170331, in which the threshold energy of Auger process is more than twice as low as for the other structures. At the same time, more detailed studies are required to reliably connect the lack of SE from structure #170331 and Auger recombination threshold.

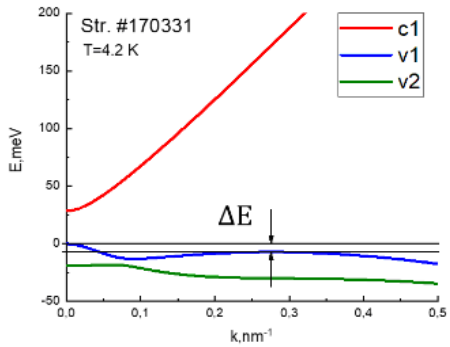

Fig. 3. Band diagram of structure #170331 at 4K

IV. Conclusion

In this work, it was demonstrated that the PC spectra measurements is a powerful tool to investigate the parameters of the HgCdTe QW heterostructures and allows to calculate their energy band diagrams. It is shown that the position of the side maxima of the first valence subband limits the maximum temperature at which stimulated emission can be obtained.

Acknowledgments

The work was supported by Ministry of Science and Higher Education (MK-4399.2018.2) and Russian Foundation of Basic Research grant ## 18-32-00628.

References

[1] S. V. Morozov, V. V. Rumyantsev, M. A. Fadeev, M. S. Zholudev, K. E. Kudryavtsev, A. V. Antonov, A. M. Kadykov, A. A. Dubinov, N. N. Mikhailov, S. A. Dvoretsky, and V. I. Gavrilenko, Applied Physics Letters 111 (19), 192101 (2017).

[2] M. S. Vitiello, G. Scalari, B. Williams, and P. De Natale, Optics express 23 (4), 5167 (2015).

[3] Williams B.S. Terahertz quantum-cascade lasers // Nature Photonics. 2007. V.1. P. 517.

[4] K. V. Maremyanin, A. V. Ikonnikov, L. S. Bovkun, V. V. Rumyantsev, E. G. Chizhevskii, I. I. Zasavitskii, and V. I. Gavrilenko, Semiconductors 52 (12), 1590 (2018).

[5] D. N. Talwar and M. Vandevyver, Journal of Applied Physics 56 (6), 1601 (1984).

[6] B. A. Bernevig, T. L. Hughes, and S. C. Zhang, Science 314 (5806), 1757 (2006).7. Lewis R.A. A review of terahertz sources // J. Phys. D: Appl. Phys. 2014. 47 374001.

[7] V. V. Rumyantsev, A. M. Kadykov, M. A. Fadeev, A. A. Dubinov, V. V. Utochkin, N. N. Mikhailov, S. A. Dvoretskii, S. V. Morozov, and V. I. Gavrilenko, Semiconductors 51 (12), 1557 (2017).

[8] N.N. Mikhailov, R.N. Smirnov, S.A. Dvoretsky, Yu.G. Sidorov, V.A. Shvets, E.V. Spesivtsev, and S.V. Rykhlitski, Int. J. of Nanotechnology 3 (1), 120 (2006).

[9] V. V. Rumyantsev, S. V. Morozov, A. V. Antonov, M. S. Zholudev, K. E. Kudryavtsev, V. I. Gavrilenko, S. A. Dvoretskii, and N. N. Mikhailov, Semiconductor Science and Technology 28 (12), 125007 (2013).

[10] A. V. Ikonnikov, L. S. Bovkun, V. V. Rumyantsev, S. S. Krishtopenko, V. Ya. Aleshkin, A. M. Kadykov, M. Orlita, M. Potemski, V. I. Gavrilenko, S. V. Morozov, S. A. Dvoretsky, and N. N. Mikhailov, Semiconductors 51 (12), 1531 (2017).

Terahertz Radiation Obtained by Doubling of Gyrotron Radiation Frequency in InP:Fe

V. V. Rumyantsev[1], A. P. Fokin[2], K. V. Maremianin[1], A. A. Dubinov[1], V. I. Malygin[1], N. N. Mikhailov[3], S. A. Dvoretsky[3], V. I. Gavrilenko[1], M. Yu. Glyavin[2], and S. V. Morozov[1]

[1] IPM RAS, Nizhny Novgorod, 603950, Russia
[2] IAP RAS, Nizhny Novgorod, Russia
[3] Rzhanov Institute of Semiconductor Physics, Siberian Branch, Russian Academy of Sciences, Novosibirsk, Russia

E-mail: rumyantsev@ipmras.ru

Abstract – Frequency doubling is observed in InP:Fe crystal pumped with intense gyrotron radiation at 263 GHz frequency. Intensity of ~50W/cm^2 at the fundamental frequency provides the conversion efficiency of (3–5)·10^{-7}, limited by sample heating and the parasitic signal resulting from the scattered radiation. The routes to enhancing the conversion efficiency and obtaining intense radiation at 526 GHz are discussed.

Keywords – InP, frequency doubling, gyrotron, nonlinear susceptibility

I. Introduction

At present, there is much activity aimed for development and application of different sources of radiation with terahertz (THz) range frequency, which are needed for a variety of scientific and practical applications [1]. Powerful sources of THz radiation like synchrotrons and free electron lasers (FELs) have high cost and large size limiting their use even for scientific applications. Complicated solutions are required to increase the frequency of the vacuum sources such as a backward wave oscillator up to 1 THz and higher [2]. Semiconductor quantum cascade lasers in THz range operate only at cryogenic temperatures [3–5]. Molecular lasers, although operating at room temperature, are available only for a fixed set of frequencies [6]. THz radiation sources based on femtosecond lasers exhibit an extremely broad spectrum (~1 THz wide), which is not always acceptable for spectroscopy applications and rather low output power [7]. Currently, the media of choice for optical rectification are LiNbO3 [8], ZnTe [9], GaP [10] crystals. They all have fairly high losses in the THz range and the conversion efficiency even for state-of-the-art experiments is approaching 10^{-3} [8] and in typical cases is an order of magnitude lower.

Alternative way to obtain intense THz radiation is to "multiply" the frequency using nonlinear susceptibility in semiconductors. This approach requires intense sources at the fundamental frequency in sub-THz range, among which there were mainly molecular lasers. However, recently a sufficient progress has been made in the development of sub-THz range gyrotrons. Continuous wave (cw) gyrotrons with frequencies of 460 GHz [11] and 527 GHz [12] have been demonstrated. IAP RAS recently developed unique switching solenoids with magnetic fields up to 50 T that allowed implementing gyrotrons with the output frequency of up to 1.3 THz with pulse duration ~50 μs [13]. On the basis of "dry" cryomagnet with magnetic fields up to 10 T cw gyrotrons with frequencies 263 GHz [14] and 250 GHz were fabricated. A generator with 889 GHz frequency (in a synchronism with the third harmonic of the cyclotron frequency) was developed, as well as a pulsed generator with a frequency of ~1 THz and power of ~10 W at the second harmonic of gyrofrequency [15]. These results were obtained by using the unique cryomagnet with the magnetic field of up to 20 T. In 2017, a two-beam gyrotron with the second-harmonic frequency of 0.8 THz was demonstrated [16].

Frequency doubling is enough to obtain frequencies above 1 THz for such sources, while previous works focused on generating the third harmonic of gyrotron radiation in n-type Ge and Si at much lower frequencies [17, 18]. Third harmonic generation was demonstrated in Ref. [17] with the effectiveness of 0.05% under gyrotron pumping with 70 GHz frequency, and in Ref. [18] under gyrotron pumping with 118 GHz frequency and 0.07% conversion efficiency. The frequency tripling is possible in semiconductor materials due to the third order nonlinearity, which is predominantly electronic (third order nonlinearity due to ionic motions is usually weaker) [19, 20]. The frequency doubling is possible in crystals lacking the inversion centre. Second-order susceptibility and corresponding frequency doubling were investigated mainly in GaAs, using CH_3F laser [21] and free electron laser [22] as the radiation sources in the spectral ranges of 0.6–1.7 THz and 4–6 THz, respectively. In this work we focus on InP:Fe crystals, which are shown to be of interest for frequency doubling in THz range [23].

II. Experimental

In this study a continuous wave gyrotron operating at 263 GHz was used. Approximately 10% of the gyrotron radiation was guided to the measurement setup, where it was focused with a horn with 3.5x8 mm output and modulated with a chopper. The second harmonic was separated from the radiation on the fundamental frequency by perforated plate, functioning as a high-pass filter (Fig. 1) [24]. The radiation was detected with n-InSb detector using Stanford Research Systems SR580

lock-in. The detector was mounted at the end of the waveguide insert, immersed into the liquid helium.

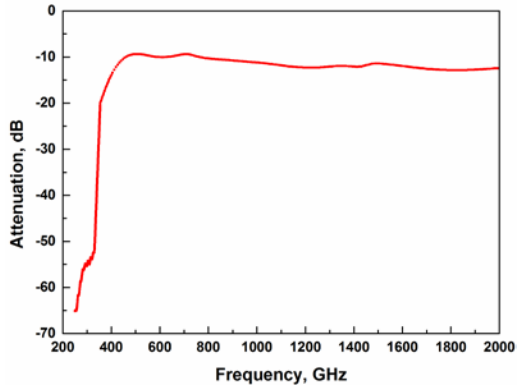

Fig. 1. Transmission spectrum of the perforated plate with 0.4-mm-diam holes

The waveguide insert also allowed the express-analysis of the radiation spectrum by magnetotransmission measurements of the $HgTe/Cd_{0.65}Hg_{0.35}Te$ quantum well (QW) structure placed inside a superconducting magnet that was mounted before the detector. The 20 nm wide HgTe QW was grown on a GaAs substrate in (013) orientation and doped with indium to a concentration of ~ 10^{17} cm^{-3} in the barriers. Due to the low effective mass of electrons in this QW, the cyclotron resonance (CR) for frequencies of 263 GHz and 526 GHz could be observed in relatively small magnetic fields of 0.3 T and 0.6 T, respectively. The magnet allowed sweeping the magnetic field from zero up to 3 T. When the CR occurs, the transmission of the QW structure was reduced by ~25–30%, resulting in the dip in the detector signal vs. magnetic field curve (see Fig. 2(b) for example).

III. Results and Discussion

It was discovered that there is an inherent (parasitic) second harmonic in the gyrotron emission spectrum. The maximum power of the second harmonic of about 25 mW was observed at 25 W power of the fundamental gyrotron frequency 263 GHz. As can be seen from Fig. 2(a) the power of the second harmonic drops as the power of the fundamental gyrotron frequency grows.

A stack of InP:Fe substrates was used as a nonlinear medium. The stack was placed at the output of the horn overlapping the entire output aperture. The radiation was incident normally to (110) facet of the stack. As it is well known, for zinc blende crystal the only non-zero components of the second order susceptibility tensor are those with all three different indices. Therefore, the described orientation is thought to be optimal for obtaining the second harmonic radiation with polarization in [100] direction.

The length of the crystal was varied from 5 mm to 18 mm and the intensity of the radiation at the fundamental frequency lied in 10–60 W/cm^2 range. For 5 mm sample length and low intensities of exciting radiation (below 40 W/cm^2) the second harmonic transmitted through the sample dominated the detector signal. However, the detector signal decreased down to the noise level for sample length of 10 mm, showing that the 2nd harmonic from the gyrotron was completely absorbed in the sample. A noticeable increase in the intensity of radiation from the stack was detected when the sample length was increased up to 18 mm. Fig. 2(c) shows the magnetotransmission spectra for the latter case. Both the 2nd harmonic and radiation at 263 GHz are present in the spectrum, suggesting that the 2nd harmonic is due to nonlinear conversion in the sample. The conversion efficiency can be estimated as $(3–5) \cdot 10^{-7}$.

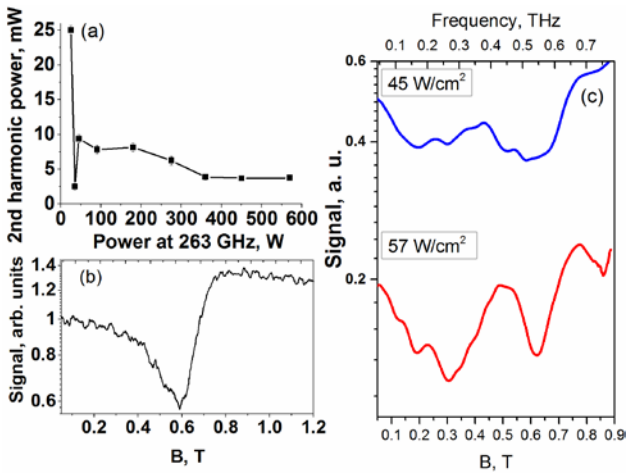

Fig. 2. (a) The inherent (parasitic) second harmonic in power as a function of the power at the fundamental frequency; (b) magnetotransmission spectrum corresponding to 2nd harmonic from the gyrotron at 25 W power at the fundamental frequency (c) magnetotransmission spectrafor radiation from the output of 18-mm-long InP:Fe crystal under excitation at 263 GHz with different intensities (labeled).

Increasing the intensity of radiation at the fundamental frequency can sufficiently enhance the 2nd harmonic generation. It should be mentioned that focusing the radiation into the 2.5-mm-diam spot is feasible [25] providing about 15 kW/cm^2 power density at 263 GHz. Transmission measurements in the far-infrared range before and after irradiation showed no degradation of the optical quality InP:Fe wafers under series of 100 ms long pulses with 15 kW/cm^2 intensity at 263 GHz (Fig. 3).

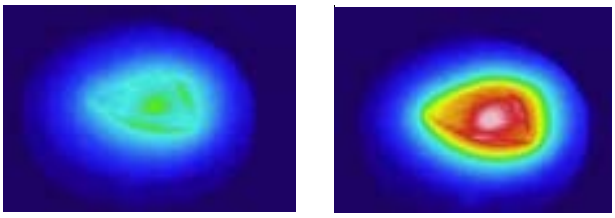

Fig. 3. Thermal images of InP:Fe wafer after irradiation of 100-ms-long pulses at 263 GHz frequency focused into the beam spot of 2.5 mm diameter: left side – 1000 pulses with 60 W power and pulse ratio 2, maximum temperature is 42 ºC; right side – 100 pulses with 550 W power and pulse ratio 10, maximum temperature is 71 ºC.

In the present work the maximum intensity of excitation radiation was limited by the sample heating and the scattered radiation at 263 GHz swamping the detector signal. To avoid both of these factors the quasioptical focusing system of sample should be placed in a metal box, providing electromagnetic shielding together with possibility of fine position tuning and effective cooling of the nonlinear crystal. The perforated plate mounted at the output of the box would reflect the remaining power of the gyrotron radiation to be absorbed in a water calorimeter.

IV. Conclusion

In this work, the conversion efficiency of (3–5) $\cdot 10^{-7}$ was achieved for frequency doubling in InP:Fe at 263 GHz frequency. It can be estimated that the conversion efficiency can be enhanced up to $3 \cdot 10^{-4}$ under intensity of ~15 kW/cm^2 at the fundamental frequency. Thus, the 2nd harmonic power obtained from InP:Fe crystal can be as high as ~300 mW, which is two order of magnitude higher than the inherent 2nd harmonic of the gyrotron.

Acknowledgments

The work was supported by Russian Science Foundation grant #18-79-10112.

References

[1] Van der Weide D. Applications and Outlook for Electronic Terahertz Technology // Optics & Photonics News. 2003. V. 14. No. 4. P. 48-53.

[2] Xiong Xu, Yanyu Wei, Fei Shen, Hairong Yin, Jin Xu et al. A watt-class 1-THz backward-wave oscillator based on sine waveguide // Phys. Plasmas. 2012. 19, 013113.

[3] Williams B.S. Terahertz quantum-cascade lasers // Nature Photonics. 2007. V. 1. P. 517.

[4] Fathololoumi S., Dupont E., Chan C.W.I., Wasilewski Z.R., Laframboise S.R., Ban D., Matyas A., Jirauschek C., Hu Q., Liu H.C. Terahertz quantum cascade lasers operating up to ~ 200 K with optimized oscillator strength and improved injection tunneling // Optics Express. 2012. 20 (4). 3866.

[5] Wang X., Shen C., Jiang T., Zhan Zh., Deng Q., Li W., Wu W., Yang N., Chu W., Duan S. High-power terahertz quantum cascade lasers with 0.23 W in continuous wave mode // AIP Advances. 2016. 6. 075210.

[6] Dodel G. On the history of far-infrared (FIR) gas lasers: Thirty-five years of research and application // Infrared Phys. Technol. 1999. 40 127–39.

[7] Lewis R.A. A review of terahertz sources // J. Phys. D: Appl. Phys. 2014. 47 374001.

[8] Sergey B. Bodrov, Aleksey A. Murzanev, Yury A. Sergeev, Yury A. Malkov, and Andrey N. Stepanov. Terahertz generation by tilted-front laser pulses in weakly and strongly nonlinear regimes // Applied Physics Letters. 2013. 103. 251103.

[9] Vidal S., Degert J., Tondusson M., Freysz E., and Oberlé J. Optimized terahertz generation via optical rectification in ZnTe crystals // J. Opt. Soc. Am. B. 2014. 31, 149-153.

[10] Taniuchi T., Nakanishi H. Collinear phase-matched terahertz-wave generation in GaP crystal using a dual-wavelength optical parametric oscillator // Journ. Appl. Phys. 2004. v. 95, 7588.

[11] Torrezan A.C., Han S.T., Mastovsky I., Shapiro M.A., Sirigiri J.R., Temkin R.J., Griffin R.G., Barnes A.B. Continuous-Wave Operation of a Frequency-Tunable 460-GHz Second-Harmonic Gyrotron for Enhanced Nuclear Magnetic Resonance. // IEEETrans. 2010. V. PS-38. № 6. P. 1150.

[12] Jawla S., Nanni E., Shapiro M. et al. // 2011 36th Int. Conf. on Infrared, Millimeter and Terahertz Waves (IRMMW-THz). Houston. 2-7 Oct. 2011. N.Y.IEEE, 2011. P. DOI 10.1109. IRMMWTHz.2011.61 05096.

[13] Glyavin M.Yu., Ginzburg N.S., Goldenberg A.L., Denisov G.G., Luchinin A.G., Manuilov V.N., Zapevalov V.E., Zotova I.V. THz Gyrotrons: Status and Possible Optimizations // Terahertz Science and Technology, V. 5, No. 2, 2012.

[14] Glyavin M. Yu., Chirkov A.V., Denisov G.G., et al. Experimental tests of a 263 GHz gyrotron for spectroscopic applications and diagnostics of various media // Review of Scientific Instruments. 2015. 86. 054705.

[15] Idehara T., Saito T., Ogawa I. The potential of the gyrotrons for development of the sub-terahertz and the terahertz frequency range – A review of novel and prospective applications, Proceedings of 2nd International Symposium on the Manipulation of Advanced Smart Materials // ThinSolidFilms. 2008. V. 517. No 4. P. 1503, 2008.

[16] Idehara T., Glyavin M., Kuleshov A., Sabchevski S., Manuilov V., Zaslavsky V., Zotova I., Sedov A. A novel THz-band double-beam gyrotron for high-field DNP-NMR spectroscopy // Rev. of Sci. Instrum. 2017. 88. 094708.

[17] Keilmann F., Brazis R., Barkley H., Kasparek W., Thumm M. and Erckmann V. Millimeter-Wave Frequency Tripling in Bulk Semiconductors // EPL (Europhysics Letters), Volume 11, Number 4, p. 337.

[18] Narkowicz R., Siegrist M.R., Moreau Ph., Hogge J.P., Raguotis R. and Brazis R. Third-Order Susceptibility of Silicon Crystals Measured with Millimeter-Wave Gyrotron // Acta Physica Polonica A. 2011. V. 119, No. 4, p. 509.

[19] Seeger K. Microwave frequency multiplication by hot electrons // J. Appl. Phys. 1963. 34, 1608-1610.

[20] Nimtz G. and Seeger K. Microwave mixing by hot electrons in homogeneous semiconductors // J. Appl. Phys. 1968. 39, 2263-2266.

[21] Mayer A. and Keilmann F. Far-infrared nonlinear optics. I. χ^2 near ionicresonance // Phys. Rev. B. 1986. 33, 6954-6961.

[22] Dekorsy T., Yakovlev V.A., Seidel W., Helm M., and Keimann F. Infrared phonon-polariton resonance of the nonlinear susceptibility in GaAs // Phys. Rev. Lett. 2003. 90, 055508-1/4.

[23] Rumyantsev V.V., Dubinov A.A., Fokin A.P., Utochkin V.V., Glyavin M.Yu., Morozov S.V. EPJ Web Conf. 195, 02010 (2018).

[24] Goldsmith P. F. Quasioptical Systems. IEEE, 1998.

[25] Alexander V. Vodopyanov, Andrey V. Samokhin, Nikolay V. Alexeev, Mikhail A. Sinayskiy, Alexander I. Tsvetkov, Mikhail Yu Glyavin, Andrey P. Fokin, and Vladimir I. Malygin // Vacuum 145, 340 (2017).

Nondestructive Acoustic Micro Imaging Analysis of Thermocompression Bonding for Improvement of THz QCL with Double Metal Waveguide Based on Au, Cu and Ag

N. V. Shchavruk[1], A. A. Zaycev[2], V. G. Babkin[3], D. S. Ponomarev[1,4], R. A. Khabibullin[1,4]

[1] V.G. Mokerov Institute of Ultra High Frequency Semiconductor Electronics of RAS, Moscow, Russia
[2] National Research University of Electronic Technology MIET, Zelenograd, Russia
[3] Ostec Group, Moscow, Russia
[4] Center for Photonics and 2D Materials, Moscow Institute of Physics and Technology, Dolgoprudny, Russia

E-mail: kolq_@mail.ru

Abstract – We propose to use the nondestructive acoustic micro imaging for analyzing of the thermocompression bonding quality for THz QCL with double-metal waveguide (DMW). Au-Au, Cu-Cu and Ag-Ag bonded samples were investigated thanks to this method.

Keywords – acoustic imaging, thermocompression bonding, quantum-cascade laser, THz region

I. Introduction

Over the past seven years, the record value of the maximum operating temperature T_{max} was 200 K for terahertz quantum cascade lasers (THz QCLs) emitting around 3.2 THz [1]. The first THz QCL operating above 200 K due to the optimization of the active region design was recently published in a conference paper [2]. However, for a further increase of T_{max}, it is necessary to reduce the propagation losses in THz QCLs, which exceeds 30 cm^{-1} at room temperature [3].

The highest T_{max} values are demonstrated for THz QCL with a double metal waveguide (DMW) with an active region sandwiched between two metal layers. For fabrication of bottom metal cladding of DMW it is necessary to transfer of active region to reciprocal substrate [4]. This requires the use of a thermocompression bonding of metal layers that is deposited on samples before high temperature/pressure treatment. In [5–7] it was shown that the use of Ag-based DMW allows to reduce losses by 2–4 cm^{-1} in comparison with Au-based DMW. However, the use of new materials for DMW requires the development of thermocompression bonding recipes and methods for quality control.

II. Experimental results and discussions

We propose to use the acoustic micro imaging for analyzing of the thermocompression bonding quality for THz QCL with DMW. This nondestructive method provides the detection of internal defects (voids, foreign particles, cracks) which can exist between samples. In Fig. 1 shows the acoustic images of two pairs of bonded GaAs samples. Acoustically opaque areas associated with voids in bonding layers are located along the periphery of samples.

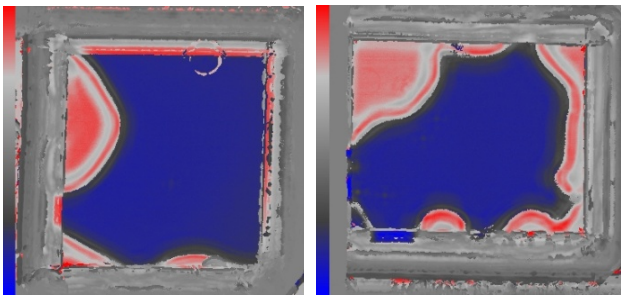

Fig. 1. Reflection-mode acoustic images of two pairs Cu-Cu bonded GaAs samples. The bright red areas are voids between samples that reflect all of the ultrasound.

We resistively deposited Ti/Au (50/500 nm), Ti/Ag (50/500 nm) and Ta/Cu (50/500 nm) layers on a semi-insulating GaAs substrate in a vacuum chamber with technological regimes used for fabricating THz QCLs [4]. The samples with metallization were cleaved along crystallographic axes into square pieces with dimensions ~1x1 cm and face-to-face thermocompression bonded with different temperatures and pressures. We analyzed the quality of bonding by acoustic micro imaging and determined the percentages of the bonded area (see Table).

Table. Temperature (T) and pressure (P) values used for the termocompression bonding based on Cu and Ag. The percentages of the bonded area (S) is presented.

Metal layers	T, ºC	P, MPa	S, %
Cu	350	1.60	58.9
Cu	400	1.75	68.6
Cu	400	2.95	80.8
Ag	300	6.17	63.9
Ag	300	10.20	95.5

ACKNOWLEDGMENTS

This work was supported by the Russian Science Foundation (RSF), Project #18-19-00493.

REFERENCES

[1] S. Fathololoumi, E. Dupont, C.W.I. Chan, Z.R. Wasilewski, S.R. Laframboise, D. Ban, A. Matyas, C. Jirauschek, Q. Hu, H.C. Liu. "Terahertz quantum cascade lasers operating up to ∼200 K with optimized oscillator strength and improved injection tunneling," *Opt. Express 20*, p. 3866–3876, 2012.

[2] M. Franckié, L. Bosco, M. Beck, E. Mavrona, and J. Faist, "Optimization and fabrication of two-quantum well THz QCLs operating above 200 K," *in Conference on Lasers and Electro-Optics*, OSA Technical Digest (Optical Society of America, 2019), paper SW4F.1.

[3] D.V. Ushakov, A.A. Afonenko, A.A. Dubinov, V.I. Gavrilenko, I.S. Vasil'evskii, N.V. Shchavruk, D.S. Ponomarev, R.A. Khabibullin. "Mode loss spectra in THz quantum-cascade lasers with gold- and silver based double metal waveguides," *Quantum Electron.* 48, p. 1005, 2018

[4] R.A. Khabibullin, N.V. Shchavruk, A.Y. Pavlov, D.S. Ponomarev, K.N. Tomosh, R.R. Galiev, P.P. Maltsev, A.E. Zhukov, G.E. Cirlin, F.I. Zubov, Z.I. Alferov. "Fabrication of a terahertz quantum-cascade laser with a double metal waveguide based on multilayer GaAs/AlGaAs heterostructures," *Semicond*. 50(10), 1377 (2016).

[5] Y. J. Han, L. H. Li, J. Zhu, A. Valavanis, J. R. Freeman, L. Chen, M. Rosamond, P. Dean, A. G. Davies, and E. H. Linfield, "Silver-based surface plasmon waveguide for terahertz quantum cascade lasers," *Opt. Express*, 26, 3814, 2018.

[6] R. A. Khabibullin, N.V. Shchavruk,D.S. Ponomarev,D.V. Ushakov,A.A. Afonenko, O.Yu. Volkov, V.V. Pavlovskiy, A.A. Dubinov. "Terahertz quantum cascade lasers with silver- and gold-based waveguides," *EPJ Web of Conferences* 195, 04002, 2018

[7] R. Khabibullin, D. Ushakov, A. Afonenko, N. Shchavruk, D. Ponomarev, O. Volkov, V. Pavlovskiy, I. Vasil'evskii, D. Safonov, A. Dubinov. "Silver-based double metal waveguide for terahertz quantum cascade laser", *Proceedings of SPIE*, 11022, 1102204, 2019.

Graphene Plasmon Transformation at a Rapid Increase of Carrier Density

A. V. Shirokova, A. V. Maslov, M. I. Bakunov

University of Nizhny Novgorod, Nizhny Novgorod, Russia

E-mail: bakunov@rf.unn.ru

Abstract – The transformation of a surface plasmon on graphene caused by an abrupt temporal increase of graphene's carrier density has been investigated by means of an accurate analytical solution of the Maxwell equations and time-domain Drude equations. The initial plasmon is transformed into two frequency upshifted surface plasmons propagating in the opposite directions, outgoing bulk radiation, and two-stream dc motion of carriers. Although the two-stream carrier motion carries zero net electric current and therefore does not generate any magnetic field, it can consume a substantial part of the initial plasmon energy in the form of the carrier kinetic energy. Our results refute the recent predictions of graphene plasmon amplification by carrier density temporal variations.

Keywords – graphene, plasmon, temporal scattering

I. INTRODUCTION

Graphene is an attractive plasmonic material for the terahertz frequency range due to its capability to support low loss and highly confined surface plasmons with the dispersion properties that can be dynamically tuned by electrical gating or optical excitation. Recently, graphene plasmon scattering by a rapid temporal variation of graphene's free-carrier density was addresed and plasmon amplification by the nonstationarity was predicted.[1,2] In Ref. 3, however, this prediction was refuted for the carrier density decrease, and the origin of the mistake was pointed out. Unlike Refs. 1, 2 the approach of Ref. 3 is based on accurate solution of the Maxwell equations with initial conditions for the carrier currents.

Here, we extend the approach[3] to a more complicated situation when graphene plasmon is scattered by an abrupt increase of the carrier density. In this case, there are two sorts of carriers – the background (that existed before the density increase) and newly born carriers. To describe their dynamics, we use the time-domain Drude equations. We show that the carrier density increase cannot amplify graphene plasmons, in contrast to Ref. 2. On the contrary, a part of the initial plasmon energy goes to a specific two-stream dc motion of carriers, thus reducing the energy of the scattered plasmons.

II. MODEL AND APPROACH

We assume that initially, at $t < 0$, a transverse magnetic surface plasmon with the tangential electric field

$$E_x\left(x,y,t\right) = E_0 e^{i\omega_1 t - ih_1 x - \kappa_1 |y|} \qquad (1)$$

propagates along a doped graphene sheet (x,z plane) with the free-carrier density N_1 and corresponding Fermi energy E_{F1}, $E_{F1} \sim \sqrt{N_1}$. We will characterize graphene by a surface conductivity

$$\sigma(\omega) = -ic\Omega/(2\pi\omega), \quad \Omega = 2e^2 E_F / \hbar^2 \qquad (2)$$

expressed through a convenient frequency parameter Ω. In Eq. (1), the propagation h_1 and decay κ_1 constants are defined by substituting ω_1 and Ω_1 to the dispersion relations for graphene plasmons:[4]

$$h\left(\omega\right) = \frac{\omega}{c}\sqrt{1+\frac{\omega^2}{\Omega^2}}, \quad \kappa\left(\omega\right) = \frac{\omega^2}{c\Omega}. \qquad (3)$$

At $t = 0$, the carrier density grows from N_1 to N_2, therefore Ω changes from Ω_1 to Ω_2 in the graphene conductivity and, as a result, to temporal scattering of the initial surface plasmon.

To find the scattered fields at $t > 0$, we use the Maxwell equations and the time-domain Drude equations

$$\frac{\partial j_x^{(b)}}{\partial t} = \frac{c\Omega_1}{2\pi}E_x, \quad \frac{\partial j_x^{(n)}}{\partial t} = \frac{c(\Omega_1 - \Omega_2)}{2\pi}E_x \qquad (4)$$

for the currents of the background ($j_x^{(b)}$) and newly born ($j_x^{(n)}$) electrons. To find initial conditions at $t = 0^+$, we integrate the Maxwell equations over the infinitesimal time of the carrier density jump and obtain continuity of the electric and magnetic fields. We further assume that current of the background electrons remains unchanged at the jump and the "new" electrons are born with zero current:

$$j_x^{(b)}\left(t=0^+\right) = j_x^{(b)}\left(t=0^-\right), \quad j_x^{(n)}\left(t=0^+\right) = 0 \qquad (5)$$

The fields and current $j_x^{(b)}$ at $t = 0^-$ are given by the initial plasmon.

To solve the Maxwell equations and Eq. (5) with the specified initial conditions, we use the Laplace transform technique and contour integration. The residues at the poles give the amplitudes of the scattered plasmons. The integrals along the branch cuts describe the transient processes.

III. RESULTS

The initial plasmon is transformed into two frequency upshifted surface plasmons propagating in the

+x (transmitted) and -x (reflected) directions, upshifted outgoing bulk radiation, and two-stream dc motion of carriers.

The amplitudes of the transmitted and reflected plasmons are given by

$$E_x^{t,r} = \frac{\omega_2^3 (\Omega_2 - \Omega_1)}{\Omega_2 (\omega_2 \mp \omega_1)(2\omega_2^2 + \Omega_2^2)} E_0, \qquad (6)$$

where ω_2 is the frequency of the plasmons

$$\omega_2 = \frac{\Omega_2}{\sqrt{2}} \left[\left(1 + 4c^2 h_1^2 / \Omega_2^2\right)^{1/2} - 1 \right]^{1/2}. \qquad (7)$$

Figure 1(a) shows the ratio of the final and initial plasmon frequencies ω_2/ω_1 as a function of Ω_2/Ω_1. The ratio increases with Ω_2/Ω_1; the closer the initial plasmon to the quasistatic regime (the higher ω_1/Ω_1), the larger the increase of ω_2/ω_1. The relative plasmon frequency ω_2/Ω_2 decreases with Ω_2/Ω_1 Fig. 1(b) and the excited plasmons become less confined. Figure 1(c) shows the transmission $t_E = E_x^t / E_0$ and reflection $r_E = E_x^r / E_0$ coefficients as functions of Ω_2/Ω_1. For $\omega_1 / \Omega_1 \gtrsim 10$, t_E and r_E approach the quasistatic dependencies, Eq. (9).

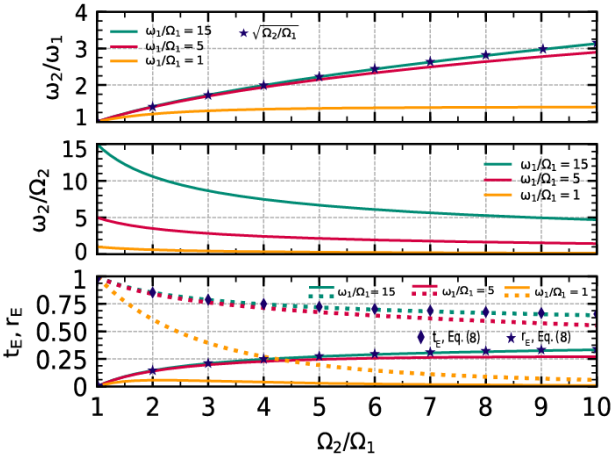

Fig. 1. (a) Frequency ω_2 of the excited plasmons relative to Ω_2 as functions of Ω_2/Ω_1 for different ω_1/Ω_1. (c) Transmission (dotted) and reflection (solid) coefficients as functions of Ω_2/Ω_1 for different ω_1/Ω_1. In (c), the rhombs and stars show the quasistatic limit, Eq. (8).

The dc currents of the background and new electrons compensate each other in every point, thus producing a zero net current and zero magnetic field. Nevertheless, these currents consume a part of the initial plasmon energy in the form of the kinetic energy of carriers.

The energy of the initial plasmon W_0 transforms into the energies of the transmitted W_t and reflected W_r plasmons, the energy of the outgoing radiation W_{rad}, and the energy of the dc motion of carriers W_{dc}. Fig. 2 shows the energy distribution as a function of the carrier density jump for strongly $\omega_1/\Omega_1 = 15$ confined initial plasmons. The energy of a strongly confined plasmon Fig. 2 is mainly divided between the transmitted plasmon and dc motion, although W_r becomes substantial at large Ω_2/Ω_1.

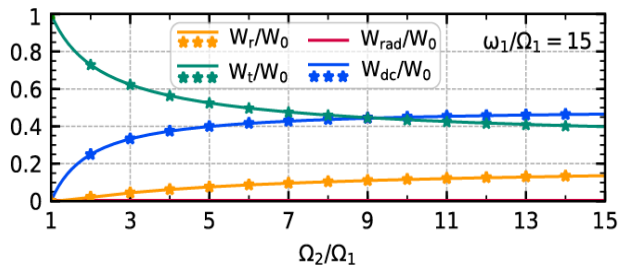

Fig. 2. Energy distribution as a function of Ω_2/Ω_1 for $\omega_1/\Omega_1 = 15$.The stars show the dependencies in the quasistatic limit, Eq. (10).

In the practically most important case of a strongly confined (with $\omega_1/\Omega_1 >> 1$) initial plasmon, the transmission and reflection coefficients are given by

$$t_E = \left(1 + \gamma^{-1}\right)/2, \quad r_E = \left(1 - \gamma^{-1}\right)/2. \qquad (8)$$

and the frequency jump is

$$\omega_2 / \omega_1 = \gamma, \quad \gamma = \sqrt{\Omega_2 / \Omega_1}. \qquad (9)$$

The energies can be written as

$$W_{t,r} = W_0 \left(1 \pm \gamma^{-1}\right)^2 / 4, \qquad W_{dc} = W_0 \left(1 - \gamma^{-2}\right)/2 \qquad (10)$$

with $W_0 = E_0 / (\pi \kappa_1)$ .These approximate formulas work very well for $\omega_1 / \Omega_1 \gtrsim 1$ (Fig. 2).

IV. Conclusions

It has been shown, that an abrupt temporal increase of carrier density in a graphene sheet leads to a transformation of a graphene plasmon into two frequency upshifted plasmons propagating in opposite directions, bulk radiation, and two stream dc motion of carriers. In the quasistatic regime, up to a half of the initial plasmon energy can be transformed into the dc motion of carriers: $W_{dc} \approx W_0/2$ at $\Omega_2 / \Omega_1 \gg 1$. The remaining energy is distributed between the transmitted and reflected plasmons. In particular, $W_t \approx W_r \approx W_0/4$ at $\Omega_2 / \Omega_1 \gg 1$.

Acknowledgments

This work was supported by the Ministry of Science and Higher Education of the Russian Federation, Project No. 3.3854.2017/4.6.

References

[1] G. A. Menendez and B. Maes, *Opt. Lett.* **42**, 5006 (2017).
[2] J. Wilson, F. Santosa, M. Min, and T. Low, *Phys. Rev B* **98**, 081411(R) (2018).
[3] A. V. Maslov and M. I. Bakunov, *Optica* **5**, 1508 (2018).
[4] M. Jablan, H. Buljan, and M. Soljačić, *Phys. Rev.* B **80**, 245435 (2009).

Terahertz Photoluminescence from Narrow Gap HgTe/CdHgTe Heterostructures and Multilayer Graphene

V. V. Utochkin[1,2], S. V. Morozov[1,2], M. A. Fadeev[1,4], V. V. Rumyantsev[1,2], N. N. Mikhailov[5,6], S. A. Dvoretsky[5], T. Komiyama[3], T. Watanabe[3], H. Fukidome[3], A. Satou[3], T. Otsuji[3]

[1] Institute for Physics of Microstructures of RAS, Nizhny Novgorod, Russia
[2] Lobachevsky State University, Nizhny Novgorod, Russia
[3] RIEC, Tohoku University, Sendai, Japan
[4] Laboratoire Charles Coulomb (L2C), Universite de Montpellier, Montpellier, France
[5] A.V. Rzhanov Institute of Semiconductor Physics, SBRAS, Novosibirsk, Russia
[6] Novosibirsk State University, Novosibirsk, Russia

Abstract–We report on long-wavelength photoluminescence from HgCdTe quantum well heterostructures at the wavelengths from 10 to 20 THzand broadband (15–45 THz) photoluminescencefromnon-Bernal-stacked multilayer graphene. Photoluminescence from graphene was observed at temperatures above 250 K under 2.3 μmwavelength pumping. No photoluminescence under CO_2 laser excitation at 10.6 μm wavelength with the same intensitywas found. We attribute thisto high doping-determined Fermi level in multilayer graphene structure.

Keywords – HgCdTe, graphene, terahertz, far IR, photoluminescence

I. Introduction

The development of terahertz (THz) emitters is one of the hottest topics in modern applied physics. For many spectroscopy related applications, it would be favorable to employ compact semiconductor lasers as the sources of long wavelength radiation. Quantum cascade lasers (QCLs) demonstrate remarkable performance in the spectral range from 1 THz to 5THz[1,2] and above 15 THz[3]. Though there is the 5–15 THz "gap", where latticeabsorptionin A3B5 materials becomes too strong for QCLs. At the same time there are alternative semiconductor systems,which could provideradiation in this spectral range. In this paper we investigate on multilayer (ML) graphene and narrow gapHgTe/CdHgTe quantum well (QW) heterostructures.These materials are believed to be good candidates for novel THz emitters.

Lasing in HgCdTe has previously beenstudied mainly in the mid IR range (2–5 μm)[10-12]. The emission wavelength of 5.3 μm was achieved at 45K in diode laser that did not exploit QWs in its design[12]. As for the HgCdTe lasers with QWs, emission only at the wavelengths up to $\lambda \sim 3$ μm was demonstrated[10]. On the other hand, we have recently reportedon stimulated emission (SE) from HgTe/HgCdTe QW heterostructures at $\lambda \sim 20$ μm (15 THz)[13]. This discovery suggests that potential of the HgCdTe structures as a medium for long-wavelength lasers is yet not exhausted. We refer such increase in SE wavelength to vastly improved technology of material growth as well as peculiar dispersion relation in narrow HgTe QWs, similar to that of graphene.

Graphene has attracted a great deal of attention as a two-dimensional electronic material having precedent peculiar properties originated from its linear gapless dispersion relation. One of such nontrivial features of graphene is the negative-dynamic conductivity in the terahertz (THz) spectral range, which opens up opportunities for a new principle THz coherent light source[4].The ultra fast non-equilibrium carrier relaxation and recombination dynamics in optically pumped graphene has been extensively studied during the last decade[5]. THz spontaneous emission in a carrier-population-inverted exfoliated monolayer graphene under fs infrared (IR) laser pumping has been experimentally demonstrated[6]. Independently, carrier population inversion in an epitaxial graphene on a SiC substrate was experimentally confirmed by time and angle-resolved X-ray photoelectron microscopy[7]. These studies provide a clear evidence that graphene can be used as a gain medium in THz range.

The main drawback of graphene is a rather low (2.3% at maximum[4,8]) quantum efficiency of optical transition in a single graphene monolayer. However, it is theoretically predicted that the non-Bernal-stacked ML graphene could multiply the gain of monolayer graphene by the number of layers[9] and greatly improve the performance of graphene-based THz sources.

Measurements of PL from these materials is the first step in development of light emitting devices for spectral range 5 – 15 THz giving the insight on the relevant physical effects. In the framework of the current work, we investigate spectra of THz PL from optically pumped narrow-gap HgTe/CdHgTe QW heterostructures as well as non-Bernal-stacked ML graphene.

II. Experimental

HgTe/HgCdTe structure was grown by molecular beam epitaxy on semi-insulating GaAs(013) substrate on top of ZnTe and CdTe buffers with ellipsometric control of the layer content and thickness. It contains

10 $HgTe/Cd_{0.55}Hg_{0.45}Te$ QWs with 11 nm thickness, which corresponds to 30 meV bandgap at 8 K. The structure was not intentionally doped. Studied samples were cleaved from the as-grown wafers with typical size of 5x5 mm^2. ML epitaxial graphene was synthesized by thermal destruction of C-face SiC substrate.

The samples were put in a closed-cycle cryostat with temperature range 8–300 K, optically conjugated with Bruker Vertex 80v Fourier spectrometer operating in the step-scanning mode. HgCdTe detector and Si bolometer were used for PL detection. OPO complex "Solar" with 1.94–2.3 µm wavelength nd pulse energy of up to 5 mJ, pulsed CO_2 laser with 10.6 µm wavelength and pulse energy up to 40 mJ and 808 nm 1.5 W continuous-wave diode laser were used for optical excitation of structures. Ge, InAs and TPX filters were used to cut off scattered pumping radiation.

III. Results and Discussion

Fig. 1 presents PL spectra of the HgCdTe structure under study, measured at 8–150 K range under 800-nm excitation. The full width at half maximum of PL lines below 100 K is determined by spectral resolution of the setup equal to 12 meV. Minimum PL peak frequency of 9 THz is achieved at 8 K. With the increase of temperature, the PL line shifts towards shorter wavelengths while its intensity decreases. This behavior shows that lattice absorption in HgCdTe does not lead to significant decrease of the PL even when the latter lies within the range of double phonon frequency in HgCdTe (~10 THz). Thus, we suggest that the impact of lattice absorption on performance of HgCdTe sources in the range at least up to 10 THz can be neglected.

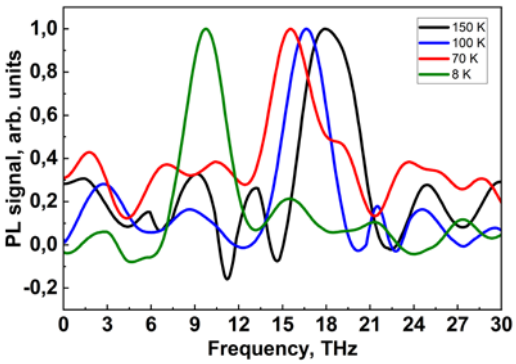

Fig. 1. PL spectra under 808 nm pumping of HgCdTe structure under study at 8 – 150 K

Fig. 2 presents PL from ML graphene in the temperature range from 250 to 300 K. At all temperatures single broad lines of PL from 15 to 45 THz were observed. The left edges of these lines are determined bythe lower limit of the detectable frequency range of the HgCdTe detector, ~19 THz. Therefore, the actual gainpeaks may extend further to lower frequency region. We presume that the growth of PL intensity with temperature can also be explained by the fact that the maximum of PL spectrum lies outside the detectable range and shifts to the higher energies with temperature. However, additional experiments are required to fully understand the underlying physics behind PL growth/shifts.

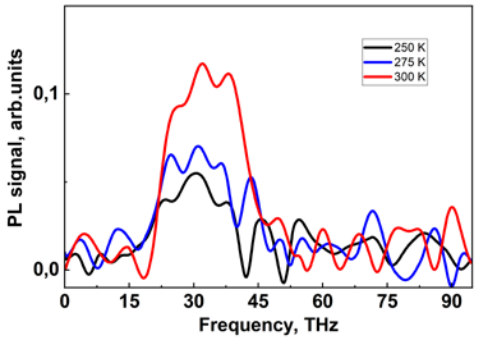

Fig. 2. PL spectra from epitaxial multilayergraphene pumped with 2.3 µm Solar OPO laser at 250–300 K. Left sides of the spectraare determined by the lower limit of the HgCdTe detectordetectable frequency range (~20 THz).

Under CO_2 laser pumping with the same intensity no photoluminescence was observed. It is reasonably understood that the photon energy of pumping laser is less than doubled Fermi level in the investigated sample so CO_2 laseris not able to make population inversion.

IV. Conclusion

In conclusion, we demonstrated wideband THz/far-IR PL from non-Bernal-stacked ML graphene and HgCdTe heterostructure with QWs. PL from HgCdTe heterostructure is observed at frequencies up to 9 THz, and does not demonstrate decay when entering double-phonon absorption region. PL from ML graphene is observed at room temperature and decreases at lower temperatures. This effect can result from PL peak shift or novel physical phenomena.

Acknowledgements

This work is supportedby Ministry of Science and Higher Education (MK-4399.2018.2) and by grants of Russian Foundation of Basic Research ## 18-32-00628, 19-02-00827, 18-52-00524. The work was done using equipment of Center "Physics and technology of micro- and nanostructures" at IPM RAS.The HgCdTe structure was synthesized in the Rzhanov Institute of Semiconductor Physics, SB RAS, Russia. Multilayer graphene was synthesized in the Nanoelectronics and Spintronics Research Facility, RIEC,Tohoku University, Japan.

References

[1] Mehdi F. Anwar, Thomas W. Crowe, Tariq Manzur, Wataru Terashima, and Hideki Hirayama, *Proc. SPIE* **9483**, 948304 (2015).
[2] Benjamin S. Williams, *Nat Photon* **1** (9), 517 (2007).
[3] M. S. Vitiello, G. Scalari, B. Williams, and P. De Natale, *Optics express* **23** (4), 5167 (2015).

[4] V. Ryzhii, M. Ryzhii, and T. Otsuji, *J. Appl. Phys.* **101**, 083114.
[5] R.R. Hartmann, J. Kono, and M.E. Portnol, *Nanotechnol.* **25**, 322001 (2014).
[6] S. Boubanga-Tombet, S. Chan, T. Watanabe, A. Satou, V. Ryzhii, and T. Otsuji, *Phys. Rev. B* **85**, 035443 (2012).
[7] T. Someya, H. Fukidome et al., and I. Matsuda, *Phys. Rev. B* **95**, 165303 (2017).
[8] R.R. Nairet al., and A.K. Geim, *Science* **320**, 1308 (2008).
[9] T. Otsuji, S. Boubanga-Tombet, A. Satou, M. Ryzhii, and V. Ryzhii, *IEEE J.Select. Top. Quantum Electron.* **19**, 8400209 (2013).
[10] Joël Bleuse, Joël Bonnet-Gamard, Guido Mula, Noël Magnea, and Pautrat Jean-Louis, *Journal of Crystal Growth* **197** (3), 529 (1999).
[11] C. Roux, E. Hadji, and J. L. Pautrat, Applied Physics Letters **75** (12), 1661 (1999).
[12] J. M. Arias, M. Zandian, R. Zucca, and J. Singh, *Semiconductor Science and Technology* **8** (1S), S255 (1993).
[13] S.V. Morozov, V.V. Rumyantsev, M.A. Fadeev, M.S. Zholudev, K.E. Kudryavtsev, A.V. Antonov, A.M. Kadykov, A.A. Dubinov, N.N. Mikhailov, S.A. Dvoretsky, and V.I. Gavrilenko, *Applied Physics Letters*, **111**(19), 192101 (2017).

AUTHOR INDEX

A

Abrosimov N. V. Tu-2-3
Afonenko A. A. Tu-1-5, P-4
Ahmedov T. I. Tu-1-6
Alam T. Tu-3-1
Aleshkin V. Ya. Su-2-3, Tu-1-2, Tu-1-5, P-3, P-5, P-9
Altukhov I. V. Tu-1-4
Alyabyeva L. N. Tu-3-2
Amouroux M. Sat-2-3
Andreev Yu. M. Su-1-3
Andrianov A. V. Tu-2-1
Andronov A. A. Tu-1-3, P-1
Anfertev V. A. Sat-2-4
Antipov S. V. Thu-2-1
Anzin V. B. Tu-3-3
Aroui H. Su-3-2
Arsenin A. V. Thu-1-1
Artamkin A. I. Mo-2-2

B

Babkin V. G. P-11
Bahriz M. Su-2-4
Bakunov M. I. Thu-1-2, Thu-1-6, P-7, P-12
Balakin A. V. Sat-1-4
Balbekin N. S. P-8
Balibar S. Su-2-2
Bandurin D. Wed-1-2
Bannikov M. I. Mo-2-2
Baranov A. N. Sat-2-4, Su-2-4, Tu-1-4
Baranova A. A. P-2
Baratta G. A. Thu-1-4
Barbieri S. Su-2-5
Bashkatov A. N. Sat-2-3
Bayer F. Mo-2-4
Bednyakov P. Tu-3-3
Bedran Z. Tu-3-3, Wed-1-6
Bekin N. A. Tu-2-3
Belyakov V. A. Tu-1-3
Belyanchikov M. Tu-3-3
Bernier M. Sat-1-5
Beugeling W. Mo-2-4
Blank V. D. Tu-2-3
Blondel W. Sat-2-3
Bocquet R. Sat-2-1
Bodrov S. B. Thu-1-3, Thu-1-5
Borisov A. V. Sat-2-1, Sat-2-3
Bormashov V. S. Tu-2-3
Boubanga-Tombet S. Tu-1-1
Boudon V. Su-3-2
Bovkun L. P-3
Boyko A. A. Sat-2-1
Buhmann H. Mo-2-4
But D. B. Su-2-1

C

Caselli P. Thu-1-4
Cassar Q. Sat-2-2, P-8
Chashin M. V. Sat-1-5
Cherkasova O. P. Sat-2-5
Chernomyrdin N. V. Mo-4-1
Chernyaeva M. B. Sat-2-4, Mo-4-2
Chigarev S. G. Tu-1-6
Chirkov A. V. Wed-2-3
Choporova Yu. Yu. Tu-2-3
Consejo C. Su-2-1
Couairon A. Sat-1-1, Sat-1-2
Cours T. Su-3-2
Coutaz J.-L. Sat-1-4, Su-1-4
Cuisset A. Sat-2-1

D

Danilov S. N. Mo-2-2
Denisov G. G. Wed-2-3
Denisyuk I. Yu. Su-1-1, Su-1-2
Deßmann N. Tu-2-3
Dhillon S. Su-2-2
Dolganova I. N. Mo-4-1
Domracheva E. G. Sat-2-4, Mo-4-2
Dressel M. Tu-3-2, Tu-3-3
Dubinov A. A. Su-2-3, Tu-1-1, Tu-1-2, Tu-1-5, P-4, P-5, P-9, P-10
Dvoretskiy S. A. Su-2-3, Mo-2-2, Mo-2-3, Tu-1-2, P-3, P-5, P-9, P-10, P-13
Dyakonova N. Su-2-1

E

Efimenko E. S. Thu-1-2
Eliet S. Su-2-5
Emelin M. Y. Thu-1-3

F
Fadeev D. A. Thu-1-7
Fadeev M. A. Su-2-3, Mo-2-3, Tu-1-2, P-5, P-9, P-13
Fateev D. V. Wed-1-3
Fedorov G. E. Wed-1-2
Fefelov A. G. Tu-1-3
Ferreira R. Su-2-2
Fokin A. P. Wed-2-3, P-10
Fokina M. Su-1-2
Fukidome H. P-13

G
Gaborit G. Su-1-4
Gagkaeva Z. V. Wed-1-6
Galeeva A. V. Mo-2-2
Galin M. A. Thu-2-2, Thu-2-3
Gareev K. G. P-2
Gavdush A. A. Mo-4-1, Thu-1-4
Gavrilenko V. I. Su-2-1, Su-2-3, Mo-2-3, Tu-1-2, P-3, P-9, P-10
Gavrilova P. G. P-2
Gayduchenko I. Wed-1-2
Genina E. A. Sat-2-3
Giuliano B. M. Thu-1-4
Glinskiy I. A. Thu-1-1
Glyavin M. Yu. Wed-2-2, Wed-2-3, P-10
Goltsman G. N. Wed-1-2, Thu-2-1
Gorbenko I. Mo-1-2
Gorshunov B. P. Tu-3-2, Tu-3-3, Wed-1-4, Wed-1-6
Grinenko V. Wed-1-6
Grouiez B. Su-3-2
Gudkova S. A. Tu-3-2
Guillet J.-P. Sat-2-2, Sat-2-5, P-8

H
Hagelschuer T. Tu-3-1
Henini M. Tu-1-6
Herault E. Su-1-4
Hesler J. Su-2-5
Hindle F. Sat-2-1
Hmida F. Su-3-2
Hosotani T. P-6
Houard A. Sat-1-2
Hübers H.-W. Mo-2-3, Tu-2-3, Tu-3-1

I
Ikonnikov A. V. Tu-1-3, P-3
Il'inskaya N. D. Tu-1-4
Ionin A. A. Sat-1-1, Sat-1-3, Su-1-3
Ivlev A. V. Thu-1-4
Iwatsuki K. P-6

K
Kachorovskii V. Yu. Mo-1-2
Kadykov A. M. Mo-2-3
Kadyrov L. S. Wed-1-6
Kagan M. S. Tu-1-4
Kanaev A. Su-2-6
Karapuzikov A. A. Sat-2-1
Karasik V. E. Mo-4-1, Wed-1-1
Katyba G. M. Mo-4-1
Kaurova N. S. Thu-2-1
Kazakov A. S. Mo-2-2
Khabibullin R. A. Tu-1-5, Thu-1-1, P-4, P-11
Khodan A. N. Su-2-6
Khokhlov D. R. Mo-2-2
Khvalkovskiy N. A. Tu-1-4
Kiessling T. Mo-2-4
Kinyaevskiy I. O. Su-1-3
Kistenev Yu. V. Sat-2-1, Sat-2-3
Kleiner R. Thu-2-2
Klimachev Yu. M. Su-1-3
Klopf J. M. Tu-2-3
Klushin A. M. Thu-2-2, Thu-2-3
Knap W. Su-2-1, Mo-1-1 (no abstract), Mo-4-2
Knyazev B. A. Tu-2-3
Knyazkova A. I. Sat-2-1
Kochubey V. I. Sat-2-3
Koelle D. Thu-2-2
Kohn I. A. Tu-1-4
Kolker D. B. Sat-2-1
Komandin G. A. Mo-4-1, Thu-1-4
Komarov K. A. Mo-3-2
Komiyama T. P-13
Kontos T. Su-2-2
Kopylova D. S. Wed-1-4
Korolev D. V. P-2
Korytin A. I. Thu-1-3, Thu-1-5
Kosareva O. G. Sat-1-1, Sat-1-2, Sat-1-3
Kostyukova N. Yu. Sat-2-1
Kotelnikov I. A. Sat-1-4
Kovalevsky K. A. Tu-2-3
Kozlov A. S. Sat-2-5
Kozlov D. V. Mo-2-3

Krasilnik Z. F. Su-2-3
Krasnov V. M. Thu-2-2, Thu-2-3
Kravtsenyuk O. V. Sat-2-2, P-8
Krishtop V. G. Tu-1-6
Krishtopenko S. Su-2-1
Kryuchkov N. P. Mo-3-2
Kuftin A. N. Wed-2-3
Kulikov N. S. Su-2-3, Mo-2-3, Tu-1-2, P-5
Kulya M. S. Sat-2-2, P-8
Kurin V. V. Thu-2-2
Kurlov V. N. Su-2-6, Mo-4-1

L
Ladenkov I. V. Tu-1-3
Ladugin M. A. Tu-1-3
Lai N. D. Su-1-1
Lampin J.-F. Su-2-5
Lavrukhin D. V. Thu-1-1
Lazareva E. N. Sat-2-3
Ledoux-Rak I. Su-1-2
Leiman V. Wed-1-1
Litvinenko K. L. Tu-2-3
Loghmari Z. Su-2-4
Loidl A. Tu-3-3
Lunkenheimer P. Tu-3-3
Łusakowski J. Mo-2-1
Lynch S. A. Tu-2-3

M
Makarov V. A. Sat-1-4
Malygin V. I. P-10
Manceron L. Su-3-2
Mangeney J. Su-2-2
Maremianin K. V. Tu-1-3, P-4, P-10
Markelov A. A. Sat-2-1
Marmalyuk A. A. Tu-1-3
Mashinsky K. V. Wed-1-3
Mashkovich E. A. Thu-1-6
Maslov A. V. Thu-1-2, P-12
Massabeau S. Su-2-2
Matsev P. P. Wed-1-1
Mikhailov N. N. Su-2-1, Su-2-3, Mo-2-2, Mo-2-3, Tu-1-2, P-3, P-5, P-9, P-10, P-13
Minin I. V. Thu-1-1
Minin O. V. Thu-1-1
Mironov V. A. Thu-1-7
Mitin V. Wed-1-1
Mitrofanov A. V. Sat-1-5
Mityagin Yu. A. Sat-1-3
Mogorychnaia A. V. Wed-1-4
Moiseenko I. M. Wed-1-3
Mokrousova D. V. Sat-1-1, Sat-1-3
Molenkamp L. W. Mo-2-4
Morozkin M. V. Wed-2-3
Morozov M. Yu. Wed-1-5
Morozov S. V. Su-2-3, Mo-2-3, Tu-1-2, P-5, P-9, P-10, P-13
Mostert A. B. Wed-1-6
Motovilov K. A. Wed-1-6
Mouelhi M. Sat-2-1
Mounaix P. Sat-2-2, Sat-2-5, P-8
Mouret G. Sat-2-1
Müller B. Thu-1-4
Murdin B. Tu-2-3
Murzanev A. A. Thu-1-3

N
Nasibulin A. G. Wed-1-4
Nazarov M. M. Sat-1-5
Nguyen-Van H. Su-2-4
Nikolaev V. V. Sat-2-3
Nikolaeva I. A. Sat-1-2
Nishimura K. P-6
Novokovskaya A. L. P-7
Nozdrin Y. N. Tu-1-3

O
Odlyanitskiy E. L. Sat-2-2, P-8
Oladyshkin I. V. Thu-1-7
Omori Y. P-6
Orlita M. P-3
Otsuji T. Tu-1-1, Wed-1-1, P-6, P-13
Ozheredov I. Su-1-2

P
Padalitsa A. A. Tu-1-3
Palumbo M. E. Thu-1-4
Panchenko V. Ya. Sat-1-5
Panov N. A. Sat-1-1, Sat-1-2, Sat-1-3
Paprotskiy S. K. Tu-1-4
Parvitte B. Sat-2-1
Pavlov S. G. Tu-2-3
Pavlovskiy V. V. P-4
Peng Y. Sat-1-4
Perebeinos V. Wed-2-1

Petrov N. V. Sat-2-2, P-8
Pogosian T. N. Su-1-1
Pohl A. Tu-2-3
Polischuk O.V. Wed-1-3
Ponomarev D. S. Wed-1-1, Thu-1-1, P-4, P-11
Popov V. G. Tu-1-6
Popov V. V. Wed-1-3, Wed-1-5
Potapov A. A. Mo-4-1
Potemski M. P-3
Pozdniakova V. I. Tu-1-3, P-1
Pravdin A. B. Sat-2-3
Pripolzin S. I. Mo-4-2
Prokhorov A. S. Tu-3-2
Pronin A. A. Wed-1-6
Proskura A. L. Sat-2-5
Proyavin M. D. Wed-2-3

R

Ratushniak A. S. Sat-2-5
Razova A. A. P-9
Redlich B. Tu-2-3
Reshetov I. V. Mo-4-1
Riccardi E. Su-2-2
Richter H. Tu-3-1
Riemann H. Tu-2-3
Rizaev G. E. Sat-1-1, Sat-1-3
Rosticher M. Su-2-2
Rotger M. Sat-2-1, Su-3-2
Roy P. Su-3-1
Rudau F. Thu-2-2
Rumyantsev V. V. Su-2-3, Mo-2-3, Tu-1-2, P-5, P-9, P-10, P-13
Ryabova L. I. Mo-2-2
Ryabikin M. Y. Thu-1-3
Ryzhii M. Wed-1-1
Ryzhii V. Tu-1-1, Wed-1-1

S

Sagitova A. M. Su-1-3
Sanjuan F. Su-1-4
Satou A. P-6, P-13
Savinov M. Tu-3-3, Wed-1-6
Savinov S. A. Sat-1-3
Schlereth R. Mo-2-4
Sciré C. Thu-1-4
Sedov A. S. Wed-2-3
Seleznev L. V. Sat-1-1, Sat-1-3
Semenov A. V. Thu-2-1
Semenova A. V. P-2
Serdyukov D. S. Sat-2-5
Sergeev Y. A. Thu-1-3, Thu-1-5
Sidorov-Biryukov D.A. Sat-1-5
Sinko A. Su-1-2
Sirtori C. Su-2-3, Tu-1-2
Shalova A. V. Sat-1-1
Shastin V. N. Tu-2-2, Tu-2-3
Shchavruk N. V. P-4, P-11
Sheklanova E. Su-1-2
Shipilo D. E. Sat-1-1, Sat-1-2, Sat-1-3
Shirokova A. V. P-12
Shkurinov A. P. Sat-1-2, Sat-1-4, Sat-1-5
Shugurov A. I. Thu-1-6
Shur M. S. Mo-1-2, Wed-1-1
Shvachkina M. E. Sat-2-3
Smolyanskaya O. A. Sat-2-2, P-2, P-8
Solyankin P. M. Sat-1-4, Sat-1-5
Soylu G. Su-1-4
Stavrias N. Tu-2-3
Stepanov A. N. Thu-1-3, Thu-1-5
Suemitsu T. P-6
Sunchugasheva E. S. Sat-1-1
Svintsov D. Mo-3-1 (no abstract), Wed-1-2
Sychugin S. A. Thu-1-2

T

Tai E. M. Wed-2-3
Tarelkin S. A. Tu-2-3
Teissier R. Sat-2-4, Su-2-4, Tu-1-4
Teppe F. Su-2-1, Su-2-3, Mo-2-3, Tu-1-2
Terentiev S. A. Tu-2-3
Thomas V. Tu-3-3
Tignon J. Su-2-2
Titova N. A. Thu-2-1
Torgashev V. I. Tu-3-2, Tu-3-3
Tovpeko N. A. Thu-2-1
Tretyakov M. Yu. Su-3-1
Trifonov A. V. Thu-2-1
Trukhin V. N. P-2
Tsapenko A. P. Wed-1-4
Tsarev M. V. Thu-1-2
Tsvetkov A. I. Wed-2-3
Tsyplenkov V. V. Tu-2-3
Tuchin V. V. Sat-2-3, Mo-4-1
Tuchina D. K. Sat-2-3
Turut J. Su-2-5

U
Ushakov D. V. Tu-1-5, P-4
Usikova A. A. Tu-1-4
Utochkin V. V. Su-2-3, Mo-2-3, Tu-1-2, P-5, P-13
Uykur E. Tu-3-3

V
Vaks V. L. Sat-2-4, Mo-4-2
Vallon R. Sat-2-1
Valmorra F. Su-2-2
van der Meer A. F. G. Tu-2-3
Vasil'evskii I. S. Tu-1-4
Vinichenko A. N. Tu-1-4
Vinnik D. A. Tu-3-2
Volkov O. Yu. P-4
Volkov V. S. Thu-1-1

W
Watanabe T. Tu-1-1, P-13
Wienold M. Tu-3-1
Winnerl S. Tu-2-3
Wojtowicz T. Mo-2-1
Wróbel J. Mo-2-1

Y
Yablokov A. A. Mo-4-2
Yadav D. Tu-1-1
Yakovlev D. D. Sat-2-3
Yakovlev E. V. Mo-3-2
Yanina I. Yu. Sat-2-3
Yavorskiy D. Mo-2-1
Yegiyan S. R. Tu-3-2
Yurchenko S. O. Mo-3-2, Thu-1-4

Z
Zakhar'in A. O. Tu-2-1
Zapara T. A. Sat-2-5
Zasedatel V. S. Sat-2-1
Zaycev A. A. P-11
Zaytsev K. I. Sat-2-2, Su-2-6, Mo-4-1, Thu-1-1, Thu-1-4, P-8
Zéninari V. Sat-2-1
Zenov K. G. Sat-2-1
Zheltikov A. M. Sat-1-5
Zhevaikin K. Su-1-2
Zholudev M. S. P-9
Zhu Y. Sat-1-4
Zhukavin R. Kh. Tu-2-3
Zhukov S. S. Wed-1-4
Zhukova E. S. Tu-3-3, Wed-1-4, Wed-1-6

2nd Conference
of International Consortium on Terahertz Photonics and Optoelectronics

PROGRAM AND PROCEEDINGS

The Proceedings of the Conference were printed on the Risograph
of the Institute of Applied Physics RAS, 46 Ulyanov Street, Nizhny Novgorod, Russia

RJUSE-2019 timetable

July 8 (Monday)	July 9 (Tuesday)	July 10 (Wednesday)	July 11 (Thursday)
8:30-17:30 Registration	8:30-18:00 Registration	8:30-12:00 Registration	8:30-12:00 Registration
10:00-10:30 Opening Ceremony **Session Mo-1** **THZ plasmonic detectors** 10:30-11:10 W.Knap (plenary) 11:10-11:30 V.Kachorovskii (inv.)	**Session Tu-1** **THz sources** 9:00-9:40 T.Otsuji (plenary) 9:40-10:10 S.Morozov (invited) 10:10-10:30 A.Andronov (oral) 10:30-10:50 M.Kagan (oral) 10:50-11:10 A.Dubinov (oral) 11:10-11:30 V.Popov (oral)	**Session Wed-1** **Carbon nanostructures** 9:00-9:40 V.Ryzhii (plenary) 9:40-10:10 G.Fedorov (invited) 10:10-10:40 D.Fateev (invited) 10:40-11:00 S.Zhukov (oral) 11:00-11:20 M.Morozov (oral) 11:20-11:40 Z.Gagkaeva (oral)	**Session Thu-1** **THz time domain spectroscopy** 9:00-9:30 D.Ponomarev (invited) 9:30-10:10 M.Bakunov (invited) 10:00-10:20 S.Bodrov (oral) 10:20-10:40 A.Gavdush (oral) 10:40-11:00 A.Sergeev (oral) 11:00-11:20 A.Shugurov (oral) 11:20-11:40 I.Oladyshkin (oral)
11:30-12:00 Coffee break	11:30-12:00 Coffee break	11:40-12:10 Coffee break	11:40-12:10 Coffee break
Session Mo-2 **THz spectroscopy** **of semiconductor heterostructures** 12:00-12:30 J.Łusakowski (invited) 12:30-12:50 A.Kazakov (oral) 12:50-13:10 D.Kozlov (oral) 13:10-13:30 F.Bayer (oral)	**Session Tu-2** **Excitons & impurities** 12:00-12:30 A.Zakhar'in (invited) 12:30-13:00 V.Shastin (invited) 13:00-13:30 S.Pavlov (invited)	**Session Wed-2** **Grapen and gyrotrons** 12:10-12:40 V.Perebeinos (invited) 12:40-13:10 M.Glyain (invited) 13:10-13:30 A.Fokin (oral)	**Session Thu-2** **THz superconductor devices** 12:10-12:40 G.Goltsman (invited) 12:40-13:00 A.Klushin (oral) 13:00-13:20 M.Galin (oral) 13:20-13:40 **Closing remarks**
13:30-15:00 Lunch	13:30-15:00 Lunch	13:30-15:00 Lunch	13:40-15:00 Lunch
Session Mo-3 **THz photonics** 15:00-15:30 D.Svintsov (invited) 15:30-16:00 S.Yurchenko (invited)	**Session Tu-3** **THz spectroscopy** 15:00-15:30 H.-W.Hübers (invited) 15:30:15:50 S.Yegiyan (oral) 15:50-16:10 M.Belyanchikov (oral)	15:00-18:00 **Excursion**	
16:00-16:30 Coffee break	16:10-16:30 Coffee break		
Session Mo-4 **Medical diagnostics** 16:30-17:00 K.Zaytsev (invited) 17:00-17:20 V.Vaks (oral)	16:30-18:00 **Poster Session**	19:00-21:30 **Banquet**	